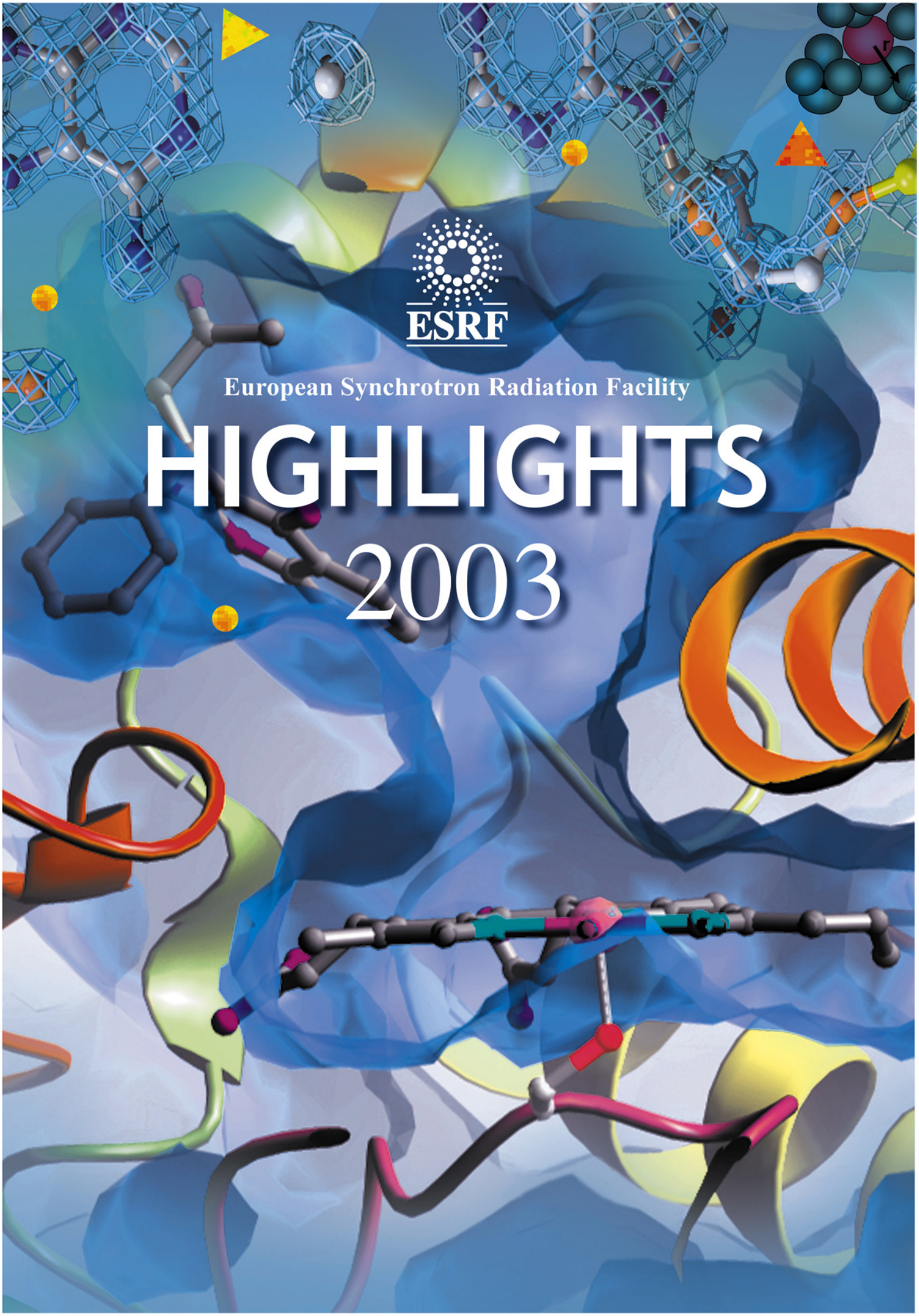
ESRF
European Synchrotron Radiation Facility
HIGHLIGHTS
2003

ESRF

HIGHLIGHTS 2003

Contents

Introduction

Over the last year there has been substantial progress in the realisation of the **Partnership for Structural Biology**. At its December meeting, the ESRF Council gave the go-ahead for our participation in the PSB laboratory / office building, to be shared with the *Institut de Virologie Moleculaire et Structurale* (IVMS) of the *Université Joseph Fourier.* This is a crucial step forward as the building will be the true centre of the Partnership where teams from the ESRF, the EMBL, the ILL and the IBS will work together on structural biology programmes focussed on human health issues. At the ESRF, the first branch of the new macromolecular crystallography beamline ID23 has already taken its first data sets and will be further enhanced by the installation of an automatic sample changer. However, the most significant event scientifically was the PSB Science Day, held at the *Château de Sassenage* on 11 December. Speakers from the institutions involved in the PSB presented an exciting programme of work, either in progress or planned, demonstrating the scientific maturity and scientific added value of the PSB. The current year will see a further consolidation of this project, of importance at the European level, with, for example, the start of construction of the PSB building and major progress on the second diffraction branch of ID23.

S. Larsen, S. McSweeney and E. Mitchell during their presentations at the PSB Science Day at the Chateau de Sassenage on 11 December 2003.

As is shown in more detail in the Chapter on the **X-ray Source**, the Machine's very efficient performance continued in 2003. The beam availability was close to 98% of the scheduled time, an excellent performance considering that severe problems were encountered with the High Quality Power Supply, which cuts in to bridge the gap when there are voltage drops on the external electrical supply. Since February 2003, the storage ring has been refilled without closing the front-end shutters on the beamlines (*injection with front-ends open*). In this way the sensitive optical elements of the beamlines do not suffer the thermal variations inherent in the previous procedure of closing the shutters during injection. This new mode of operation further increases the efficiency of the ESRF's operation; many beamlines can continue to take data during re-injection.

Many of our complex projects require close **collaboration between the different divisions, services and groups**. A good example is the modernisation of the Machine control system, a close collaboration between the Computing Services and the Machine Division. After more than ten years of reliable and stable operation, major progress has been made over the last twelve months on a complete overhaul of the vacuum control system. This project will continue throughout 2004 and completion is expected during 2005.

Each year international **workshops and conferences** on a remarkably diverse range of topics are held at the ESRF. During 2003, the Machine Division organised a workshop on superconducting insertion devices and was host to the European Synchrotron Light Source (ESLS) workshop which brings together accelerator experts from all European synchrotron sources. Experiments Division staff were responsible for a large number of workshops, including meetings on X-ray detectors, hard X-ray spectroscopy, inelastic scattering, radiation damage to biological crystalline samples, and X-ray absorption spectroscopy. In addition, the ESRF was the venue for the 2003 Younger European Chemists' Conference. It is important also that the work of the ESRF be understood and appreciated in our local community as well as in the worldwide scientific community. The success of the ESRF Open Days in March, the first to be held since

2000, demonstrated the level of interest in the Grenoble area in the ESRF. Over the weekend of the Open Days almost 2000 visitors listened intently to the presentations on science at the ESRF and challenged our staff with demanding and perceptive questions.

P. Elleaume and S. Milton (APS) discuss the SASE-type undulators at the Workshop on Superconducting Undulators and Wigglers, held at the ESRF on 30 June 2003.

There was also a focus on **internal communication** in the latter part of the year as a large number of staff were involved in working groups discussing staffing and organizational issues as part of a Personnel Audit, launched in June and carried out by PROFIL, a Lyon-based consultancy firm. This audit, coming almost ten years after the inauguration of the ESRF, dealt with a number of fundamental questions including: Is the ESRF appropriately organized for its purpose? Are the different units appropriately staffed, quantitatively and qualitatively? The preliminary findings and recommendations of the consultants were presented to the staff in early January 2004. They focus on an intensified project-oriented culture with stronger and more coherent management. The detailed report will be discussed with an international panel of experienced laboratory managers. Management's intention is to consider the implementation of the detailed recommendations in close and continued dialogue with the ESRF's staff.

Turning to **membership matters**, it is gratifying to record that in January 2003 the Austrian Academy of Sciences joined the ESRF as the third Scientific Associate, while Portugal, a Scientific Associate since 1998, decided to renew its agreement with the ESRF. In an informal ceremony at the ESRF, Professor Thomaz, Portuguese Secretary of State for Science and Technology, and Professor Comès, Chairman of the Council of the ESRF, signed a contract for a further five years. A similar renewal contract has been agreed with the Academy of Science and Humanities of Israel. This will be signed at a ceremony in Jerusalem during January 2004, as part of a workshop on Israeli science carried out at the ESRF. Throughout 2003, contacts have continued with several countries potentially interested in joining the ESRF. The discussions with Poland and Slovakia are at the most advanced stage, whilst preliminary contacts with the Greek scientific community have demonstrated a strong interest in the benefits of ESRF membership.

The next few years will be critical for the ESRF. The current **Convention**, signed in 1988 between the 12 partner countries, was concluded for an initial period ending on 31 December 2007. The ESRF Council has started to consider a possible renewal of this Convention for a further ten-year period. In parallel, Management has initiated discussions on an ambitious long-term strategy. This will be concerned with all aspects of the ESRF's activities such as new scientific directions, the future development of the X-ray source, new and modified beamlines, personnel issues, and infrastructure requirements. The Science Advisory Committee enthusiastically discussed a draft document outlining our ideas for the long-term development of the ESRF. The Users' Meeting of February 2004 will be focussed on a further discussion of the long-term strategy, which will be a crucial component of the case for renewal of the Convention.

The Highlights 2003 provides an overview of the activities of the ESRF. As in previous years, the ESRF's users and staff have studied a very wide range of science on the forty beamlines. Scientific work at the ESRF has resulted in a total of over 1000 refereed publications for the year 2003. We hope that you enjoy reading about the life and work of the ESRF and that 2004 proves likewise to be a year of progress and success.

W.G. Stirling, R. Dimper, P. Elleaume, H. Krech, S. Larsen, F. Sette, P. Thiry, K. Witte

(January 2004)

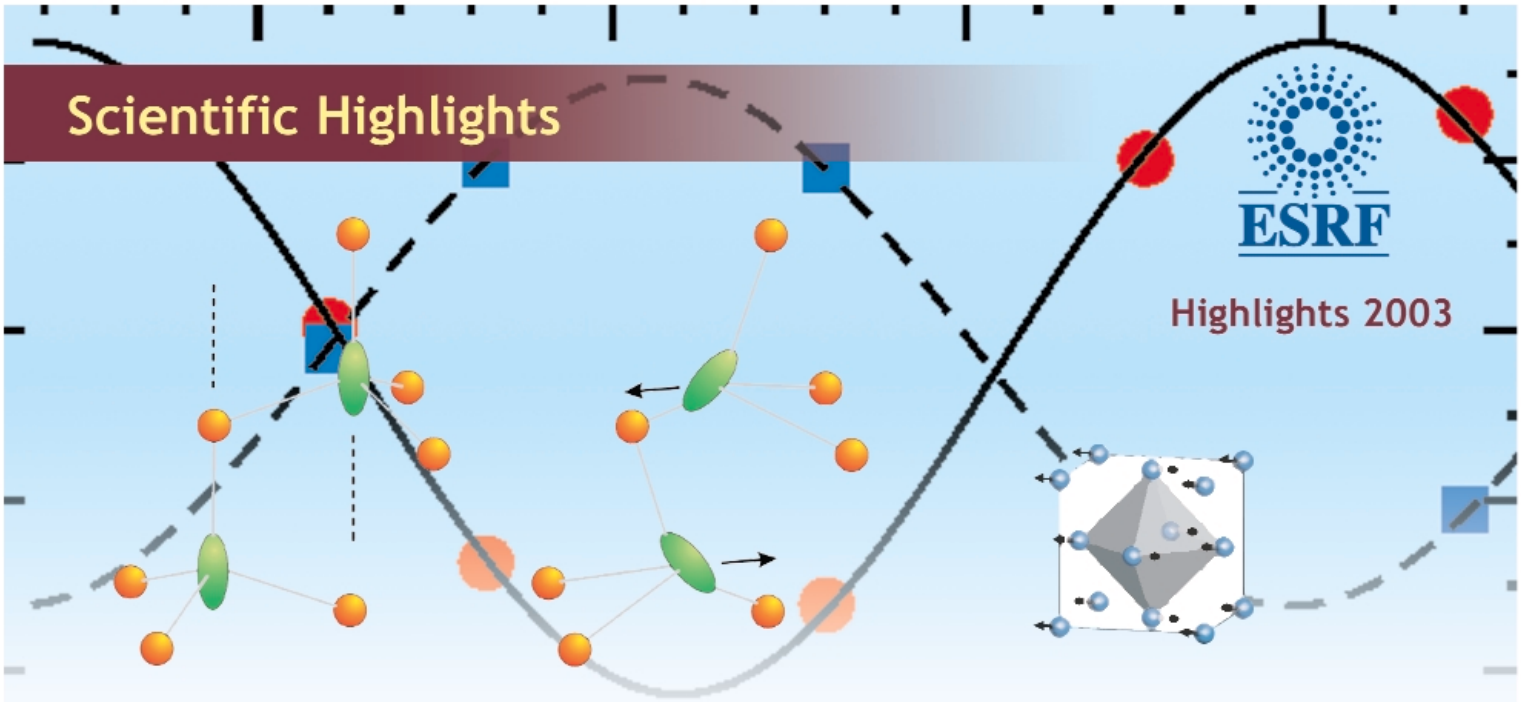

High Resolution and Resonance Scattering

Introduction

A large variety of experiments covering a wide range of scientific topics and applications were conducted on the beamlines of the High Resolution and Resonance Scattering Group in 2003. Since it is impossible to report on all of them, two main areas have been selected: "Studies under extreme conditions" and "Studies of glasses and disordered systems". Both topics are excellent examples of the complementarity of the different techniques and the increasing complexity of the sample environment (high-pressure, external magnetic fields and low/high temperatures).

Another important research field deals with nano-structured materials, surfaces, interfaces, and multilayers. First investigations on diffusion of iron within iron films on MgO and in iron islands (coverage about half a monolayer) on vicinal tungsten showed an enhanced diffusion characteristic compared with bulk [1]. Magnetic properties of iron islands on tungsten could be investigated utilising nuclear resonance scattering techniques and a newly-applied theoretical formalism [2]. Further activities comprise the study of the high-frequency dynamics in quantum liquids such as neon [3]. Finally, the determination of the phonon dispersion in tiny single crystals (down to a few 10^{-5} mm^3) remains an active field of investigations. Examples are the studies on $HgBa_2CuO_4$ [4] and graphite [5].

Beamline instrumentation and sample environments were also an important area of effort, complementing the scientific research. Along with the optimisation of insertion devices for highest brilliance, cooling of the first optical element (the high heat-load monochromator) is crucial for our beamlines. Studies show that the applied cryogenic cooling scheme is capable of preserving the quality of the most powerful beam delivered by the X-ray source to date. Furthermore, this system should be able to handle the higher heat-loads envisaged in the future [6]. The demand for the investigation of micrometre-sized and "nano-structured" materials makes micro-focusing indispensable. Thanks to the in-house development by the Optics group, Kirkpatrick-Baez (KB) optics and compound refractive lenses (CRL) have been, or will be, installed at all our beamlines

The closing article on "Thermal-motion-induced Scattering from Zinc Oxide" from the CRG beamline BM28 shows nicely that "forbidden" reflections are not only the privilege of nuclear resonance scattering but may also appear due to electronic resonances.

R. Rüffer

References

[1] M. Sladecek *et al., Surface Science* **507-520**, 124 (2002); M. Sladecek *et al., Surface Science* (2004).
[2] R. Röhlsberger *et al.*, *Phys.Rev.* B **67**, 245412 (2003).
[3] A. Cunsolo *et al.*, *Phys.Rev.* B **67**, 024507 (2003).
[4] M. D'Astuto *et al.*, *J. Phys.: Cond. Matt.* **15**, 8827 (2003).
[5] J. Maultzsch *et al.*; *Phys. Rev. Lett.*, in print.
[6] A.I. Chumakov *et al.*, article in the Methods and Instrumentation chapter of this Highlights.

Structural and Dynamical Studies under Extreme Conditions

Introduction by G. Wortmann, Universität Paderborn (Germany) and M. Krisch, ESRF

The investigation of materials under extreme conditions such as high pressure and high temperature constitutes an important field in modern condensed matter research, covering a large variety of disciplines including solid-state physics, materials design, and earth and planetary science. The high brilliance of undulator-based X-ray sources, together with important progress in focusing optics, makes it possible to obtain spot sizes in the few micrometre range, and thus to perform experiments routinely at multi-megabar (1 Mbar = 100 GPa) pressures. Coupling pressure with temperature and/or magnetic fields further extends our knowledge about the phase diagram as well as the electronic and magnetic properties of materials.

High-pressure instrumentation comprises, besides the widely utilised diamond anvil cell (DAC), large volume cells such as, the Paris-Edinburgh cell, where temperatures up to 2300 K at 10 GPa can be reached. This temperature range can now be further extended by combining DAC experiments with laser heating thus reaching the conditions of Earth and planetary cores. On the other end of the temperature scale, specially designed cryomagnets, compatible with DACs, give access to magnetic studies in the few Kelvin regime.

X-ray diffraction (XRD) is historically the first and still the most wide-spread synchrotron radiation based high-pressure technique, providing invaluable insight into structural properties and phase stability of solids. The outstanding characteristics of third generation synchrotron X-ray sources have helped to push the frontiers of XRD further, and also extended studies under extreme conditions to other synchrotron techniques. Amongst these are inelastic X-ray scattering (IXS) and nuclear resonant scattering (NRS). For example, IXS and nuclear inelastic scattering (NIS), both with meV resolution, are now applied well above 1 Mbar to study lattice dynamics and sound velocities in samples of actual geophysical interest, such as the high-pressure phase of iron (ε-Fe) and iron bearing compounds [1-4]. Magnetic and electronic properties under extreme conditions can be studied by nuclear forward scattering (NFS), thus complementing other synchrotron radiation based spectroscopies such as X-ray magnetic dichroism, magnetic scattering and absorption techniques. X-ray emission spectroscopy may probe local magnetic spin moments, as exemplified in a high-pressure study of the high-spin/low-spin transition in a Fe mineral of the Earth´s lower mantle, presented in the following article.

As in the case of ε-Fe, it is often the complementarity and interplay of different synchrotron radiation techniques that helps to advance the understanding and to identify future challenges. This is demonstrated in the following selected highlights. SmS is a compound well-known for its first-order valence transition. A NFS study detected for the first time magnetic order in SmS at pressures above 2 GPa, where Sm is trivalent. An IXS study of the same system [5] revealed a soft mode in the LA[111] phonon branch in the same pressure range, speculatively connected with the possible occurrence of superconductivity. In a similar way, complementary structural and dynamical studies constitute a very powerful ensemble as is nicely exemplified in the studies of caesium in the bcc and fcc crystal structure as well as of the polymorphism in liquid phosphorus.

The selected highlights on studies under extreme conditions give a representative cut through the various techniques utilised in the High Resolution and Resonance Scattering Group, and show the rich diversity of the investigated topics.

References

[1] R. Lübbers, H.F. Grünsteudel, A.I. Chumakov and G. Wortmann, *Science* **287**, 1250 (2000).
[2] G. Fiquet, J. Badro, F. Guyot, H. Requardt and M. Krisch, *Science* **291**, 468 (2001).
[3] H.-K. Mao *et al.*, *Science* **292**, 914 (2001).
[4] G. Fiquet *et al.*, *accepted in Physics of the Earth and Planetary Interiors*.
[5] S. Raymond *et al., Phys. Rev.* **B** 66, 220301 (2002) and *ESRF Highlights 2002*, page 55.

Iron Partitioning in the Earth's Mantle: Layering and Deep Lower-Mantle Heterogeneities

Recent seismic observations [1] suggest that compositionally distinct domains exist in the Earth's lower mantle, with a boundary located between 1700 and 2300-km depths. In order to interpret these observations, the chemical and physical properties of the dominant phases in the lower mantle, namely $(Mg,Fe)SiO_3$ magnesium silicate perovskite and (Mg,Fe)O ferropericlase have to be determined at the pressure and temperature conditions of the deep mantle. Due to the thermodynamic stability of these phases at the pressure and temperature conditions of the lower mantle, one cannot explain such geophysical observations on the basis of a chemical breakdown or a structural phase transition, as in the case of other seismic discontinuities. On the other hand, more subtle effects, driven by the chemistry of iron in the lower mantle, can affect the iron content in perovskite and ferropericlase, *i.e.* the partition coefficient of iron between the two compounds.

We measured the spin state of iron in ferropericlase ($Mg_{0.83}$ $Fe_{0.17}$)O at high pressure and found a high-spin to low-spin transition occurring in the 60 to 70 gigapascal pressure range (**Figure 1**), corresponding to depths of 2000 kilometers in Earth's lower mantle. The measurements were performed on beamline **ID16** at the ESRF. It has been predicted [2] that such a transition would increase the partition coefficient of iron between ferropericlase and perovskite by several orders of magnitude, almost entirely depleting perovskite from its iron. Since the transition pressure increases with temperature and with iron content, the transition will be gradual and spread over a large range of depths rather than a sharp discontinuity, consistent with seismic observation of heterogeneities [1]. The transition could also be accompanied by phase separation between iron-rich high-spin and magnesium-rich low-spin ferropericlases.

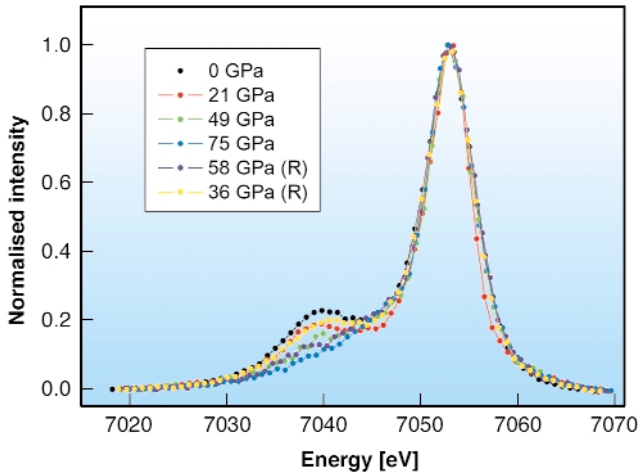

Fig. 1: X-ray emission spectra collected on ferropericlase ($Mg_{0.83}$ $Fe_{0.17}$)O at different pressures. The presence of a satellite structure (Kβ′ line) on the low energy side of the iron main emission line ($K\beta_{1,3}$ line) is characteristic of a high spin *3d* magnetic moment. This structure collapses at high pressure upon compression, and then reforms upon pressure decrease (spectra annotated with letter "R" in the legend).

Perovskite is the major lower-mantle phase, and iron-free perovskite is much more viscous that iron-rich perovskite, implying the transition could have a fairly strong rheological signature, and could affect the geodynamics in the lowermost mantle. Investigation of that matter could contribute to constrain geodynamical interpretations of the seismic observations, and quantify the effect of such a viscous layer on the dynamics of plumes. It should also be noted that such a layering model requires no isolated convection cells, as the chemistry of the two layers is reversible as a function of depth (the transition is reversible upon decompression); uplifted materials will recover the partitioning properties of the top layer.

In conclusion, we provide a mineral-physics basis for lower-mantle layering and chemical heterogeneities. The upper layer would consist of a phase mixture with about equal partitioning of iron between magnesium silicate perovskite and ferropericlase, whereas the lower layer would consist of almost iron-free perovskite and iron-rich ferropericlase. This stratification is likely to have profound implications for the transport properties of the Earth's lowermost mantle.

References

[1] R. van der Hilst and S. Kárason, *Science* **283**, 1885 (1999).

[2] E. Gaffney and D.L. Anderson, *J.Geophys. Res*. **78**, 7005 (1973).

Principal Publication and Authors

J. Badro (a), G. Fiquet (a), F. Guyot (a), J.-P. Rueff (b), V.V. Struzhkin (c), G. Vankó (d), and G. Monaco (d), *Science* **300**, 789 (2003).

(a) LMCP, Université Paris VI, Inst. de Phys. du Globe de Paris (France)

(b) LMR, Université Paris VI (France)

(c) Geophysical Labo., Carnegie Institution of Washington (USA)

(d) ESRF

Pressure-induced Magnetic Order in Non-magnetic SmS

The physics of magnetic quantum critical points (QCPs) is currently attracting much interest, especially after the discovery of the appearance at a QCP of unconventional superconductivity and of the causative role of spin and charge fluctuations. In this respect, one of the classes of systems whose electronic and magnetic properties deserve to be more deeply understood is that of strongly correlated 4*f* electron systems known as Kondo insulators [1]. Among them, SmS is known since the 70's to be a non-magnetic (Sm^{2+}) semiconductor at ambient pressure (black phase). It becomes metallic (golden phase) under the effect of a modest pressure (0.65 GPa at room temperature), at which the Sm ions are in an intermediate valence state. So far it has been considered that, by increasing further the pressure, the golden phase could evolve into a magnetic state where the Sm ions are trivalent (Sm^{3+}). Despite the numerous attempts to find this magnetic phase, to date there has been no clear evidence of it [2].

The availability of an intense X-ray beam which can be focussed to a tiny spot matching the size of a sample in a diamond anvil cell makes it now possible to perform high-pressure nuclear resonant scattering experiments at beamline **ID22N**. Here we have applied ^{149}Sm nuclear forward scattering to study the electronic properties of SmS across its complicated pressure-temperature

phase diagram. Our results give the first direct evidence that a magnetic ground state appears for SmS at a pressure of 2 GPa.

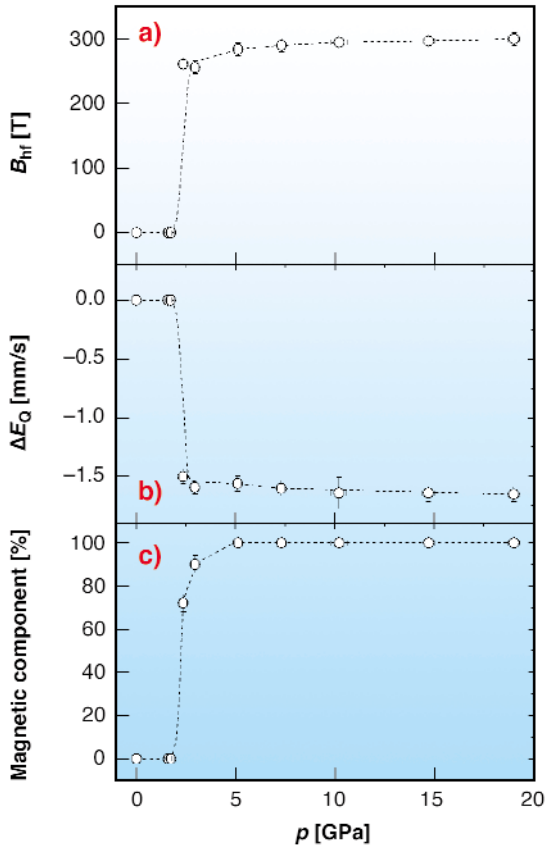

Fig. 2: Pressure dependences of (a) the magnetic hyperfine field (B_{hf}), (b) the quadrupole splitting (ΔE_Q) and (c) the magnetic component fraction at T = 3 K. The dashed lines through the data points are guides to the eye.

Figure 2 shows the pressure dependence of the hyperfine parameters (magnetic hyperfine field B_{hf} and electric quadrupole splitting ΔE_Q) and of the magnetic component fraction at 3 K. The pressure-induced phase transition from a non-magnetic state (where the hyperfine parameters at the ^{149}Sm nuclei are zero) into a magnetically-ordered state at $p_c \approx 2$ GPa is evident. The steep variation of both B_{hf} and ΔE_Q as well as the coexistence of the low and high-pressure phases in the vicinity of p_c point towards a first-order transition. The absolute values of B_{hf} and ΔE_Q are consistent with the occurrence of a Γ_8 crystal field ground state for the Sm^{3+} ions, with a magnetic moment of the order of 0.5 μ_B. The high-pressure magnetically-ordered phase is stable up to at least 19 GPa, as shown by the very weak pressure dependence of the hyperfine parameters and by the increase with pressure of the ordering temperature T_m (see **Figure 3**).

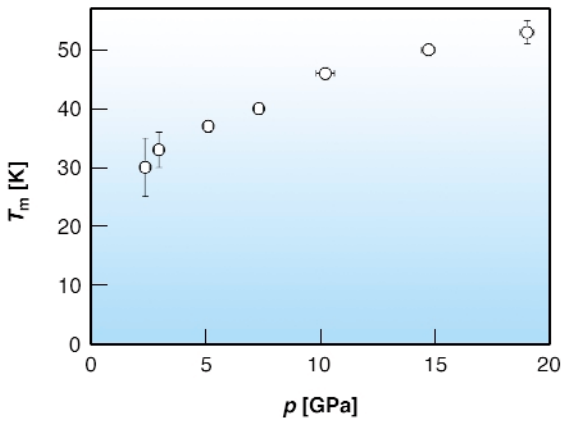

Fig. 3: Pressure dependence of the magnetic-ordering temperature T_m of SmS.

In conclusion we have used the microscopic probe of ^{149}Sm nuclear forward scattering to obtain the first clear evidence of the existence at pressures greater than about 2 GPa of a magnetically-ordered ground state in SmS. These results constitute a strong basis for further experimental and theoretical work.

References

[1] For an overview see P. Wachter, in *Handbook on the Physics and Chemistry of Rare Earths, Vol. 19*, edited by K. A. Gschneidner Jr., L. Eyring, G.H. Lander and G.R. Choppin, (North-Holland, Amsterdam, 1994), p. 383.
[2] V.N. Antonov, B.N. Harmon and A.N. Yaresko, *Phys. Rev. B* **66**, 165208 (2002).

Principal Publication and Authors

A. Barla (a), J. P. Sanchez (b), Y. Haga (b,c), G. Lapertot (b), B. P. Doyle (a), O. Leupold (a), R. Rüffer (a), M. M. Abd-Elmeguid (d), R. Lengsdorf (d), J. Flouquet (b), accepted by *Phys. Rev. Lett.*
(a) ESRF
(b) CEA, Grenoble (France)
(c) Japan Atomic Energy Research Institute, Tokai (Japan)
(d) Universität zu Köln (Germany)

Inelastic X-ray Scattering in Cs under Pressure

At ambient conditions, the alkali metals are considered as prototype examples of nearly-free-electron metals, the so-called “simple metals”. All of them adopt the high-symmetry body-centred cubic (bcc) crystal structure. Pressure-induced structural phase transitions in the alkali metals have been studied in much detail since Bridgman’s pioneering works on Cs in the 1930’s. Under pressure, all alkali metals undergo a transition to the face-centred cubic (fcc) structure and subsequently to a variety of lower-symmetry structures. In recent years, very complicated crystal structures of several high-pressure phases of the heavier alkali elements have been observed – a brief overview is given in [1].

Theoretical treatments have been quite successful in reproducing the observed structural sequences as a function of pressure. Most of these studies considered the

energetics of the static lattice. Structural transitions may, however, also be driven by dynamical instabilities due to phonon softening near or at the Brillouin-zone boundary. In the case of Cs, this issue was addressed in recent theoretical investigations [2]. Their central result is the prediction of a pronounced phonon softening near the upper limit of the fcc-Cs stability range (~ 4 GPa) that could lead to a dynamical instability of the fcc phase with increasing pressure. Hardly any experimental data have been available to test these important and unexpected predictions.

Therefore we performed an inelastic X-ray scattering (IXS) study of the longitudinal acoustic (LA), ***Q*** = (1 0 0) phonons in the bcc and fcc phases of Cs at pressures up to 4 GPa (upper stability limit of fcc Cs), at beamline **ID28**. The monochromatic beam with a photon energy of 17.8 keV was focused onto a 250-μm Cs sample in a diamond anvil cell (DAC). The scattered photons were analysed by a high-resolution Si analyser giving an overall spectral resolution of 3.0 meV. Cs crystals were grown in the DAC by heating the Cs sample close to its melting line and then cooling it slowly to ambient temperature. The *in situ* crystal growth was monitored by X-ray diffraction at the beamline **ID09**.

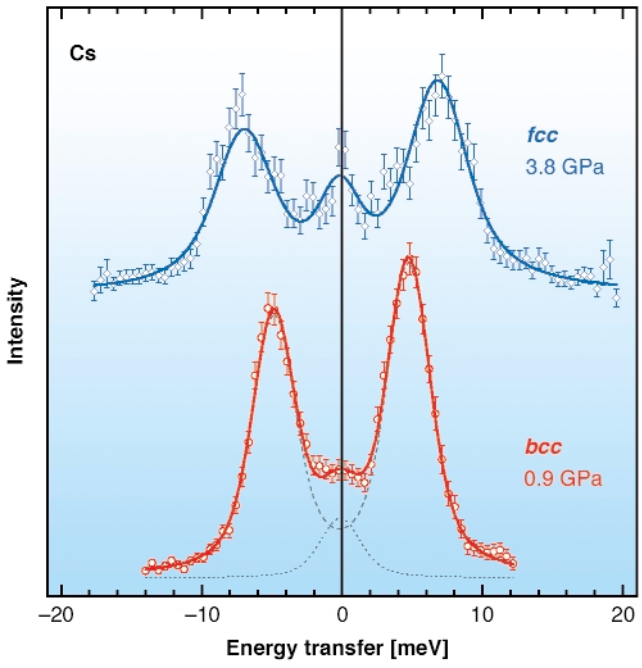

Fig. 4: Inelastic X-ray scattering spectra of Cs at Q = (1 0 0) in its bcc and fcc phases (T = 300 K). The open symbols represent the experimental data. The solid line corresponds to the best fit to a model function composed of Lorentzians for the phonon contribution (dashed lines) and the elastic contribution (dotted line), convoluted with the experimental resolution function.

The IXS spectra of bcc and fcc Cs (**Figure 4**) exhibit well-defined Stokes- and anti-Stokes peaks of the LA zone-boundary phonons. It should be noted that the ambient-pressure phonon energy of ~ 4 meV (≈ 30 cm^{-1}) is rather small, which made the experiment quite challenging.

The pressure dependences of the phonon energies are depicted in **Figure 5**. In the bcc phase, the phonon frequency initially increases with pressure as expected, but with a slope approaching zero near the bcc–fcc transition. In the fcc phase the LA-(1 0 0) phonon frequency is pressure independent within the experimental uncertainty. Our experiments were complemented by first-principles calculations. They also indicate an anomaly near the bcc–fcc transition (**Figure 5**), although not quite as pronounced as in the experiment. The general picture that emerges from the experimental and theoretical results is that of (i) a gradual decrease of the pressure dependence of the bcc LA-(1 0 0) phonon frequency when the bcc–fcc transition is approached and (ii) an anomalously small pressure dependence in the fcc phase, with a small softening near the upper fcc stability limit in the calculation. This picture is consistent with experimental results on the spatially averaged sound velocities in polycrystalline Cs at high pressures by Voronov *et al*. [3].

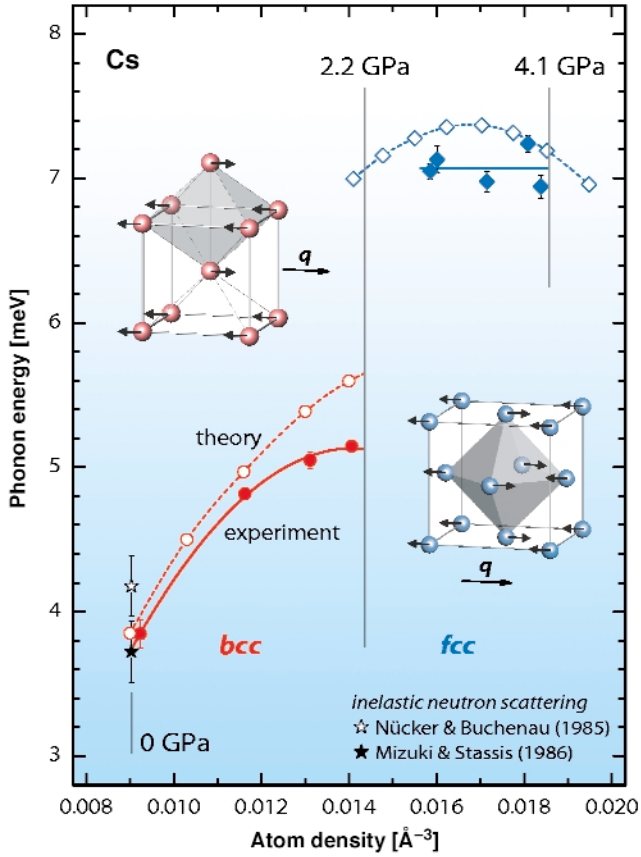

Fig. 5: Experimental and calculated phonon energies of Cs in the bcc and fcc phases. Solid symbols and lines refer to the experimental data, open symbols and dashed lines to the theoretical data.

The inelastic X-ray scattering experiments and corresponding calculations outlined here provide clear evidence of anomalies in the lattice dynamics of Cs near the bcc–fcc phase transition and in the fcc-phase. These results substantiate and refine the unexpected predictions of recent theoretical work, and they appear to be relevant also for other heavy alkali metals.

References

[1] K. Syassen in *Proceedings of the International School of Physics "Enrico Fermi" Course CXLVII*, Eds. R. J. Hemley *et al.*, pp 251–273 (2002).

[2] N. E. Christensen *et al.*, *J. Phys.: Condens. Matter* **12**, 3293 (2000) & *Phys. Rev.* B **61**, R3764 (2000); J. Xie *et al.*, *Phys. Rev.* B **62**, 3624 (2000); Y. Kong and O. Jepsen, *J. Phys.: Condens. Matter*, **12**, 8973 (2000).

[3] F. F. Voronov, O. V. Stal'gorova, and E. L. Gromnitskaya, *J. Exp. Theor. Phys.*, **95**, 77 (2002).

Principal Publication and Authors

I. Loa (a), K. Kunc (a), K. Syassen (a), M. Krisch (b), A. Mermet (b), and M. Hanfland (b), *High Pressure Res.* **23**, 1 (2003).

(a) MPI für Festkörperforschung, Stuttgart (Germany)
(b) ESRF

Joint Study of Structure and Dynamics across the First-order Phase Transition in Fluid Phosphorus

Liquid-liquid transitions, *i.e.* first-order transitions between two liquid states characterised by different local structures and thermodynamic properties, are common in multi-component systems and liquid crystals, where composition and molecular orientation are the respective order parameters. Recently, the possible occurrence of liquid-liquid transitions in pure, isotropic liquids has been suggested [1], thus stimulating the development of models and computer simulations, where these transitions are indeed possible. From the experimental side, however, the support for the existence of these transitions is still rare and even controversial, mainly as a consequence of the technical difficulties of the experiments reported so far. However, a remarkably clear example of a pure, isotropic system displaying a liquid-liquid transition has recently been discovered in phosphorus [2]. There, an abrupt, pressure-driven, reversible structural transformation between a low-pressure molecular liquid and a high-pressure polymeric liquid has been reported at a temperature of 1050°C and a pressure of about 1 GPa [2]. Here we further study this interesting case with the aim of characterising the structural and dynamical changes across the transition with diffraction and inelastic X-ray scattering experiments, respectively.

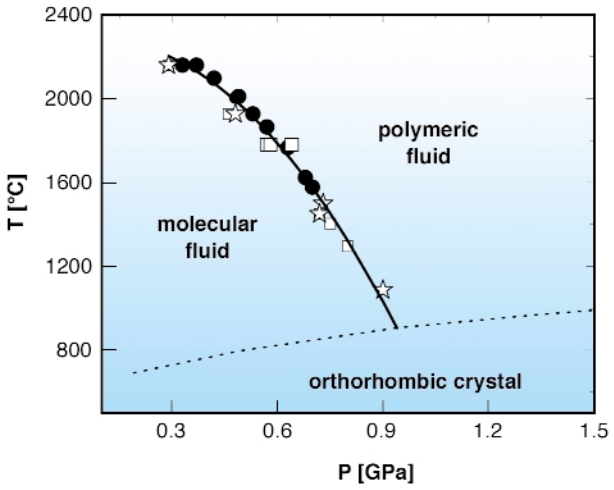

Fig. 6: Phase diagram of phosphorus at high temperature and pressure. Stars correspond to coexistence points; solid circles and open squares correspond to data in the polymeric and in the molecular phase, respectively; the full line is the second order polynomial that best represents the transition line; the dotted line is the melting line of orthorhombic phosphorus.

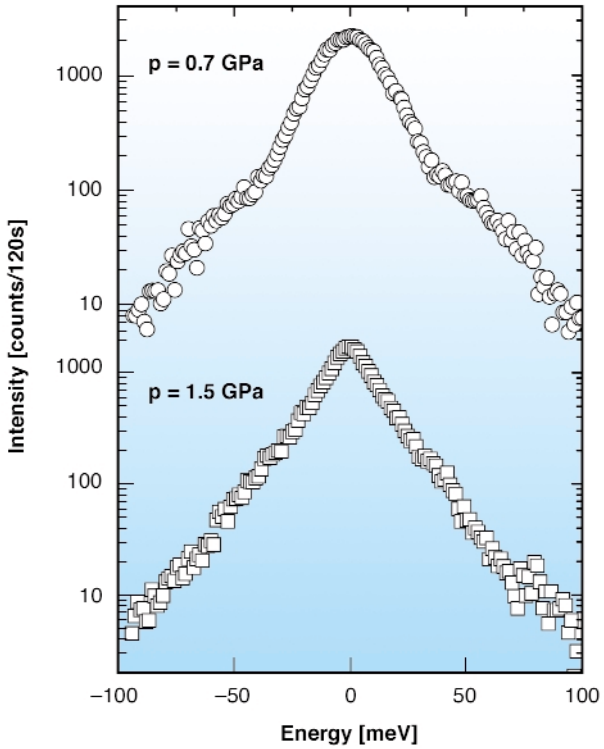

Fig. 7: Inelastic X-ray scattering spectra of the molecular form of fluid phosphorus at T = 1300°C and p = 0.7 GPa (upper spectrum) and of the polymeric form of fluid phosphorus at T = 1300°C and p = 1.5 GPa (lower spectrum). Both spectra have been collected at q = 4.3 A^{-1}.

The diffraction experiment has been carried out at beamline **ID30** using a Paris-Edinburgh large volume apparatus to reach the extreme thermodynamic conditions of interest here. As the diffraction patterns of the two fluids of phosphorus are clearly distinguishable [2], we could measure the transition line over an extended temperature range up to 2200°C at 0.3 GPa (**Figure 6**). The addition of the high-pressure high-temperature data to the known phase diagram of phosphorus allows us to conclude that this is a first order transition between a dense molecular fluid and a polymeric fluid. The slope of the transition line is negative in the whole of the explored thermodynamic

range, which implies that the entropy of the polymeric fluid is larger than that of the molecular one. Actually, from the shape of the transition line, a thermodynamic characterisation of the transition is obtained in terms of latent heat and internal energy change.

The Inelastic X-ray Scattering (IXS) experiment has been carried out at **ID16** using a high-pressure set up similar to that used for the diffraction measurements. IXS spectra of fluid phosphorus were collected on both sides of the first-order transition at T = 1300°C and p = 0.7 GPa in the molecular fluid phase and at T = 1300°C and p = 1.5 GPa in the polymeric fluid one. At each of these thermodynamic points a series of spectra was collected for several q values between 2.0 and 13.0 A^{-1}. For q values up to 4.3 A^{-1} the spectral intensities of the two fluids show pronounced differences (**Figure 7**) which can be interpreted in terms of their different vibrational dynamics. At higher q, however, the spectral intensities of the two fluids become more and more similar, thus suggesting that the polymeric fluid keeps a local structure very similar to that of the molecular one. These results, together with the thermodynamic characterisation of the transition, give us hints on how to better understand the nature of this unusually abrupt polymerisation process in fluid phosphorus.

References

[1] P.H. Poole, F. Sciortino, U. Essmann, and H.E. Stanley, *Nature*, **360**, 324-328 (1992).
[2] Y. Katayama, T. Mizutani, W. Utsumi, O. Shimomura, M. Yamakata, and K.A. Funakoshi, *Nature*, **403**, 170-173 (2000).

Principal Publications and Authors

G. Monaco (a), S. Falconi (b), W. Crichton (a), M. Mezouar (a), *Phys. Rev. Lett.,* **90**, 255701 (2003); S. Falconi (b), G. Monaco (a), W. Crichton (a), M. Mezouar (a), R. Verbeni (a), in preparation.
(a) ESRF
(b) Universita' di Roma Tre (Italy)

High Resolution Inelastic Scattering in Disordered systems

Introduction by G. Ruocco, Universitá di Roma "La Sapienza" and Istituto Nazionale di Fisica della Materia, Roma (Italy)

High-resolution Inelastic X-ray Scattering techniques are spectroscopic tools particularly suited for the investigation of single particle and collective dynamics in disordered systems. A significant effort has been put into developing these technique over the last ten years at the ESRF, with the construction of state-of-the-art beamlines: ID16 and ID28 for Inelastic X-ray Scattering (IXS), ID18/22N for Nuclear Resonance Scattering (NRS) and both ID16 and ID26 for Raman Scattering. The inelastic-scattering capabilities are routinely exploited for studies on condensed and disordered matter systems ranging from quantum fluids, to biological materials, to liquid metals, to glasses, to high T_c superconductors, etc.. Thanks to these techniques, it has been possible to pose (and sometime answer) questions on the structure and dynamics of disordered materials as:

• Are there collective excitations in liquids and glasses with wavelengths approaching the inverse interparticle separation? If so, to what extent do these modes deviate from the plane waves found in crystals? Are these deviations responsible for the anomalous thermal conductivity found in glasses at low temperatures? Similarly, how do they relate to the sound excitations observed in the long-wavelength limit?
• With respect to the Debye behaviour of the corresponding crystal, what are the origins of the excess specific heat at low temperature and the excess density of vibrational states found in glasses?
• What is the microscopic description of the relaxation processes in liquids and in glasses?
• Are short-wavelength excitations still affected by relaxation processes as observed in the long-wavelength case? This last point relates to the issue of how the high-frequency dynamics may be affected by the liquid-glass transition in glass-forming liquids, and whether any critical behaviour is present in this dynamics.

The possibility of contributing to the understanding of such problems with an experimental method has created a worldwide interest in the inelastic scattering techniques, and important results have already been documented. Some examples of successful application of these techniques follow. Sergueev *et al.* report on the use of nuclear resonance scattering to study a typical organic glass-forming material, whereby the translational and rotational relaxation times were determined

separately using both nuclear forward scattering and perturbed-angular correlation. The knowledge of these two times, and their comparison with those measured by other standard techniques, such as dielectric spectroscopy, gives us an insight into the origins of the beta-process in supercooled liquids and glasses. In another example T. Neisius reports on the use of the Raman-scattering technique for the study the intensity of the 4p-1s transition in liquid germanium and its temperature dependence. As the intensity is related to the amount of tetrahedrically-bonded atoms in the melt, the authors were able to find the existence of a transition from a four to a six nearest-neighbours atomic arrangement. On the IXS side, Scopigno *et al.* analysed the temperature dependence of the elastic-to-inelastic intensity ratio in the IXS spectra of several glasses. They revealed the existence of an unexpected correlation between the fragility of a liquid (an index that quantifies how fast the viscosity of a supercooled liquid increases on approaching the glass transition) and the temperature dependence of the amplitude of the collective vibrations on approaching zero temperature. This correlation, which allows us to predict the behaviour of the viscosity of a liquid from the vibrational properties of its glass is waiting for a microscopic explanation.

Many fields in disordered condensed matter physics have not yet been tackled with the inelastic scattering techniques, and for many others only the surface has only just been grazed. So there are no doubts that this area will not reach the steady state of mature spectroscopic techniques for quite some time. Rather it will continue to be a source of excitement and scientific surprises for the next few decades.

Direct Observation of the Covalency of Liquid Germanium by X-ray Emission Spectroscopy

The detailed understanding of the electronic structure of liquids remains a challenge, due to the complete lack of long range order. Nevertheless in the last few years a considerable progress in the electronic theory of liquids has been made, mainly based on molecular-dynamic calculations.

On the experimental side, data of the electronic structure of high vapour pressure liquids are still scarce due to severe experimental difficulties. X-ray emission spectroscopy is an alternative method to study the electronic structure of matter under extreme conditions.

Liquid germanium is one of the most often studied liquid metal systems. The element shrinks upon melting and undergoes a semiconductor-metal transition. In contrast to the structure of simple liquid metals with a coordination number around 12, liquid germanium has a lower coordination number around 6 [1]. Among the theoretical models explaining the complex structure of liquid germanium, the one claiming the persistence of covalent bonded tetrahedral units in the melt is favoured [2].

A valence band emission study was performed on beamline **ID26** to obtain temperature-dependent information of the valence states of liquid germanium well beyond the melting temperature using a Rowland spectrometer equipped with a spherical bent Si(931) crystal.

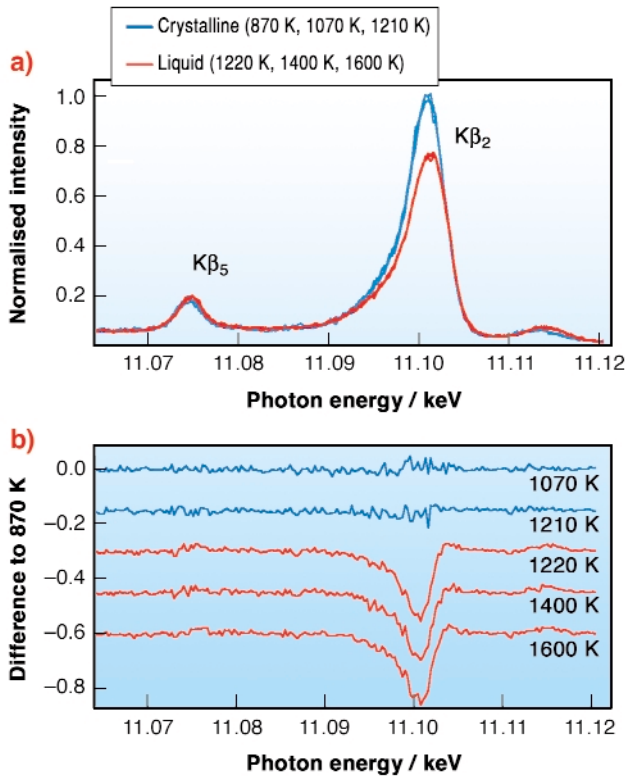

Fig. 8: a) Superposition of X-ray emission spectra taken at six different temperatures; b) Difference spectra in respect to the one taken at 870 K.

Figure 8a shows a series of spectra taken at six different sample temperatures, ranging from 870 K to 1600 K. All spectra are showing the $K\beta_2$ band which come from the dipole-allowed 4p-1s transition and the $K\beta_5$ line from the 3d-1s-quadrupolar transition. The most striking change upon melting is the decrease in intensity of the $K\beta_2$ emission (**Figure 8b**). The structure of crystalline germanium shows a local geometry similar to that found in simple tetrahedral molecules. This suggests that we should describe the bonding in terms of s and p orbitals and use the sp^3-hybridisation as a first approximation to understand the electronic structure of crystalline and also of liquid germanium. The basic ideas are depicted schematically in **Figure 9**. The wave function of the four electrons participating in the tetrahedral covalent bond is a linear combination of one s- and three p- wave functions. Three electrons per atoms are

contributing to the $K\beta_2$-emission. The isolated germanium atom has a $4s^24p^2$ configuration and only two electrons are allowed to decay in the 1s core-hole. This argumentation strongly suggests that the intensity decrease of the $K\beta_2$ band upon melting is a direct consequence of the breaking of the covalent sp^3-bonds in the crystalline solid. The melting process is accompanied by a relaxation of electrons with p-symmetry out of the sp^3- bond to an energetically deeper lying s-state. Following this interpretation the intensity of the $K\beta_2$ band can be taken as a direct measure for the amount of covalently bonded tetrahedral units in the melt.

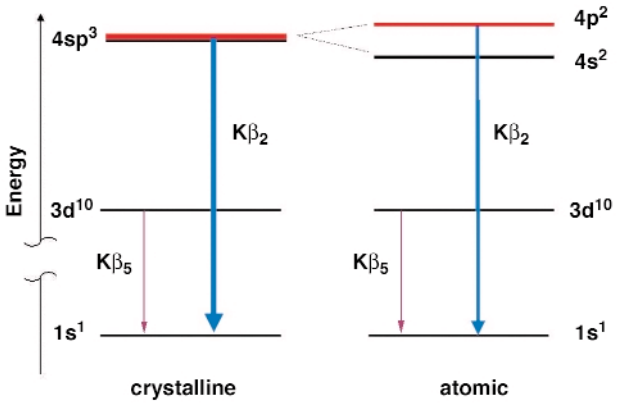

Fig. 9: Schematic energy diagram showing the different contributions to the X-ray emission spectrum.

Interestingly there is no further spectral evolution visible in the spectra by increasing the temperature. This indicates that the bonding properties around the absorbing atom in the liquid remain the same over the measured temperature range. Notably no gradual decrease in the concentration of covalent tetrahedral bonds in the melt can be detected, in contrast to the predictions of recent *ab initio* molecular-dynamics studies [3].

References

[1] V.M. Glazov *et al.*, Liquid Semiconductors (Plenum, New York. 1969).
[2] N.W. Ashcroft, *Nuovo Cimento* **D12**, 597 (1990).
[3] R.V. Kulkarni *et al.*, *Physical Rev. B* **55**, 6896 (1997).

Author

T. Neisius.
ESRF

Rotational and Translational Glass Dynamics Studied by Nuclear Resonant Scattering

Relaxation times and transport properties of moderately supercooled liquids exhibit a universal dependence on temperature. When the glass transition temperature T_g is approached, the relaxation of organic glass formers usually splits into two processes. A slower process, structural α relaxation, corresponds to cooperative molecular dynamics, which is practically frozen at T_g. Another process, slow β relaxation, occurs on a shorter time scale and exists also below T_g. The microscopic origin of this process is still disputed.

In order to understand the relaxational processes on a microscopic level and to distinguish between translational and rotational modes of motion we have applied Nuclear Forward Scattering (NFS) of synchrotron radiation and Synchrotron Radiation based Perturbed Angular Correlation (SRPAC). Both methods are sensitive to nuclear spin dynamics, which is coupled to the molecular rotations. In addition, NFS is also sensitive to translational motions on an atomic length scale. Thus the combination of NFS and SRPAC allows one to separate rotational and translational dynamics.

We applied NFS and SRPAC to investigate the dynamics of the glass former dibutyl phthalate (DBP) (T_g = 178 K) using probe molecules of ferrocene enriched with ^{57}Fe. The experiment was carried out at beamline **ID18**. SRPAC was measured up to 330 K and NFS up to 210 K, where the Lamb-Mössbauer factor, and therefore also the NFS intensity, vanish. Typical time spectra are shown in **Figure 10**. At the lower temperatures, the SRPAC intensity follows an exponential decay modulated by quantum beats. In the regime of slow relaxation, the beats are damped at a rate proportional to rotational relaxation. Similar quantum beats modulate the decay of the NFS intensity, where the damping depends on the sum of rotational and translational relaxation. At higher temperatures, in the regime of fast relaxation, only SRPAC spectra can be measured, which exhibit a characteristic approach of the natural decay (Abragam-Pound limit).

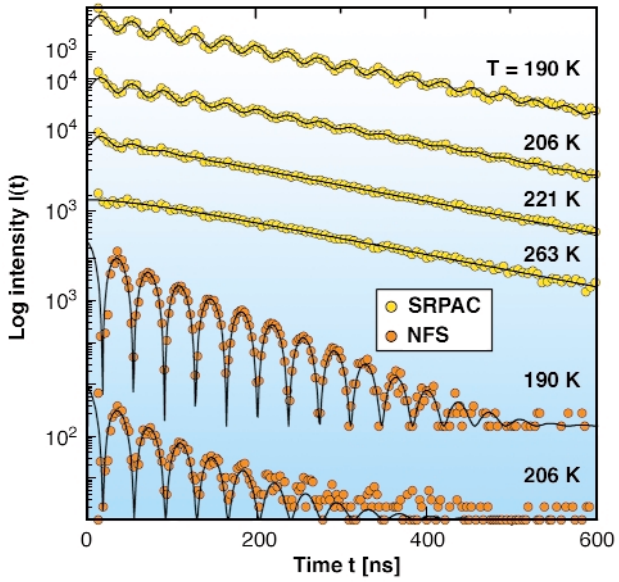

Fig. 10: Time evolution of SRPAC and NFS intensities for several temperatures. The solid lines show the fit according to the full theory.

In **Figure 11a**, we compare the rotational relaxation rate obtained by SRPAC to the sum of the rotational and translational relaxation rates obtained by NFS and Mössbauer Spectroscopy (MS) [1]. Below 190 K the data sets coincide, which means that translational dynamics is absent in the experimental time window. Above 190 K the NFS and MS data begin to deviate from the SRPAC data because translational dynamics is activated. From these results the pure translational relaxation rate can be derived.

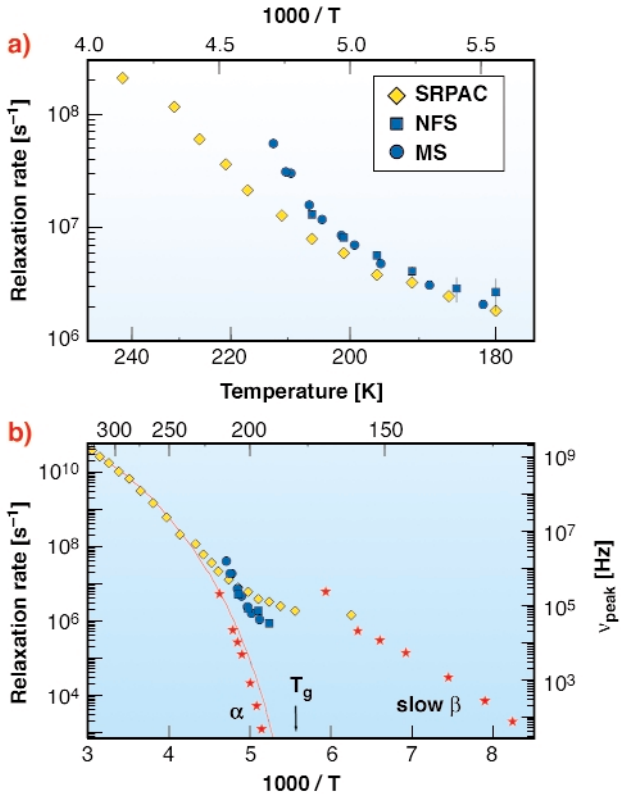

Fig. 11: a) Comparison of the rotational relaxation rate of the ferrocene molecule derived from SRPAC (◆) to the relaxation rate derived from NFS (■) and from Mössbauer spectroscopy (●); b) Comparison of the rotational (◆) and translational (■,●) relaxation rates of the FC molecules to the DS data for pure DBP (red line, ★).

In **Figure 11b** we compare the rotational and translational relaxation rates of the ferrocene molecules in DBP with each other and with data of pure DBP as obtained from dielectric spectroscopy (DS) [2,3]. At low temperatures, the DS data split into two branches. The branch of slow β relaxation follows our data of rotational dynamics, whereas the branch of α relaxation decreases in parallel with our data of translational dynamics. This correlation suggests an interpretation of the ferrocene data also in terms of decoupling, where one branch corresponds to rotational, the other to translational relaxation. In particular, the coincidence of the slow β relaxation branches for probe and solvent suggests that also in pure DBP the slow β relaxation is connected with rotational dynamics.

References

[1] S.L. Ruby, B.J. Zabransky, P.A. Flinn, *J. Physique* **37,** C6-745 (1976).

[2] S.A. Dzyuba and Yu.D. Tsvetkov, *J. Struct. Chem.* **28**, 343 (1987).

[3] P.K. Dixon *et al*., *Phys. Rev. Lett.* **65**, 1108 (1990).

Principal Publication and Authors

I. Sergueev (a,b), U. van Bürck (a), A.I. Chumakov (b,c), T. Asthalter (d), G.V. Smirnov (c), H. Franz (e), R. Rüffer (b), W. Petry (a), submitted to *Phys. Rev. Lett.*

(a) TUM Physik E13, Garching (Germany)

(b) ESRF

(c) RRC, Moscow (Russia)

(d) Univ. Stuttgart (Germany)

(e) DESY, HASYLAB, Hamburg (Germany)

Fragility of Liquids or Fragility of Glasses?

Glasses and the glass transition stand, in the much quoted estimate of a Nobel laureate, as “perhaps the deepest and most interesting unsolved problem in condensed matter physics” [1]. In this respect, one of the most provocative aspects, concerns the slowing down of the dynamics on decreasing the temperature of the melt. When a liquid is cooled, the loss of kinetic energy leads to an ordering of the molecules which ultimately crystallise at the melting temperature T_m. However, if cooled fast enough, some materials (glass forming materials) are capable of sustaining a metastable liquid state and, upon further cooling, to freeze into a disordered glassy state at the glass transition temperature $T_g<T_m$ [2]. Approaching this transition from the liquid side, different systems show qualitatively different temperature dependencies of the viscous flow, commonly represented in the celebrated Angell plot (**Figure 12**). Consequently, on a quantitative ground, liquids have been classified by introducing the term kinetic “fragility” [3]:

$$m = \lim_{T \to T_g} \frac{d \log \eta}{d(T_g / T)}$$

A “fragile” liquid shows a fast change in its viscosity, when approaching the glass transition temperature (T_g) and, empirically, it is found that the fragility is related to the interaction potential (Van-der-Waals, hydrogen-bonding, covalent) among the elementary units.

The idea of looking for correlations between fragility and other quantities relevant to the glass transition is not terribly new, its importance was soon recognised as the main road to the understanding of the universality of the Angell plot. But, in the most obvious way, all the efforts have been addressed looking from the liquid side of the glass-transition.

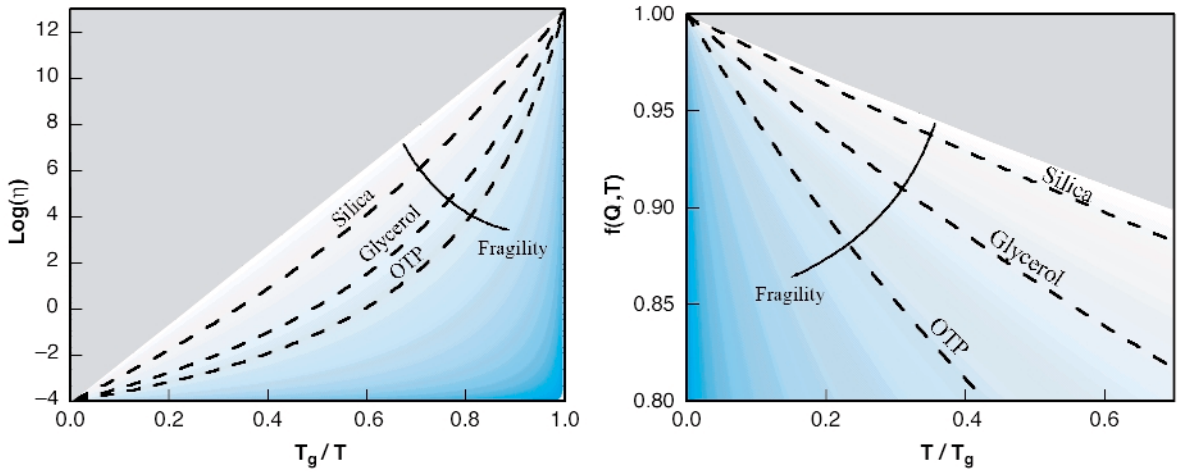

Fig. 12: (Left) kinetic fragility defined as the viscosity derivative at T_g (Angell plot); (Right) glass fragility defined as the derivative of the non-ergodicity factor at T = 0. Shaded areas (blue) indicates regions of increasing fragility, gray areas mark regions of unphysical fragilities.

We report here a new experimental observation relating the microscopic properties of the glassy phase to the kinetic fragility. We found that the vibrational properties in the glass away from T_g are correlated to the viscous flow in the liquid on approaching T_g.

Recent Inelastic X-ray Scattering (IXS) measurements of the dynamic structure factor have allowed the constitution of a sizeable library of high-frequency (THz) dynamical properties of glasses. Of interest here, the IXS measurements allow the determination of the non-ergodicity factor, f(Q,T), *i.e.* the long time limit of the normalised density-density correlation function. This quantity represents the amount of decorrelation introduced by the vibrational dynamics, and it depends on both the (T-dependent) amplitude of the vibrations and the degree of disorder of the glassy structure.

We show that the low temperature dependence of the non ergodicity factor for several glasses stands in a fashion similar to the one exhibited by the Angell plot. It is indeed possible to define a glass fragility as the derivative of f(Q,T) in the T = 0 limit (there is almost no Q dependence in the small Q region of interest here) .

$$m_\alpha = \lim_{T\to 0} \frac{df(Q,T)}{d(T/T_g)}$$

Consequently, we extend the fragility concept to the glassy state and indicate how to determine the fragility uniquely from glass properties far away T_g (**Figure 13**). More specifically, exploiting the harmonic approximation, one has an analytical dependence of the f(Q,T) which can be used to determine m_α from the experimental data. Through this, we establish a way to determine the fragility of a system in the glassy phase well below T_g, independent of

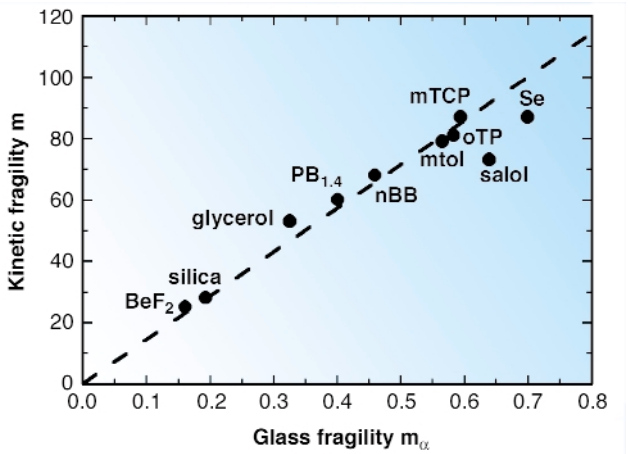

Fig. 13: Correlation of glass and liquid fragilities for an ensemble of glass-formers.

the way the viscosity changes with decreasing temperature from the liquid side. This conceptually surprising link between vibrational motion in glasses and diffusive processes in supercooled liquids represents a further aspect that requires clarification and, at the same time, suggests a new direction of investigation for the ultimate understanding of the glass transition phenomenology.

References

[1] P. W. Anderson, expressing a viewpoint in the journal *Science*, **267**, 1616 (1995).
[2] P.G. Debenedetti, *Metastable liquids*, Princeton University Press, NJ, (1996).
[3] C.A. Angell, *Science*, **267**, 1924 (1995).

Principal Publication and Authors

T. Scopigno (a), G. Ruocco (a), F. Sette (b) and G. Monaco (b), *Science* **302**, 850 (2003).
(a) INFM and Universitá di Roma “La Sapienza” (Italy)
(b) ESRF

Phonon Spectroscopy on Selected Systems

The following two contributions on phonon spectroscopy have benefited from the combination of an excellent synchrotron-radiation beam and the specific techniques available at the High Resolution and Resonance Scattering Group's beamlines.

The investigation of phonons in plutonium was possible thanks to the inelastic X-ray scattering technique and the microfocusing capabilities, whereby the complete set of phonon dispersion curves were mapped from a single grain of plutonium. In the subsequent article, the polarisation properties of synchrotron radiation and the element specificity of the nuclear inelastic scattering technique allowed the determination of the directional dependence on the vibrational modes of the metal center in a myoglogin single crystal.

Catching Phonons in Plutonium

Phonon dispersion curves (PDCs) in plutonium (Pu) and its alloys have defied measurement for the past few decades since the discovery of this element in 1941. This is due to a combination of the high thermal-neutron absorption cross section of plutonium and the inability to grow the large single crystals (with dimensions of a few millimeters) necessary for inelastic neutron scattering. These limitations have recently been overcome by using a tightly focused undulator X-ray microbeam scattered from single-grain domains in polycrystalline specimens. This experimental approach has been applied successfully to map the complete PDCs of an fcc δ-Pu-Ga alloy using the high resolution inelastic X-ray scattering (HRIXS) capability on **ID28**.

Pu is well known to have complex and unique physico-chemical properties [1]. Notably, the pure metal exhibits six solid-state phase transformations with large volume expansions and contractions along the way to the liquid state: $\alpha \rightarrow \beta \rightarrow \gamma \rightarrow \delta \rightarrow \delta' \rightarrow \varepsilon \rightarrow$ liquid. Unalloyed Pu melts at a relatively low temperature ~ 640°C to yield a higher density liquid than that of the solid from which it melts (**Figure 14**). PDCs are key experimental data to the understanding of the basic properties of Pu materials such as: force constants, sound velocities, elastic constants, thermodynamics, phase stability, electron-phonon coupling, structural relaxation, etc.

The complete PDCs for an fcc Pu-0.6 wt% Ga alloy are plotted in **Figure 15**, and represent the first full set of phonon dispersions ever determined for any Pu-bearing materials. The solid (red) curves are calculated using a standard Born-von Kármán (B-vK) force constant model. An adequate fit to the experimental data is obtained if interactions up to the fourth-nearest neighbours are included. The dashed (blue) curves are recent dynamical mean field theory (DMFT) results by Dai *et al.* [2].

The elastic moduli calculated from the slopes of the experimental phonon dispersion curves near the Γ point are: C_{11} = 35.3 ± 1.4 GPa, C_{12} = 25.5 ± 1.5 GPa and C_{44} = 30.53 ± 1.1 GPa. These values are in excellent agreement with those of the only other measurement on a similar alloy (1 wt% Ga) using ultrasonic techniques as well as with those recently calculated from a combined DMFT and linear response theory for pure δ-Pu [2].

Several unusual features, including a large elastic anisotropy, a small shear elastic modulus C', a Kohn-like anomaly in the T_1[011] branch, and a pronounced softening of the [111] transverse modes are found. These features can be related to the phase transitions of plutonium and to strong coupling between the lattice structure and the 5f valence instabilities. The HRIXS results also provide a critical test for theoretical

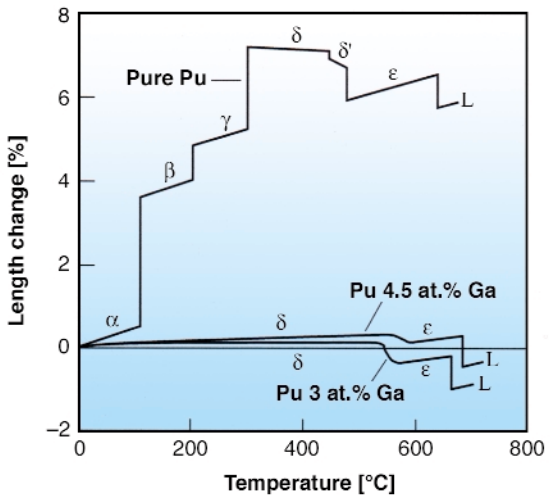

	Pu crystal structure	Density (g/cc)
α	Simple monoclinic	19.86
β	Body-centered monoclinic	17.70
γ	Face-centered orthorhombic	17.14
δ	Face-centered cubic	15.92
δ'	Body-centered tetragonal	16.00
ε	Body-centered cubic	16.51
L	Liquid	16.65

Fig. 14: Transformations in Pu to different crystal structures are accompanied by very large volume changes. Alloying with Ga or Al avoids the transformation to γ, β and α and stabilizes the δ phase all the way to room temperature and below [1].

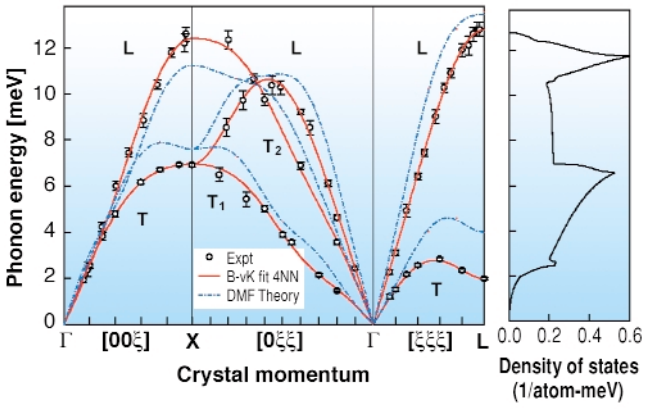

Fig. 15: Phonon dispersions along high symmetry directions in δ-Pu-0.6 wt% Ga alloy. The longitudinal and transverse modes are denoted L and T respectively. The experimental IXS data are shown as circles. Along the [0ξξ] direction, there are two transverse branches [011]<01-1> (T_1) and [011]<100> (T_2). Note the softening of the TA[ξξξ] branch towards the L point. The lattice parameter of our samples is a = 0.4621 nm. The red solid curves are the fourth-nearest neighbour Born-von Kármán model fit. The derived phonon density of states, normalised to 3 states per atom, is plotted in the right panel. The blue dashed curves are calculated dispersions for pure δ-Pu based on DMFT [2].

treatments of highly correlated 5f electron systems as exemplified by recent dynamical mean field theory (DMFT) calculations for δ-plutonium.

The experimental-theoretical agreements shown in **Figure 15** in terms of a low shear elastic modulus C', a Kohn-like anomaly in the T_1[011] branch, and a large softening of the T[111] modes give credence to the DMFT approach for the theoretical treatment of 5f electron systems of which δ-Pu is a classic example. However, quantitative differences remain. These are the position of the Kohn anomaly along the T_1[011] branch, the energy maximum of the T[111] mode s and the softening of the calculated T[100] branch near the X point, which is not observed experimentally. These differences are significant and thus provide a framework for refined theoretical treatments. Systematic HRIXS experiments as a function of temperature and concentration in the fcc Pu-Ga alloys are underway.

References

[1] S.S. Hecker, *Challenges in Plutonium Science*, Los Alamos Sci, **26**, 290 (2000).
[2] X. Dai *et al.*, *Science* **300**, 953 (2003).

Principal Publication and authors

J. Wong (a), M. Krisch (b), D.L. Farber (a), F. Occelli (a), A.J. Schwartz (a), T-C. Chiang (c), M. Wall (a), C. Boro (a), and R. Xu (c), *Science*, **301**, 1078 (2003).
(a) Lawrence Livermore National Laboratory (USA)
(b) ESRF
(c) University of Illinois at Urbana-Champaign (USA)

Anisotropic Vibrations Labelled by the Haem Iron in Metmyoglobin

Proteins are essential for life and are therefore an outstanding object of research. The function of a protein is determined by its architecture and also strongly by its dynamics. Whereas the structure is nowadays often solved to atomic resolution, the understanding of the dynamics is still inadequate. It is well known, that below a dynamical transition temperature T_c harmonic, solid state like vibrations occur. Above T_c protein specific dynamics appears and superimposes the harmonic vibrations. The nature of this specific dynamics is still under discussion.

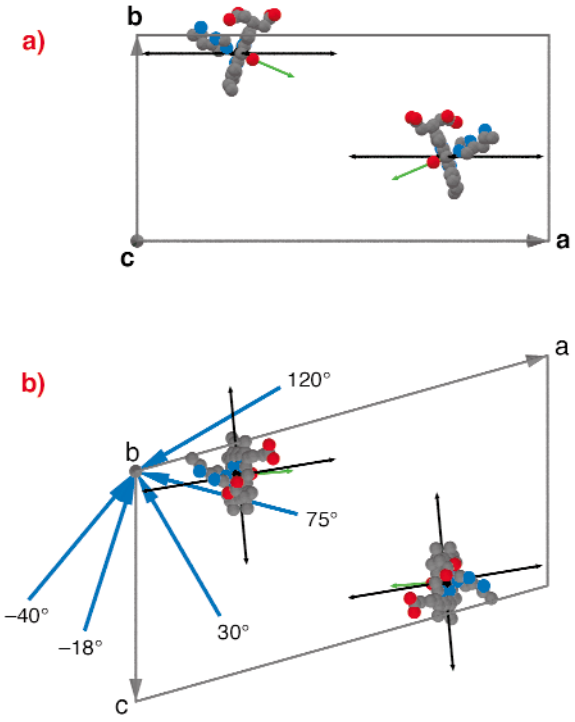

Fig. 16: Sketch of the unit cell of myoglobin. a) View along the c-axes. b) View along the b-axes. Only the haem plane, the ligated oxygen and the His93 are shown with its equivalent in P_{21} symmetry. Blue arrows around the b-axes indicate the incoming beam direction. The green arrow is the haem normal. The black arrows indicate two selected vibrations enlarged by a factor of 500.

In iron containing proteins dynamics can be investigated by many spectroscopic methods. Already thirty years ago Mössbauer spectroscopy on ^{57}Fe was shown to be a valuable tool for the detection of harmonic vibrations and protein specific motions with energies in the neV region in haem proteins [1]. While Mössbauer absorption spectroscopy yields mean square displacements coming from all modes of motions coupling to the iron, Mössbauer effect with synchrotron radiation, also called phonon assisted Mössbauer effect, allows an energy selective measurement of vibrations in the meV energy regime. This suits the investigation of phonons perfectly. Temperature dependent measurements on myoglobin in

the deoxy, met and CO-ligated state proved, that the vibrations accessible by this method stay harmonic even above T_c [2]. Recently this method could be extended to investigate anisotropic motions by using a single crystal of myoglobin. Anisotropic mean square displacements of the haem iron as a function of energy are obtained as the projection onto the incoming beam direction.

Each unit cell of the metmyoglobin single crystal contains two molecules *i.e.* about 5000 atoms plus about 800 water. The natural haem iron was enriched in the Mössbauer isotope ^{57}Fe. The protein crystallised in P_{21} symmetry forming a crystal of 1·2·3 mm^3. The crystal was rotated around its crystallographic b-axes perpendicular to the synchrotron beam. Five orientations were measured as sketched in **Figure 16**. The density of phonon states was extracted from the inelastic scattering spectra, taken at **ID18**. The mean square amplitude $\langle x^2 \rangle$ of modes was calculated within several energy intervals, as exemplary marked in red and blue in **Figure 17**. A $\cos^2$-dependence plus background described the angular dependent projection very well (see **Figure 17c**). The fit gave the mean vibrational direction of some vibrations as given in **Figure 17** exemplary for two vibrations.

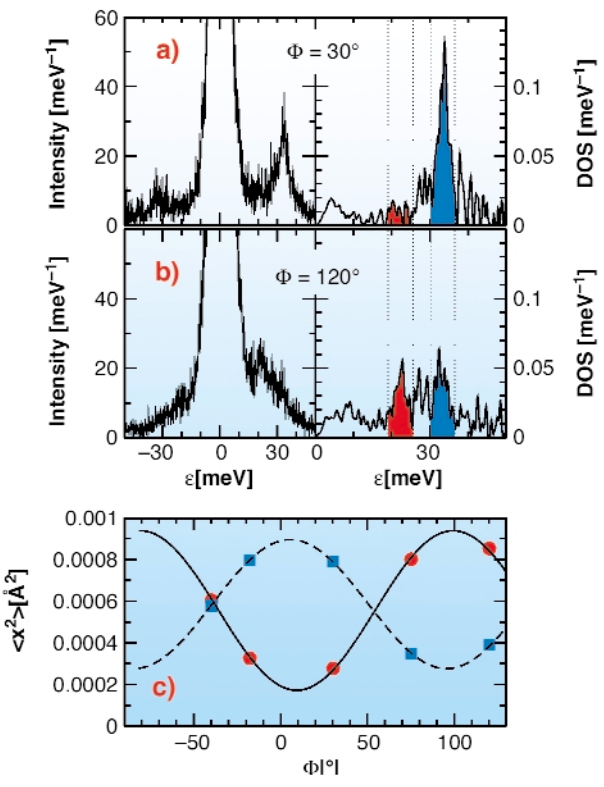

Fig. 17: a,b) Left: two selected energy spectra at Φ = 30° and 120°. Right: density of phonon states extracted from the energy spectra. c) Fit of the projection of $\langle x^2 \rangle$ of iron in Mb to the incoming beam direction within energy intervals marked similar colours in the density graph.

In conclusion, the experiment is a further step in the separation of harmonic vibrations from the protein specific motions by extending the classical Mössbauer absorption to the meV energy regime. Protein-specific motions fall beyond this border and can clearly not be explained by increasing anharmonicity of solid state vibrations. Nevertheless, how the protein-specific motions emerge from the harmonic vibrations with temperature remains unknown. The energy and angular dependence of the vibrations in the active centre will be the basis for a determination of the forces acting in the active centre of a protein.

References

[1] F. Parak, H. Formanek; *Acta Cryst. A* **27**, 573-578 (1971).
[2] K. Achterhold, C. Keppler, A. Ostermann, U. van Bürck, W. Sturhahn, E.E. Alp, F.G. Parak; *Phys. Rev. E* **65**, 051916-1 - 051916-13 (2002).

Principal Publication and Authors

K. Achterhold and F.G. Parak; *J. Phys.: Condens. Matter* **15,** S1683–S1692 (2003).
Technische Universität München (Germany)

Thermal-motion-induced Scattering from Zinc Oxide

One of the greatest virtues of the X-ray diffraction technique is that measurements can usually be related directly to the density of electrons in a material – a property of fundamental importance to many areas of science. However, hidden in the finest details of the scattering, and its dependence on X-ray energy and polarisation, lies an array of increasingly complex and subtle physical phenomena. The most well known of these include magnetic scattering, and the signatures of orbital ordering in some metal oxide crystals [1]. Usually, these observations are made possible by measuring at positions where the 'normal' strong scattering is completely eliminated by the symmetry of the material under investigation.

Taking this approach to the next level, one can find reflections for certain crystal structures where the simplest (and strongest) scattering mechanism is subtler still, and must be described mathematically by a tensor of third rank. Two physical processes have been put forward for explaining the presence of such a signal: a mixed dipole-quadrupole resonance [2] and thermal-motion-induced scattering [3] (**Figure 18**). Both of these effects are of considerable importance in solid state physics, and, perhaps, co-exist in germanium [4]. Strangely, though, the resonance spectrum of germanium lacks significant structure or temperature dependence.

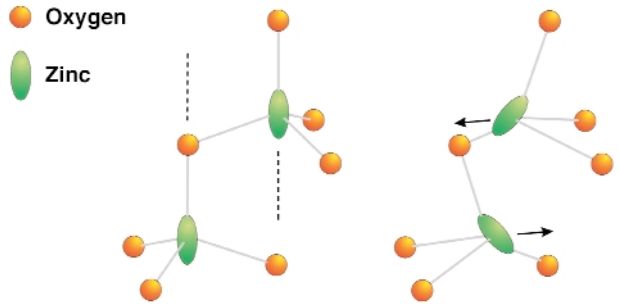

Fig. 18: Thermal-motion-induced scattering in ZnO. In the absence of thermal motion, the (anisotropic) scattering from zinc atoms related by glide-reflection symmetry cancels exactly for certain reflections (left). Dotted lines indicate three-fold rotation axes. Optical phonon modes cause the zinc atoms to move relative to the oxygens (right), inducing opposite tilts in the ellipses that characterise their resonance response. The symmetry between the scattering from each zinc atom, and hence the cancellation of the scattered wave, is broken by the different orientations of the ellipses with respect to the X-ray polarisation.

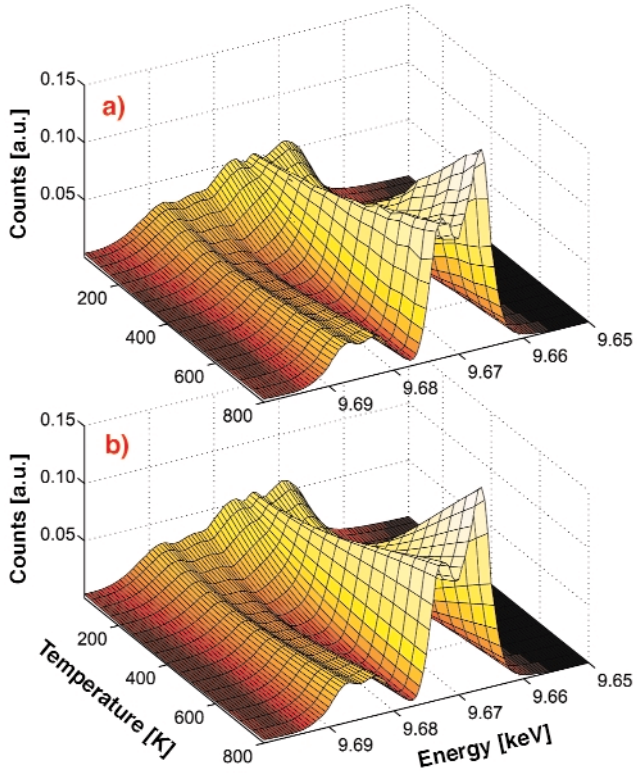

Fig. 19: a) The variation in the resonance spectrum of the ZnO 115 'forbidden' reflection with temperature, showing features that strengthen sharply with temperature, features that weaken, and others that vary very little. b) The results of a fit to a phenomenological based on the interference of two amplitudes – thermal-motion-induced scattering and mixed dipole-quadrupole scattering. Differences between the measured signals and calculations are so small as to be barely visible.

In contrast, we have observed, on **BM28**, very different behaviour of forbidden reflections in the wide-gap semiconductor, zinc oxide. The resonance spectrum of forbidden scattering highly structured, and it exhibits a very strong variation with temperature (**Figure 19**). The results are found to be in remarkably good agreement with a phenomenological model, proposed in [3]. In this model the total scattering is derived from a combination of temperature-independent (dipole-quadrupole) amplitude, and a second amplitude that scales with the average atomic displacement due to optical phonons, and therefore increases with temperature. By applying this analysis, we were able to extract not only the relative magnitude of the two processes, but also their relative phase. We find that the amplitudes mostly interfere destructively, and this explains the tendency of the scattering strength to drop initially as temperature is increased, before rising sharply.

Both physical processes are of immense interest. Mixed dipole-quadrupole resonances vanish in the absence of hybridisation, and therefore provide a direct signature of mixing of electronic valence states. The thermal-motion-induced scattering amplitude is perhaps even more unique as it depends on the change in resonance response with atomic position – a spectroscopy that has not previously been available. Detailed theoretical calculations are being developed to compare with these results, and further experiments are planned in order to study related materials, and similar effects that may arise from point-defects in crystals.

References

[1] S. Ishihara and S. Maekawa, *Repts. Prog. Phys*. **65**, 561 (2002).
[2] D.H. Templeton and L.K. Templeton, *Phys. Rev. B* **49**, 14850 (1994).
[3] V.E. Dmitrienko, E.N. Ovchinnikova, and K. Ishida, *JETP Lett.*, **69**, 938 (1999).
[4] J. Kokubun *et al*. *Phys. Rev. B* **64**, 073203 (2001); A. Kirfel *et al*. *Phys. Rev. B* **66**, 165202 (2002).

Principal publication and Authors

S.P. Collins (a), D Laundy (b), V.E. Dmitrienko (c), D. Mannix (d) and P. Thompson (d), *Phys. Rev B* **68**, 064110 (2003).
(a) Diamond Light Source Ltd (UK)
(b) Daresbury Laboratory (UK)
(c) Institute of Crystallography, Moscow (Russia)
(d) XMaS UK CRG, ESRF

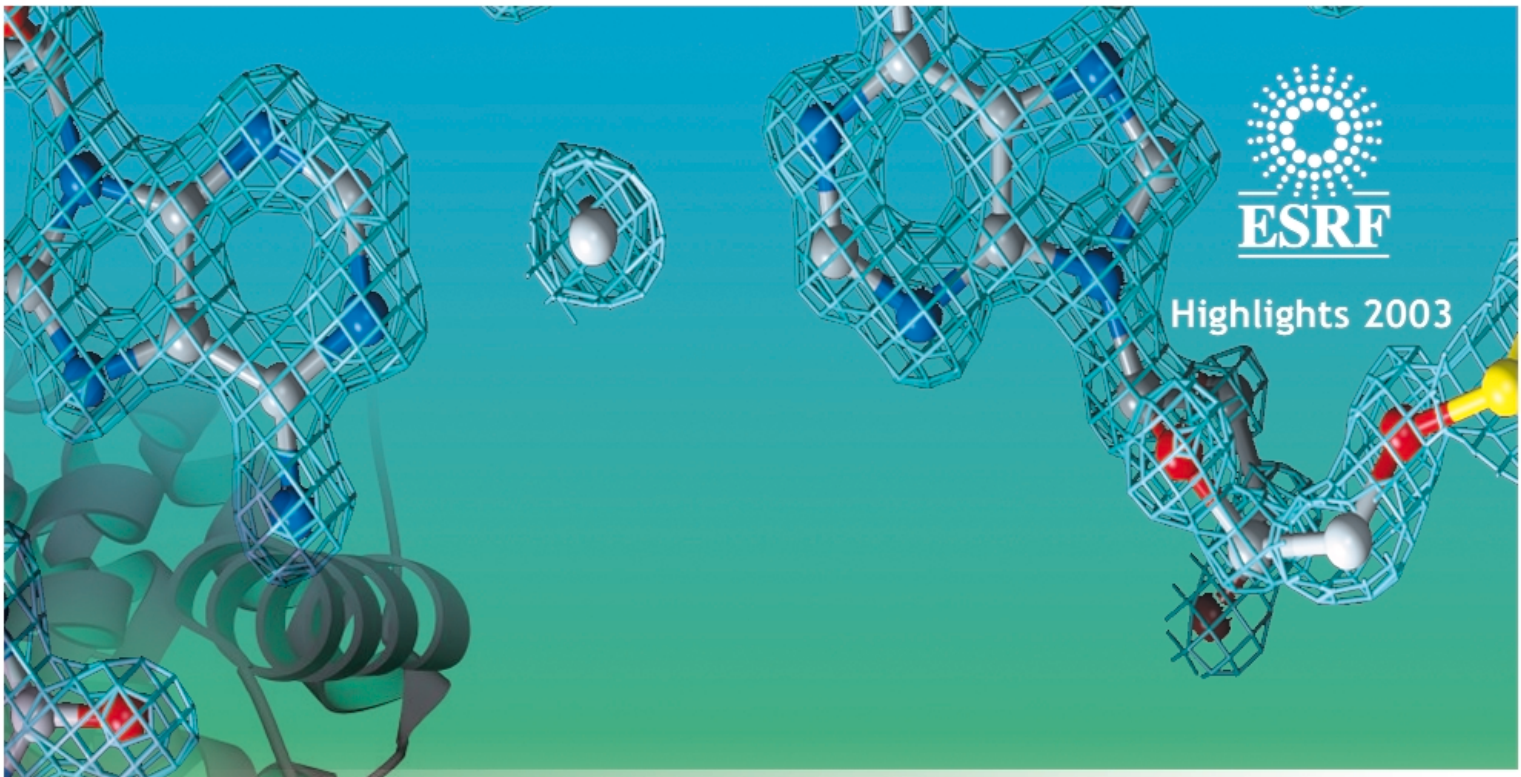

Macromolecular Crystallography

Introduction

The year 2003 was one of great excitement and hard work at the Macromolecular Crystallography (MX) beamlines of the ESRF (ID14 A&B, ID29), and the year's closing brings about a welcome chance to report on some of the work carried out there. Scientifically a large number of interesting crystal structures were produced, and a flavour of these is given in the choice of highlights presented here.

During the year, more than 2000 visitors came to perform experiments at the MX beamlines with, on average, visitors using 24 hours of beamtime per visit. In all, around 500 distinct experimental sessions were scheduled. This high throughput of visits could not be sustained without the excellent support provided by the User and Travel offices, Experiments Division secretariat and the ESRF Support Groups and Services. The MX group itself functions as an effective and highly-dedicated team providing excellent operational support as well as spearheading technical improvements to the beamlines.

The Partnership for Structural Biology (PSB), has continued to develop. In particular the plans for the dedicated laboratory space have progressed to the extent that planning permission has been obtained. Ground break for the new building is expected for April 2004 with about 12-month build time. The related project, the construction of the 2 end-stations on ID23 has reached the conclusion of the first part the adventure with the commissioning of the end-station ID23-1. Test experiments indicate that the beam-line will provide good quality diffraction data and that it operates well in the energy range 5 - 20 keV. User access to the end-station will begin in April 2004. Construction of the second end-station (ID23-2) will continue during 2004. This facility will operate at fixed energy (14.2 keV) and the aim is for a focal spot size of ~ 10 μm^2. We expect to be finalising commissioning for this part of ID23 during the latter part of year and early 2005.

The automation of the MX beamlines continues in earnest. At the ESRF we view automation as a pipeline involving the following processes: automatic beam delivery, characterisation and optimisation; sample delivery (changing and centering); experimental design; data analysis and post processing.
A team comprising staff from both the ESRF and the EMBL Grenoble outstation has been formed which will address these issues and support for this initiative will be provided via the EU project grants SPINE and bioXhit. The year 2003 has seen the installation of many of the components necessary for the operation of our "pipeline" and a summary of progress in this regard is given in the following article by J. McCarthy and B. Shepard on

behalf of all of those involved. The report covers the automatic provision of focussed beam on ID29; the installation of improved optical visualisation systems; the ESRF/EMBL sample changer which is now installed on ID14-3; steps towards automatic experimental design for both single and multiple wavelength experiments.

The External Scientific Programme has seen an increased tendency towards the study of the structures of macromolecular complexes, several of which are presented here. **Nelson** *et al.* (page 22) report the structure of photosystem I from a higher plant (pea). This multi-subunit transmembrane protein complex has a molecular weight of ~ 540 kDa and represents one of the largest assemblies solved by macromolecular crystallography. The structure, and in particular the arrangement of chlorophylls around the reaction centre, provides significant insight into the mechanism of solar energy conversion in plants. An understanding of the mechanistic forces driving muscle movement is underpinned by studies of the interactions between myosin and actin. **Houdusse** and collaborators (page 23) report the structure of the Rigor State of myosin as determined to 2.0 Å resolution using data collected on ID29. This reveals the structural rearrangement necessary in order to effect the force generating state of myosin. In some cancerous tumors it appears that the over-expression of the tumor suppressor pRb is unfavorable to clinical treatment. The work of **Gamblin** and colleagues (page 24) sheds some light on why this may be so. Their structure of the complex formed between pRb and a peptide fragment representing the core pRb-binding domain of the transcription factor E2f also reveals interactions which may aid the design of molecules that might help improve the efficiency of current treatments for a number of cancers.

Of the visitors to the ESRF MX beam-lines, about 20% carried out industrially-related activities. Such use of the MX beamlines continues to grow steadily and, in addition to the sale of beam-time, the ESRF now offers the possibility of 'mail-in' data collection via the MXpress service. A typical example of the work carried out by industrial users of the facility is that reported here by **Astex Technology (**page 26**).** This details the structure of Cytochrome P450 in complex with S-warfarin, and may help to provide a structural basis for the occurrence of *in vivo* drug-drug interactions.

In addition to providing beam-time through national institutions, the CRG beamlines BM30 and BM14 also provide significant amounts of beam-time for use in the External Scientific Programme of the ESRF. The tunable nature of these beam-lines means they are ideally suited to the exploitation of anomalous scattering in MX and beam-time allocated here helps to alleviate the significant over-demand for beam-time on the ESRF's dedicated MAD beam-lines ID14-4 & ID29. The quality of the science achievable on these beamlines is demonstrated by two articles in this chapter. **Acharya** and colleagues (page 31) describe the structure of human Angiotensin1 Coverting Enzyme (ACE) that may allow the rational design of a new generation of ACE inhibitors for use in the treatment of cardiovascular diseases. The structure of the hepititus C Virus core antigen is described by **Menez** *et al*. (page 25).

The in-house research of the MX group continues to develop and is based on three fundamental elements: methods development; collaboration with external groups and the development of in-house molecular & structural biology skills. Examples from all three of these elements are represented here.

Methodological developments have always represented a major part of the ESRF's MX in-house research interests. Collaborations between ESRF and EMBL Grenoble outstation scientists were the first to produce systematic studies of the effect of high intensity X-rays on biomolecules. This work led to several major breakthroughs in our understanding of the structural changes caused in crystals by radiation damage. Continuing this work, careful studies by **Ravelli** and collaborators (page 30) have identified the possibility of exploiting these structural changes to enhance the phasing opportunities in the use of 3rd generation SR sources. Perhaps in the future radiation damage will no longer be viewed as only an obstacle to structure determination.

The structure of CDP-ME Kinase by **Hunter** and colleagues (page 27) represents some of the fruit of a long standing collaboration between ESRF and the University of Dundee. Development of new antibiotic agents presents a major challenge to the pharmaceutical community and there is a continuous search for possible new drug targets. CDP-ME kinase represents a potential new target and its structure determination may pave the way for the development of a new class of antibiotics.

As part of an effort to enhance the platforms for both molecular & structural biology available at the ESRF, the MX group has undertaken a pilot structural genomics project with an emphasis on the radiation resistant bacterium *D.radiodurans*. This project has so far lead to the cloning of > 100 targets. Extended analysis of ~ 30 of the cloned proteins (**Hall** and collaborators page 29) has produced pure protein for 21 of the targets. 10 of these have been crystallised and 6 crystal structures have thus far been produced. The proteome of the organism is also being investigated as a function of radiation dose in order to refine the search for further targets for structural investigation.

The scientific exploitation of the MX beamlines continues to flourish, when the technical advancements foreseen for 2004 are in place we expect that the MX community will be able to perform more and more difficult experiments whilst still focusing on their underlying biological goals.

G. Leonard and S. McSweeney

Further Steps Towards Beamline Automation

Reviewed by J. McCarthy and W. Shepard, for the Joint Structural Biology Group (JSBG) of the ESRF and the EMBL Grenoble Outstation.

Macromolecular crystallography (MX) has proven to be the most effective method of determining the structures of biological macromolecules. Each year thousands of data collections that form the basis for such structure determinations are carried out at the ESRF. To cope with this high demand, it is essential to maximise beamline efficiency and to simplify beamline control procedures. We are therefore automating much of the crystallographic experiment which may be divided into two parts: firstly beamline and crystal alignment, and secondly data collection and processing.

Beamline setup is extremely important since many crystals of biological macromolecules do not grow much larger than tens of micrometres in size. Often the X-rays need to be micro-focussed into a small uniform spot. An elegant and automated procedure based on wavefront analysis has been developed at the ESRF using a position sensitive X-ray camera. This method, called Automatic Beamline Alignment (ABA), allows the correct orientation of the X-ray optics to be deduced from the measurement of only a few parameters. **Figure 20** shows the unfocussed and ABA micro-focussed beam on **ID29**.

Aligning micrometre-sized crystals in a micro-focussed X-ray beam has been facilitated by a special microscope that allows visualisation along the axis of the X-ray beam, **Figure 21**. The position of the X-rays can be directly observed and the sample aligned appropriately. This device is simple, modular and can be adapted to virtually any experimental setup. A prototype has been installed on ID29 and production models will be installed on the **ID14** beamlines in early 2004. New software for centring the crystal sample in the beam has been used on ID14-3 since May 2003. This software allows the crystal to be centred using a 3-click procedure via a graphical interface. Software for fully automatic centring of crystals in the beam is currently under development.

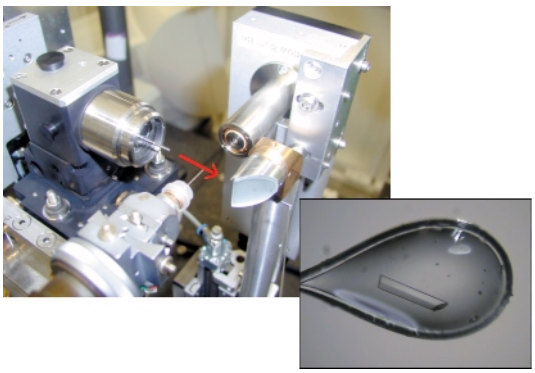

Fig. 21: On-axis sample visualisation (top left) allows much-improved viewing of small crystals. The red arrow indicates the X-ray beam path.

A sample changer robot, which can hold up to 50 frozen samples, was installed on ID14-3 in December 2003. Additionally, the DNA software that allows for automatic crystal characterisation is now available on all MX beamlines. Once fully implemented, the combination of sample changer robot, automatic sample centring protocols and DNA software will mean virtually 'hands-free' beamlines that will allow crystal screening and data collection processes to be carried out rapidly and efficiently.

Techniques exploiting anomalous diffraction (MAD, SAD) are pre-eminent for the *de novo* determination of macromolecular structures. The correct choice of wavelength for data collection based on a scan of the absorption edge of a heavy atom in the crystal is a crucial first step. These calculations have been automated on ID14-4 and ID29. This 'one-click' procedure known as AEscans, carries out all necessary configuration of X-ray source and beam; optimises X-ray beam attenuation; performs a XANES scan; analyses the scan to deduce the correct wavelengths then passes this to the data collection interface. MAD and SAD experiments are thus simple and straightforward to carry out at the ESRF.

The tools described above should, in the coming year, help to provide an efficient and effective environment for high-throughput molecular crystallography that should be of great benefit for the user community.

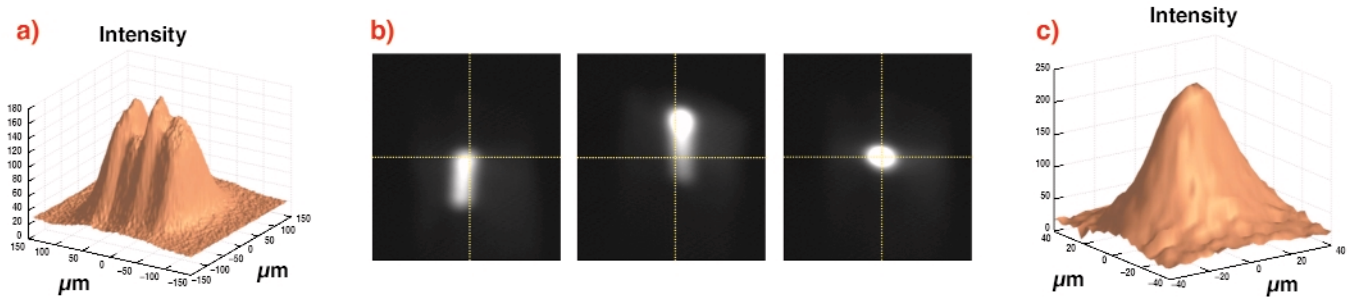

Fig. 20: Automatic beam alignment on ID29: a) Defocussed and non-uniform X-rays before ABA; b) X-ray camera images of the beam at different stages of ABA; c) X-rays after ABA, focussed to 47 μm x 31 μm (H x V) with improved uniformity.

The Structure of Plant Photosystem I

The conversion of solar energy into chemical bonds by the photosynthetic machinery of plants, green algae and cyanobacteria is essential for the survival of all higher life forms. The primary event of this process - light induced charge translocation - is catalysed by photosystem I (PSI) and photosystem II (PSII), two multisubunit protein complexes embedded in the thylakoid membrane that act in series. PSI harnesses light energy to transfer an electron from the soluble copper protein, plastocyanin, on one side of the membrane to ferredoxin and eventually NADPH on the opposite side. In the dark, NADPH (and ATP) provides the energy for assimilation of CO_2 into carbohydrates. PSI is composed of a 12 subunit reaction center and a 4 subunit membranal light-harvesting antenna (LHCI) that captures light and channels its energy to the reaction center. LHCI is exclusively found in plants and green algae and consists of four different but homologous chlorophyll a/b binding proteins, termed Lhca1-4.

We have determined the crystal structure of the entire PSI complex from a higher plant (pea) to 4.4 Å resolution [1]. Phases were obtained by the MIRAS (multiple isomorphous replacement including anomalous scattering) method using several heavy-atom derivatives and the anomalous signal of intrinsic Fe-S clusters at 0.93 Å wavelength. With a mass of 530 KDa, 45 transmembrane helices and 172 co-factors (mostly chlorophylls), this is the largest and most intricate membrane assembly solved by X-ray crystallography and the first one from higher plants (**Figure 22**). The high intensity of beamline **ID14-4** proved crucial for obtaining the reported resolution. All data used for this structure solution were collected there.

The four LHCI proteins assemble into two dimers, forming a half-moon shaped belt that docks to the subunit F side of the reaction center. The association of the reaction center with the LHCI belt is both weak and asymmetric (**Figure 22a**). Only one of the four Lhca proteins firmly attaches to the reaction center through interactions involving transmembrane helices and may serve as an "anchor" for the assembly of the other monomers. Within the membrane, the Cα backbone of LHCI maintains a distance of 20 Å from most parts of the reaction center. Thus, LHCI chlorophylls are positioned 18 Å from the nearest reaction center chlorophyll except at three regions where much shorter inter-pigment distances are observed and which may play an important role in energy migration. The arrangement of the ~90 chlorophylls within the reaction center in plants is similar to that in the cyanobacterial counterpart [2]. Apparently, adaptation of the reaction center chlorophyll arrangement to receiving energy from LHCI required the addition of only an extra 10 chlorophylls at strategic positions between LHCI and the reaction center.

Formation of the LHCI dimers and the interaction between the dimers does not involve transmembrane helices. The solvent exposed C and N termini of the light-harvesting protein monomer attach to solvent-exposed loops of its neighbouring monomer (**Figure 22**). "Linker chlorophylls" between LHCI monomers facilitate energy migration along the LHCI belt. This mode of binding maximises the number of LHCI chlorophylls

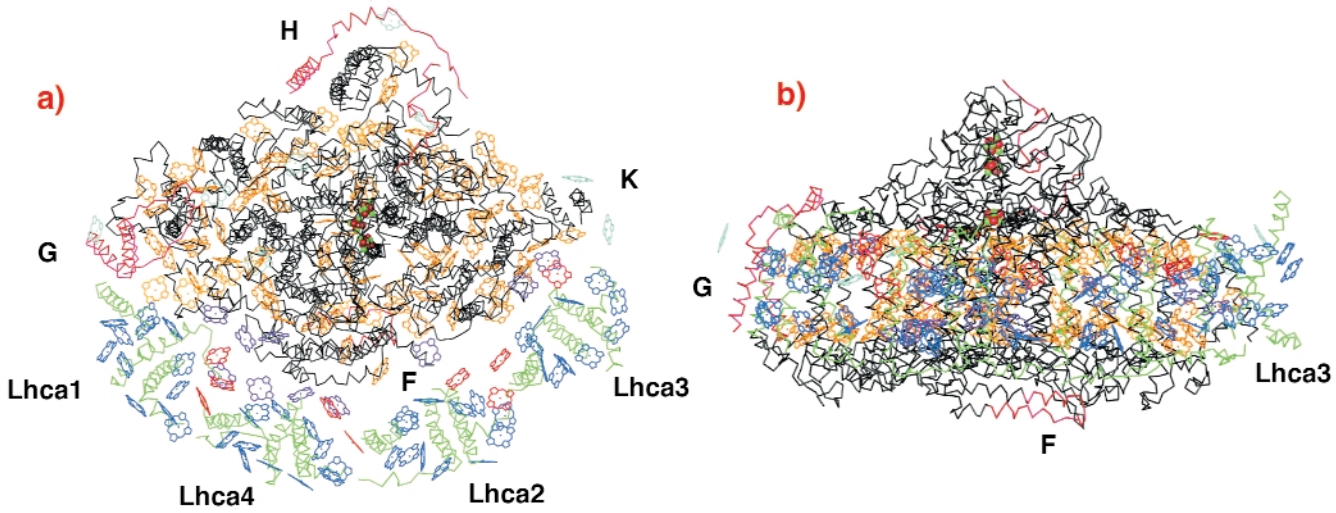

Fig. 22: The structural model of plant photosystem I (PSI) at 4.4 Å resolution: (a) View from the stroma with subunits F, G, H and K of the reaction center indicated; (b) A view from the LHCI side with subunits F, G of the reaction center and Lhca3 indicated. The four light-harvesting proteins Lhca1-Lhca4 are depicted in green. Novel structural elements within the core, not present in the cyanobacterial counterpart, are coloured red, the conserved features of the reaction center are in grey. The three Fe_4-S_4 clusters are depicted as red (Fe) and green (S) balls. The chlorophylls are coloured according to their possible functional assignment: core chlorophylls similar to that of cyanobacterial reaction center in yellow, added chlorophylls to the plant reaction center in cyan, LHCI chlorophylls in blue, linker chlorophylls between LHCI units in red and contact chlorophylls between LHCI and the reaction center in magenta.

facing the reaction center. Furthermore, we suggest that this dimerisation mode, together with the above-described interactions between LHCI and the reaction center serve the need of PSI to adjust LHCI composition according to varying environmental conditions.

The structure reveals further details concerning, for example, interactions of PSI with other light-harvesting proteins (LHCII) and with plastocyanin. It provides a framework for investigating both the mechanisms regulating the activity and composition of PSI's numerous subunits and the evolutionary forces that shaped the photosynthetic apparatus of terrestrial plants.

References

[1] A. Ben-Shem, N. Nelson, and F. Frolow, *Acta Crystallographica Section D-Biological Crystallography* **59**, 1824-1827 (2003).
[2] P. Jordan, P. Fromme, H.T. Witt, O. Klukas, W. Saenger, and N. Krauss, *Nature* **411**, 909-917 (2001).

Principal Publication and Authors

A. Ben-Shem, F. Frolow, and N. Nelson, *Nature,* **426**, 630-635 (2003).
Tel Aviv University (Israel)

The Rigor State of Myosin Visualised at 2.0 Å Resolution

Movement is one of the hallmarks of life. Myosins are molecular motors that use cellular ATP to power interactions with actin filaments and create force and directed movement. Myosin II is essential for muscle contraction and cytokinesis but other members of the myosin superfamily play roles in phagocytosis, cortical cell tension, signal transduction, endocytosis, exocytosis, and intracellular vesicle transport. Conformational changes in the myosin motor allow it to cycle through defined structural states which differ in their nucleotide- and actin- affinities (**Figure 23**) [1].

Myosin hydrolyses ATP in states that have a weak affinity for actin, and strain is produced when myosin rebinds to the actin filament, which accelerates the release of the ATPase products from the motor. The proposed mechanism for force generation, the swinging lever arm hypothesis (**Figure 23**), is largely based on high-resolution structures of the weakly bound states. It postulates that the swing of the lever arm is responsible for the force production. However, since force production occurs when myosin is strongly bound to actin, details of the strongly-bound states of myosin are essential to understand how force is produced.

The affinity of myosin for actin depends directly on the bound nucleotide in the myosin active site. So far, high-resolution structures of myosin have provided atomic details of three structural states of the motor that correspond to weak actin-binding states. While these studies provided a detailed description of how ATP hydrolysis occurs, they were insufficient to describe the details of the structural changes that lead to the strong actin-affinity states. Based on kinetic evidence that an unconventional myosin, class V myosin, populates a unique state in the absence of nucleotide and actin, we hypothesised that its high resolution structure could for the first time reveal features of a strong actin-binding, force generating state.

We expressed and crystallised a class V myosin containing only a motor domain and the first calmodulin-binding site (first part of the lever arm). The 2.0 Å refined structure (from a dataset collected on **ID29**) revealed a novel conformation for the myosin head (without bound nucleotide) in which all of the key features that were predicted to occur in the myosin state with the strongest affinity for F-actin (*i.e.* rigor state) are realised. The nucleotide-binding site has adopted new conformations of the nucleotide-binding elements that reduce the affinity for the nucleotide. The major cleft in the molecule has closed resulting in a drastically different actin-binding interface (**Figure 24**), and the lever arm has assumed a position consistent with that in an actomyosin rigor complex. However, the way in which this was achieved was totally unexpected. The distortion of the central seven-stranded beta-sheet of the motor domain is essential to allow large relative movements of

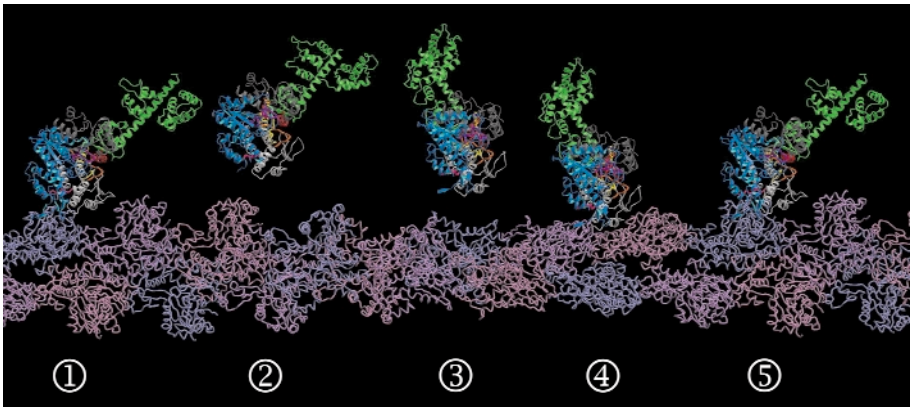

Fig. 23: Structural states of myosin during the contractile cycle. 1-Without bound nucleotide, myosin is strongly bound to actin (rigor state). 2-ATP binding dissociates the complex actin-myosin. 3-ATP is then hydrolysed in ADP+Pi. There is a swing of the lever arm (green). 4-Myosin can rebind to actin, release its hydrolysis products and produce its force. 5- Myosin is again strongly bound to actin without nucleotide bound.

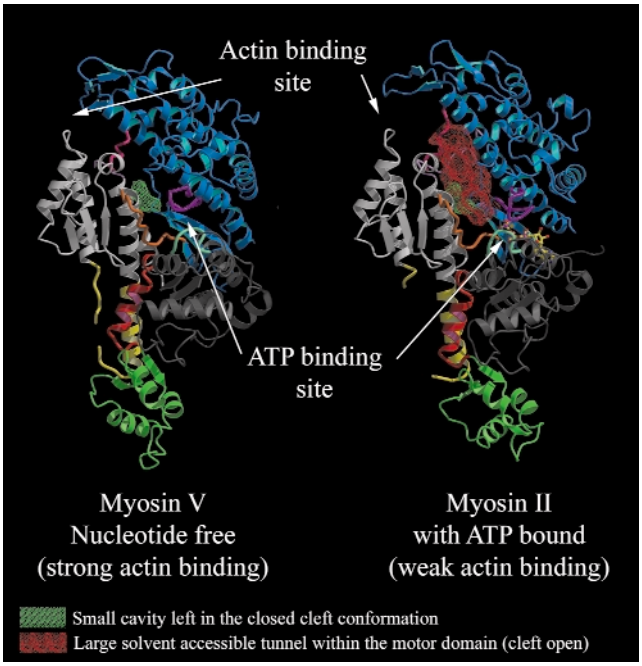

Fig. 24: Comparison of the rigor-like state of myosin V and the ATP-bound state of myosin II. The myosin V structure reveals at atomic resolution how the major cleft in the molecule closes and leads to a new actin-binding interface.

the subdomains. These changes in the motor reveal elements of the structural communication between the actin-binding interface and the nucleotide binding site of myosin that underlie the mechanism of chemo-mechanical transduction.

In conclusion, the high-resolution structure of the motor domain of class V myosin provides critical information for our understanding of how myosin produces force. In revealing unexpected rearrangements in the molecule, this new structure reveals the structural basis of the coupling between the binding and release of actin and nucleotide, and the strong inverse linkage that has remained enigmatic. While closure of the 50 kDa cleft generates a strong actin-binding interface, ATP binding in the myosin active site allows myosin to re-open this large cleft and to separate the actin-binding interface into two separate entities which allow myosin dissociation from actin.

References

[1] A. Houdusse, and H.L. Sweeney, *Curr. Opin. Struct. Biol.* 11,182-194 (2001).
[2] A.D.E. Mehta *et al.*, *Nature* **400**, 590-593 (1999).

Principal Publication and Authors

P.D. Coureux (a), A.L. Wells (b), J. Menetrey (a), C.M. Yengo (b), C.A. Morris (b), H.L. Sweeney (b), A. Houdusse (a). *Nature* **425**, 419-23 (2003).
(a) Institut Curie CNRS, UMR144, Paris (France)
(b) University of Pennsylvania School of Medicine (USA)

Crystal Structure of the Retinoblastoma Tumour-suppressor Protein bound to E2F and the Molecular Basis of its Regulation

The first tumour-suppressor protein to be identified was the product of the retinoblastoma gene (pRb). Loss of its function contributes to the development of a majority of human malignancies [1]. pRb plays important roles in regulating the cell-cycle, apoptosis and differentiation, and all of these activities are pertinent to its role as a tumour suppressor. The growth-inhibitory effects of pRb are dependent on its regulation of the E2F family of transcription factors. In order to better understand the regulation of the E2F transcription factor by pRb, we have determined the crystal structure of the pRb pocket domain (pRbAB) bound to residues 409-426 of E2F-1. The AB-pocket of pRb is the major focus of tumourigenic mutations in the protein and the $E2F_{(409-426)}$ fragment represents the core of the pRb-binding region of the transcription factor.

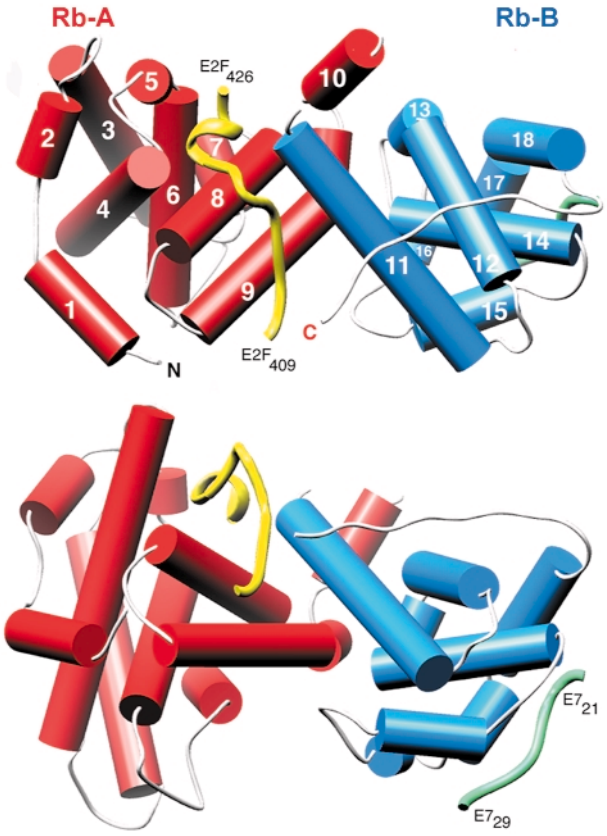

Fig. 25: The structure of RbAB/$E2F_{(409-426)}$, shown in two orthogonal views (drawn with Ribbons). The helices of the A domain are shown as red cylinders and those of the B domain as blue cylinders. The main-chain trace of E2F and E7 (from PDB entry 1GUX) are shown as yellow and green worms respectively.

Initial attempts at data collection, using synchrotron X-ray sources, were hindered by very high crystal mosaicity and poor data scaling and reduction. Finally, a good quality dataset was collected to 2.6 Å resolution using the microfocus diffractometer on beamline **ID13**. At the time this was the only such device installed at a synchrotron source. The structure was solved by molecular replacement and the E2F peptide could be readily located in the initial electron density maps. The structure shows that the packing of the A and B domains generates a waist-like interface groove into which $E2F_{(409-426)}$ binds in a largely extended manner (**Figure 25**). A high proportion of the hydrogen bond interactions between the two molecules involve the side chains of conserved pRb residues interacting with the main chain of E2F.

Some oncogenic viruses, such as human papillomavirus (HPV) code for proteins that disrupt pRb/E2F interaction. In the case of HPV this function is mediated by the small, zinc-binding protein E7 that binds to pRb via the characteristic LxCxE motif of the oncoprotein. The crystal structure reveals that the core binding site of E2F is located more than 30 Å away from the $E7_{(21-29)}$ binding site (green worm in **Figure 25**). To examine the mechanism of how E7 targets the pRb/E2F complex, a series of biochemical experiments have been carried out using intact HPV E7 and a construct of E2F that contains both the marked box and the core binding region. The data demonstrate that intact E7 protein binds at least 15-fold tighter to pRb than a short LxCxE based E7 peptide. These results also reveal that the tight biding of the HPV oncoproteins to pRb prevents subsequent interactions with the marked box region of E2F but does not affect binding of the tumour suppressor to the core binding-region of E2F.

With the detailed molecular description of the interactions between E2F and pRB, it should be possible to design site-specific mutants of pRb that no longer bind E2F, but whose other properties are unaltered. Such mutated pRb would be a valuable tool for cell biology experiments aimed at probing the function of pRb/E2F interactions. There are some tumours, such as pancreatic carcinoma, where over-expression of functional pRb appears to be detrimental to clinical treatment [2]. Given our description of the molecular interactions between E2F and the A/B interface of pRb we can develop compounds that bind to pRb and inhibit complex formation. Such a compound, administered in parallel with conventional chemotherapy, may offer a means of treatment for pancreatic cancer and perhaps related diseases.

References

[1] R.A. Weinberg, *Cell* **81**, 323-30 (1995).
[2] T. Plath, M. Peters, K. Detjen, M. Welzel, Z. von Marschall, C. Radke, B. Wiedenmann, and S. Rosewicz, *J Natl. Cancer Inst.* **94**, 129-142 (2002).

Principal Publication and Authors

B. Xiao (a), J. Spencer (a), A. Clements (b), N. Ali-Khan (a), S. Mittnacht (c), C. Broceño (c), M. Burghammer (d), A. Perrakis (e), R. Marmorstein (b) and S.J. Gamblin (a), *Proc. Natl. Acad. Sci. USA* **100**, 2363-2368 (2003).
(a) National Institute for Medical Research (UK)
(b) University of Pennsylvania (USA)
(c) Institute of Cancer Research (UK)
(d) ESRF
(e) The Netherlands Cancer Institute (The Netherlands)

Structure of a Hepatitis C Virus Immunodominant Antigenic Site

Hepatitis C virus (HCV) is the major causative agent of transfusion associated hepatitis. Among the structural proteins of the virus, the core protein is highly conserved in the various HCV genotypes and elicits a rapid response after the onset of the disease. Thus, the measurement of HCV antibodies (Abs) titer in serum is widely used to screen for HCV infection [1].

Several studies, mainly based on peptide scanning using chemical or recombinant approaches, have established that the first 120 residues of the HCV core protein contain highly immunogenic B cell epitopes that are predominantly recognised by HCV-infected patient serum; one of them has been identified in the N-terminal region (20-45) of the core protein.

To analyse the structural characteristics of that HCV-immunodominant epitope we generated different monoclonal antibodies (mAbs) by immunising mice with a truncated recombinant 1-120 region. Among the mAbs obtained, 19D9D6 appeared to be specific for an epitope encompassed by residues 29-33 [2]. This antibody was crystallised as was its complex with a synthetic 28 amino-acids peptide that encompasses the recognised portion 13-40 of core. Crystals of the free antibody ($P2_12_12$; a = 63.48 Å, b = 173.68 Å, c = 41.73 Å) diffracted to 1.6 Å resolution on beamline **ID14-EH1** while crystals of the complex ($P2_1$; a = 42.18 Å, β = 101.7 Å, c = 55.18 Å, β = 98.6°) diffracted to 2.34 Å resolution on beamline **BM30**.

Both structures were solved by molecular replacement followed by rigid body refinement and cycles of conjugate gradient and isotropic temperature factor refinement using CNS.

The final electron density maps of the complex between the 19D9D6 Fab' and the 13-40 peptide allows the positioning of all the 438 residues of the Fab' and 15 of

the 28 peptide residues. The peptide is bound in a crevice between the VL and the VH domains (**Figure 26**). It was a curved construction and only nine residues interact with mAb 19D9D6. Detailed comparison of the free and complexed 19D9D6 Fab' structures shows that only minor structural adjustments are needed in the VL domain to accommodate binding of the peptide. The crystal and solution structures of the core peptide are different. In solution, its small hydrophobic core is protected by two helices that pack against each other. In the crystal, the peptide conformation is stabilised by hydrogen bonds and van der Waals interactions with the antibody. Only a short stretch of five residues can be superimposed between the solution and crystal structures.

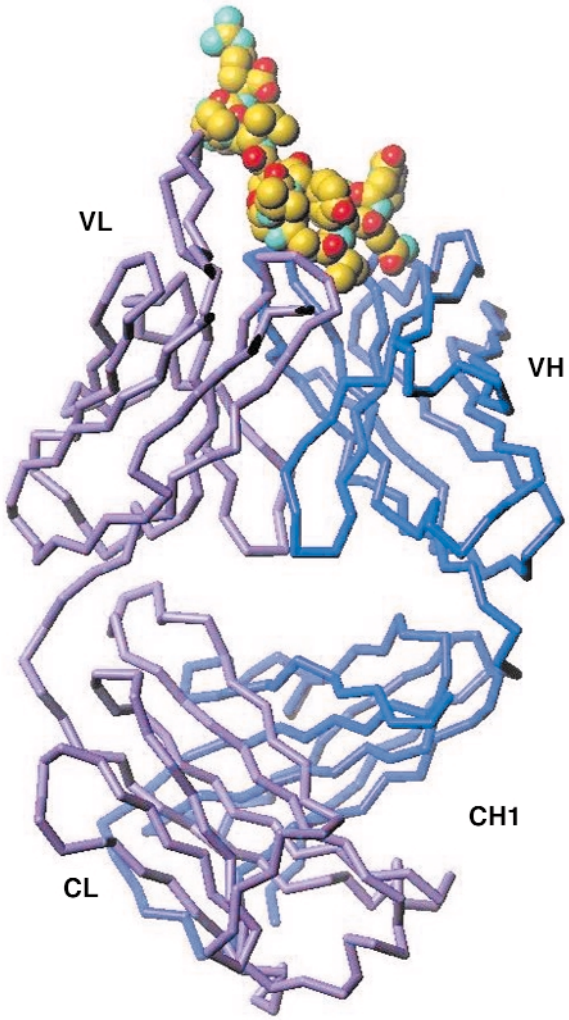

Fig. 26: Schematic representation of the complex of core peptide (RNTNRRPQDVKFPGGGQIVGGVYLLPRR) and 19D9D6 antibody.

This is the first structure of a fragment of HCV core antigen. The structure of the complex of Fab' 19D9D6 with core peptide 13-40 offers an unique opportunity to understand how antibodies act in acqueous solutions and in lipidic environments. Given that this monoclonal antibody competes effectively with human sera, it is suggested that human anti-HCV Abs may share many of the features of mAb 19D9D6, including the ability to destabilise, partially at least, the solution conformation of the antigen often found associated with a lipidic phase.

References

[1] H.J. Park, S.M. Byun, Y.J. Ha, J.S. Ahn and H.M. Moo, *J. Immunoassay,* **16**, 167-181 (1995).

[2] C. Jolivet-Reynaud, P. Dalbon, F. Viola, S. Yvon, G. Paranhos-Baccala, N. Piga, L. Bridon, M.A. Trabaud, N. Battail, G. Sibai and M. Jolivet, *J. Med. Virol.,* **56**, 300-309 (1998).

Principal Publication and Authors

R. Ménez (a), M. Bossus (a), B.H. Muller (a), G. Sibai (b), P. Dalbon (b), F. Ducancel (a), C. Jolivet-Reynaud (c) and E.A. Stura (a), *The Journal of Immunology,* **170**, 1917-1924 (2003).

(a) UMR CEA-bioMérieux DIEP, Saclay (France)

(b) R&D bioMérieux, Marcy l'Etoile (France)

(c) UMR CNRS-bioMérieux, Lyon (France)

Cytochrome P450 2C9 with Bound S-warfarin

Cytochromes P450 are haem-containing enzymes found in many bacteria, fungi, plants and animals. P450s catalyse the biotransformation of a wide range of structurally-diverse endogenous and exogenous substrates. A number of human cytochromes P450 are of great interest to the pharmaceutical industry, due to their role in phase I metabolism of drugs. During phase I the reaction most commonly catalysed by P450s is the hydroxylation reaction

$$RH + O_2 + 2H^+ + 2e^- \rightarrow ROH + H_2O$$

The electrons required are donated by NADPH-cytochrome P450 reductase and cytochrome b_5. In phase II metabolism this group is then conjugated, thus increasing the solubility of the compound and facilitating excretion. By understanding the way in which P450s recognise and metabolise compounds, it is hoped that modifying these interactions may alter the pharmaceutical profile of compounds.

In contrast with many of the bacterial P450s whose structures have been solved, the mammalian drug-metabolising P450 enzymes are membrane-associated proteins, and this hampered production of protein suitable for structural studies. We have generated an active, truncated 2C9 protein that crystallises and diffracts to a resolution of 2.6 Å. We collected data from P450 2C9 crystals on ESRF beamline **ID14-1** to 2.6 Å resolution and solved the structure by molecular

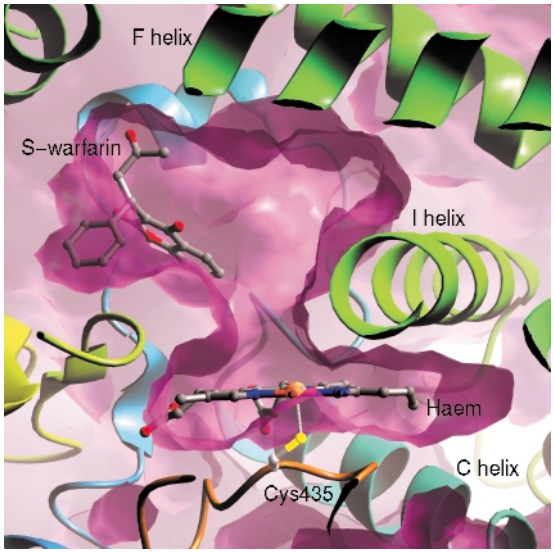

Fig. 27: The binding site of S-warfarin within the active site of 2C9 leaves the haem, shown edge on in the figure, accessible to other compounds.

replacement. The haem group forms the bottom of a large active site, with different regions of the polypeptide chain forming the active site. We then went on to solve the structure of 2C9 in complex with the anticoagulant substrate, S-warfarin, using data collected on beamline **ID14-2**. Contrary to expectations, the S-warfarin binding site is some 10 Å away from the haem (**Figure 27**). The location of the binding site suggests an allosteric mechanism, and leaves sufficient room directly above the haem for an additional compound molecule to bind, giving a structural basis for drug-drug interactions.

Principal Publication and Authors

P.A. Williams (a), J. Cosme (a), A. Ward (a,b), H.C. Angove (a), D. Matak Vinković (a), H. Jhoti (a), *Nature* **424**, 464-468 (2003).

(a) Astex Technology, Cambridge (UK)
(b) Current address: AstraZeneca, R&D Charnwood, Loughborough (UK)

The Crystal Structure of CDP-ME Kinase: a Target for the Development of Novel Antimicrobial Drugs

Due to increasing levels of antibiotic drug resistance there is an urgent need to develop new drugs for microbial infections. Structural biology has much to offer towards this goal by contributing to structure-based design or discovery of potent enzyme inhibitors. The key to the development of novel antibiotics however, is the choice of the enzyme target to be inhibited. Ideally such an enzyme must be essential to pathogens and absent from humans. Recently, a complete metabolic pathway comprising seven enzymes that fulfill this criterion has been delineated [1]. This pathway, termed the 1-deoxy-D-xylulose-5-phosphate (DOXP) pathway, generates isopentenyl diphosphate (IPP) and dimethylallyl diphosphate (DMAPP), the universal precursors of isoprenoids. These are compounds that contribute to key cellular functions including respiration, hormone-based signaling, apoptosis, meiosis, protein cleavage and degradation. They are also components of cell membranes. Organisms that utilise the DOXP pathway include the causal agents for many serious diseases including leprosy, malaria, various gastrointestinal and sexually transmitted infections, trachoma, tuberculosis and certain types of pneumonia. Crucially, mammals utilise a different pathway containing completely different enzymes to make IPP and DMAPP and this makes enzymes in the DOXP pathway very attractive targets for novel antimicrobial drugs.

We have thus determined the crystal structure of 4-Diphosphocytidyl-2*C*-methyl-D-erythritol (CDP-ME) kinase that catalyses the single ATP-dependent phosphorylation stage affording 4-diphosphocytidyl-2*C*-methyl-D-erythritol-2-phosphate (**Figure 28**), a reaction at the core of the DOXP pathway.

Although the enzyme crystallised readily, the crystals were poorly ordered and the ESRF facilities were essential to obtain high-quality diffraction data. After testing a great many samples, the structure of a ternary complex with substrate and an ATP analogue was determined at 2.0 Å resolution using the single-wavelength anomalous dispersion method. The asymmetric unit of the crystals contains two copies of the enzyme, which form an extended homodimer with C_2 symmetry (**Figure 29**). The structure of the enzyme itself is characteristic of the Galacto-Homoserine-Mevalonate-Phosphomevalonate kinase superfamily, and consists of two domains, one of which binds the co-factor and one of which binds the substrate. The catalytic center is positioned in a deep cleft between domains. The cofactor ATP binds with its adenine base in an aliphatic cleft where it forms hydrogen-bonding interactions that stabilise the uncommon *syn* orientation of the base. Both the ribose and phosphate groups of the cofactor are solvent accessible. CDP-ME binds with the cytosine tucked inwards and sandwiched between two aromatic side chains. Its tail is directed towards the cofactor γ-phosphate at the catalytic center, which consists of Lys10 and Asp141 (**Figure 28b**). These residues polarise the O2M hydroxyl group of CDP-ME and facilitate proton abstraction. Asp141 acts as a general base and generates a nucleophile that attacks the ATP γ-phosphate group while Lys10 stabilises the transition state.

The sequence identity of CDP-ME kinase averages 45% over all species with conservation extending throughout

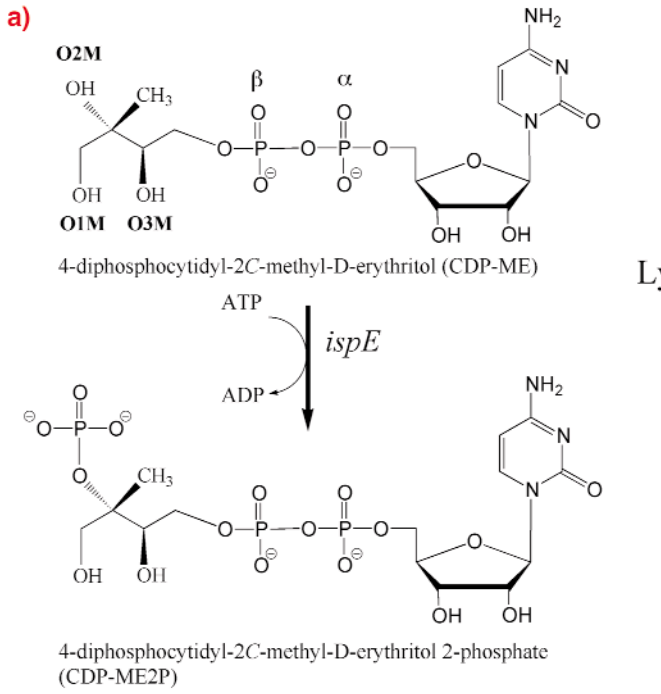

Fig. 28: (a) The reaction catalysed by CDP-ME kinase. (b) The proposed catalytic mechanism for CDP-ME kinase as deduced from the structure determination described in the text.

the sequence. In particular the key residues for ligand binding and catalysis are conserved. This high level of sequence similarity indicates that our model of the structure of CDP-ME kinase provides an excellent high-resolution template for a structure-based approach to aid the search for novel broad-spectrum antimicrobial drugs. One of the keys to the success of this endeavor will be the continued use of synchrotron radiation to ensure that accurate structural information for potential enzyme-drug complexes is attained.

Reference

[1] F. Rohdich, S. Hecht, A. Bacher and W. Eisenreich, *Pure Appl. Chem.* **75**, 393-405 (2003).

Principal Publication and Authors:

L.Miallau (a,b), M.S. Alphey (a), L.E. Kemp (a), G.A. Leonard (b), S.M. McSweeney (b),S. Hecht (c), A. Bacher (c), W. Eisenreich (c), F. Rohdich (c) and W.N. Hunter (a), *Proc. Natl. Acad. Sci. USA* **100**, 9173-9178 (2003).

(a) School of Life Sciences, University of Dundee (UK)

(b) ESRF

(c) Institute für Organische Chemie und Biochemie, Technische Universität München (Germany)

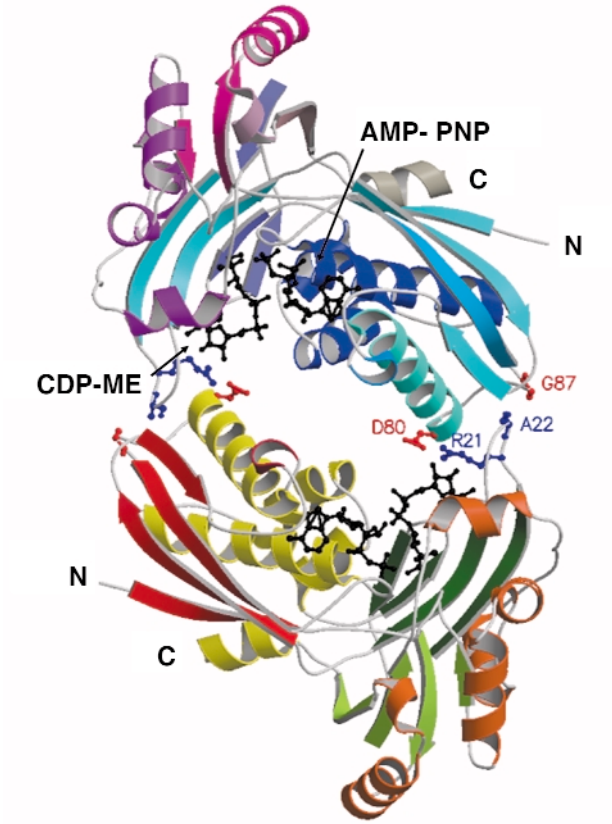

Fig. 29: Ribbon diagram representation of the structure of the CDP-ME kinase dimer. Amino acid residues contributing to dimer formation are shown as coloured balls and sticks while both the substrate and cofactor analogue are shown as black balls and sticks.

Structural Genomics at the ESRF: studying *Deinococcus radiodurans*

The non-pathogenic red-pigmented Gram-positive bacterium *Deinococcus radiodurans* is extremely resistant to ionising radiation and other damaging agents such as ultraviolet (UV) radiation and desiccation. It is able to withstand up to 15,000 grays of ionising radiation and the mechanisms it uses to achieve this extraordinary extremophile capability have made this bacterium the subject of intense study. *D. radiodurans* was amongst the first organisms for which the complete genome sequence was made available and a thorough analysis of this genome has been carried out to try to elucidate the mechanisms by which this organism survives extreme radiation doses [1,2].

To complement such studies, the ESRF's Macromolecular Crystallography group has instigated a structural genomics initiative studying *D. radiodurans*. An initial round of protein targets have been selected for structural studies. Targets chosen included proteins involved in DNA-damage repair, desiccation resistance, and oxidative stress response. Additionally a number of hypothetical proteins with no known homologues in other organisms were also selected as targets.

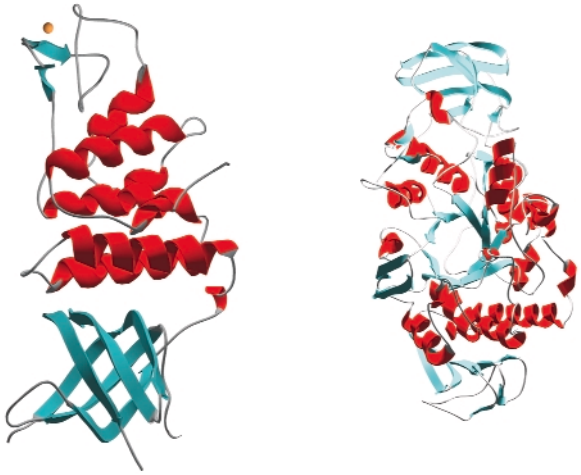

Fig. 30: Examples of protein structures solved from *Deinococcus radiodurans*.

Once targets from the *D. radiodurans* R1 strain were chosen, cloning and small-scale protein expression testing was performed in collaboration with ProteinXpert (Grenoble). Using these results as a springboard we have thus far expressed 21 proteins on a scale necessary for crystallisation studies and successfully purified 18 of these. Crystallisation trials have produced diffraction quality crystals for 10 targets and of these 6 have proven amenable to structure solution (**Figure 30**). The structures were solved from data collected on the ESRF's macromolecular crystallography beamlines using single wavelength anomalous diffraction (SAD), multiple isomorphous replacement (MIR) and molecular replacement methods. At the time of writing a further seven targets are in crystallisation trials and native data have been collected from crystals of one target. The remaining projects are now the subject of further screening for large-scale expression and purification.

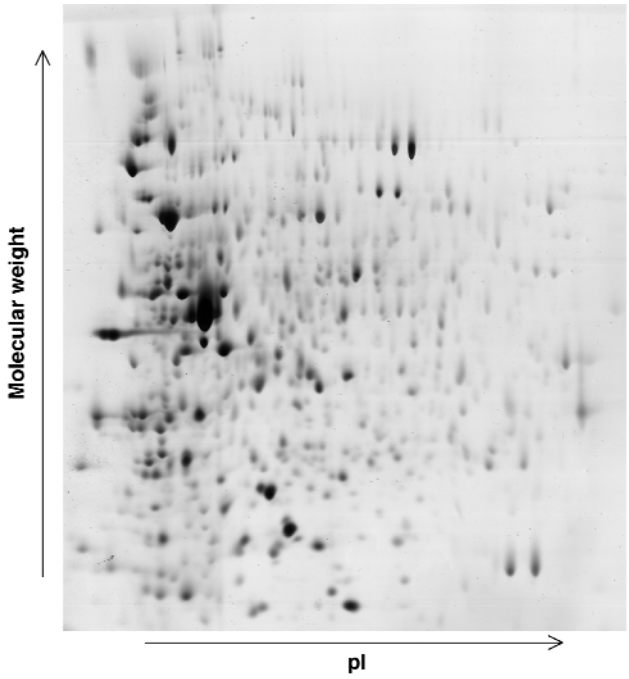

Fig. 31: Example of a 2D gel: the *D. radiodurans* proteome 30 minutes after irradiation.

In conjunction with the work briefly described above, a study is under way using beamline **ID17** to investigate the effects of radiation dosage on the expression levels of proteins within the cells of *D. radiodurans*. 2D-gel electrophoresis (**Figure 31**) is being used to identify changes in protein expression levels after exposure of *D. radiodurans* to large doses of radiation and during the recovery stages of the organism. Any proteins identified in these studies as contributing to the extremophile nature of *D. radiodurans* will then be investigated by a combination of molecular and structural biology.

Reference

[1] White *et al., Science,* **286,** 1571-7 (1999).
[2] Madarova et al., *Microbiol. Mol. Biol. Rev*. **65**, 44-79 (2001)

Authors

D. Hall, I. Leiros, H-K. Leiros, E. Micossi, E. Gordon, S. Macedo, U. Kapp, C. Jamin, J. Timmins, G. Leonard, S. McSweeney.
ESRF

Putting Radiation Damage to Good Use

For a number of years it was believed that the problem of radiation-damage in macromolecular crystallography had largely been overcome by using cryo-cooling techniques. These appeared to give protein crystals an almost endless lifetime on laboratory X-ray sources as well as on beamlines of second-generation synchrotron sources. However, during the design of new beamlines at third-generation synchrotrons, it became clear that even cryo-cooled macromolecular crystals could be destroyed rapidly. Whilst it was realised that it could become difficult to collect highly redundant data sets on these powerful new sources, it was generally believed that radiation-damage would only affect the resolution of the data, and not the structures of macromolecules themselves.

Surprisingly, systematic studies of radiation-damage on cryo-cooled crystals of macromolecules performed at the beamline ID14, showed some highly specific structural changes. These changes include the breakage of disulphide bonds and the decarboxylation of acidic residues [1-3]. Additionally, 'stressed regions' in proteins, such as active site residues or metal ion binding sites, were found to be noticeably more susceptible to the effects of ionising radiation than the rest of the structure. Further studies have confirmed that these effects are general.

Rather than regarding radiation-damage as a problem to be avoided, we have developed a new technique that allows the elucidation of crystal structures of native macromolecules by exploiting the specific structural changes induced upon X-ray exposure. The method has been used to determine the structure of a 23.5 KDa molecular weight protein and that of a synthetic RNA oligonucleotide.

In both cases an initial, complete diffraction data set was collected from the crystals studied. They were then exposed to X-rays for a dose that far exceeded the dose needed for the initial data collection – we term this process 'burning' the crystal - after which further complete data sets were collected. Intensity differences between the data sets obtained before and after the 'X-ray burn' could be interpreted using existing software packages and a model of the specific structural differences induced by the X-ray beam was built iteratively. The final model of structural differences was used, in a manner analogous to classic isomorphous replacement techniques, to produce initial estimates of phases and preliminary electron density maps. Powerful automatic model building routines were applied in order to improve these protein phases and to autobuild the entire structure. For the oligonucleotide, the structure could be deduced directly from the spectacularly detailed preliminary electron density maps **(Figure 32)**.

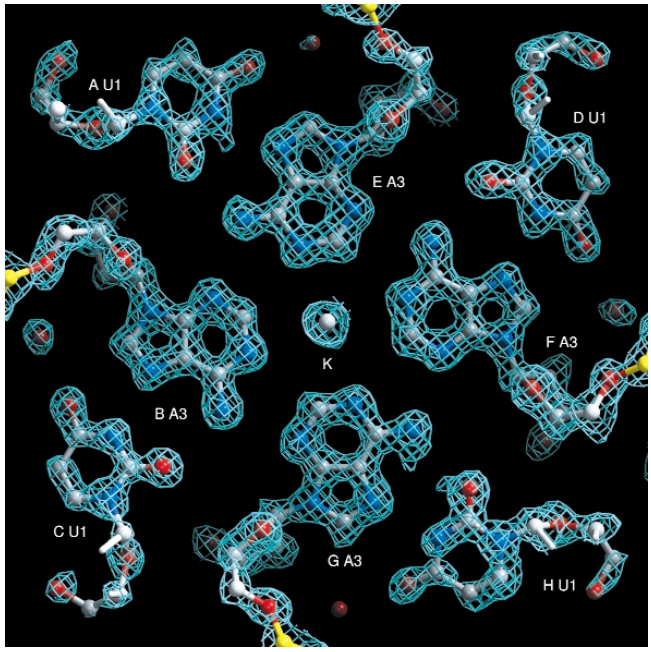

Fig. 32: Section of the experimental electron-density map for the oligonucleotide. The map is shown after radiation-damage induced phasing (*rip*) and solvent flattening. The correlation between this map and the final map after refinement is 0.90. The final model consists of eight copies (labeled A-H) of six nucleotides each.

We have named this method of structure determination 'radiation-damage induced phasing' (*rip*). We have derived *de novo* phases using *rip* exclusively, but it could also be very useful to exploit the technique in combination with other phasing techniques such as anomalous dispersion. Current developments in crystallographic theory, hardware and software should make the technique more powerful. Programs are being adapted to deal with data collected during the 'burn' of the crystal. These developments make us optimistic that the use of *rip*, either as primary or secondary source of phase information, will help to render the phase problem a less significant barrier to macromolecular structure determination.

References

[1] W.P. Burmeister, *Acta Cryst* **D56**, 328-41 (2000).
[2] R.B.G. Ravelli and S.M. McSweeney, *Structure Fold Des* **8**, 315-28 (2000).
[3] M. Weik, R.B.G. Ravelli, G. Kryger, S.M. McSweeney, M.L. Raves, M. Harel, P. Gros, I. Silman, J. Kroon and J.L. Sussman, *Proc Natl Acad Sci U S A* **97**, 623-628 (2000).

Principal Publication and Authors

R.B.G. Ravelli (a), H.K. Leiros (b), B. Pan (c), M. Caffrey (c) and S.M. McSweeney (b), *Structure (Camb)* **11**, 217-24 (2003).
(a) EMBL, Grenoble Outstation (France)
(b) ESRF
(c) The Ohio State University, Columbus (USA)

Human Angiotensin I Converting Enzyme Structure Revealed

Since the 1980s, inhibitors of angiotensin converting enzyme (ACE inhibitors) have achieved great success as first-line therapy for cardiovascular diseases, including high blood pressure, heart failure, coronary artery disease, and kidney failure. These anti-hypertensive drugs were not designed based on any knowledge of the three-dimensional structure of ACE, but on an assumed mechanistic homology to carboxypeptidase A, whose structure has been known for some time. However, prolonged administration of current ACE inhibitors leads to several undesirable side effects, such as a persistent dry cough, headaches and dizziness [1].

There are two isoforms of ACE in the human body, somatic and testicular. Somatic ACE exists in most cells in the body and testicular ACE, which is half the size of somatic ACE, is found only in the testes. Both convert inactive angiotensin I to its active form, angiotensin II, which stimulates blood vessel constriction. Both forms of ACE also inactivate bradykinin, which stimulates blood vessel dilation. The X-ray structure of testicular ACE, and its complex with the widely used ACE inhibitor lisinopril, at 2.0 Å resolution has been elucidated. This structure was determined using the anomalous scattering of the bound Zn atom at beamline **BM14** of the ESRF.

The three-dimensional structure reveales that ACE is composed of α-helices for the most part, and incorporates a zinc ion and two chloride ions (**Figure 33**). In fact it bears little resemblance to carboxypeptidase A except in the active site zinc-binding motif. Instead, it resembles rat neurolysin and *Pyrococcus furiosus* carboxypeptidase, despite sharing little amino-acid sequence similarity with these two proteins. This similarity extends to the active site, which consists of a deep, narrow channel that divides the molecule into two subdomains. On top of the molecule is an amino-terminal 'lid', which seems to allow only small peptide substrates (25–30 amino acids) access to the active site cleft – this accounts for the inability of ACE to hydrolyse large, folded substrates.

Somatic ACE consists of two parts (called the N- and C-domains), each having a different function, and current drugs inhibit both domains. The newly described structure of testicular ACE (which is identical to the C-domain of somatic ACE) will now serve as a 'template' for the design of next-generation, domain-selective ACE inhibitors with the potential for greater efficacy, fewer side effects and new treatment indications for hypertension.

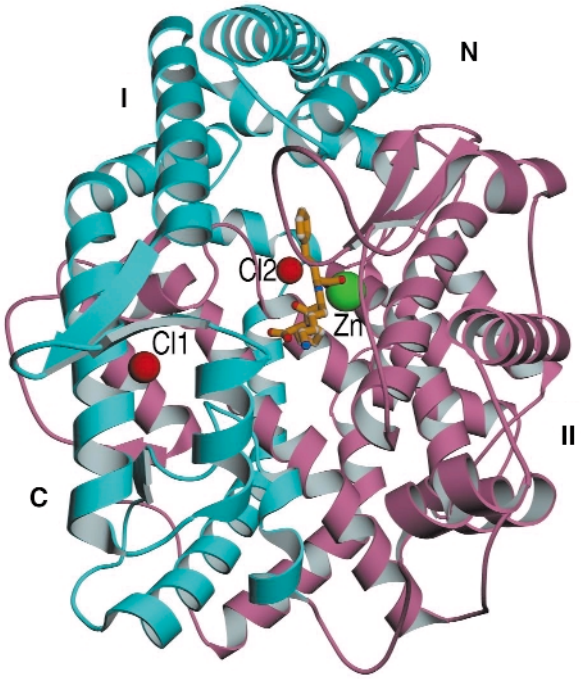

Fig. 33: Crystal structure of human testicular ACE with the inhibitor (lisinopril) molecule bound at the centre of the molecule. The green sphere represents the zinc ion and the red spheres represent the bound chloride ions.

References:

[1] K.R. Acharya, E.D. Sturrock, J.F. Riordan and M.R.W. Ehlers, *Nature Reviews- Drug Discovery.* **2**, 891 (2003).

Principal Publication and Authors:

R. Natesh (a), S.L.U. Schwager (b), E.D. Sturrock (b) and K.R. Acharya (a), *Nature* **421**, 551 (2003).
(a) University of Bath, Bath (UK)
(b) University of Cape Town (South Africa)

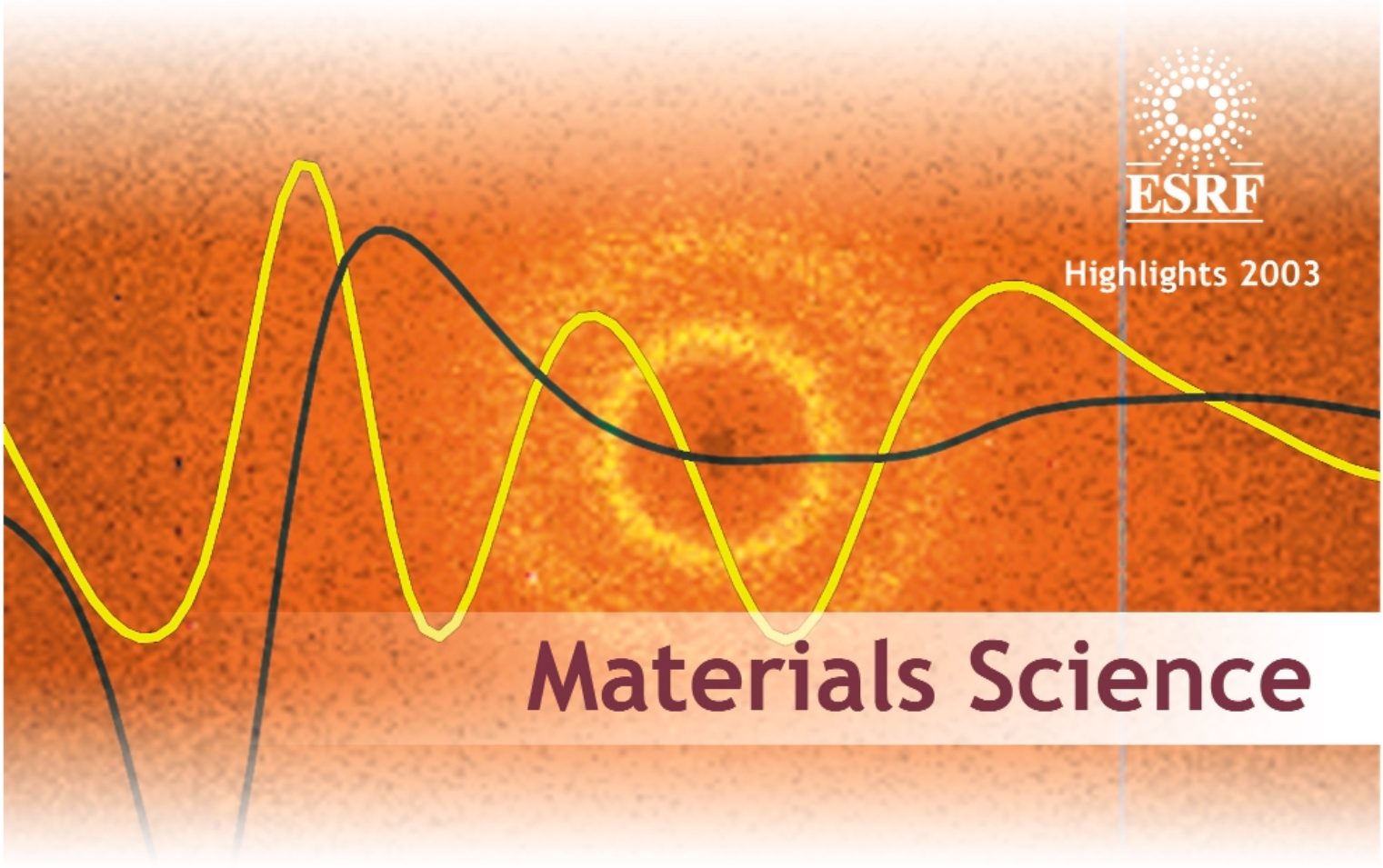

Introduction

Materials science research continues to play a major role at the ESRF and spans a wide range of applications. The present trend is that, with increased brilliance and the ability to produce sub-micrometre focussing of the X-ray beam, new experiments are becoming accessible to the beamlines. The complexity of the structures studied are increasing, the sample sizes and measuring gauges are decreasing, the accessible range of pressures and temperatures are increasing and the available time-resolution is in the picosecond regime. Since materials science is so broad, other chapters also cover many applications in this highlight presentation.

This chapter is structured into four different sections:
- Materials science and solid-state chemistry at work
- High-pressure diffraction
- Subnanosecond-resolved diffraction
- Stress and strain studies at the ESRF

In the solid-state chemistry part we highlight the structure determination of very large supramolecular assemblies by single crystal determination from tiny and rather difficult crystals. The powder diffraction method has been extended by the implementation of a new insertion device enabling the *ab initio* solution of previously inaccessible complex structures. Studies of nanostructure evolution and spin / magnetic phase transitions are other areas illustrated. The high-pressure diffraction field is expanding and a new high-brilliance high-pressure beamline is being constructed. The science spans a wide range from studies of iron-silicon alloys and spinels at extreme conditions to structural properties of diamond at high pressures and pressure modulated structures of antimony. The sub nanosecond-resolved diffraction has reached maturity as illustrated by a picosecond “movie” of myoglobin in action and structural kinetics studies of photochemical reactions in solution. The stress and strain studies are geared towards novel studies of residual stress in industrially important compounds. Notable studies are the combined study of metal matrix interfaces by diffraction and imaging as well as depth-resolved studies of friction stir welding. The FaME38 project is a collaboration between seven British research institutions, the ILL and the ESRF. Its aim is to improve and streamline engineering experiments and so provides new opportunities for engineers at the two facilities.

Å. Kvick

Materials Science and Solid-state Chemistry at Work

Introduction by A. Fitch, ESRF

Innovative materials with improved or novel properties are emerging from research programs in pure and applied materials science, solid-state physics and chemistry. Fundamental to an understanding of any material's behaviour is detailed knowledge of the structure, encompassing the arrangement of the constituent atoms, their electronic structure, and an appreciation of their means of interaction. From such awareness, further developments can flow. Synchrotron radiation provides several complementary techniques such as diffraction, spectroscopy and imaging, to investigate the structures of materials from the atomic level through to the microstructure. The structure of a material is, however, no more than a snapshot under specific conditions. Dynamic properties are also of crucial importance as materials evolve under the influence of changing temperatures, pressures, or chemical environment. Synchrotron techniques, because of the rapidity with which measurements can be made, also provide the capacity to observe dynamic systems evolving or transforming *in situ*.

In the following articles, we highlight several applications of X-ray diffraction to probe the structure in different states of matter, such as single crystals, powders, deposited thin gold films and even a molten metal oxide at very high temperature. The fabrication of certain of the samples and the diffraction measurements themselves present their own challenges. The results provide fundamental insights into a range of phenomena, including magnetic and electronic properties, microstrain, texture and microstructure, phase separation, and unusual thermal-expansion behaviour, with applications ranging from potential systems of data storage, through to the characterisation of distinct forms of crystalline drug molecules.

Self-Assembly, Structure and Dynamic Interconversion of Metallosupramolecular Architectures

The spontaneous but controlled generation of functional architectures by self-assembly has emerged as a major development in the field of supramolecular chemistry, aiming at the design of self-organising systems of increasing complexity [1,2]. Of special interest among the great variety of possible superstructures are those containing metal ions arranged in a grid-type fashion. As multisite species, they present intriguing features that make them potential components of nanoscale information storage devices.

It is crucial to obtain an atomic level crystal structure in order to understand the stability criteria and self-assembly mechanisms of such compounds. However, high molecular weight species tend to produce poor and unstable van-der-Waals crystals not amenable to structure solution and refinement by laboratory methods. It is only possible to obtain tractable data on such crystals using a high-intensity synchrotron X-ray source.

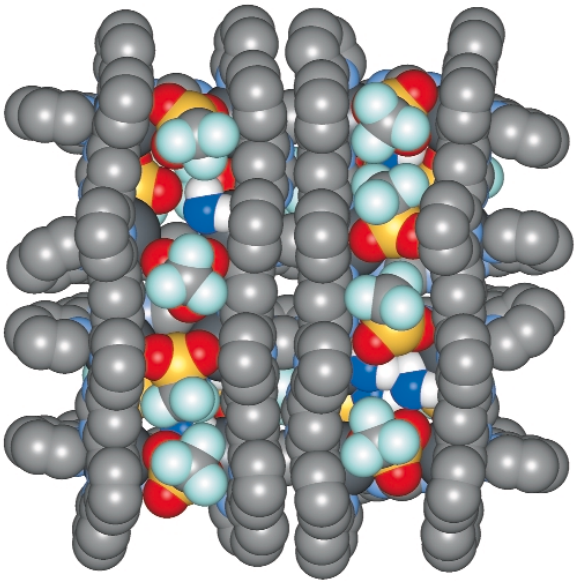

Fig. 34: Space-filling representation of the crystal structure of the [4x4]Pb^{II}_{16} grid complex.

Among the most complicated of the systems studied so far are the [4x4]Pb^{II}_{16} grid (**Figure 34**) and [4#4]Pb^{II}_{12} double-cross (**Figure 35**) architectures. These systems contain arrays of lead ions in a well-defined arrangement, which is accessible in a single operational step via self-assembly of respectively 24 and 16 components. This self-organisation is driven by the formation of respectively 96 and 48 coordinative bonds between the tetratopic terpyridine ligand and the lead(II) ions.

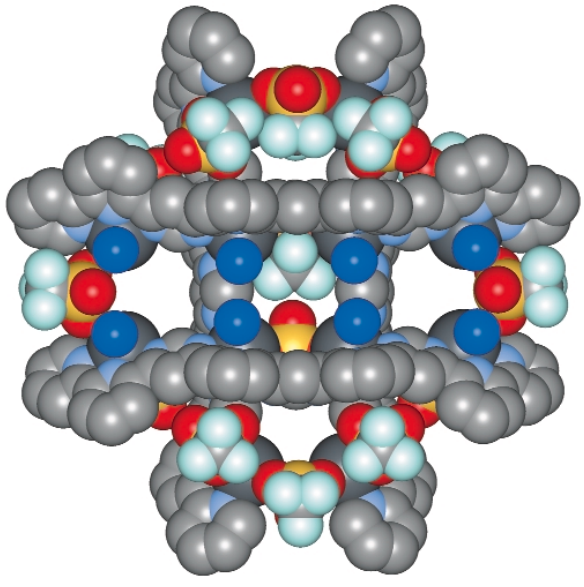

Fig. 35: Space-filling representation of the crystal structure of the [4#4]Pb^{II}_{12} double-cross complex.

X-ray diffraction measurements were carried out at beamline **ID11** using a wavelength of 0.32826 Å. The best crystals which could be produced were very poor (> 2° mosaic!), small (some tens of μm^3) and unstable in air (lifetimes outside the mother liquor <1 hour). Structure solution and refinement required accumulation of data from several crystals and extensive data treatment.

The $[4x4]Pb^{II}_{16}$ grid and the $[4\#4]Pb^{II}_{12}$ double-cross result from the appropriate design of the ligand which is programmed for efficient self-assembly under the principle of "maximum coordination site occupation". The coordination array is further stabilized by π–π interactions, which stack subsets, and by internal bridge-type coordination of the lead cations by the triflate counterions, which decrease the total charge of the complex cation and thus the coulombic repulsion between the Pb^{II} cations.

The overall total volumes of the $[4x4]Pb^{II}_{16}$ grid and of the $[4\#4]Pb^{II}_{12}$ double-cross are ~ 8.6 nm^3 and 6.9 nm^3 respectively, placing these entities within the nanostructural domain.

In terms of programmed self-assembly, the formation of the different metallo-architectures underlines the fact that, despite the role of the coordination interactions and of maximal site occupation, other factors, such as stacking, preferential pyridine coordination, and binding of anions and solvent molecules may interfere and influence the nature of the favoured output species. Atomic level crystal structures provide crucial information for understanding such self-assembly processes.

References:

[1] J.-M. Lehn, *Supramolecular Chemistry-Concepts and Perspectives*, VCH, Weinheim, chap 9 (1995).
[2] M. Barboiu, G.B.M. Vaughan, N. Kyritsakas, J.-M. Lehn, *Chem. Eur J.*, **9**, 763 (2003).

Principal Publication and Authors:

M. Barboiu (a,d), G.B.M. Vaughan (b), R. Graff (c), J.-M Lehn (d), *J. Am. Chem. Soc*. **125**, 10257 (2003).
(a) Institut Européen des Membranes, Montpellier (France)
(b) ESRF
(c) Service Commun de RMN, Strasbourg (France)
(d) ISIS, Laboratoire de Chimie Supramoléculaire, Strasbourg (France)

Solving Larger Molecular Crystal Structures from High-resolution Powder Diffraction Data

Powder diffraction is an important and often unique crystallographic tool to determine the structures of polycrystalline materials for which suitable single crystals cannot be grown. This includes, for example, certain crystalline forms of pharmaceutically-active molecules. However, overlap of the Bragg reflections in the powder diffraction pattern obscures the data and reduces the accuracy of the extracted diffraction-peak intensities. Consequently, traditional single-crystal methods for crystal structure determination are less reliable and often fail when used with powder data, limiting the number of atoms that can be located by this approach to around 30 for equal-atom structures such as organic molecules.

Significant improvement in data quality can now be obtained. Herein, we illustrate this with the routine direct-methods solution of a 48-atom fully-organic crystal structure, which was achieved by exploiting anisotropic thermal expansion, using high-resolution powder X-ray diffraction.

One way to reduce the effective peak overlap is to exploit the anisotropy in thermal expansion that many low-symmetry materials naturally exhibit [1]. At different temperatures the relative positions of Bragg reflections change, owing to the anisotropic changes in the lattice dimensions, but maintain approximately the same intensities. By collecting data at multiple temperatures it is possible to assess the individual contribution of reflections that are overlapping at one temperature, but are better resolved at another.

Changes in the overlap of the reflections as the temperature is varied are best revealed with an intrinsically high-resolution instrument, so that the effects of small peak shifts are more readily discernable. The high-resolution powder diffraction beamline has recently been upgraded, by being moved from a bending-magnet (BM16) to an undulator source (ID31), where it receives a significantly more intense incident X-ray beam. The performance is now such that the systematic use of anisotropic thermal expansion to study more-complex crystal structures by powder diffraction can be envisaged.

During our continuing studies on the low temperature structures of small globular organic molecules, we were unable to solve the arrangement of molecules in 9-ethylbicylco[3.3.1]nona-9-ol ($C_{11}H_{20}O$) despite having deduced the unit cell dimensions, the number of independent molecules in the cell and the crystal symmetry, from measurements made on BM16. Having

48 non-hydrogen atoms in the asymmetric unit (four independent molecules), this complex structure was clearly a promising candidate for an attempt at using the anisotropic thermal expansion approach.

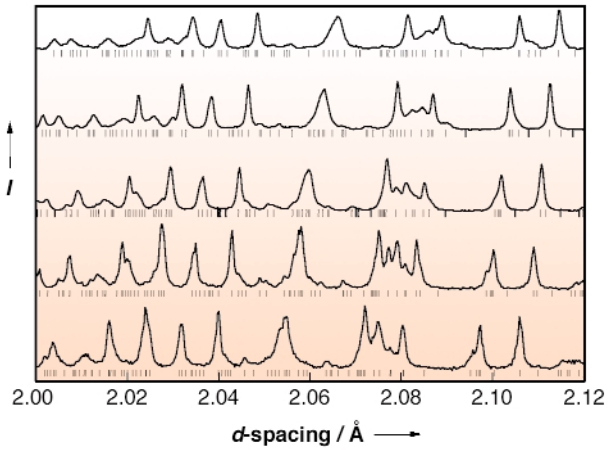

Fig. 36: Selected regions of the five diffraction patterns showing anisotropic thermal expansion. The relative thermal expansion of the a, b and c cell parameters must be different in order to change the relative positions of the peaks. The five diffraction patterns are fitted simultaneously with a single set of peak intensities. Vertical bars indicate Bragg peak positions.

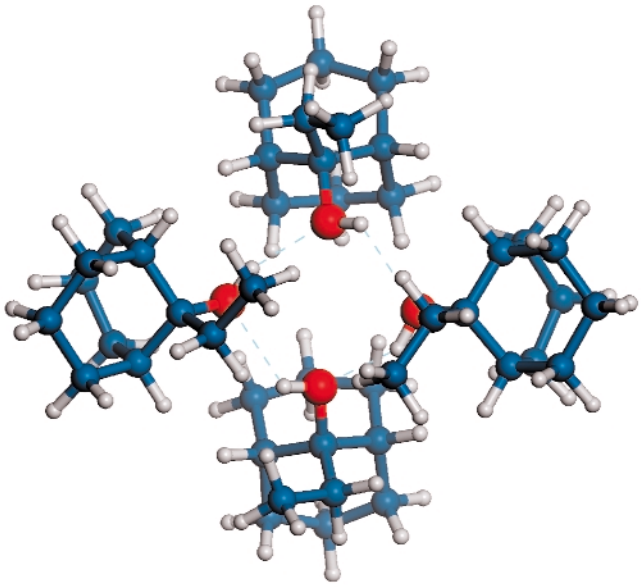

Fig. 37: View of the arrangement of the four independent 9-ethylbicyclo[3.3.1]nona-9-ol molecules. The molecules form a tetramer linked by an approximate square of O-H···O hydrogen bonds between hydroxide groups at the heart of the cluster. The cluster's outer surface is composed of hydrogen atoms. Interactions between adjacent clusters are therefore of a Van-der-Waals nature.

Five powder diffraction patterns at different temperatures in the range 80 – 180 K were collected on **ID31**. Figure 36 illustrates the changes in the diffraction pattern due to peak shifts as a consequence of the anisotropic thermal expansion manifested between 80 K and 180 K. Individual integrated peak intensities were extracted by a multipattern Pawley-style refinement procedure[1], fitting a single set of diffraction peak intensities to the multiple data sets. The four independent molecules, in their entirety, could be found simply using the standard single-crystal direct-methods program SHELXS plus Fourier recycling.

The solution of this structure illustrates a considerable advance in the complexity of a crystal structure derived by direct methods from powder data, and in the quality of data. The data collection was completed in about 12 hours during the first day of scheduled user experiments on the newly-commissioned beamline, with the structural model being derived the very next day. The speed and simplicity of both the data collection and analysis strongly suggest that even larger structures will also be tractable with high-resolution powder X-ray diffraction data.

References

[1] K. Shankland, W.I.F. David, D.S. Sivia, *J. Mater. Chem.* **7,** 569 (1997).

Principal Publication and Authors

M. Brunelli (a), J.P. Wright (a), G.B.M. Vaughan (a), A.N. Fitch (a) and A.J. Mora (b), *Angew. Chem. Int. Ed.*, **42**, 2029-2032 (2003).
(a) ESRF
(b) Universidad de Los Andes, Mérida (Venezuela)

[1] Profile matching procedure in which the diffraction profile is calculated as a sum of overlapping reflections and the intensities are variables in a least-squares procedure.

Temperature-induced Valence Transition in Intermediate Valence $Sm_{2.75}C_{60}$

Metal intercalation compounds of C_{60} are narrow band systems whose understanding poses considerable challenges owing to the dominant role of electronic correlations [1]. Rare-earth fullerides further constitute an intriguing class of strongly correlated electron systems because, in addition to the electronically active anion (C_{60}) sublattice, they accommodate a highly correlated cation (rare-earth) sublattice.

A prominent example of a rare-earth fulleride is $Sm_{2.75}C_{60}$ which adopts a complex orthorhombic structure (space group *Pcab*) characterised by long-range ordering of tetrahedral samarium vacancies and orientational ordering of C_{60} about local three-fold symmetry axes (**Figure 38**). When we probed the structural properties of $Sm_{2.75}C_{60}$ by high-resolution

X-ray diffraction on beamline **ID31**, we found that it exhibits isotropic negative thermal expansion (NTE) in the temperature range 4.2 to 32 K. The NTE coefficient reaches values two orders of magnitude higher than those observed in metal oxides like ZrW_2O_8 [2]. We attribute the origin of the lattice collapse on heating to a quasi-continuous isosymmetric phase transformation driven by the temperature-induced valence transition of Sm from +2 to an intermediate valence of +(2+ε). This effect is reminiscent of the pressure-induced valence transitions in intermediate-valence Kondo insulators like SmS [3].

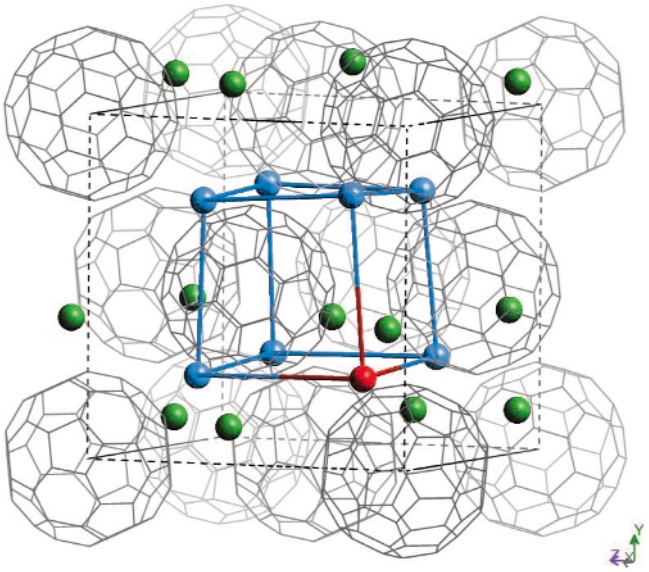

Fig. 38: Building block of the orthorhombic superstructure of $Sm_{2.75}C_{60}$, which can be obtained by doubling along all three lattice directions. Distorted octahedral and tetrahedral samarium cations are depicted as green and blue spheres, respectively. The tetrahedral samarium defect (~ 25% occupancy) is shown as red sphere. The five symmetry-inequivalent C_{60} units present in the unit cell ($C_{60}(1)$ at (000), $C_{60}(21)$ at $(0\,^1/_4\,^1/_4)$, $C_{60}(22)$ at $(^1/_4\,0\,^1/_4)$, $C_{60}(23)$ at $(^1/_4\,^1/_4\,0)$ and $C_{60}(3)$ at $(^1/_2\,^1/_2\,^1/_2)$) are optimally rotated anticlockwise by 37.5° about local three-fold symmetry axes ([111], $[1\bar{1}\bar{1}]$, $[\bar{1}1\bar{1}]$, $[\bar{1}\bar{1}1]$ and [111], respectively).

The lattice response is evident when we follow the behaviour of the (444) Bragg peak as a function of temperature (**Figure 39**). At low temperatures, its position continuously shifts to higher angles on heating, implying anomalous structural behaviour whereby the material contracts as the temperature increases. The trend is reversed above 32 K and normal behaviour is restored with the lattice expanding on heating to 295 K. However, no changes in peak intensities are apparent in the whole temperature range, implying the absence of a phase transition to a structure with different crystal symmetry. Structural analysis at all temperatures resulted in the evolution of the unit cell volume shown in **Figure 40**. Initially the lattice contracts slowly on heating above 4.2 K.

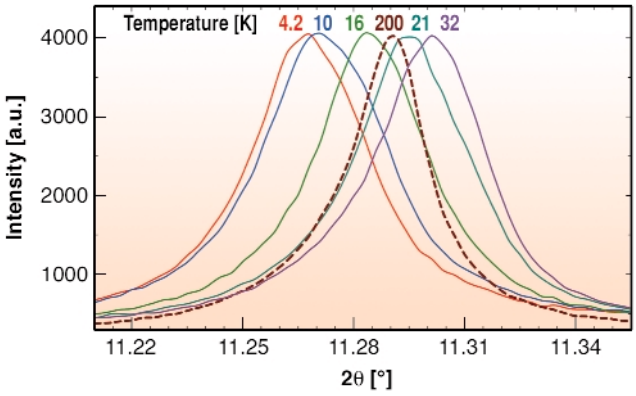

Fig. 39: Selected region of the diffraction profile of $Sm_{2.75}C_{60}$ showing the temperature evolution of the (444) Bragg reflection (λ = 0.79980 Å).

Then the rate of contraction increases to $\alpha_V \approx -1000$ ppm K^{-1} resulting in a volume decrease of 0.84% between 4.2 and 32 K. The sign of the thermal expansivity then changes and the lattice expands on heating to 295 K at approximately +20 ppm K^{-1}, comparable to that in other metal fullerides. Despite this, the $Sm_{2.75}C_{60}$ lattice dimensions at room temperature are smaller than those at 4.2 K.

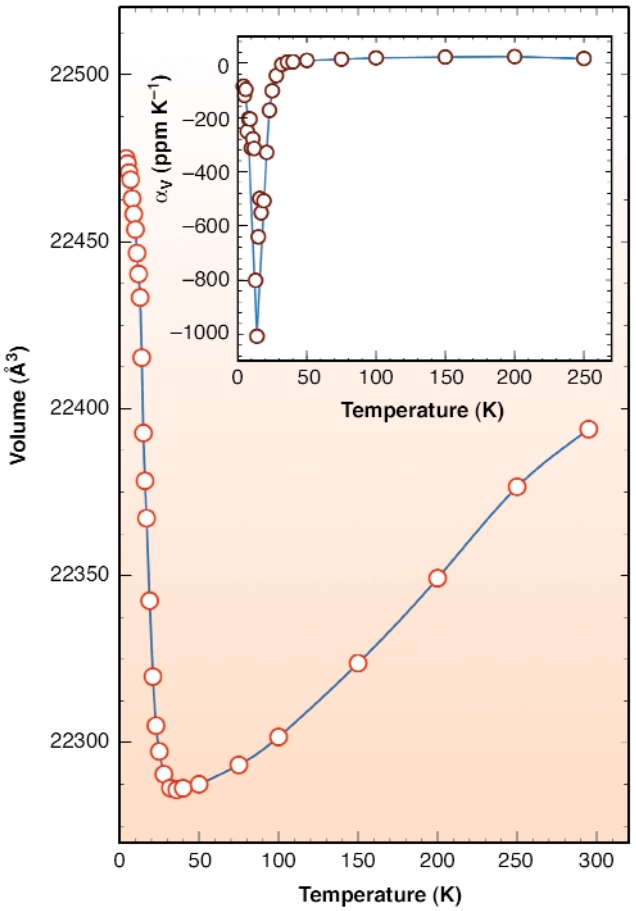

Fig. 40: Temperature evolution of the orthorhombic unit cell volume of $Sm_{2.75}C_{60}$. The inset shows the temperature dependence of the coefficient of thermal expansion, $\alpha_V = d\ln V/dT$.

The explanation of the remarkable lattice response of $Sm_{2.75}C_{60}$ comes from the fragility of the valence states of Sm and its tendency to exhibit intermediate valence. Firstly we note that the unit cell size of metal fullerides is sensitively controlled by the size of the ions residing in the small tetrahedral interstices. In $Sm_{2.75}C_{60}$, the tetrahedral hole has a radius of 1.12 Å, straddling the values of the ionic radii of Sm^{2+} (1.14 Å) and Sm^{3+} (0.96 Å). A valence transition of Sm from +2 towards an intermediate value of +(2+ε) with smaller ionic size, induced on heating, has a profound effect on the lattice size and is consistent with the observed dramatic volume decrease. Complementary magnetic susceptibility measurements provide an estimate of the average Sm valence at high temperatures as ≈ +2.3.

The results presented here open the way for the synthesis and study of new families of molecular-based highly-correlated Kondo and heavy fermion systems with strong coupling between the charge, lattice and spin degrees of freedom. What is unprecedented in the present fulleride analogue is that intermediate valence behaviour is encountered in a system for which strong correlations dominate the electronic properties of both the rare-earth cation and C_{60} anion sublattices. Such synergy has not been encountered before and the rare-earth fullerides should have properties intrinsically unattainable in comparable rare-earth chalcogenides with closed shell anions.

References

[1] O. Gunnarsson, *Rev. Mod. Phys.* **69**, 575 (1997).
[2] T.A. Mary *et al.*, *Science* **272**, 90 (1996).
[3] A. Jayaraman *et al.*, *Phys. Rev. Lett.* **25**, 1430 (1970).

Principal Publication and Authors

J. Arvanitidis (a), K. Papagelis (a), S. Margadonna (b), K. Prassides (a), A.N. Fitch (c), *Nature* **425**, 599-603 (2003).
(a) University of Sussex (UK)
(b) University of Cambridge (UK)
(c) ESRF

Re-entrant Magneto-elastic Phase Transition in $HoFe_4Ge_2$

The compound $HoFe_4Ge_2$ undergoes on cooling a sequence of re-entrant magneto-elastic phase transitions from a tetragonal high symmetry, high temperature (HT) $P4_2/mnm$ phase, to an orthorhombic low symmetry, intermediate temperature (IT) *Cmmm* phase, then to a tetragonal high symmetry, low temperature (LT) $P4_2/mnm$ phase (**Figures 41** and **42**) following the path $P4_2/mnm$ HT (T_c,T_N = 52 K) → *Cmmm* IT ($T_{c'}$,T_{ic1} = 15 K) → $P4_2/mnm$ LT.

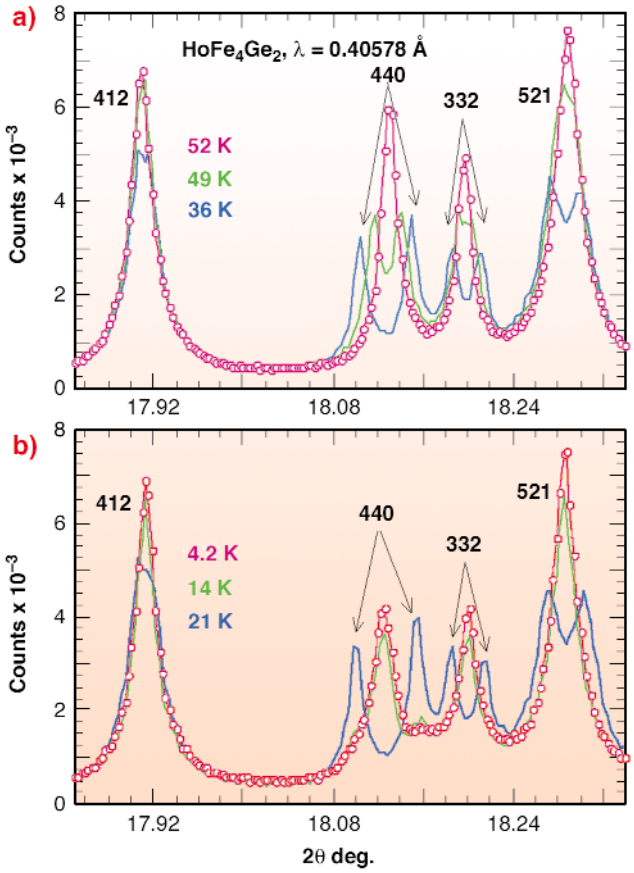

Fig. 41: Detail of the XRPD patterns for various temperatures displaying the pronounced peak splitting (a) below the T_c,T_N, and closing (b) below $T_{c'}$,T_{ic1} of the tetragonal $hhl_t \rightarrow \{hhl_r, h\bar{h}l_r\}$ reflections towards hkl_t reflections in the re-entrant transition tetragonal HT → orthorhombic IT → tetragonal LT.

The analysis of high-resolution powder X-ray diffraction patterns collected at **BM16** for temperatures in the range 1.5 K – 293 K has shown that: a) the HT and LT transitions are of second- and first- order respectively, b) the HT and LT tetragonal phases are identical, differing exclusively in the nature of the micro-strain, see **Figure 43**, and c) enabled us to establish a straightforward relationship between the structural transitions and the underlying magnetic order and to demonstrate their interdependence in a phase diagram, **Figure 42**.

The phase diagram comprises three temperature intervals pertaining to distinct structures and two transitions between them occurring simultaneously with magnetic transitions: 293 K > T > T_c,T_N: HT tetragonal; T_c,T_N > T> $T_{c'}$,T_{ic1} = 15 K: IT orthorhombic- and $T_{c'}$,T_{ic1} > T > 1.5 K: LT tetragonal phases. Below the first order transition at $T_{c'}$,T_{ic1} the latter two phases coexist in strongly variable proportions down to 1.5 K. The LT tetragonal phase reaches 73.6% at 4.2 K (**Figure 41b**). The magnetic ordering is characterised by the wave vectors $\mathbf{q}_{1o}$ = (0,1/2,0) $\mathbf{q}_{2o}$ = (0,q_y,0) for the orthorhombic- and $\mathbf{q}_{1t}$ = (0,1/2,0) for the tetragonal LT phase. The vector components refer to the reciprocal lattice of the C-cell. The magnetic ordering comprises an

additional first-order transition at T_{ic2} = 40 K from the commensurate $\mathbf{q}_{1o}$ phase to the incommensurate $\mathbf{q}_{2o}$ phase. Also this transition is related with anomalies in the lattice parameters and volume observed in the X-ray data (Figure 42a).

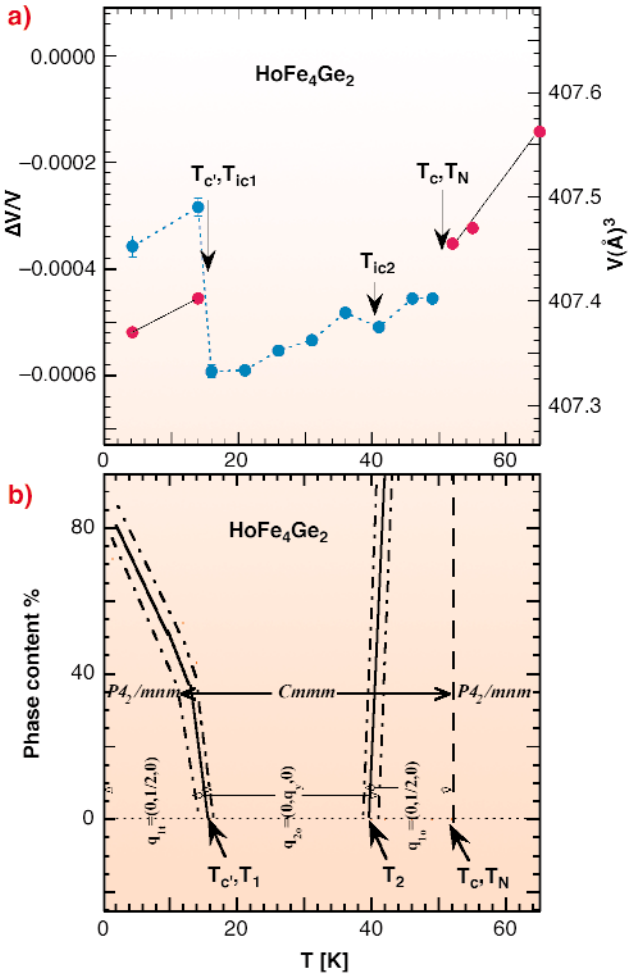

Fig. 42: (a) Thermal variation of the volume, referring to the C-cell. All observed transitions are accompanied by volume anomalies. The first order LT transition is related with volume expansion. (b) The structural and magnetic phase diagram of $HoFe_4Ge_2$. Full and dashed lines are first and second order transitions respectively. Dash dotted lines denote the upper and lower limit of coexistence regions around first order transitions of the adjacent magnetic and/or crystal structures.

All transitions are accompanied by strong micro-strain effects leading to a noticeable (*hkl*) dependence of the line broadening. The anisotropic peak broadening was refined using the instrumental resolution and modeling the anisotropic strain at each given temperature. The strain anisotropy of the tetragonal LT phase at 4.2 K was found to be much smaller, Figure 43. Apparently the lock-in magnetic transition at 15 K is related with an area dilatation and a contraction of the *c*-axis that restores the tetragonal symmetry and a volume increase. Most likely this sequence of transitions is related to competing magneto-elastic mechanisms involving the Ho crystal field anisotropy, the Ho–Ho, Ho–Fe and the Fe–Fe exchange interactions and their coupling with the lattice strains. The shear strain accompanying the $P4_2/mnm \rightarrow Cmmm$ transition was attributed to the magneto-elastic coupling between the Ho–Ho dominant interaction and the lattice strains [1]. The observed $a_o / b_o \neq 1$ deformation (referring to the $\sqrt{2}a_t$, $\sqrt{2}a_t$, c_t C-cell) is due to the fact that the Ho–Ho exchange interaction is negative along b_o and positive along a_o. Furthermore our system comprises two competing mechanisms of geometrical frustration, one arising from the Fe compact tetrahedral arrangement with antiferromagnetic interactions, and the second from the zero molecular field created at the Ho sites by the four surrounding Fe atoms located at the corners of an oblong square and the Ho at the center with antiferromagnetic Fe–Ho interactions.

Reference

[1] P. Schobinger-Papamantellos, J. Rodríguez-Carvajal, G. Andre, C. Ritter and K.H.J. Buschow. *Submitted to J. Magn. Magn. Mat.*

Principal Publications and Authors

P. Schobinger-Papamantellos (a), J. Rodríguez-Carvajal (b), K.H.J. Buschow (c), E. Dooryhee (d), A.N. Fitch (d). *J. Magn. Magn.* **250,** 225 (2002).
(a) ETHZ Zürich (Switzerland)
(b) Lab.Leon Brillouin, (CEA - CNRS) Saclay (France)
(c) University of Amsterdam (The Netherlands)
(d) ESRF

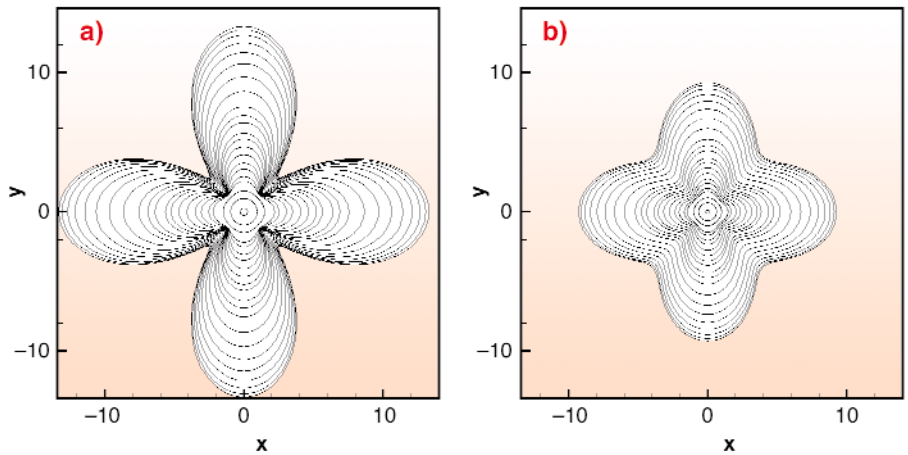

Fig. 43: Refined anisotropic strain distribution (a) in the HT tetragonal phase at 52 K (paramagnetic state) and (b) in the LT tetragonal phase at 4.2 K.

The Nanostructure Evolution During and After Magnetron Deposition of Au Films

Nanocrystalline materials have unique properties and a great potential for industrial applications [1]. As the nanostructure strongly influences the physical and chemical properties, tailoring for specific applications requires an understanding of the mechanisms that control its formation and evolution. This is especially important as grain growth in nanocrystalline materials takes place at significantly lower temperatures than in coarser-grained materials, deteriorating the nanomaterial.

We chose magnetron sputtering as a versatile technique for deposition of thin-film nanocrystalline materials and gold as a model material (no oxidation) to study the formation and evolution of the nanostructure during growth and the evolution during thermal annealing after growth. The measurements were carried out in a deposition chamber, which was mounted on a six-circle goniometer at the **ROBL** (**BM20**) beamline (**Figure 44**). By *in situ* off-plane X-ray diffraction and in-plane Grazing-incidence X-ray Scattering (GIXS), the development of the preferred orientation of the grains, the lattice constant (stress), the grain size, and the microstrain were studied (the latter two by deconvolution of the diffraction profiles into Lorentzians and Gaussians).

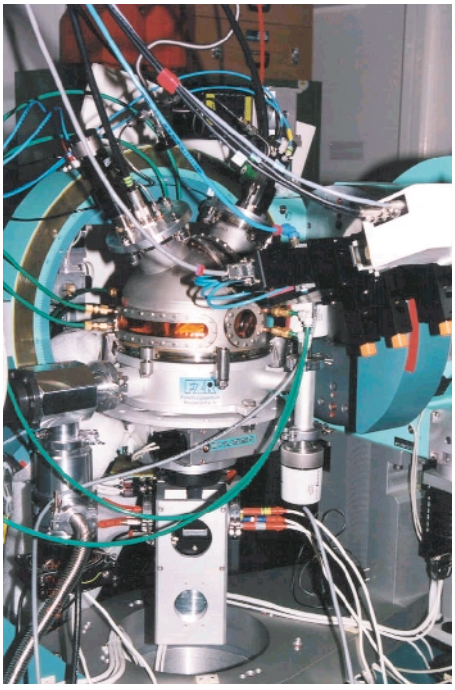

Fig. 44: Magnetron-sputter deposition chamber mounted on the six-circle diffractometer at ROBL. The vertical and horizontal X-ray windows allow a 3-dim. *In situ* characterisation of the structure and morphology of the growing film.

With the deposition parameters chosen (1 inch Au target, dc power 10 W, base pressure 5 x 10^{-4} Pa, Ar 0.6 Pa during deposition at RT, Si(100)/a-SiO_2 substrates mounted on a resistive heater, bias –30 V, growth rate 1.3 Å/s), Bragg-Brentano diffraction measurements revealed a dominating <111>-fibre texture, *i.e.* Au(111) lattice planes parallel to the film surface ((111) grains). Additionally, GIXS geometry identified (111)* grains (GIXS Au(111)) and (200)* grains (GIXS Au(200)), which were found to be more or less uniformly distributed throughout the film thickness. The (111) grains, on the contrary, were concentrated mainly in the upper part of the film.

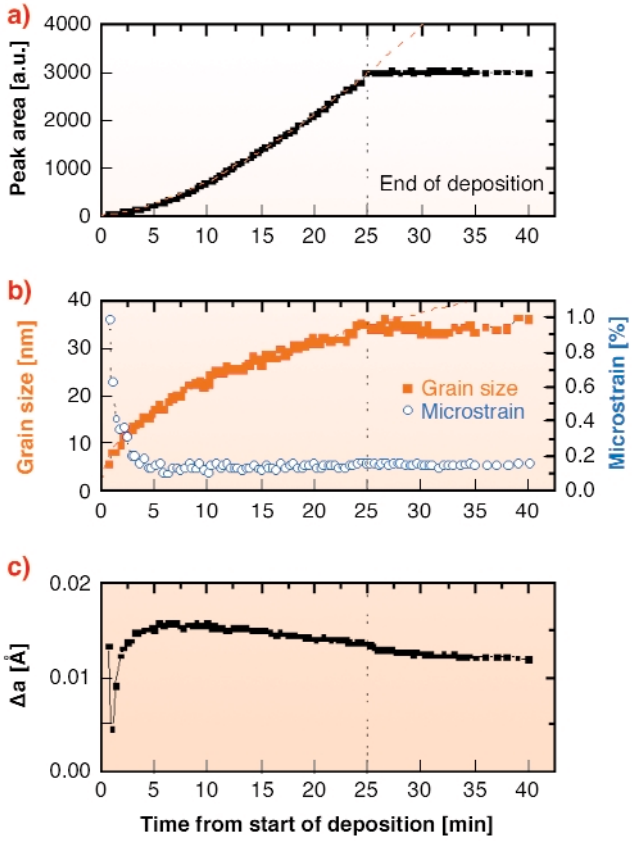

Fig. 45: The Bragg-Brentano Au(111) peak was measured as a function of deposition time during room temperature growth: (a) peak area (dashed line: power law fit); (b) microstrain and grain size (actually, the size of the coherently diffracting domains); (c) deviation of the lattice constant from the tabulated bulk value.

Figure 45 shows the typical growth behaviour. The initial, more-than-linear, increase in the Au(111) peak area with film thickness during deposition (**Figure 45a**) can be explained by a change of texture with time of growth and by an increase in (111) grains relative to (111)* grains during growth. Furthermore, during the initial growth, the microstrain dramatically decreased and the size of the coherently diffracting domains (equal to the grain size if the concentration of defects is sufficiently small) increased (**Figure 45b**). In the first minute of growth, the film stress decreased owing to a tensile contribution because of coalescence of initially-formed islands (**Figure 45c**).

During annealing at various temperatures, the Au(111) peak was similarly monitored. The microstrain rapidly

decreased during the initial annealing, indicating annihilation of defects. At the same time, the coherently diffracting domains increased (with the activation energy of 0.25 ± 0.03 eV). Subsequently, normal grain growth was observed (activation energy 0.99 ± 0.04 eV).

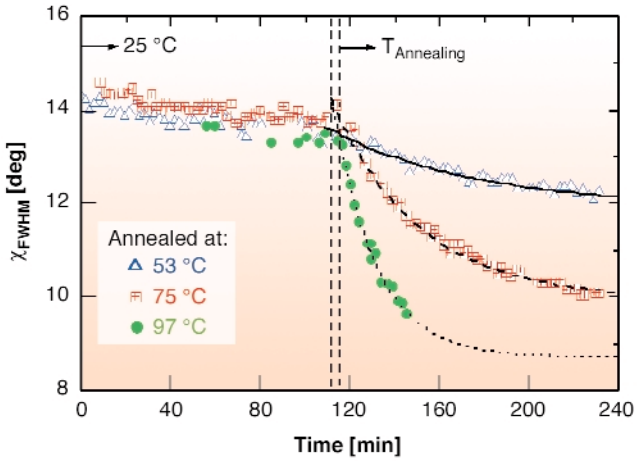

Fig. 46: FWHM of grain orientation distributions around the film-surface normal as a function of the time elapsed after the depositions stopped for various annealing temperatures.

Annealing revealed another interesting feature. Tilting the sample (with θ and 2θ kept fixed at angles corresponding to standard Bragg-Brentano diffraction from Au(111)) with the tilt axis lying at the intersection of the film surface and the scattering plane, χ-scans were made that yielded grain orientation distributions. The angular widths (FWHM) of these distributions were used as a measure of the texture. **Figure 46** shows the typical behaviour of the measured widths. Such data together with the observation of the corresponding lack of grain growth lead to the interpretation that small rotations of individual grains with an activation energy of 0.64 ± 0.05 eV were responsible for the decrease in widths.

In conclusion, we could characterise the 3-dimensional evolution of the nanostructure of magnetron-sputtered nanocrystalline Au films during growth and subsequent annealing, and determine the mechanisms responsible with their corresponding activation energies, (defect annealing, grain rotations, normal grain growth and recrystallisation).

References:

[1] A.S. Edelstein, R.C. Cammarata (Eds.), *Nanomaterials: Synthesis, Properties and Applications*, Institute of Physics Publishing, Bristol (1998).

Principle Publication and Authors:

N. Schell (a, b), T. Jensen (c), J.H. Petersen (c), K.P. Andreasen (c), J. Bøttiger (c), J. Chevallier (c), *Thin Solid Films* **441**, 96 (2003).
(a) Forschungszentrum Rossendorf, Dresden (Germany)
(b) ROBL-CRG, ESRF
(c) University of Aarhus (Denmark)

Anomalous X-ray Scattering on Molten Levitated Y_2O_3

Since most of the physical properties of a high-temperature liquid material are related to its atomic arrangement, it is important to develop methods to probe the local environment of the atoms in the sample. At very high temperature, the use of conventional furnaces presents major problems. In particular, the sample can be contaminated by the container and its structure thereby corrupted. One solution is to perform experiments under contactless conditions [1].

As opposed to crystals, liquids are disordered systems for which the structure is generally described in terms of distribution functions for interatomic distances and bond angles. In particular, the pair correlation function *G(r)* is proportional to the probability of finding an atom at a distance *r* from another taken at the origin. Such pair-distribution functions are directly accessible from the structure factor *S(Q)* obtained with classical X-ray diffraction measurements. However, the information obtained on a multi-component liquid with such diffraction experiments is limited because the measured average structure factor *S(Q)* and the corresponding pair correlation function *G(r)* are weighted sums of the partial functions for the different atom pairs, so that various structural models can be consistent with the experimental results. One solution is to use anomalous X-ray scattering (AXS) which is a more selective technique.

We have performed AXS experiments on levitated liquid yttrium oxide (Y_2O_3) at 2770 K. The measurements were carried out at two energies below and above the yttrium K absorption edge at the **BM02** beamline. The principle of the method [1,2] is to subtract the two measured intensities to extract the yttrium structure factor $S_Y(Q)$, containing information on the local environment of yttrium atoms.

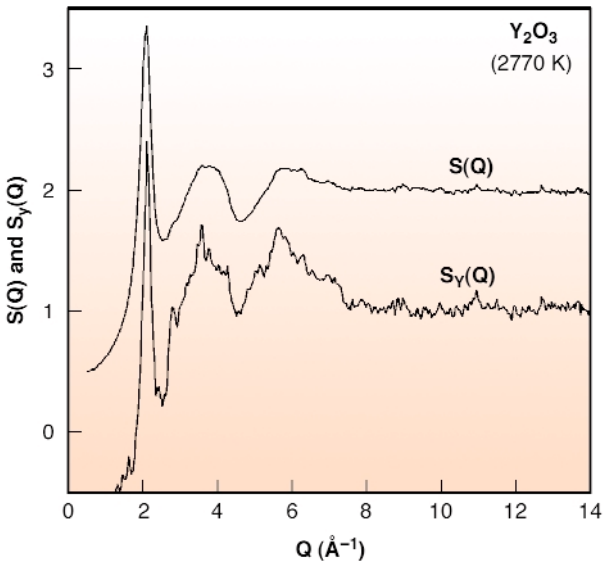

Fig. 47: Average structure factor *S(Q)* measured at 16.75 keV and yttrium structure factor $S_Y(Q)$ for liquid Y_2O_3 at 2770 K.

Figure 47 shows the X-ray-weighted average structure factor *S(Q)* and the yttrium structure factor $S_Y(Q)$ obtained on the high-temperature liquid. The sharpness of the first peak at Q = 2.07 Å^{-1} in both *S(Q)* and $S_Y(Q)$ is remarkable and implies a relatively long-range of chemical ordering in the liquid.

The corresponding average and yttrium pair correlation functions *G(r)* and $G_Y(r)$ obtained using a classical Fourier transform of *S(Q)* and $S_Y(Q)$ are shown in **Figure 48**. *G(r)* is the weighted average of the partial functions for the three atomic pairs: Y–O, Y–Y and O–O whereas $G_Y(r)$ involves only Y–O and Y–Y. By combining the two results we have derived bond distances and coordination numbers for all three pairs. The two first peaks in $G_Y(r)$ corresponds to Y–O and Y–Y nearest-neighbour pairs giving distances of about 2.26 Å and 3.74 Å respectively. We estimated the O–O distance to about 3.06 Å. The values obtained for the Y–O and Y–Y coordination numbers, slightly below 7 and 12, respectively, together with the position of the sharp main peak in S(Q), which coincides with the strongest Bragg peaks of the high-temperature H-type solid phase, imply that the close packing of this phase is preserved on melting.

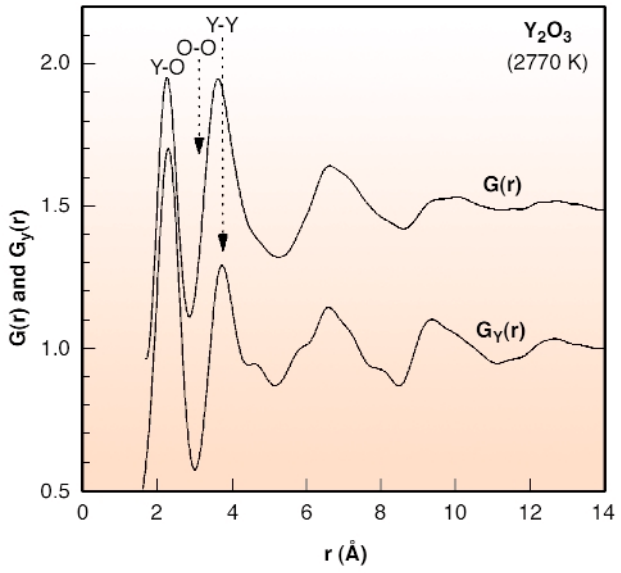

Fig. 48: Average pair correlation function *G(r)* obtained at 16.75 keV and yttrium pair correlation function $G_Y(r)$ for liquid Y_2O_3 at 2770 K.

This work shows that the combination of aerodynamic levitation, laser heating and AXS is a powerful technique for obtaining reliable partial structure information in complex high-temperature liquid materials.

Reference

[1] L. Hennet, D. Thiaudière, C Landron, J.-F. Bérar, M.-L. Saboungi, G. Matzen, D.L. Price, *Nucl. Instrum. Meth. B*, **207**, 447-452 (2003).

[2] D.L. Price and M.L. Saboungi, in *Local Structure from Diffraction*, S.J.L. Billinge, M.F. Thorpe (Eds), Plenum Press, New York, 23-33 (1998).

Principal publication and Authors

L. Hennet (a), D. Thiaudière (a), C. Landron (a), P. Melin (a), D.L. Price (a), J.P. Coutures (b), J.-F. Bérar (c) and M.-L. Saboungi (d), *Appl. Phys. Lett.*, **83**, 3305-3307 (2003).

(a) CRMHT, CNRS, Orléans (France)

(b) IMP, CNRS, Perpignan (France)

(c) ESRF

(d) CRMD, CNRS, Orléans (France)

Insights into a Spin Transition: Three Stable States of a Spin-crossover Crystal Built from Bi-stable Molecules

The spin state of certain octahedral d^6 iron(II) complexes may be switched between a low spin (LS) and a high spin (HS) state of nearly equal energies (LS, S = 0, $t_{2g}^6e_g^0$; HS, S = 2, $t_{2g}^4e_g^2$). The collective behaviour of such bi-stable molecules packed into a crystal lattice may lead to multi-stability in the solid state with a complex temperature and pressure dependence. Such phenomena are not only of basic scientific interest, they also hold the potential for technological applications [1, 2].

The compound $[Fe^{II}(2\text{-pic})_3]Cl_2\cdot EtOH$ (pic = picolylamine), **1**, studied extensively for more than 20 years, shows stable HS and LS phases bracketing an intermediate phase (IP) with approximately equal concentrations of HS and LS molecules. (**Figure 49**) Inconclusive and contradictory characterisations of the nature of the IP have been given: a superstructure built from LS and HS molecules [3] as well as a glass-like state with short-range correlations between molecules in different spin states [1], both based on theoretical deliberations. Most interpretations of the experimental information favour a glass-like state with short-range correlations between HS and LS molecules [1].

We have investigated small crystals of **1** by X-ray diffraction at 16 temperatures between 12 and 298 K making use of the intense monochromatic X-ray flux and large-area image-plate detector at SNBL, beamline **BM01A**. The diffuse scattering expected from a glass-like state was not seen. Instead additional Bragg reflections, observed between T_1 ~124(1) K and T_2 ~114(1) K, revealed two successive phase transitions of the order-disorder type, thus indicating long-range correlations between LS and HS molecules and corroborating a superstructure in the IP. At temperatures above T_1 a single iron site is occupied predominantly but not entirely with HS iron. Below T_2 the single site is occupied predominantly with LS iron. The superstructure between T_1 and T_2 shows a doubling of the unit cell volume and two coexisting, but different, iron sites, one predominantly HS, the other predominantly LS.

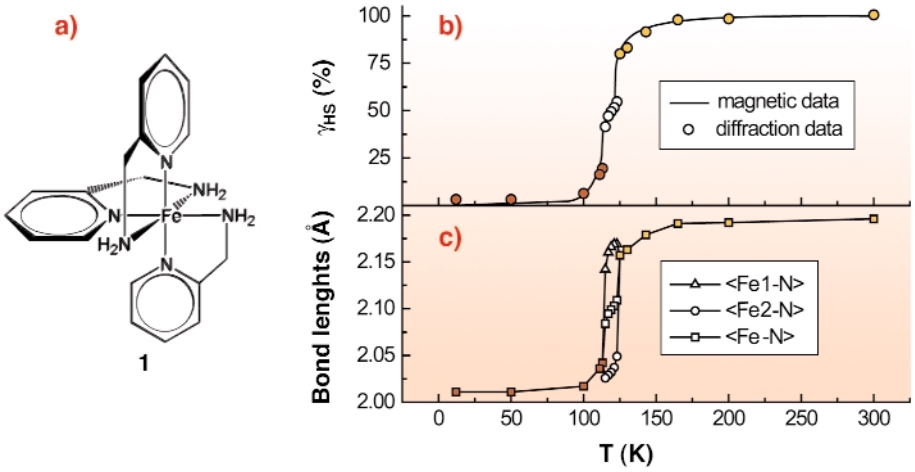

Fig. 49: (a) Iron(II) *tris*-2-picolylamine complex $[Fe^{II}(2\text{-pic})_3]^{2+}$. (b) Comparison of spin transition behaviour from diffraction and magnetisation experiments. The HS fraction $\gamma_{HS}(T)$ was estimated from the temperature dependence of the average <Fe–N> bond length. Standard uncertainties are approximately equal to symbol sizes. (c) Temperature dependence of the average <Fe–N> bond lengths. In the intermediate phase the bond lengths at the two iron sites differ (the lines are guides to the eye).

At first glance the structure of the yellow HS phase and that of the red LS phase appear to be the same. On closer inspection it becomes evident that the unit-cell parameters and the atomic coordinates change discontinuously between the two phases (**Figure 50**). In the absence of an intermediate phase, the discontinuous changes in structural parameters would indicate a so-called isostructural phase transition, which is always of first order, analogous to a liquid-vapour transition. The actual sequence of the three phases is 're-entrant' in the sense that the symmetry of the HS structure reappears in the LS structure and vice versa. Such an isostructural/re-entrant sequence is relatively rare, and its detailed characterisation was only possible with an experimental protocol allowing for many crystal structures to be measured over as large a range of temperatures as possible. We are currently investigating relatives of **1**, in which the ethanol molecule is replaced by methanol, 1-propanol, 2-propanol, allyl alcohol or t-butanol. Although these compounds have structures similar to that of **1**, at least at 200 K, their spin-crossover behaviour is quite different, thus again calling for individually designed temperature dependent diffraction experiments.

The results presented here, probably the most detailed and accurate structural description of a spin crossover coupled to an order-disorder phase transitions hitherto published, serve as a basis for developing and testing new models of these processes and their couplings. A Landau-type analysis of the diffraction data based on the symmetry changes observed in **1** leads to a generic phase diagram - to be given elsewhere - which appears to apply to related spin-crossover compounds as well. The combination of multiple-temperature diffraction data with a phenomenological theoretical analysis thus provides a unified description of different spin crossover scenarios occurring in chemically different compounds.

References

[1] P. Gütlich, Y. Garcia, H. Spiering, in *Magnetism: Molecules to Materials IV*, J.S. Miller, M. Drillon, eds, Wiley-VCH, 271-344 (2002).

[2] O. Kahn, C. Jay-Martinez, *Science*, **279**, 44-48 (1998).

[3] A. Bousseksou, J. Nasser, J. Linares, K. Boukheddaden, F. Varret, *J. Phys. I*, **2**, 1381-1403 (1992).

Principal Publication and Authors

D. Chernyshov (a, c), M. Hostettler (a), K.W. Törnroos (b), and H.-B. Bürgi (a), *Angew. Chem. Int. Ed.* **42**, 3825-3830 (2003).

(a) Universität Bern (Switzerland)

(b) University of Bergen (Norway)

(c) Petersburg Nuclear Physics Institute, Gatchina (Russia)

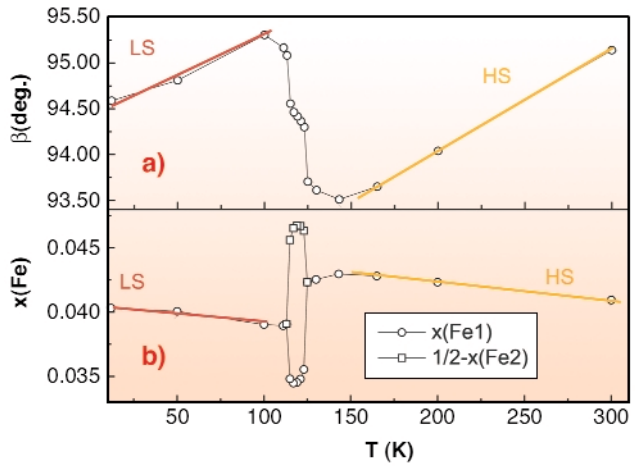

Fig. 50: Temperature dependence (a) of the monoclinic angle β and (b) of the x-coordinates of the Fe-atoms. The coordinate of the second Fe atom in the intermediate phase is given as $^1/_2$ - x(Fe2) for easier comparison with the first Fe atom. The yellow and red lines highlight the temperature dependence of β and x(Fe) in the HS and LS structures. Standard uncertainties are approximately equal to symbol sizes.

High-pressure Diffraction

Introduction by M. Hanfland, ESRF

Diffraction experiments have become a powerful tool to study the behaviour of matter at high pressures. They permit the investigation of diverse fields, the examples presented here range from the fundamental properties of solids to the chemistry in the interior of the Earth.

The volume of cubic diamond together with the optical phonon frequency has been measured to 140 GPa [1]. Comparisons with theoretical calculations will considerably improve our understanding of the fundamental behaviour of solids. A more practical aspect of the data is a possible revision of the pressure scale used at very high pressures.

The structure of a modulated guest host phase (Sb-II) has been described using a four-dimensional superspacegroup for the first time [2]. The structural investigation is accompanied by an *ab initio* band structure calculation, which confirms the energetic stability of the modulated phase in the observed pressure range. Modulated phases at high pressure are becoming quite common. Recently new types of modulated structures were discovered for I, and for Te and Se [3].

The equation of state and structural behaviour of synthetic spinel, a model for phases that are stable under Earth mantle conditions, have been studied to 30 GPa [4]. Structural investigations of the iron-silica interaction at extreme pressures and temperatures [5] probe chemical reactions at the core mantle boundary and provide a possible explanation for the anomalously high electrical conductivity of this region.

A major improvement to the ESRF's high-pressure facilities will be the move of the High-pressure Beamline from ID30 to ID27, planned to start in autumn 2004. The move from a high beta section (ID30, large source size, small divergence) to a low beta section (ID27, small source size, large divergence) will allow greater precision because of a significant decrease in the horizontal beam size. Two experimental hutches will provide separate setups for large-volume cell, diamond-anvil cell and laser heating. Two in-vacuum undulators in series will augment the flux by at least one order of magnitude.

References

[1] F. Occelli *et al.*, *Nature Materials* **2**, 151 (2003).
[2] U. Schwarz *et al.*, *Phys. Rev. B* **67**, 214101 (2003).
[3] K. Takemura *et al.*, *Nature* **423**, 971 (2003); C. Hejny and M.I. McMahon, *Phys. Rev. Lett.* **91**, 215502 (2003).
[4] D. Levy *et al.*, *Am. Mineral.* **88**, 93 (2003).
[5] L. Dubrovinsky *et al.*, *Nature* **422**, 58 (2003).

Structural Properties of Diamond under Hydrostatic Pressures up to 140 GPa

Diamond is the archetypical covalent material. Each atom in a sp^3 configuration is bonded to four nearest neighbours. Although diamond is known as the thermodynamically-preferred allotrope of carbon at high-pressure, sufficient pressure should favour a more uniform electronic distribution and a more compact structure. The stability of diamond under pressure and the possibility of producing high-density polymorphs of diamond, including metallic forms, is still a matter of discussion but lacking reliable experimental data. Structural changes have been reported in diamond under non-hydrostatic pressures around 150 GPa and large deformation [1]. However, the measurements of the properties of diamond under hydrostatic pressure have been limited to below 40 GPa [2]. Here, we report the determination of the equation of state of diamond under hydrostatic pressure to 140 GPa. Diamond is observed to be more compressible than expected. It is also deduced that diamond remains very stable under pressure.

Because diamond is a very incompressible material, significant changes in the properties of diamond and detection of non-linear pressure effects require pressures in excess of 100 GPa. Such pressures are now within the capabilities of the diamond-anvil cell (DAC). The experimental difficulty in making accurate quasi-hydrostatic measurements on diamond in the 100 GPa range essentially arises because the sample chamber becomes very thin, less than 10 μm, and thus a very small diamond crystal has to be loaded, embedded in a helium-transmitting medium. Additionally, the signal of the diamond sample needs to be separated from the much larger signal of the diamond anvils. Using the ESRF synchrotron source and the energy-dispersive single-crystal X-ray diffraction technique, investigation of the structural properties of most low-Z systems have been

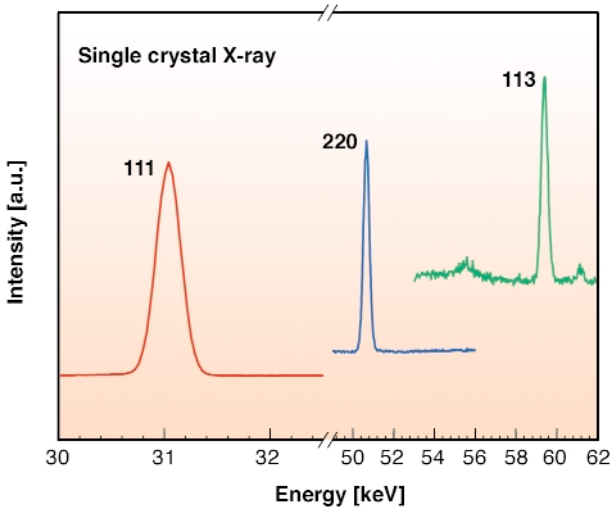

Fig. 51: Reflections of a diamond single-crystal at 140 GPa.

extended into the 100 GPa range. We have used the same technique, at the **ID30** beamline, to overcome the very small X-ray scattering power of a 4 µm diamond crystal [3]. Furthermore, this technique allows an easy separation of the signal of the diamond crystal and the one of the diamond anvils because of their different orientations. Three different runs were dedicated to these measurements. As shown in **Figure 51**, the first three classes of the diamond reflections (111), (220) and (113) were measured, and six reflections could be followed that remained perfectly correlated by the orientation matrix of the structure of diamond up to the maximum pressure. The pressure was measured by the ruby luminescence gauge (a ruby ball of 3 µm diameter was placed near the diamond crystal).

The V(P) data are presented in **Figure 52**. These data have been fitted by the Vinet formulation of the equation of state (EOS). It is considered to be a good formulation of the EOS and it depends on three parameters: the volume, V_0, the isothermal bulk modulus, K_0, and the pressure derivative of bulk modulus, K'_0, at ambient pressure. In the case of diamond, it was seen that the V(P) data above 40 GPa are essential to correctly constrained K'_0. Our determination of the EOS is seen to be more compressible than the one more commonly obtained by extrapolation. This is essentially due to a value of K'_0 equal to 3, whereas a value of 4 is currently assumed for diamond. Complementary information was obtained with the measurement of the optical phonon of diamond at the centre of the Brillouin zone. No sign of a weakening, not even a slight increase in the covalent character, could be qualitatively deduced from the combination of the elastic data and the Raman measurements of the optical phonon frequency.

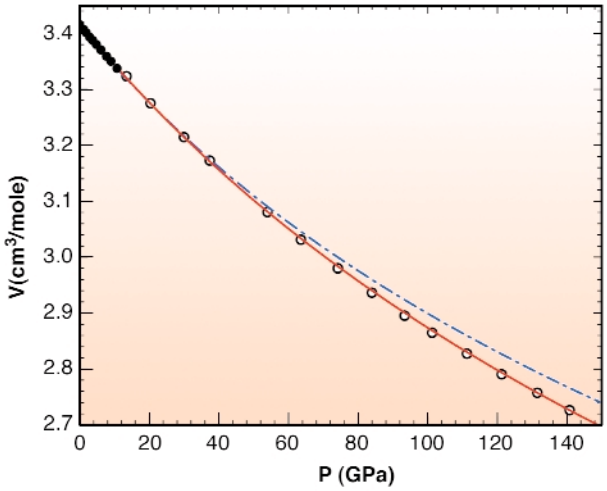

Fig. 52: Pressure dependence of the volume of natural diamond. The dots and circles indicate respectively different runs. The error bars are smaller than the size of the symbols. The red line is the fitted Vinet equation $P = 3K_0(1-X)X^{-2}\exp(3(K_0'-1)(1-X)/2)$, with $X = (V/V_0)^{1/3}$, $V_0 = 3.4170(8)\text{cm}^3/\text{mole}$, $K_0 = 446(1)$GPa and $K_0' = 3.0(1)$. The blue line represents the EOS of diamond assumed before this study.

In conclusion, we have observed that diamond under hydrostatic pressure is very stable. This is in contrast to its behaviour under non-hydrostatic or uniaxial compression.

References

[1] H.K. Mao, and R.J. Hemley, *Nature* **351**, 721 (1991).
[2] Ph. Gillet *et al., Phys. Rev. B* **60**, 14660 (1999).
[3] P. Loubeyre *et al., Nature* **383**, 702 (1996).

Principal Publication and Authors

F. Occelli, P. Loubeyre and R. LeToullec, *Nature Materials* **2,** 151 (2003).
CEA (France)

Iron-silicon Alloy at Extreme Conditions

The boundary between the Earth's metallic core and its silicate mantle is characterised by sharp changes of density, seismic wave velocities, electrical conductivity, chemical composition, and lateral heterogeneity. Although iron (with ~ 5 wt% Ni) is a dominant component of the Earth's core, Fe-Ni alloy is too dense by ~ 10% for the outer liquid core and by 2-5% for the solid inner core to satisfy the observed density along any reasonable geotherm. On the basis of cosmochemistry, it has been proposed that the core also contains one or more light elements, such as H, C, O, S, and/or Si. It is likely that 2-6 wt% Si was dissolved into the liquid metal during core formation in a magma ocean (pressure around 25 GPa and temperature ~2800 K) during the early history of the Earth. On the basis of a simple thermodynamic model, Gessmann *et al.* proposed that the solubility of Si at core conditions is close to zero [1]. Thus, following core formation, Si should be expelled from liquid Fe as the metallic core evolves toward chemical equilibrium. Theory predicts that, as pressure increases, the alloy should dissociate to a mixture of silicon-poor *hcp* Fe and the Si-rich *B2* structured phase.

Note that the theoretical calculations were done at T = 0 K, while at high temperature, entropic contribution may be important. Therefore, theoretical predictions were tested through a series of high-P,T DAC experiments on Fe-Si alloys containing 9.6(1), 5.1(1), and 4.3(4) wt% Si. We found that all alloys behave similarly and **Figure 53** shows representative X-ray patterns obtained *in situ* at high-P,T using the 5.1 wt% Si alloy as the starting material. **Figure 53d** (see also left inset in **Figure 53**) shows an example of a diffraction pattern collected after 5 hours of external electrical heating of the Fe-5.1 wt% Si alloy at 140(10) GPa and 1380(25) K. Two new lines at 2.494 Å and 1.762 Å belong to the *B2* structured alloy (a = 2.493(1) Å) as predicted by *ab initio* calculations. When the same sample was heated for 8

hours at 30(2) GPa and 1100(10) K, the extra lines disappeared indicating that the reaction was reversed and only the *hcp* phase remained (**Figure 53e**).

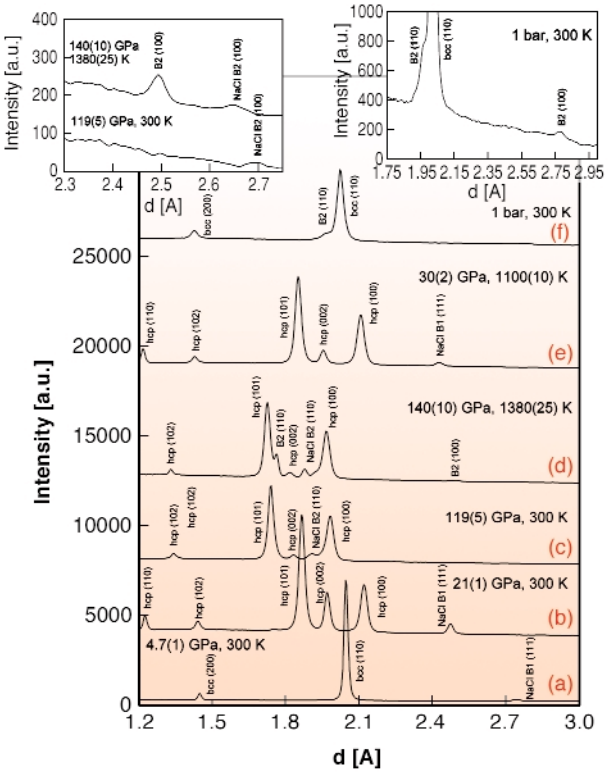

Fig. 53: Examples of X-ray diffraction patterns collected in experiments with Fe – 5.1 Si wt%. (a) At 4.7(1) GPa the alloy has *bcc* structure. Transformation to a *hcp* phase occurs between 14 GPa and 21(1) GPa (b). No phase transformations were observed on compression to over 119(5) GPa at room temperature (c). However, after five hours of external electrical heating at 140(10) GPa and 1380(25) K (d and left inset), two new lines appeared at 2.494 Å and 1.762 Å belonging to the *B2* structured alloy (a = 2.493(1) Å). The same sample was then heated for 8 hours at 30(2) GPa and 1100(10) K (e). The extra lines have disappeared due to back reaction of iron alloys with different concentration and only *hcp* phase remained. NaCl was used as the pressure medium (reflections marked as *NaCl B1* below 30 GPa and *NaCl B2* at higher pressures). Spectrum (f) and right inset show an X-ray diffraction patterns of the sample recovered after laser-heating of Fe-10 wt% Si alloy at 105(5) GPa and 2500(100) K. The reflections at 1.969 Å and 2.781 Å correspond to the (110) and (100) peaks of quenched *B2* FeSi phase.

Our results on the behaviour of the Fe-Si alloys in solid and liquid states with different Si concentrations are summarised in **Figure 54**. We found that at pressures above 60 GPa and high temperatures the alloys dissociate into a mixture of *hcp*-structured Si-poor and *B2*-structured Si-rich phases.

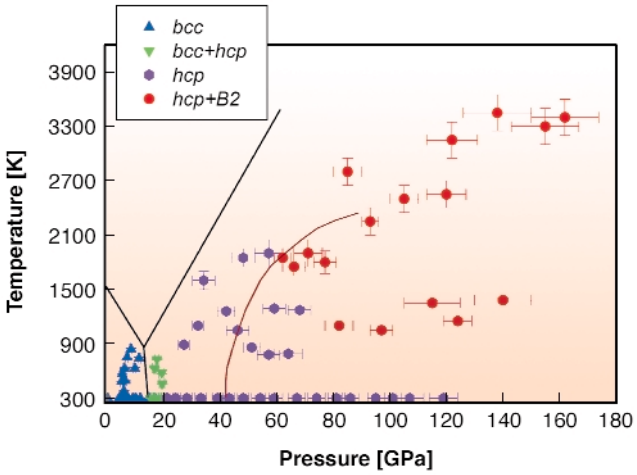

Fig. 54: Phases observed in electrically- (below 1500 K) and laser- (above 1500 K) heated DAC experiments with iron-silicon alloys (9.6(1), 5.1(1), 4.3(4) wt% Si). We found that all alloys behave similarly and symbols show only phase relations. Continuous black lines show phase relations in pure iron, and a red curve – a phase boundary between *hcp* and *hcp+bcc* regions in Fe – 7.9 Si wt% alloy according to Lin *et al.* (2002) [2].

At the core–mantle boundary (CMB) pressure (140 GPa), the density of *B2* FeSi (~ 9.0 g/cm^3) is significantly lower than the density of the core (~ 10.0 g/cm^3) immediately below the CMB and significantly higher than the density of the overlying mantle (~ 5.6 g/cm^3). Iron silicide *B2* FiSi does not react with silicate perovskite and periclase (or ferripericlase at conditions of Earth's lower mantle. This means that the silicon-rich alloy produced by re-equilibration of proto-core metal that equilibrated with silicates in a magma ocean, or produced at the CMB by reaction between iron and silicate will accumulate at the boundary between the lower mantle and core. *Ab initio* simulations and measurements on *B2* FeSi recovered from multianvil experiments show that this compound is an electric conductor (with measured at ambient conditions conductivity of 6(1) 10^5 S/m). The presence of *B2* FeSi at the base of Earth's mantle could thus explain its anomalously high electrical conductivity and provide a key for understanding why the amplitude of the Earth's nutation is out-of-phase with tidal forcing.

References

[1] C. K. Gessmann, B. J. Wood, D. C. Rubie, M. R. Kilburn, *Earth Planet. Science Let*. 184, 367-376 (2001).
[2] J.-F. Lin, D. L. Heinz, A. J. Campbell, J. M. Devine, G. Shen, *Science* 295, 313-315 (2002).

Principal Publication and Authors

L. Dubrovinsky (a), N. Dubrovinskaia (a), F. Langenhorst (a), D. Dobson (a), D. Rubie (a), C. Geßmann (a), I. Abrikosov (b), B. Johansson (b), *Nature*, **422**, 58-61 (2003).
(a) BayerRisches Geoinstitut, Universität Bayreuth (Germany)
(b) Uppsal University (Sweden)

Crystal Structure of the Modulated Composite Arrangement of Elemental Antimony

The crystal structure of the high-pressure modification Sb-II has been a long-standing matter of controversy. A conventional tetragonal solution has been suggested and refined using powder-diffraction data [1]. The resulting model comprises one type of Sb-atoms building up a three-dimensional framework and a second kind occupying every second tetragonal antiprismatic void in the resulting channels. Our investigations revealed that at pressures above 13(1) GPa pure patterns of this phase are observed. However, the correct indexing of the peak positions requires the application of the four-index method for composite structures and shows that the crystal structure comprises two tetragonal lattices with a_c = 805.53(4) pm and two *c*-axes c_h = 389.91(2) pm and c_g = 297.33(4) pm. The common lattice parameter of both sub-structures is labelled a_c, the *c*-axis of the 'host' sub-lattice is termed c_h, and c_g corresponds to the *c*-axis of the 'guest' lattice.

Beside the main reflections (*hkl*0) and (*hk*0*m*), the diffraction pattern contains weak first-order satellite reflections (*hklm*) revealing modulations of the crystal structure. The sub-structures of host atoms Sb_h and guest atoms Sb_g were determined and the resulting atomic positions are compatible with three different superspace groups. In two of these groups, first-order modulation waves of the Sb_g positions are not symmetry-allowed. Thus, a complete refinement using full profiles including main reflections plus positions of the satellite reflections is performed in the superspace group L^{I422}_{-111}:L^{I422}_{-111}. The modulation functions for the Sb_h and Sb_g positions were created using a generator of the symmetry-allowed Fourier series. The refined coordinate *x* = 0.15776(3) of the Sb_h atoms corresponds well to the value of 0.1536(3) obtained for the structurally-related modification Bi-III at 6.8 GPa [2].

The structural pattern of host and guest atoms is commensurate along the *a*-axes while the arrangement of atoms within the channels and the resulting misfit causes incommensuration along the *c*-axes. The modulation of the Sb_h atoms facilitates a continuous adjustment of interatomic distances. For the interactions among host and guest atoms, *d*4 and *d*5, the modulated displacement of antimony atoms induces an additional reduction in the regime of short interatomic contacts and an elongation at long distances (**Figure 55**). Within the stability region of the modification Sb-II, the axial ratio c_h/c_g of 1.311 (12 GPa) does not achieve the next higher rational value 4/3 which would result in a commensurate structure with the smallest possible common lattice parameter *c* of guest and host lattice. However, we used this commensurate model of the composite, which

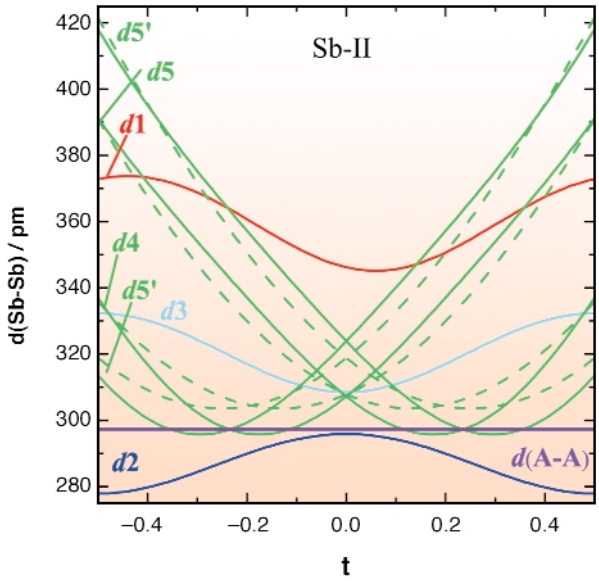

Fig. 55: Interatomic distances of Sb-II at *P* = 12 GPa as a function of the fourth coordinate x4. Dashed lines represent distances calculated for a non-modulated structure, full lines correspond to those of the modulated atomic arrangement, and the dotted line reproduces the distance between channel atoms.

reproduces the basic features of the atomic organisation adequately as a model structure for the total energy calculations. The crystal structures being considered as models for the total-energy calculations were restricted to the experimentally evidenced modifications of antimony or varieties thereof. The sequence of phase transitions predicted by the calculations is in perfect agreement with the experimental findings. In order to provide a quantitative measure between experimental and theoretical results, we show a comparison between experimental and theoretical pressure-volume curves (**Figure 56**). Since measured and calculated volumes match almost perfectly (ambient pressure: 30.1×10^6 pm^3 versus 29.7×10^6 pm^3, respectively), both data sets are plotted by using absolute volumes rather than scaled values. The agreement between theory and experiment is excellent for the Sb-I phase and the Sb-III modification. Note that for Sb-II, a commensurate model is used instead of the actual incommensurately-modulated composite. Nevertheless, the transition pressure of 8.7 GPa, and the volume decrease of 5.9% (with respect to theoretical volume) are in reasonable accord with the experimental data. Only the transition pressure for the Sb-II to bcc transition is predicted to be smaller: 17.7 GPa calculated versus 28 GPa measured [3].

References

[1] H. Iwasaki and T. Kikegawa, *High Pressure Res.* **6**, 121 (1990).
[2] M.I. McMahon, O. Degtyareva, and R.J. Nelmes, *Phys. Rev. Lett.* **85**, 4896 (2000).
[3] K. Aoki, S. Fujiwara, and M. Kusabe, *Solid State Commun.* **45**, 161 (1983).

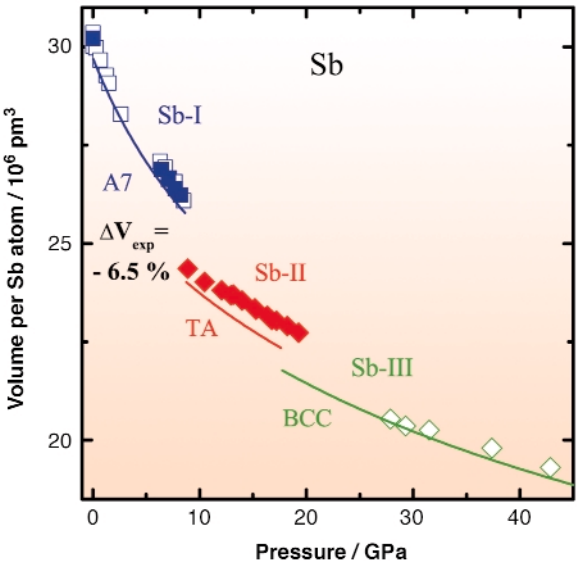

Fig. 56: Volume per antimony atom at pressures up to 42 GPa. Solid symbols represent data from the present investigation; open icons indicate values taken from literature. Curved lines represent Birch-Murnaghan-type equations fitted to the results of the quantum mechanical calculations.

Principal Publication and Authors

U. Schwarz (a), L. Akselrud (a), H. Rosner (a), A. Ormeci (a), Yu. Grin (a) and M. Hanfland (b), *Phys. Rev. B* **67**, 214101 (2003).

(a) MPI CPfS, Dresden (Germany)

(b) ESRF

Synthetic $MgAl_2O_4$ (spinel) at High Pressure Conditions up to 30 GPa

The study of spinels at high pressure (*P*) provides information relevant to geophysics, as their structure is a model for phases stable at conditions occurring in the mantle of the Earth. In particular, $MgAl_2O_4$ is a constituent of the upper mantle in the spinel-type structure ("spinel in *sensu strictu*"), and it is supposed to stabilize in the $CaFe_2O_4$-type structure in subducted oceanic crust.

Notwithstanding the importance of MgAl-spinel, little was known about its behaviour in the high pressure regime (> 10 GPa). Therefore, this studies aim was to investigate the equation of state (EoS) and the structural behaviour of MgAl-spinel from ambient conditions to 30 GPa, at room temperature, by *in situ* high-pressure powder diffraction using X-rays from a synchrotron source.

The $MgAl_2O_4$ sample used in the present investigation was synthesised by a high-temperature solid state reaction of MgO and Al_2O_3. The high-pressure powder diffraction experiments were carried out on the **ID09A** beamline using a diamond-anvil cell, with N_2 as a pressure-transmitting medium; pressure was estimated by the fluorescence line shift of ruby. The diffraction patterns were treated by the Rietveld method (GSAS-Expgui software), and provided the cell edge (*a*) (see **Figure 57**), the oxygen coordinate (*u*) and the atomic displacement parameters. The elastic parameters (bulk modulus, K_0, its first and second derivatives *vs* *P*, K'_0 and K''_0, respectively) were determined by fitting different EoS models to the observed pressures (Birch-Murneghan (BM), Vinet (V) and Poirier-Tarantola (PT)). An comparison between the issues of the different EoS's suggests one to choose the results from the 3rd order BM, yielding the following elastic parameters: K_0 = 191(1) GPa, K'_0 = 6.7(2) and K''_0 = -0.075 GPa^{-1} (implied value).

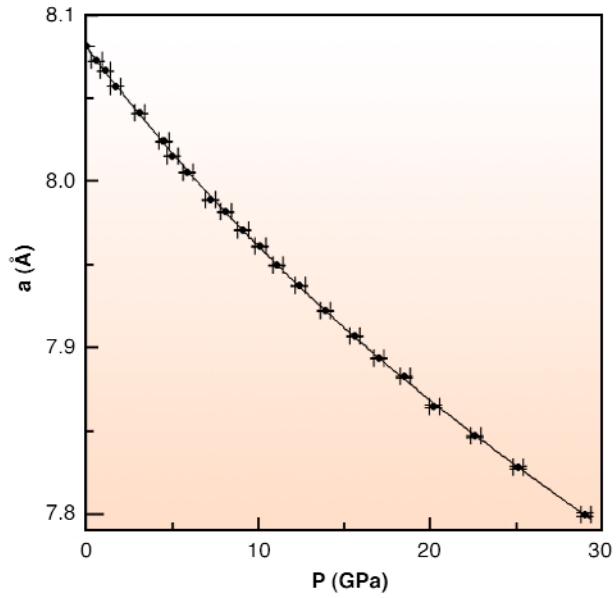

Fig. 57: Cell edge (Å) as a function of pressure (GPa). The solid line is the third order polynomial fit.

Bulk modulus values previously measured by diffraction are in good agreement with ours, whereas those obtained by spectroscopy are systematically higher. The cation replacement in spinels affects significantly the elastic properties; for instance, $ZnAl_2O_4$ [1] exhibits K_0 = 201.7(±0.9) GPa and K'_0 = 7.62(±0.09), hinting that the substitution of Zn with Mg yields a "softening", in keeping with the expectations relying on the cation size. The structure of spinels is fully described by the one independent coordinate of oxygen, *u*, displayed in **Figure 58** as a function of *P*. Save statistical oscillations, *u* exhibits a practically flat trend; if a linear function, u_0+u_1P, is fitted to the observed *u*'s one obtains u_0 = 0.2625(1) and u_1= 0.9(8.9) 10^{-6} GPa^{-1}. This indicates that the structural behaviour under compression of MgAl-spinel is mainly governed by the shrinking of the cell edge and *P* acts upon $MgAl_2O_4$ producing a scaling of the structure.

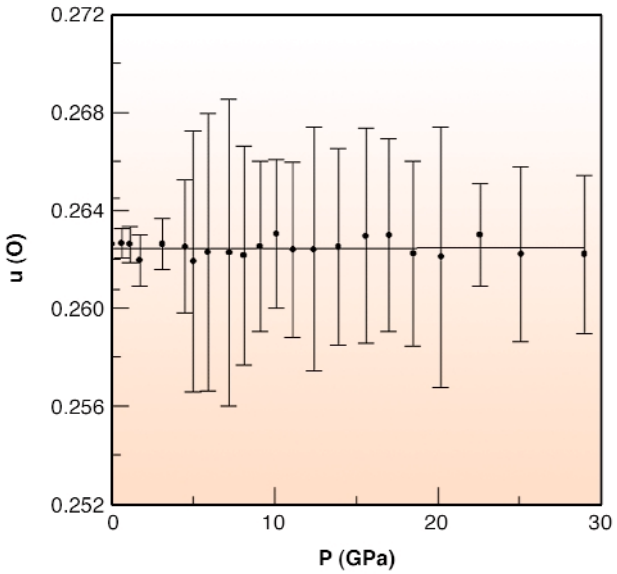

Fig. 58: *u* as a function of pressure (GPa). Error bars correspond to 3σ.

References

[1] D. Levy, A. Pavese, A. Sani and V. Pischedda, *Phys Chem Miner,* **28**, 612-618 (2001).

Principal Publication and Authors

D. Levy (a), A. Pavese (b,c), M. Hanfland (d), *American Mineralogist*, **88**, 93–98 (2003).
(a) Università degli Studi di Torino (Italy)
(b) Università degli Studi di Milano (Italy)
(c) CNR (Italy)
(d) ESRF

Subnanosecond-resolved Diffraction: A New Dimension for the Study of Atomic Positions in Moving Molecules

Introduction by M. Wulff, ESRF

It is now possible to use the pulsed X-ray beam to "film" the structure of a laser-excited molecules as they evolve though internal conversion or interaction with the environment. A specialised setup, sometimes called the molecular camera, has been built on ID09B for this purpose. The camera can record the transient structure of liquids, glasses and crystals by time-resolved diffraction to a time resolution of 100 picoseconds, a limit set by the X-ray pulse length. The main components in the camera are an X-ray chopper, a femtosecond laser and a CCD detector (**Figure 59**). The experiments become time resolved by controlling the delay between the laser and X-ray pulse. The camera is used for Laue diffraction from proteins, for small molecule and powder diffraction and for angular dispersive diffraction from glasses and liquids. This new ultrafast X-ray diffraction technique (UXD) is complementary to ultrafast electron diffraction (UED) since the latter is limited to gas-phase samples due to the high scattering power of electrons.

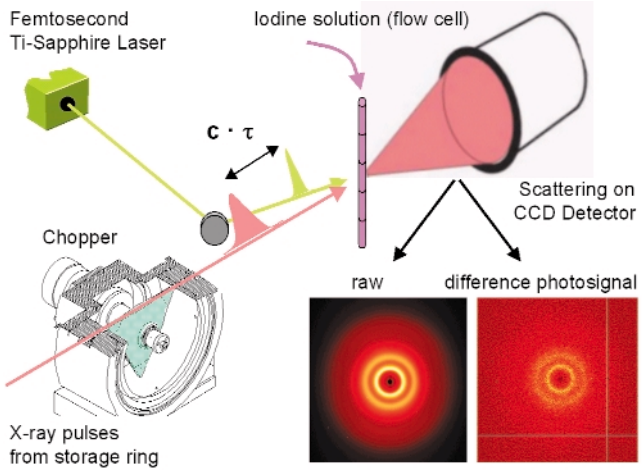

Fig. 59: The molecular camera for picosecond diffraction experiments.

The most striking films are taken with excited protein crystals such as the carbon monoxide complex of myoglobin and hemoglobin. In the following article by F. Schotte *et al.*, they show how myoglobin directs the dissociated CO away from its initial binding site next to iron. The CO migrates though a network of tiny cavities, to finally end up in the solvent outside of the protein. The ability of the protein to shield the CO from direct recombination is an intricate feature of myoglobin, which is essential for respiration. The quality of the data depends on the ability to dissociate, non-destructively, a substantial fraction of unit cells. It turned out to be beneficial to increase the laser pulse length from 150 fs to 2 ps to maximise the dissociation yield. This trick increased the number of "correctly excited" unit cells by 10, which gave a 10-fold improvement in the signal to noise. This effect is due to the presence of short-lived, high-absorption electronic states that tend to obstruct the entry of the laser pulse.

The experiments on excited molecules in liquids are reported subsequently by A. Plech *et al.*, who studied the excited-state structure of iodine in liquid CCl_4. The initial aim was to extract the diffracted signal from excited iodine, determine the change in the I_2 bond length and the degree of dissociation. It came as a surprise, therefore, to see that a local change in structure around iodine can induce a global change in structure in the bulk liquid, driven by the flow of energy from the solute to the liquid. This forces the liquid to expand. The expansion shows up after 10 ns and is over after 100 ns. This pattern is quite general in photo-excited liquids and we now classify the liquid structure into a pre-expansion,

an expansion and post-expansion phase. The expansion amplitude, defined by the change in distance between neighbouring solvent molecules, is typically a fraction of a milliangstrom, but is shows up since it integrates all the solvent molecules in the sample. From the expansion amplitude, it is possible to check the associated energy input from the laser, which is a way to check if the total energy is conserved.

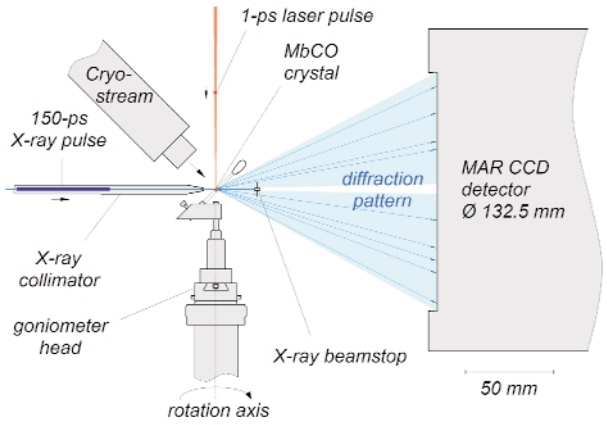

Fig. 60: Experimental setup used to acquire picosecond time-resolved X-ray diffraction data. The crystal is photolysed by a laser pulse and then probed by a time delayed X-ray pulse, whose diffraction pattern is recorded by an area detector. A cooling stream allows the flash photolysis to be repeated at 3.3 Hz. The orientation of the sample is fixed during each exposure; the goniometer spindle rotated between exposures. The 200 µm crystal is mounted in a sealed X-ray capillary.

Picosecond Crystallography: Myoglobin in Action

Proteins perform their life-giving function dynamically while interacting with other molecules. The ability to watch a protein as it responds to stimuli will help researchers solve many mysteries regarding how it achieves its function. A new step toward that goal was recently taken by a team of scientists working on the time-resolved beamline **ID09B**, were the first ever movie of a protein executing its function with sub-nanosecond time resolution was produced. The system studied by this team, the oxygen storage protein myoglobin, is similar to hemoglobin but is found in muscle cells rather than blood cells. It supplies oxygen to cells when blood fails to deliver it fast enough (for example, when circulation is blocked during muscle contraction). The aim of the experiment was to identify pathways for oxygen diffusion within the protein and to see how oxygen is finally released into the surrounding solvent. By using CO as a substitute for oxygen, they took advantage of the photosensitivity of the Fe-CO bond, allowing them to trigger ligand release synchronously throughout a crystal by a short laser flash. The mutant L29F of myoglobin [1], in which a leucine residue is replaced by a phenylalanin, proved to be an interesting test case because substantial protein conformational changes take place during the first few hundred picoseconds after laser photolysis.

This experiment makes use of the time structure of synchrotron radiation, which consists of 50 to 150 ps long X-ray pulses. The **ID09B** beamline is equipped with a high-speed chopper capable of isolating single X-ray pulses from the synchrotron pulse train and houses an ultrashort pulsed laser that is synchronized to the X-ray pulses. Time-resolved crystallographic data were acquired using the "pump-probe" technique: the sample was first hit by a laser pulse to trigger the reaction (pump) and then a time-delayed X-ray pulse was scattered off the protein crystal (probe) and its pattern of diffracted X-rays recorded (**Figure 60**). Since CO rebinds to myoglobin within a few milliseconds, the pump-probe sequence could be repeated on a single myoglobin crystal thousands of times without degradation. To speed up data collection, the unfiltered X-ray beam from an undulator (no monochromator) was used to record polychromatic Laue patterns that contained thousands of reflections at each crystal orientation (**Figure 61**). The intensity of each reflection is a measure of a Fourier component of the electron density within the unit cell of the crystal. About 20,000 such structure factors were required to calculate, by inverse Fourier transformation, an electron density map with 1.8-Å resolution. By changing the pump-probe delay, the evolution of the electron density as function of time after photolysis was determined.

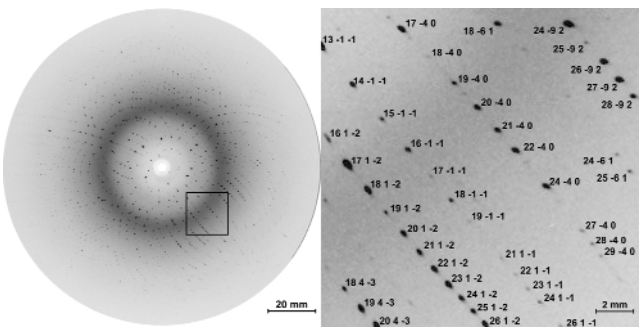

Fig. 61: One of 155 time-resolved Laue diffraction images recorded from a single crystal. This image contains about 3000 diffraction spots. Only a small fraction of these spots would appear when probed with monochromatic X-ray radiation. The enlarged view identifies Miller indices associated with the crystallographic planes that generated the Bragg reflections. This exposure represents the diffracted intensity from 32 X-ray pulses with the laser-to-X-ray delay set to 100 ps, accumulated over 10 seconds.

The earliest map, 100 ps after photolysis (Figure 62a), shows that the protein responds promptly to CO dissociation from the iron, revealing distortions spanning across the entire molecule. The time series (Figure 62b-g) suggests a mechanism responsible for the rapid CO expulsion that is characteristic of the L29F mutant. To make room for the free CO, the mutant side chain Phe29 is pushed aside together with the His64. The strain energy stored in this configuration helps drive CO out of its primary docking site on a timescale a thousand–fold faster than in wild-type myoglobin. The CO does not immediately escape into the surrounding water from this site, but is still found inside the protein after three microseconds as it migrates through an interconnected web of hydrophobic cavities and seeks an escape channel.

Given the level of structural detail obtained with picosecond X-ray crystallography, there is hope that it will contribute to our understanding of protein function at an atomic level.

References

[1] T.E. Carver, R.E. Brantley Jr, E.W. Singleton, R.M. Arduini, M.L. Quillin, G.N. Phillips, J.S. Olson, *J. Biol. Chem*. **267**, 14443-14450 (1992).

Principal Publication and Authors

F. Schotte (a), M. Lim (b), T.A. Jackson (c), A.V. Smirnov (a), J. Soman (d) J.S. Olson (d), G.N. Phillips Jr (e), M. Wulff (f), P.A. Anfinrud (a), *Science*, **300**, 1944-1947 (2003).
(a) National Institutes of Health, Bethesda (USA)
(b) Pusan National University (Korea)
(c) Harvard Medical School (USA)
(d) Rice University, Houston (USA)
(e) University of Wisconsin, Madison (USA)
(f) ESRF

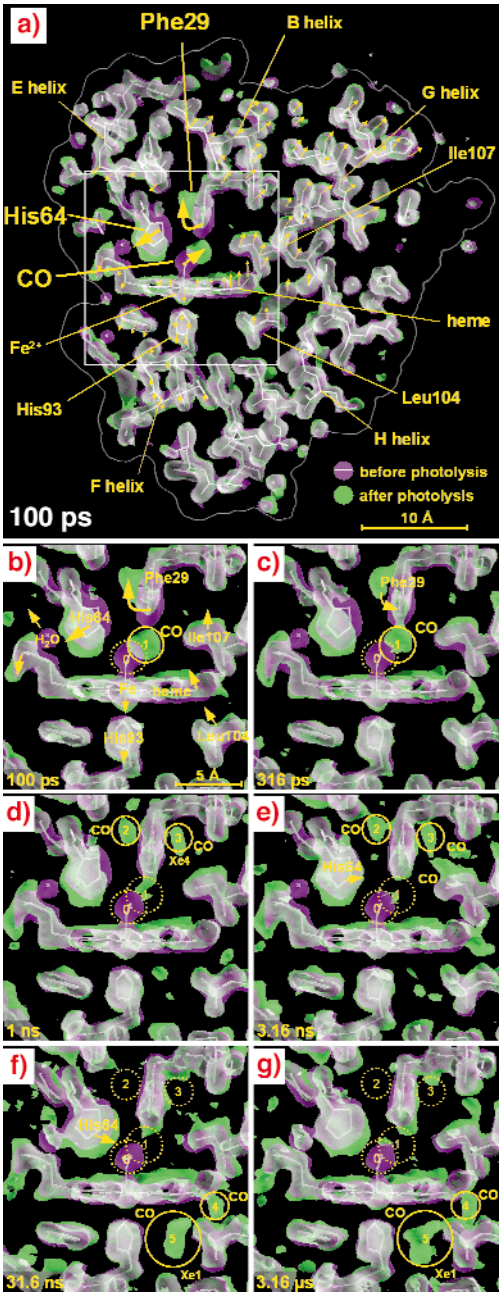

Fig. 62: 1.8 Å resolution electron density maps determined at from Laue diffraction data. For clarity, the electron density shown is confined to a 6.5 Å slab through the heme. The photolysed maps are coloured green and the unphotolysed maps are coloured magenta. Where both densities overlap, they blend to white. A white stick model of the unphotolysed structure is included to guide the eye. The direction of molecular motion follows the magenta to green colour gradient. (a) Three large scale displacements near the CO-binding site (large arrows) are accompanied by more subtle correlated rearrangements throughout the entire protein (small arrows; not drawn to scale). (b-g) Enlarged views of the boxed region in panel (a) at time delays specified in the lower left of each panel. (b) Upon photolysis, the bound CO (magenta; site 0) dissociates and becomes trapped approximately 2 Å away in a docking site (green; site 1), close to the Phe29. To accommodate the "docked" CO, the Phe29 is displaced and rotates, pushing His64 outward, which in turn dislodges a bound surface water molecule (magenta). (c-e) From 316 ps to 3.16 ns, the structural changes are largely confined to the vicinity of the binding site. As the CO migrates from site 1 to site 3 (Xe4), the Phe29 and His64 relax toward their deoxy conformations, which are similar to their unphotolysed states. (f-g) By 31.6 ns, CO has migrated to sites 4 and 5, where it remains trapped out to the microsecond time scale. The magenta and green maps were contoured at the same absolute level (1.5 σ of the unphotolysed density) using O 7.0, author A. Jones. The maps of the photolysed state were extrapolated from 20 to 100% photolysis.

Global Structure Kinetics of Photochemical Reactions in Solution

It is well known that chemical reactions in solution are strongly determined by the role of the solvent as reaction barrier and energy reservoir. The photoreaction of iodine in solution has long been the model system of choice for the study of reaction kinetics. In particular, I_2 in CCl_4 is very important due to its reduced-rate kinetics [1].

A method has been developed to resolve the structural dynamics of a photoexcited system by pulsed X-ray scattering, that allows a natural time resolution of 100 ps. Stroboscopic data acquisition is achieved by synchronising a femtosecond laser to the chopped X-ray pulses from an in-vacuum undulator at ID09 using its full emission spectrum at 3% bandwidth. The high flux of 10^{11} photons per second at 900 Hz pulse rate is indispensable regarding the low photo induced modulation signals of the full scattering in the intensity range of 10^{-4} [2].

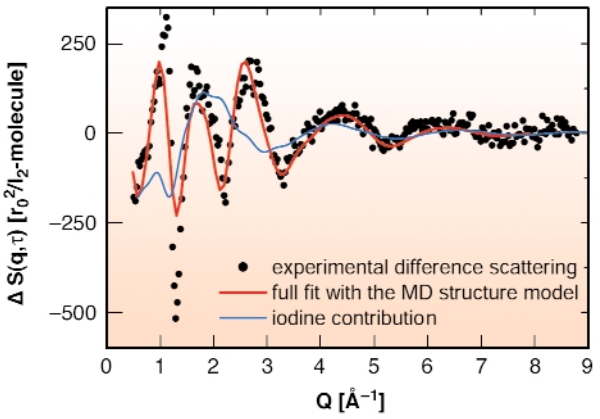

Fig. 63: Difference in scattering cross section in between the nonexcited sample and 1 ns after the excitation of the iodine absorption band by femtosecond laser pulses at 519 nm wavelength. The red line represents the model data derived by molecular dynamics simulations of the complete system of iodine within the CCl_4 solvent using time resolved scattering theory. The blue line shows only the local signal change of iodine and its solvation cage.

The information content differs depending on the region in q space considered (see **Figure 63**). At high momentum transfer, where strongly correlated atomic structures manifest, the distance changes of the iodine atoms can be observed. A mixture of states is observed within the first 2 nanoseconds, the stretched molecule (so-called A/A' state) and iodine atoms from the dissociation reaction. Occupancies and lifetimes can be inferred from the time-resolved q scans.

New, subtler changes manifest in the low q-region, where long range distances and liquid structures are observed. There, the solvent makes a large contribution to the signal due to the heat released by the chemical reaction. Part of the signal also arises from the changes in the pair distribution function of iodine to adjacent Cl atoms within the solvation cage and the outer shells. The collapse of the cage around a single iodine atom causes the solvent to come closer to an iodine scattering centre, whereas the extended I_2 state pushes the solvent outwards. The sum of all contributions is seen in **Figure 64**, which represents the Fourier inversion of the difference scattering data. The interpretation is confirmed by molecular dynamics (MD) studies (red line in **Figure 63**). For this purpose a MD simulation has been performed with a box of 256 CCl_4 molecules and one iodine molecule using appropriate pair potentials and steps of 1 fs in a 1ns observation interval.

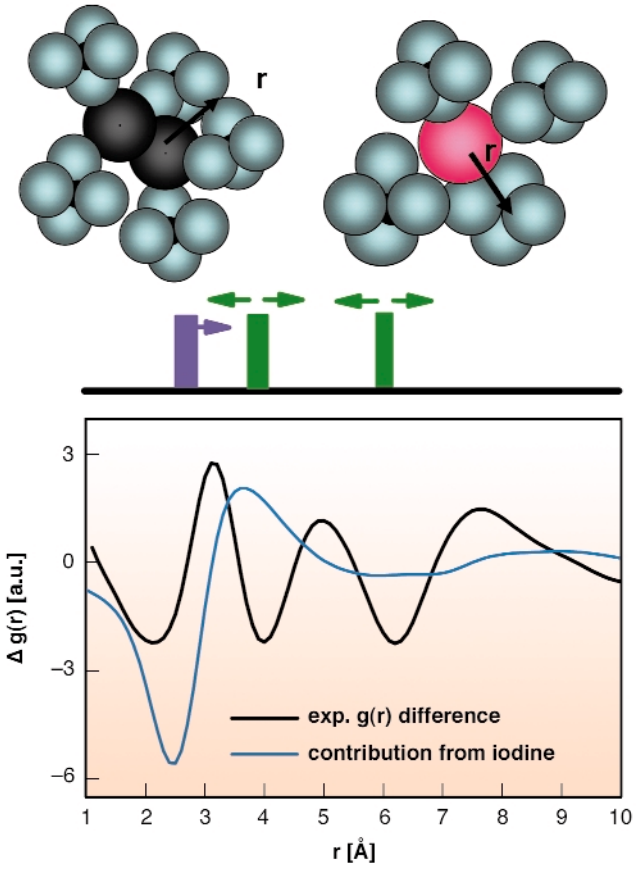

Fig. 64: Change in the pair distribution function obtained by Fourier inversion of the difference scattering in Figure 63 (black line). Again the blue line marks the contribution from iodine and its cage. The signal can be understood as a change of intermolecular distances of the iodine (magenta) in the excited A/A' state and distance changes between chlorine atoms of CCl_4 (green), which shift both to lower and higher distances, giving rise to the observed oscillations (black curve).

At larger time delays hydrodynamics comes into play as the energy flow from the excited iodine centres to the solvent is completed and the pressure in the excited region relaxes. At about one microsecond the system is equilibrated, both thermally and mechanically, with recombined iodine molecules and the heated solvent, whose difference scattering signal persists. Thus the solvent acts as a calorimeter that mirrors the energy

deposited into the system by the photoreaction. This energy can be compared to the number of excited iodine molecules to give information about ultrafast geminate reactions beyond the time resolution.

The challenge for the future will be to extend the procedure to larger molecules and biologically relevant aqueous solutions of photoactive molecules.

References

[1] A.L. Harris, J.K. Brown and C.B Harris, *Ann. Rev. Phys. Chem.* **39**, 341-366 (1988).
[2] M. Wulff, A. Plech, L. Eybert, R. Randler, F. Schotte and P. Anfinrud, *Faraday Disc.* **122**, 13-26 (2002).

Principal Publication and Authors

A.Plech (a), M. Wulff (d), S. Bratos (b), F. Mirloup (b), R. Vuilleumier (b), F. Schotte (c) and P. Anfinrud (c), *accepted in PRL.*
(a) Fachbereich Physik der Universität Konstanz Germany)
(b) Université Pierre et Marie Curie, Paris (France)
(c) National Institutes of Health, Bethesda (USA)
(d) ESRF

Stress and Strain Studies at the ESRF

Introduction by V. Honkimäki, ESRF

The conservative field of structural engineering is getting new ideas from new scientific tools such as synchrotron radiation. Gauge volumes down to micrometre dimensions are achievable using microfocussed high-energy X-ray radiation. This even enables the study of individual grains. Fast data acquisition makes *in situ* investigations possible. Fame38, a joint venture between some British Universities, the ILL and the ESRF, encourages European engineers to take advantage of these new possibilities in their research.

Residual stresses exist in engineering components in the absence of external loads. Generally residual compression near the surface enhances the materials resistance and near surface tension can lead to fracture. Mechanical forming, welding and heat treatment are the major ways to introduce residual stresses in the material. X-ray and neutron diffraction are the only non-destructive methods to determine these residual stresses. The diffraction method of measuring strain relies on the determination of interplanar atomic spacing along different directions and knowing the elastic constants of the material the state of stress in the specimen can be determined. The high penetration power of the high-energy X-ray radiation makes it possible to spatially-resolve stresses deep within material.

Strain measurements are possible at four beamlines at the ESRF: ID11, materials science beamline, ID15A and B, high-energy beamlines and ID31, powder diffraction beamline. These beamlines have several techniques to measure X-ray diffraction patterns: the traditional scanning method with monochromatic radiation, the white beam energy dispersive diffraction method, and monochromatic 2D-diffraction methods with area detectors to collect many reflections simultaneously. The depth resolution is achieved by slits with area detectors. These slits are more sophisticated with a conical or spiral construction. Furthermore, the incident beam can be focussed down to micrometre dimensions using mirrors, multilayers, bent Laue crystals or refractive lenses.

The engineering problems span a wide range of applications and it is impossible to cover all stress and strain studies at the ESRF in this short highlight presentation. One article describes the first direct measurements of the strains at a fibre and metal matrix interface. By combining *in situ* micro diffraction at ID11 and X-ray tomography at ID19 it has been possible to build up a comprehensive picture of the fibre fracture sequence. Another article describes the novel and efficient method of strain and phase scanning at ID15B and its application to study friction stir-welded joints between dissimilar materials.

Monitoring the Interface in Metal Matrix Composites

A composite material is much more than just a matrix and a set of fibres. Pivotal to the performance of a composite is the behaviour of the matrix/fibre interface. If too strong, then, once a crack starts to grow in the matrix, it will break all the fibres causing brittle failure. If too weak, then the strength and mechanical properties of the composite will be compromised. This makes it very important to be able to measure the interface properties for a given processing route.

Until recently it has not been possible to measure the properties of the interface directly and as a result experimenters have had to rely on indirect measurements based on micromechanical models.

Our measurements on beamline **ID11** have provided the first direct measurements exploiting the highly focused and penetrating beam available there to map the development of strains along the fibres as a function of applied loading. By combining these strain maps with three-dimensional X-ray tomographs collected on beamline **ID19** it has been possible to build up a comprehensive picture of the fibre fracture sequence and the associated changes in internal stress.

For these studies a single carbon coated SiC monofilamentary fibre was embedded in a Ti-6Al- 4V matrix. By straining this composite the fibre breaks into smaller and smaller segments, the lengths of which are determined by the shear sliding strength of the fibre/matrix interface. The elastic strains, as a function of loading, derived from changes in lattice spacing measured by micro diffraction on ID11 are shown in **Figure 65a**.

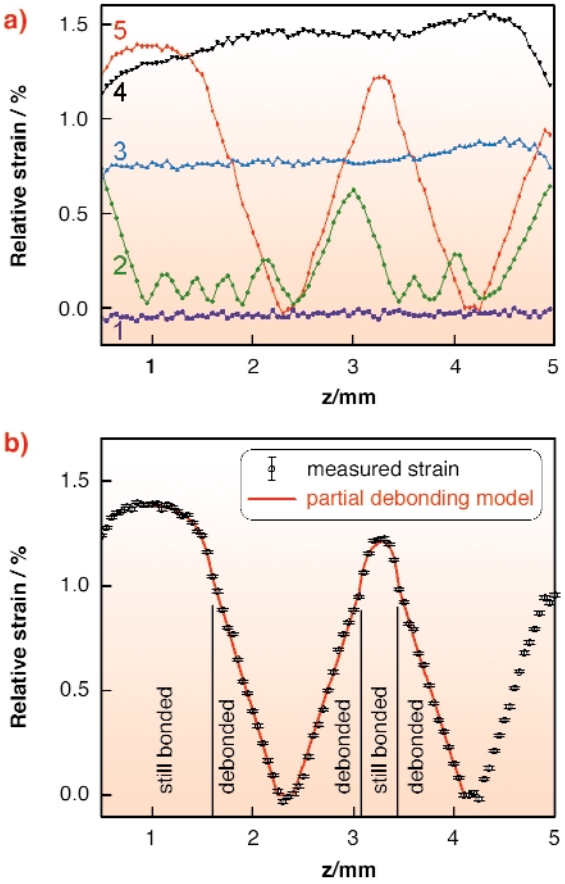

Fig. 65: a) The variation in axial fibre strain as the applied load is increased; only a few of the loading steps (numbered by increasing load) are shown, b) a fit to the model after two breaks (at 2.3 and 4.1mm).

As the applied load is increased the fibre strains approximately uniformly until fibre fracture occurs at which point sharp drops in the fibre strain are observed. From the gradients of the resulting slopes the fibre matrix interface strength can be measured accurately (200 MPa). The results of a finite element model simulation are shown in **Figure 65b**.

It is clear from the figure that the fibre breaks into successively smaller segments and this is confirmed by the virtual section through a 3-D X-ray tomograph, shown in **Figure 66**. One single and many double cracks were observed in the tomograph. The double cracks occur because of cracks that initiate on the surface of the fibre as a wedge-crack. These appear as double cracks in the slice but their morphology is clearly resolved in the 3-D reconstruction shown in **Figure 66**.

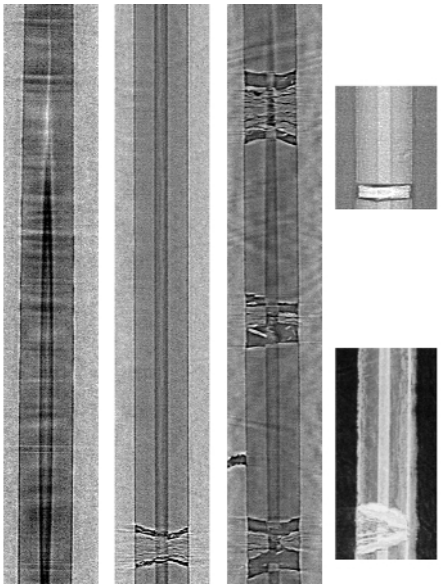

Fig. 66: Tomographic sections taken through the centre of the C-cored fibre before testing, at an intermediate stage, and after full fragmentation. The first core initiated single crack (above) and a 3D semi-transparent visualisation of a wedge-crack (below) are also shown.

The first single crack initiates from the carbon core of the fibre seen in **Figure 66**. The elastic shock wave that passes down the fibre causes damage on the surface, which results in the formation of wedge-cracks at much lower loads than were necessary to form the original crack.

In conclusion this work represents the first direct measurements of the interfacial sliding stress for Ti/SiC metal matrix composites. The tomographic images presented here provide the first observation of the formation of wedge-cracks caused by damage initiated at the surface of the fibre. This work is crucial to the development of crack resistant metal matrix composites for applications in aerospace.

References

[1] M. Preuss, P.J. Withers, E. Maire, J.Y. Buffiere, *Acta Mater*, **50**, 3175 (2002).
[2] G. Rauchs, M. Preuss, P.J. Withers, *Acta Mater*, **50**, 2477 (2002).

Principal Publication and Authors

P.J. Withers (a), M. Preuss (a), E. Maire (b), J.-Y. Buffiere (b).
(a) Manchester Materials Science Centre (UK)
(b) GEMPPM, INSA de Lyon (France)

Depth-resolved Investigation of Friction Stir Welds using a Novel Strain and Phase Mapping Technique

Friction stir welding (FSW) is a solid state welding process in which a spinning tool is forced along the joint line, heating the abutting components by friction, and producing a weld joint by strong plastic mixing (stirring) of material from the two components. Compared to classical fusion welding techniques, FSW can overcome problems such as weld porosity and cracking in the heat affected zones [1]. As opposed to dissimilar material combinations, the joining of similar materials (mainly Al alloys) by FSW is becoming widely implemented in industrial production. In the framework of the EU funded JOIN-DMC project (JOINing Dissimilar Materials and Composites), FSW of dissimilar materials were characterised, applying for the first time a novel non-destructive strain and phase mapping technique, recently developed at **ID15** at the ESRF. This technique provides depth-resolved information about intensity and

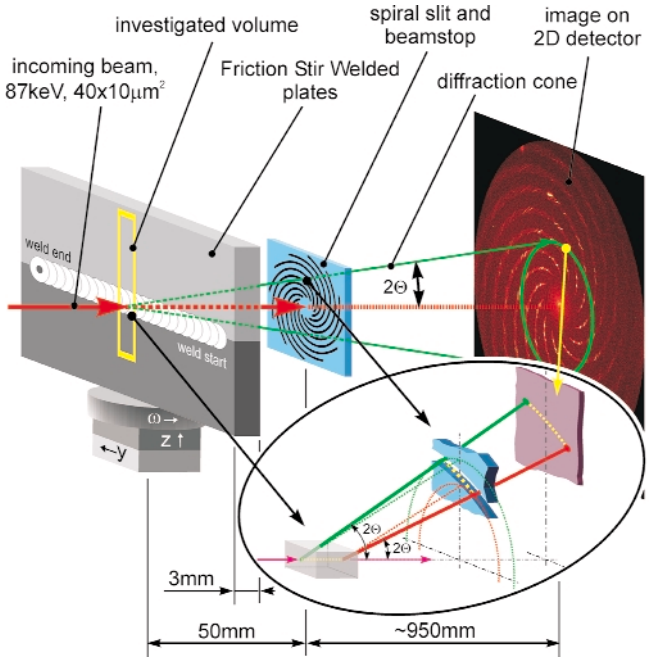

Fig. 67: Schematic of the experimental setup with spiral slit and online image plate scanner on ID15B.

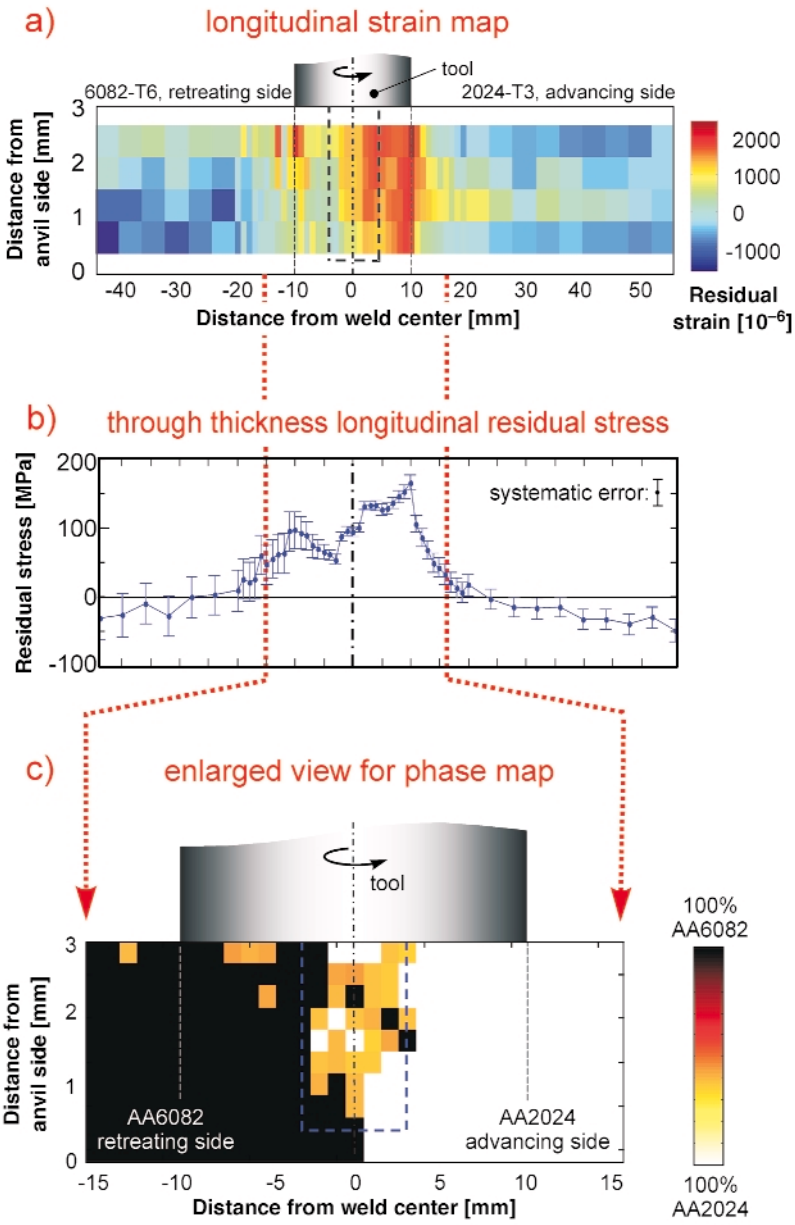

Fig. 68: a) Depth resolved residual macrostrains in longitudinal direction (parallel to weld); b) through thickness longitudinal residual stress component, calculated from the strain measurements in three dimensions; c) enlarged view of the distribution of the plate material (AA6082 and AA2024) in the stirring zone.

position of all the Bragg reflections emanating from the sample within the angular acceptance given by the experimental setup. Bulk investigations of several mm thick Al plates are realised by using high energy X-rays. The depth resolution is achieved by the use of a spiral slit. Simply, it consists of twelve equidistant concentric spiral appertures cut into a W plate. All paths through the 2mm thick plate lie on cones, which have one common apex (*i.e.* the focal point of the slit system; here 50mm). The azimuth-selective depth-resolved signal is recorded with an online image plate scanner. A sketch of the experimental setup is shown in **Figure 67**.

This is first technique allowing the mapping of a weld zone in a non-destructive manner with depth resolution, material composition and strain distribution. The results presented relate to a FSW between AA2024-T3 and AA6082-T6 (single phase Al alloys). The strain tensor was derived from the diffraction-cone distortions, recorded at two different angular sample positions. The differences in the diffraction spectra of both materials were used as an indicator for the material mixing in the stirring zone. Part of the results are shown in **Figure 68**. For a better comprehension the welding tool is shown schematically (tool pin marked by thick dashed line). **Figure 68a** shows the depth resolved strain map for the longitudinal component (parallel to the weld). The strain distribution is particularly inhomogenous on the retreating side with high tensile strains (around $+2000x10^{-6}$) under the tool shoulder (about –10 mm from the center) and values around zero close to the anvil side. The distribution of the longitudinal residual stresses (**Figure 68b**), integrated over the plate thickness, and calculated from the strain data set shows a maximum stress of about +160 MPa under the advancing tool shoulder (at +10 mm). The strong asymmetry of the stress ditribution and the strain map arises from the mixing of the dissimilar materials (**Figure 68c**) and the different response of the materials to the tool force. In the present case a good mixing of the two materials is observed, resulting in a smoother residual stress profile in the stirring zone as compared to results (not shown here) from a weld with reversed material combination.

Reference

[1] D.P. Field, T.W Nelson, Y. Hovanski, K.V. Jata, *Metallurgical and Materials Transactions A*, 32A (2001).

Authors

R.V. Martins (a) and V. Honkimäki (b), *Textures and Microstructures* (2003), *accepted for publication*.
(a) Risø National Laboratory (Denmark); present address: GKSS-Research Center Geesthacht (Germany)
(b) ESRF

First Results from the FaME38 Project

FaME38 is the joint ESRF and ILL support Facility for Materials Engineering. It provides, in close collaboration with beamline staff, the additional support that most *Engineers* require to enable them to perform materials engineering experiments at the ESRF and the ILL.

The initial emphasis, since the inauguration of the FaME38 laboratory in November 2002, has been in the strain/stress measurement field but support is also available for materials engineering experiments generally. The laboratory provides off-line experiment preparation, advanced metrology tools and data analysis facilities. Particular objectives are to improve the reliability, accuracy and efficiency of engineering experiments. Engineering samples (such as railway rails or replacement hip implants) can have complex shapes, or can differ significantly from their design shape due to distortion (as is often the case in welds) or due to wear (as occurs during service). An experiment may involve measuring strain in three or more directions as a function of position within a component so that the stress field may be determined. To map the strains in such components it is necessary first of all to know precisely their shape, their location and orientation, and then to manipulate them relative to the 'gauge volume' defined by the incident beam and detector optics. The international VAMAS TWA20 project, that develops *standards* for measuring residual stresses using neutrons and synchrotron X-rays, has shown that, although strain measurement has been in general satisfactory, sample positioning has often been inadequate [1].

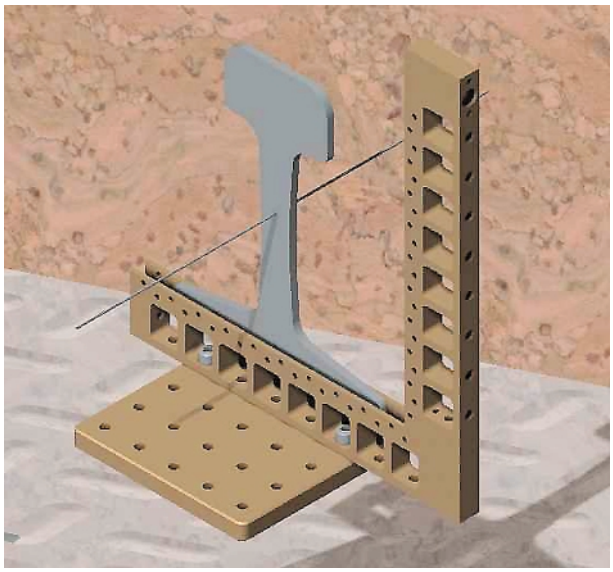

Fig. 69: Standard VAMAS recommended base-plate system with L-shaped mount (and illustrative sample) that provides rapid and precise sample positioning.

A disproportionate amount of beamtime is also often spent on the beamline, mounting and aligning samples and in generating the appropriate scanning macros. The FaME38 philosophy is that this type of work should be performed off-line wherever possible. It is the same philosophy as that adopted by airlines that train their pilots, and test the limits of their aircraft, 'off-line' using flight simulators prior to flying their passengers from major airports. In the FaME38 metrology laboratory a Co-ordinate Measuring Machine (CMM) is used to determine sample shapes and location relative to a standard mount and base-plate (**Figure 69**) to an accuracy of ±2 micrometres. Samples can then be mounted in minutes to ~ ±0.01mm on a matching base-plate on the beamline. A mechanical simulator and web-based 'virtual instruments' are being developed, using CAD knowledge of the beamlines and sample information from the CMM, on which mounting systems, scanning matrices, and collision avoidance, can be developed and assured off-line (**Figure 70**).

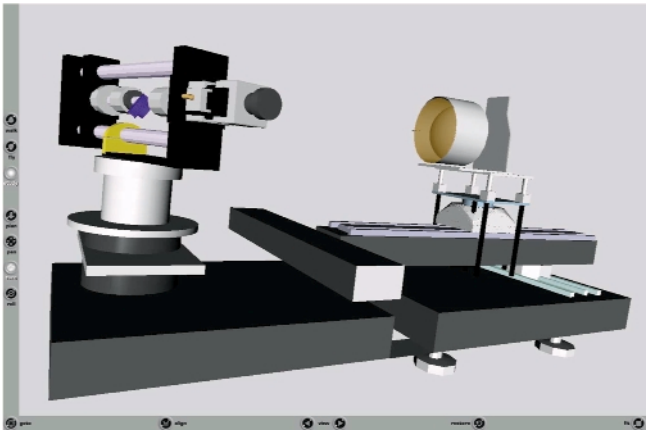

Fig. 70: A web-based 'virtual instrument'. The illustration shows a sample mounted in a test rig on ID11. All the components can be manipulated remotely to provide an accurate scan simulation.

In combination, the gains in reliability, positioning, collision avoidance, setting-up time, counting time, Local Contact time, scan optimisation, near-on-line data processing and the visualisation of results, are considerable and users are exploiting the benefits. The enhancements will lead not only to substantial improvements in efficiency and data quality for existing users but to an increasing user base that will include many more academic and industrial engineers who until now have not considered using synchrotron radiation as an analytical tool.

For further information contact the FaME38 team at (FaME38@esrf.fr).

Reference

[1] Technology Trends Assessment ISO/TTA 3:2001.

Author

FaME38
ESRF-ILL

Soft Condensed Matter

Introduction

The soft condensed matter (SCM) group is composed of the public beamlines ID02, ID10A, ID10B, ID13 and the CRG beamlines BM02, BM26 and BM32. Soft condensed matter science addresses questions on microstructure, kinetics, dynamics and rheology of complex and nanostructured materials. Similar activities are pursued at many other ESRF beamlines, which shows that borders with neighbouring disciplines are transparent. In the future, one can expect that the SCM beamlines will increasingly address problems in nanoscience and biotechnology.

The following highlights give an overview on the diversity of topics investigated at the SCM group beamlines, which shows that both scientific applications and methodological approaches are evolving rapidly. The increasing use of surface-sensitive techniques is particularly interesting as it provides more collaborative possibilities for the SCM group.

X-ray photon correlation spectroscopy (XPCS) is a technique for probing bulk dynamics, which has been pioneered at the Troika beamline. Two methodological advances are reported from ID10A, which provide new and exciting opportunities. Thus Gutt *et al.* and Madsen *et al.* (page 58) have used grazing-incidence XPCS on ID10A to study capillary wave propagation in water/glycerol mixtures. Among the possible future applications are fluctuating lipid membranes, which are currently studied by static diffuse scattering techniques (see below). XPCS has also been extended up to ≈ 20 keV by Thurn-Albrecht *et al.* (page 59), for a model colloidal silica suspension. The use of higher energies reduces absorption and allows thicker samples and longer acquisition times. This method should therefore have an impact on studies of polymeric and biological samples, which are particularly "photon hungry".

Recently, anomalous small-angle X-ray scattering (ASAXS) has found new applications in soft condensed matter. At the ID02 beamline, N. Dingenouts *et al.* (page 60) have exploited this technique to address one of the long-standing issues in the physics of polyelectrolytes, namely the spatial correlation of the counterions with the macroions. In another important development at ID02 during the year, the high count-rate RAPID gas detector from the Daresbury Laboratory [1] was employed for a series of millisecond time-resolved experiments involving muscle diffraction and fast kinetics in solution. This exercise allowed the first combination of the high brilliance of a third generation source with a state-of-the-art photon-counting detector for sub-millisecond time-resolved small-angle diffraction experiments.

The use of microbeam techniques has been further developed at ID13. Thus understanding the local structure of high-performance fibres is of considerable technological importance. Davies *et al.* (page 61) have studied the local structure of different brands of poly(p-phenylene benzobisoxazole) fibres as a function of uniaxial stress. Differences in skin-core structures and crystallite orientation could be related to spinning and postprocessing conditions. Grazing-incidence small-angle scattering (GISAXS) techniques have been extended by Roth *et al.* to micrometre-sized beams (page 63). This "μGISAXS"-technique allowed them to characterise a lateral gradient of nanometric gold clusters on a substrate. The future use of submicrometre beams is of particular interest for applications in constrained environments such as thin fibres, channels or heterogeneous surfaces.

The setup available at ID10B has been developed in particular for studies of organic or biological surfaces/interfaces by surface-sensitive techniques. Dürr *et al.* (page 64) have investigated the growth mechanism of diindenoperylene molecules by a combination of atomic-force microscopy, specular X-ray reflectivity and diffuse X-ray scattering. The observed rapid roughening suggests a subtle competition between domain shape and local crystal structure. This is a particularly interesting domain of research as semiconducting organic films have promising applications in electronic devices. De Jeu *et al.* (page 65) report on a fundamental study of the 2D/3D transition of a single top layer of a stack of smectic layers. This grazing-incidence X-ray diffraction study aims at probing theoretical models of defect mediated melting processes.

Lipid membranes are of great interest as they might result in novel biomolecular materials. Stacks of lipid membranes on silicon at full hydration have been studied at the ID01 beamline by nonspecular, diffuse X-ray reflectivity measurements by the group of Salditt *et al.* (page 67). These quasi 2D-objects show a correlation of thermal fluctuations and positional parameters, which can be treated only approximately with current elasticity models. This example also emphasises the pursuit of SCM-topics at other ESRF beamlines.

C. Riekel

References

[1] R.A. Lewis *et al.*, *NIM A*, **392**(1-3), 32-41 (1997).

Dynamic Properties of Liquid Surfaces Revealed by XPCS

Correlation spectroscopy with coherent X-rays (XPCS) is a speciality of beamline **ID10A** (TROÏKA) and it offers the interesting possibility to probe bulk dynamics as well as dynamic properties of surfaces. The surface application resides in the fact that when the X-ray beam is applied at an incidence angle α_i below α_c (the critical angle for total external reflection) a unique surface sensitivity is obtained. Moreover, multiple scattering effects can largely be ignored for X-rays and with the advent of fast avalanche photo-diode (APD) detectors it has become possible to quantify dynamic phenomena up to MHz frequencies. This shows that the gap to energy-domain techniques, especially neutron spin-echo (NSE) [1] has been bridged.

Recently, the first surface XPCS experiment employing heterodyne mixing was reported [2]. In the heterodyne mixing scheme, coherent interference between the scattered field (carrying the dynamic information) and a static reference field is evoked. Interference with a strong reference field amplifies the (weak) scattered signal while preserving the dynamic information. This leads to the presence of a heterodyne component in the time-correlation function of the scattered intensity. When capillary wave dynamics is quantified by XPCS performed under grazing incidence conditions, the heterodyne component of the correlation function can be strong (**Figure 71**). This heterodyning is caused by interference between the diffuse scattering and the totally reflected signal close to the specular condition *i.e.* where the incidence angle α_i and the exit angle α_e are equal. Hence, the specular reflection acts as the required static reference signal which is very intense when $\alpha_i < \alpha_c$. In future, the aim will be to control and manipulate the reference signal in order to choose the region of reciprocal space where heterodyning is desired. For diffuse scattering from a liquid surface, which becomes weaker as $|\alpha_i-\alpha_e|$ is increased, such control could offer the unique possibility to quantify dynamic surface phenomena at atomic length scales.

Using heterodyne grazing incidence XPCS it was recently possible to quantify the transition from propagating to over-damped capillary waves on a simple liquid surface [3]. The propagation frequency ω_p and the damping constant Γ of capillary waves is determined by the surface tension γ, the viscosity η and the wave vector k. At a certain critical k_c the damping gets so large that the propagating modes become unstable and eventually vanish. This influences the time-correlation function where the oscillating behaviour, which is characteristic for propagating waves, gradually disappears. Hence, by XPCS the dispersion of ω_p and Γ can be measured as shown in **Figure 72**. The data are well modelled by linear response theory (solid lines) and in particular the cross-over behaviour of ω_p before the actual transition at $q = k_c$ is well described by the model.

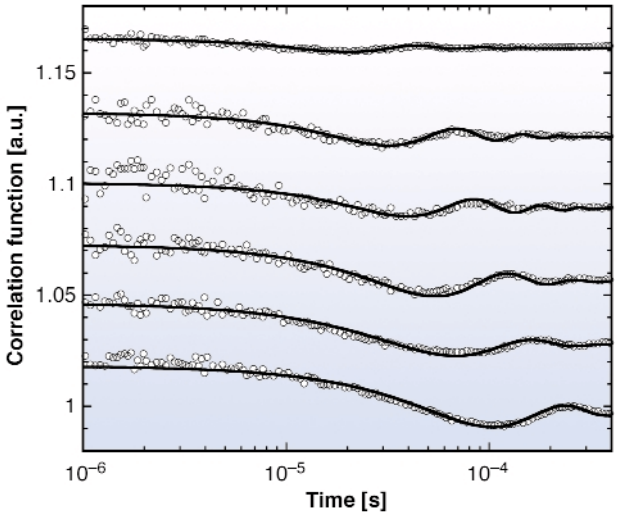

Fig. 71: Correlation functions taken at increasing exit angles α_e corresponding to an increase in momentum transfer q parallel to the surface (bottom to top). The data were taken on a water surface at T = 5°C with $\alpha_i < \alpha_c$ and the oscillatory behaviour indicates the presence of propagating capillary waves. The q dependence of the propagation frequency wp is clearly visible (dispersion) and follows $\omega_p \propto q^{3/2}$. The solid lines are fits assuming heterodyne mixing [2].

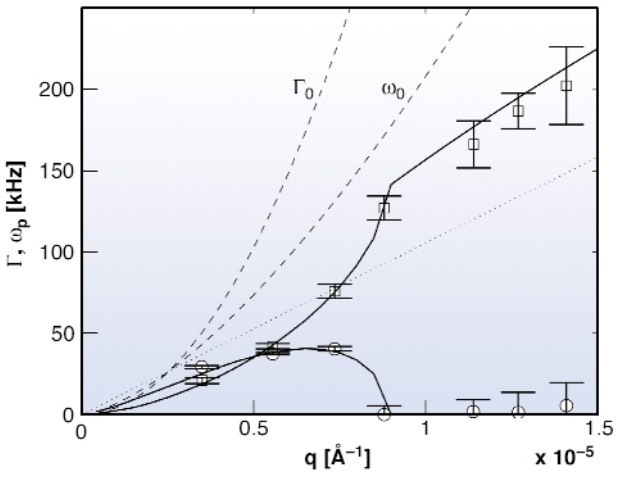

Fig. 72: Propagation frequency ω_p (circles) and damping constant Γ (squares) determined by XPCS in a water/glycerol mixture at T = 12°C. The dispersion relations derived in the limit of small damping ($\omega_0 \propto q^{3/2}$, $\Gamma_0 \propto q^2$, dashed lines) and strong damping ($\Gamma \propto q$, dotted line) clearly fail to describe the observed behaviour in this transition region. Nevertheless, the data are well-modelled by linear response theory and the cross-over from propagation to over-damped behaviour is obvious at $q \approx 8\times10^{-6}$ Å^{-1} [3].

We conclude that grazing-incidence XPCS is an emerging technique with interesting perspectives for further development. In the near future, it will be applied to the study of dynamics under confinement and to investigate dynamic properties of lipid membranes and multilayers.

References

[1] I. Sikharulidze, B. Farago, I.P. Dolbnya, A. Madsen and W.H. de Jeu, *Phys. Rev. Lett.* **91**, 165504 (2003).
[2] C. Gutt, T. Ghaderi, V. Chamard, A. Madsen, T. Seydel, M. Tolan, M. Sprung, G. Grübel, S.K. Sinha, *Phys. Rev. Lett.* **91**, 076104; 179902(E) (2003).
[3] A. Madsen, T. Seydel, M. Sprung, C. Gutt, M. Tolan and G. Grübel, *in print, Phys. Rev. Lett.* (2004).

Authors

A. Madsen (a) and G. Grübel (a,b).
(a) ESRF
(b) Present address: HASYLAB (Hamburg)

Photon Correlation Spectroscopy with High-energy Coherent X-rays

X-ray photon correlation spectroscopy (XPCS) allows measurement of slow dynamics on a small spatial scale in a scattering experiment [1, 2]. Since its development the technique has been used to explore the dynamics of a variety of colloidal and liquid crystal systems. Applications to polymer systems, although of basic interest, have been limited, partly due to severe problems with radiation damage. While it is known that radiation damage to organic samples can be reduced substantially by using higher-energy radiation, such an approach has never been seriously explored for XPCS experiments, since in these experiments a coherent primary beam is needed and coherent flux from a synchrotron source scales with the square of the wavelength. A positive aspect of higher-energy X-rays is the reduced absorption, which allows one to use thicker samples and longer acquisition times. We demonstrated that XPCS experiments can indeed be performed with higher-energy X-rays (~ 20 keV) and, based on scaling arguments we argue that despite a loss of coherence it will often be possible to realise a gain in signal to noise ratio under circumstances where thick samples can be used.

X-ray photon correlation spectroscopy is based on the same concept as the more commonly known Dynamic Light Scattering technique except for the use of coherent X-rays. If a scattering experiment is performed under highly-coherent conditions, the scattering pattern exhibits random interferences, so called 'speckles'. Microscopic dynamics in the sample leads to fluctuations in the speckle pattern and the corresponding intensity fluctuations constitute the signal observed in photon correlation spectroscopy. The intensity fluctuations are quantified via a normalised intensity correlation function $g(q, t)$, which for simple translational diffusion can be modeled by an exponential function

$$g(t) = c(q,\lambda) \exp(-2Dq^2) + 1$$

Here c(q, λ) is the contrast of the correlation function and D the diffusion constant. c(q, λ) is a direct measure of coherence.

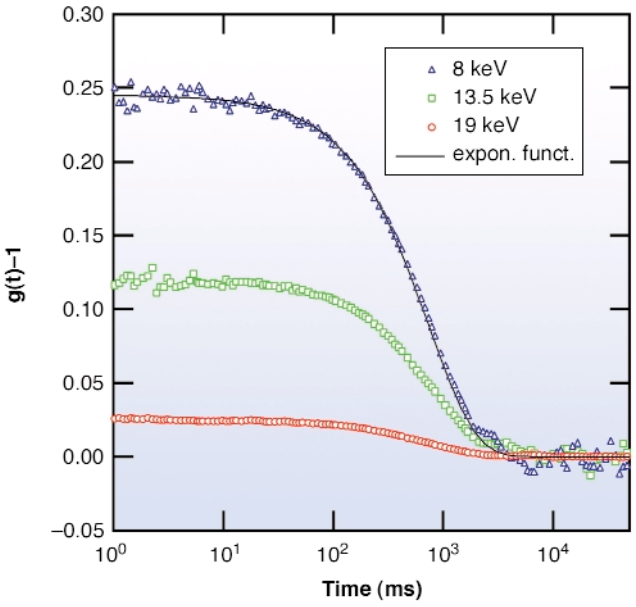

Fig. 73: Exemplary correlation functions of colloidal silica suspension measured at q ~ 7.6·10^{-4}Å^{-1} using three different X-ray energies as indicated.

We performed X-ray photon correlation spectroscopy experiments at the new Troika III station of beamline **ID10A** on a model suspension of colloidal particles using X-rays of three different energies. Exemplary correlation functions are shown in **Figure 73**. As expected we observe a strong change in contrast, *i.e.* coherence, while the time scale, on which the correlation functions decay, remains unchanged. The contrast of a series of correlation functions taken at different energies is shown in **Figure 74**. The dotted lines indicate the expected value of the contrast based on an extrapolation from the value determined for E_x = 19 keV. The estimated values are consistent with the data, although there are deviations, especially at 8 keV, which are most likely caused by static background signal. These results give an experimental basis to our arguments concerning the statistics of XPCS measurements at different energies. In conclusion, our data clearly show that it is feasible to perform XPCS experiments with higher X-ray energies than used in previous experiments. The reduced absorption can be used for a net gain in signal if sample

thickness and acquisition time are optimised. The use of higher energy X-rays constitutes a promising option for future XPCS-experiments on polymeric and biological sample systems.

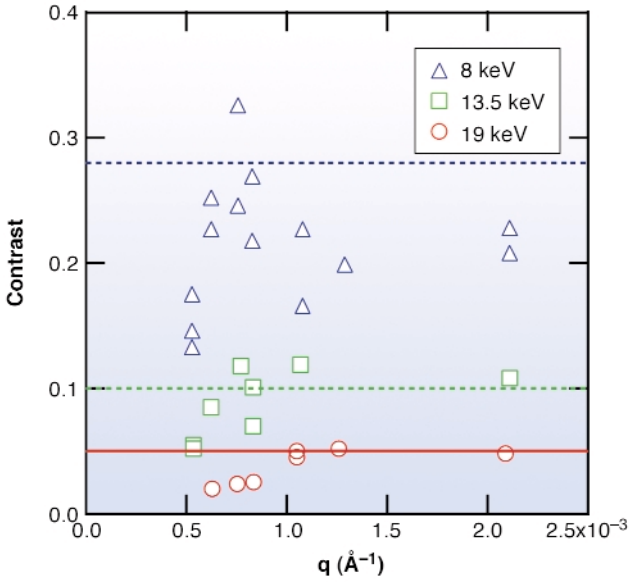

Fig. 74: Contrast c(q, λ) of correlation function vs. scattering vector q as determined from a series of measurements taken with different X-ray energies as indicated.

References:

[1] S.G.J. Mochrie, A.M. Mayes, A.R. Sandy, M. Sutton, S. Brauer, G.B. Stephenson, D.L. Abernathy and G. Grübel, *Phys. Rev. Lett.* **78**, 1275 (1996).

[2] T. Thurn-Albrecht, W. Steffen, A. Patkowski, G. Meier, E. W. Fischer, G. Grübel, and D.L. Abernathy, *Phys. Rev. Lett.* **77**, 5437 (1996).

Principal Publication and Authors:

T. Thurn-Albrecht (a), F. Zontone (b), G. Grübel (b), W. Steffen (c), P.Müller-Buschbaum (d), A. Patkowski (e), *Phys. Rev. E* **68**, 031407 (2003).

(a) Martin-Luther-University Halle (Germany)

(b) ESRF

(c) Max-Planck-Institute for Polymer Research, Mainz (Germany)

(d) Technische Universität München, Garching (Germany)

(e) A. Mickiewicz University, Poznan (Poland)

Counterion Distribution in Spherical Polyelectrolyte Brushes

Polyelectrolytes represent a special class of polymers having ionisable groups. They are involved in many practical applications in everyday life. When suspended in water or a polar solvent, the counterions will be dissociated. The characteristic features of polyelectrolytes arise from the electrostatic repulsion between the chains as opposed to the entangled nature of their uncharged counter parts. The distribution of counterions around the polymer macroion is a long-standing issue in the physics of polyelectrolytes. A polyelectrolyte brush is formed when linear polyelectrolytes are affixed onto a planar or curved surface. Moreover, the polyelectrolyte brush represents a unique case of macromolecular self-assembly, owing to their architecture and constitution bring together various notions common in soft matter physics. Hence these systems have been studied intensively both theoretically as well as experimentally [1]. In this work, we have developed a new method to probe the spatial distribution of counterions around the colloidal macroion. The approach combines high-resolution small-angle X-ray scattering (SAXS) with the anomalous dispersion by the counterions near their absorption edge.

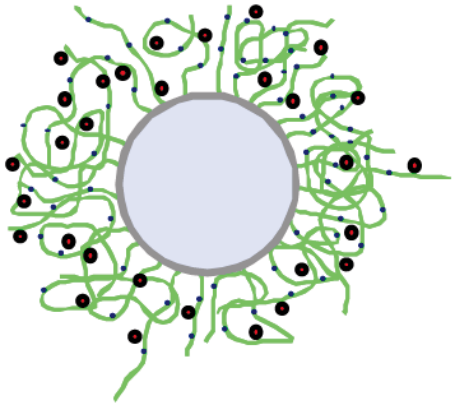

Fig. 75: Radial structure (schematic) of a spherical polyelectrolyte brush consisting of polystyrene core and chemically-grafted poly acrylic acid chains.

The radial structure of a brush-like polyelectrolyte is depicted schematically in **Figure 75**. The system consisted of dilute salt-free spherical brushes, each composed of a polystyrene core and polyacrylic acid chains chemically grafted onto the core surface. The counterions are rubidium whose K-edge falls in a convenient energy (15.2 keV) range for performing high-resolution SAXS. The measured scattered intensities become a complex function of energy near the absorption edge of the counterions. **Figure 76** depicts the typical variation of SAXS intensity, I(q), as a function

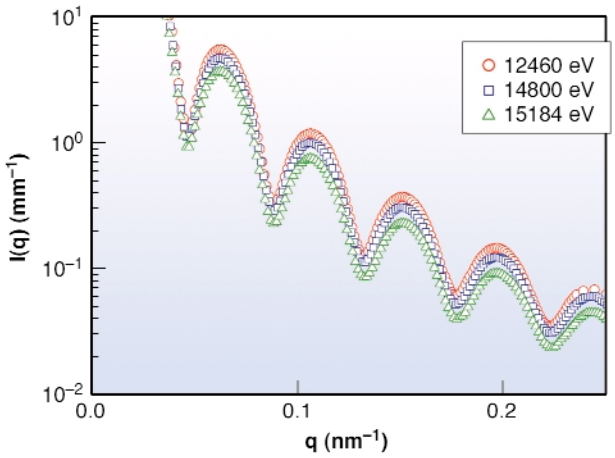

Fig. 76: Typical variation of SAXS intensity as the K-edge of the counterions (Rb^+) is approached from below. The lowering of intensity corresponds to the decrease of the real part of the scattering factor of the counter ions.

of scattering vector (q) in the neighbourhood of the Rb K-edge. The differential intensity scales with the known variation of the real part of the scattering amplitude (*f'*) of the counter ions [2]. From the systematic energy dependence, the measured SAXS intensities can be decomposed into three terms: (i) the non-resonant term which corresponds to the conventional SAXS intensity removed from the absorption edge (F_0^2), (ii) a cross-term involving the product of non-resonant and resonant scattering amplitudes (F_0 v), and (iii) the resonant part of the scattered intensity arising solely by the counter ions (v^2). Note that the intensity is given by the complex product of the scattering amplitudes. The key outcome of this work is that owing to high q and energy resolution, it became possible to deduce the smallest term – the resonant term due to the counter ions. **Figure 77** summarises the main results and shows the relative magnitudes of the F_0^2 and v^2 terms. The spatial correlation of the counter ions is directly given by the Fourier transform of v. The inset depicts the electron density profiles obtained from the decomposed scattered intensities and directly demonstrates that fine details of the spatial distribution of counterions can be obtained by the high resolution anomalous SAXS. In the polyelectrolyte brush system, the counterions are strongly correlated to the macroion. The method presented here has great potential for the analysis of charged soft matter systems.

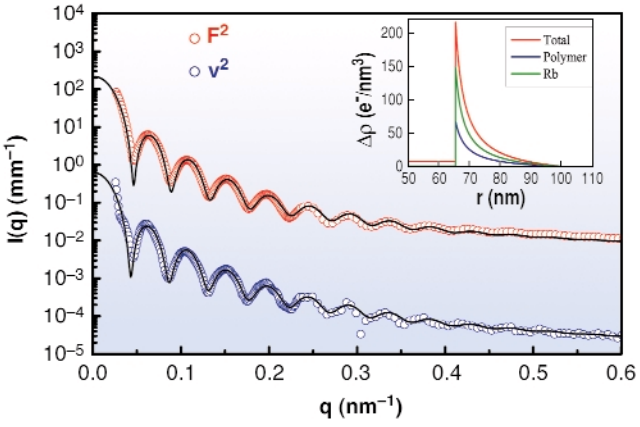

Fig. 77: Decomposition of SAXS intensity into non-resonant (F_0^2) and resonant (v^2) terms. From the individual scattering amplitudes, the corresponding radial electron density profiles (inset) can be obtained.

References

[1] A. Jusufi, C.N. Likos, and H. Loewen, *Phys. Rev. Lett.*, **88**, 018301-1 (2002).

[2] N. Dingenouts, R. Merkle, X. Guo, T. Narayanan, G. Goerigk, and M. Ballauff, *J. Appl. Cryst.*, **36**, 578 (2003).

Authors

N. Dingenouts (a), M. Ballauff (a,b), D. Pontoni (a,c), and T. Narayanan (c).

(a) Universität Karlsruhe (Germany)

(b) Universität Bayreuth (Germany)

(c) ESRF

Deformation Studies of Single PBO Fibres

Poly(*p*-phenylene benzobisoxazole) or PBO fibres are so called 'high-performance' polymer fibres which are amongst a group of materials known as 'rigid-rods'. Their molecular backbone repeat unit has a rigid structure (**Figure 78**) which contributes towards the fibres' remarkably high mechanical properties, typically more than double those of other high performance fibres such as poly(*p*-phenylene terephthalamide) or PPTA (Kevlar®) [1].

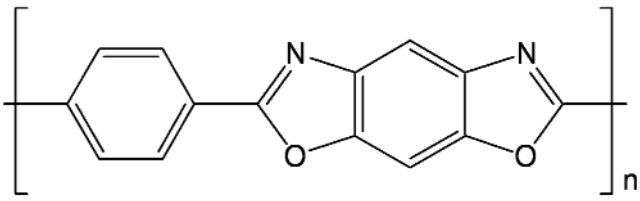

Fig. 78: Chain repeat unit of PBO.

Three varieties of PBO fibre were examined within this study, AS, HM and HM+. All three were manufactured by Toyobo (Japan), using a dry-jet wet-spinning process [2]. The AS fibre was provided literally 'as-spun'. The HM and HM+ fibre types were given a heat-treatment process to increase their fibre modulus. This involved the application of tension at high temperature. To further increase the modulus of the HM+ variety, a modified coagulated process was used [2]. The resulting fibre modulus values were 180 GPa, 254 GPa and 330 GPa for PBO AS, HM and HM+ respectively [1].

It is clear from the modulus variations between fibre types that processing parameters are important in determining final mechanical properties. The aim of this experiment was therefore to investigate this influence of the microscopic structure upon the macroscopic mechanical properties. It is well established that crystallite orientation is one of the most critical factors in this relationship. Microdiffraction can readily provide such information and may additionally be used to probe inhomogeneities such as 'skin-core' structural differences in single fibres.

Microdiffraction was carried out on beamline **ID13**. A scanning set-up was used with a beam spot-size of 3 µm. The fibres were mounted within a deformation device and deformed *in situ*. At predetermined load levels, diffraction patterns were generated across the fibres at 2 µm intervals. This is shown in **Figure 79** where diffraction patterns generated across a single fibre are superimposed on a scanning electron micrograph (scaled for spot-size and position, the vertical offset being for clarity only). Thus, differences in structure between the fibre 'skin' and 'core' may be investigated.

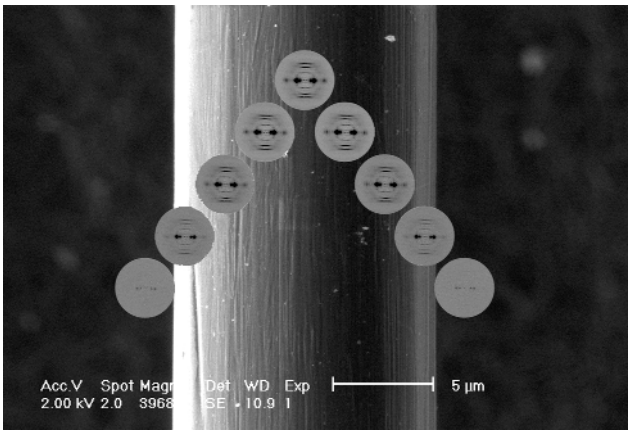

Fig. 79: Across-fibre diffraction patterns imposed over a SEM micrograph of a single PBO AS fibre (diffraction patterns scaled for beam-size and position).

Crystallite orientation was calculated from azimuthal broadening of the (200) equatorial reflection. The $\langle \sin^2\theta \rangle$ orientation parameter was used, ranging from $\langle \sin^2\theta \rangle = 0.667$ for an un-oriented structure and $\langle \sin^2\theta \rangle = 0$ for perfect crystallite orientation.

Figure 80a shows the change in orientation parameter across a single fibre (in this case PBO AS) with respect to stress. Initially (prior to loading), the fibre 'core' has a lower degree of crystallite orientation than the 'skin'. This can be attributed to shear forces generated during the spinning process. This 'skin-core' structural difference was only found in the AS fibre type indicating that heat-treatment increases fibre structure homogeneity. Additionally, the degree of crystallite orientation increases with increasing stress at all positions across the fibre.

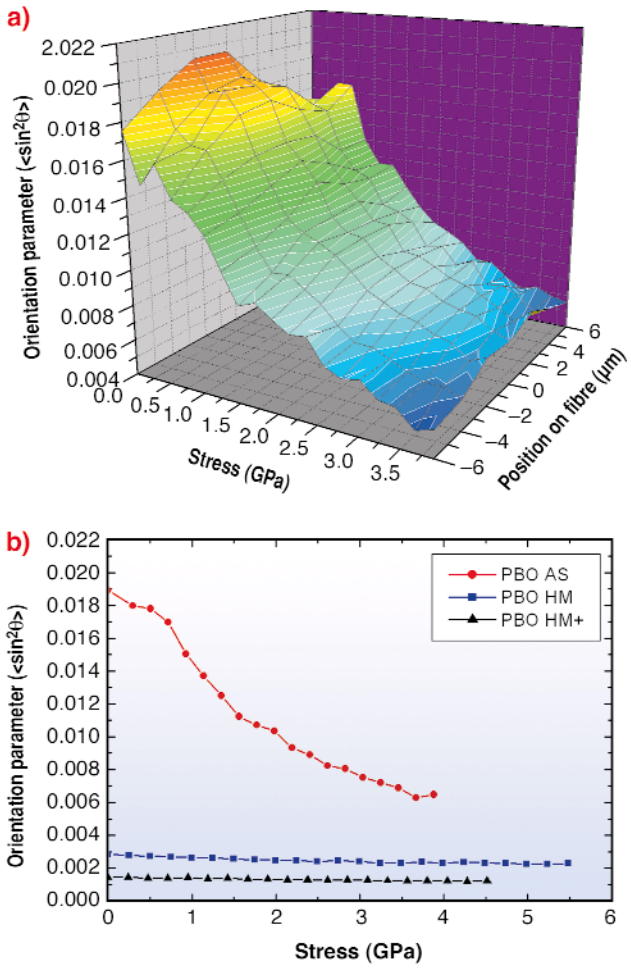

Fig. 80: (a) Changes in crystallite orientation parameter across a single PBO AS fibre with applied stress and (b) weighted-average crystallite orientation with applied stress for PBO AS, HM and HM+.

Figure 80b shows differences in the weighted-average orientation parameter with stress for all fibre types. The PBO AS fibre has the lowest degree of crystallite orientation and the greatest increase in orientation with applied stress. Both the HM and HM+ fibre types show a significantly higher degree of orientation and less change in orientation with stress. It is clear that both the degree of crystallite orientation and orientation change with stress is in the same fibre order as tensile modulus.

In conclusion, the microbeam scanning setup at ID13 offers an ideal means of investigating structural differences in single fibres. The addition of an *in situ* deformation device enables simultaneous generation of tensile and crystallographic structural information. The results presented here demonstrate that crystallite orientation is one of the most important structural factors in determining fibre tensile modulus. This can be attributed to the fact that increasing crystallite orientation increases the influence of direct chain stretching during deformation.

References

[1] R.J. Davies, M.A. Montes-Morán, C. Riekel and R.J. Young, *J. Mater. Sci.* **36**, 3079 (2001).

[2] T. Kitagawa, M. Ishitobi and K. Yabuki, *J. Polym. Sci.; Polym. Phys. Ed.* **38**, 1605 (2000).

Principal Publication and Authors
R.J. Davies (a), M.A. Montes-Morán (a), C. Riekel (b), R.J. Young (a), *J. Mater. Sci.* **38**, 2105 (2003).
(a) UMIST/University of Manchester (UK)
(b) ESRF

A Novel Method to Investigate Gradient Multilayers on Multiple Length Scales

Nanometre-sized noble metal clusters are of great technological and scientific importance being widely used in biomedical analysis, *e.g.* DNA sequencing [1], due their special optical properties being distinctly different from bulk material. This results from plasmon resonances occurring as a consequence of the confinement of the free electron gas inside the nanometric noble metal cluster. Due to the electromagnetic dipole interaction even a single molecule in the close vicinity of a cluster can be detected and characterised using optical spectroscopy.

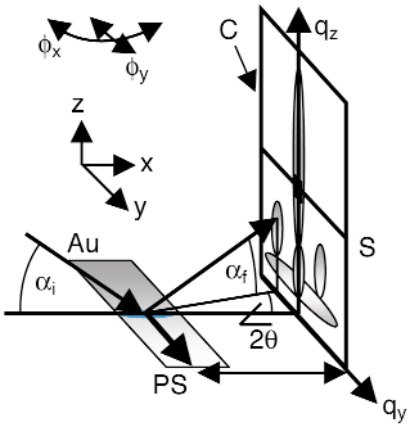

Fig. 81: Geometry of the microbeam grazing-incidence small-angle X-ray scattering (μGISAXS) experiment at ID13. The monochromatic beam (λ = 0.9755Å^{-1}) impinges on the gradient sample at an angle of α_i = 0.975°. The beam is specularly (S) and off-specularly ($\alpha_f \neq 0$ or $\theta \neq 0$) scattered from the sample, which is mounted on a xyz-translation stage and a two-dimensional goniometer (ϕ_x, ϕ_y). The gradient in the gold nano-cluster layer is along y and indicated as a color gradient. The data are recorded with a two-dimensional detector (C). The reciprocal space coordinate system is indicated (q_y,q_z).

The optical properties of the cluster layer strongly depend on their three-dimensional shape and in-plane arrangement. Typical systems consist of a layer of

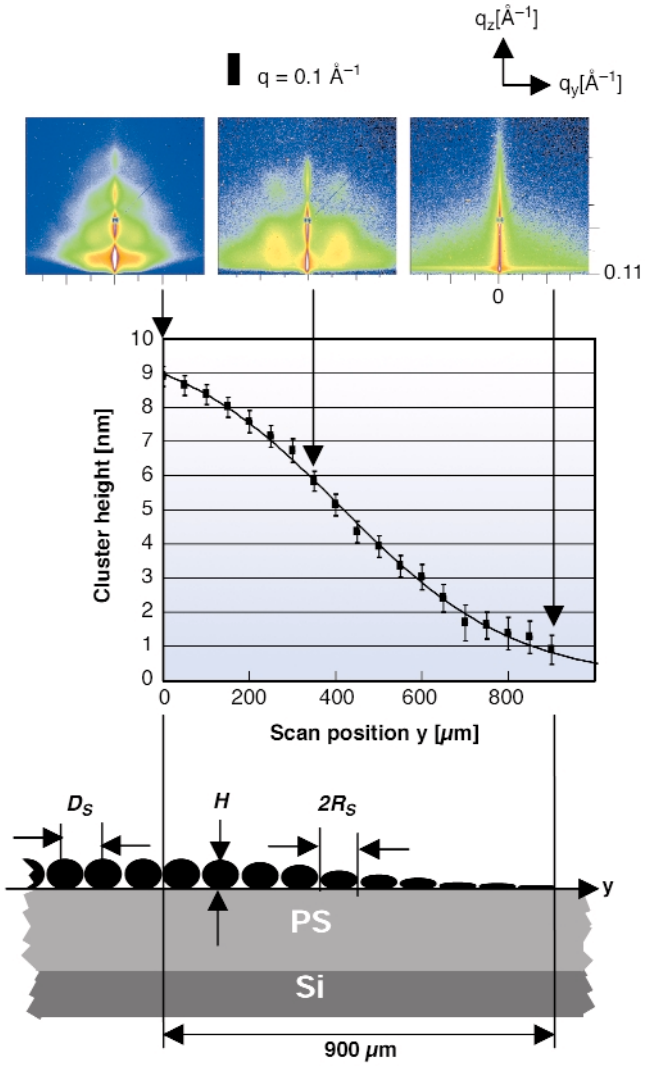

Fig. 82: Upper part: μGISAXS patterns recorded at y = 0, 350, 900 μm respectively. Middle part: Change in gold cluster height as a function of the scan position y. The solid line shows a fit of the experimentally-determined cluster height using a hyperbolic tangent function. Lower part: Schematic side view of the gold cluster arrangement along the gradient. D_S denotes their in-plane distance, $2R_S$ their in-plane diameter. The polystyrene (PS) film has a nominal thickness of 40 nm. The substrate is Si. The gradient extends over 900 μm.

nanometre-sized noble metal clusters on top of a polymer film. Especially for property optimisation, it is necessary to vary the structure and morphology of the cluster layer and to produce laterally-heterogeneous multilayer systems. Hence, we investigated the morphology and structure of a lateral gradient layer of nanometre-sized gold clusters on top of a polystyrene (PS) layer on a Si mirror substrate.

Our novel approach is based on a combination of grazing-incidence small-angle X-ray scattering (GISAXS) with a microbeam available at beamline **ID13** (giving rise to the μGISAXS method [2]). Here, a 5 μm monochromatic X-ray beam impinges under a low angle onto the sample surface (**Figure 81**). In this way, we were

able to spatially resolve the morphology of the nanometre-sized gold cluster layer along the gradient on a micrometre scale .

In **Figure 82** we present typical μGISAXS patterns. The gradient was scanned with a step size of 50 μm. The μGISAXS patterns clearly change along the gradient. Analysing the full two-dimensional pattern yields the arrangement and the three-dimensional shape of the gold clusters. To do so we simulated the μGISAXS pattern (program IsGISAXS by R. Lazzari) for each scan point y using a detailed model assumption for the gold cluster layer and including the Si-substrate and the PS-layer. **Figure 83** shows a typical example. From the position of the side maxima one can deduce the in-plane radius and distance of the gold clusters. It turned out that these two parameters stay constant along the gradient (R_S = (10.6 ± 5.3) nm, D_S = (14 ± 10) nm). Assuming an ellipsoidal model for the cluster shape, their height can be deduced from the position of the minima at each scan point y. The middle inset in **Figure 82** shows the cluster height as a function of y. It follows a hyperbolic tangent profile.

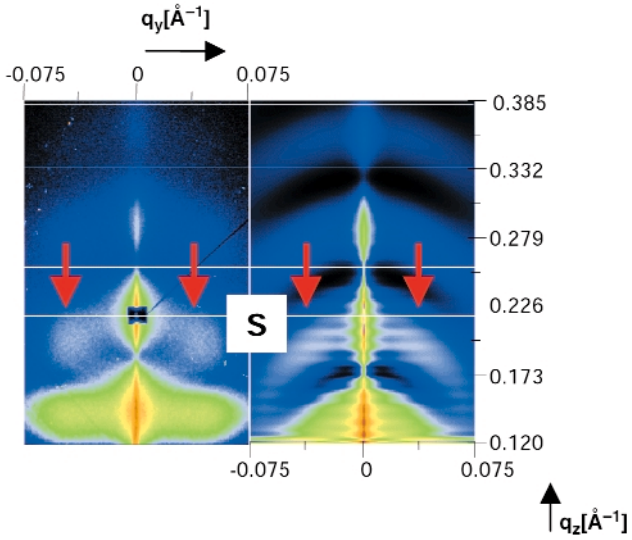

Fig. 83: Comparison of data (left) and simulation (right). The data show two principal features: minima along q_z and side maxima at finite q_y and q_z. The minima (white lines) indicate the cluster height, while from the side maxima (red arrows) the in-plane radius R_S and the in-plane distance D_S can be derived. The best fit is obtained using an ellipsoidal model for the gold clusters, where only their aspect ratio changes as a function of y.

To conclude, μGISAXS was shown to be a powerful non-destructive method to scan and thus to reconstruct the structure and morphology of laterally inhomogeneous multilayer systems on a micrometre scale. The gradient of ellipsoidal nanometre-sized gold clusters on PS/Si is characterised by one single parameter: the cluster height. Hence their aspect ratio changes along the gradient. We plan to extend the beam size to the sub-micrometre range in the near future.

References

[1] B. Dubertret, M. Calame and A. J. Libchaber, *Nature Biotech.* **19**, 365 (2001).

[2] P. Müller-Buschbaum, S.V. Roth, M. Burghammer, A. Diethert, P. Panagiotou, C. Riekel, *Europhys.Lett.* **61**, 639 (2003).

Principal Publication and Authors

S.V. Roth (a), M. Burghammer (a), C. Riekel (a), P. Müller-Buschbaum (b), A. Diethert (b), P. Panagiotou (b), H. Walter (c), *Appl. Phys. Lett.* **82**, 1935 (2003).

(a) ESRF

(b) Technische Universität München, Garching (Germany)

(c) November AG, Erlangen (Germany)

What Roughness is Produced by Organic Rain?

Deposition of any kind of material on a smooth surface generates roughness, *i.e.* the height of the individual points on the surface deviates from the mean height. The phenomenon of surface roughening is a key element in thin-film formation and knowledge about the evolution of the roughness σ as a function of film thickness D is crucial for many nanoscale applications. A lot of theoretical effort has been spent to predict the roughness evolution for various kinds of growth scenarios and materials. The theory of self-affine surfaces is based on the scaling behaviour of $\sigma(L,D)$: σ scales as a function of the lateral probed length scale, L, as $\sigma \propto L^{\alpha}$ for $L << \xi$ and as a function of D as $\sigma \propto D^{\beta}$ for $L >> \xi$. The lateral correlation length ξ scales as $\xi \propto D^{1/z}$. In this theoretical framework each film growth mechanism can be related to a distinct set of scaling exponents α, β and $1/z$ which may be determined by AFM and/or X-ray scattering [1, 2].

Thin films of organic semiconducting molecules are of increasing research interest due to their promising applications in electronic devices. However, the growth of organic thin films may differ considerably from the growth of inorganic or metal films. This is to be expected because of the different substrate-film interaction, and also because organic molecules are usually not spherical and may have large extensions compared to the individual atoms used in metal or inorganic film growth.

We have investigated the roughening dynamics for thin films of a specific organic molecule, diindenoperylene (DIP), grown under ultra-high vacuum conditions (**Figure 84b-d**). It was shown previously that these films exhibit excellent crystalline order normal to the surface with the molecules standing essentially upright with a tilt-angle φ presumably around 15°-20°, see **Figure 84a** [3].

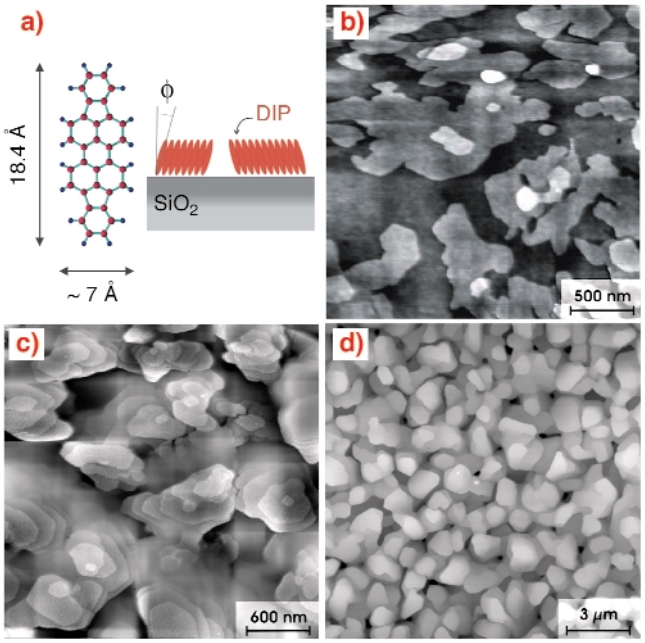

Fig. 84: (a) The molecule DIP ($C_{32}H_{16}$) and a sketch illustrating the formation of tilt-domains; NC-AFM images for films with various thickness: (b) D = 126 Å, (c) D = 1100 Å, (d) D = 9000 Å. An analysis of the AFM images reveals a = 0.628 ± 0.05.

Remarkably, an unusually large growth exponent β = 0.748 ± 0.05 of the DIP film (see **Figure 85**) was found in X-ray experiments at beamline ID10B. This is beyond the well-known kinetic limit for randomly deposited material $\sigma \propto D^{1/2}$. Also, $1/z = 0.92 \pm 0.20$ is unusually large. At present, the only model which consistently explains the rapid roughening related to the observed scaling exponents involves random spatial inhomogeneities in the local growth rate, which are fixed during the growth process.

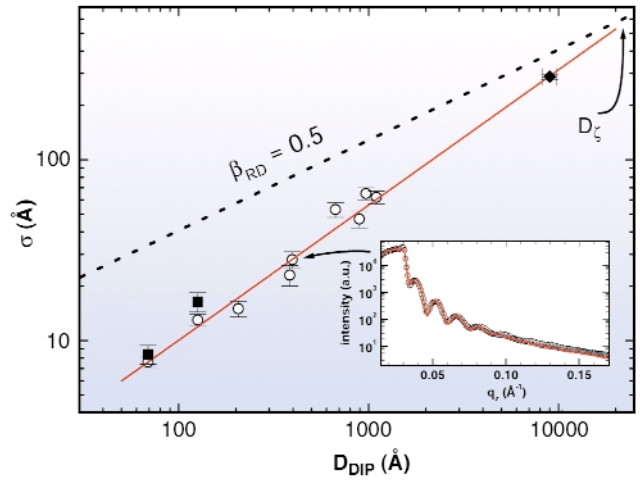

Fig. 85: Log-log plot of σ vs. D and a linear fit to the data which gives α = 0.748 ± 0.05. For D ≤ 1100 Å, X-ray-reflectivity was used to determine σ (O), see inset as a typical example for a sample with D = 396 Å. For some samples the saturation roughness σ has been determined (also) by AFM-measurements (■ = OMICRON AFM, ◆ = DI AFM). The black dotted line with slope σ_{RD} = 0.5 corresponds to the random deposition limit σ_{RD}, which would be reached at D = D_ζ .

We attribute these spatial inhomogeneities to the tilt-domains of the film (**Figure 84a**). The latter form as a consequence of the shape anisotropy of the individual molecules in combination with the crystalline structure of the thin film (upright standing molecules). We hope that our study will spark interest in detailed investigations into the microscopic origin of rapid roughening in organic thin films to arrive at a more thorough understanding – and control – of the growth mechanisms for this new class of materials.

References

[1] A.-L. Barabási and H.E. Stanley, *Fractal Concepts in Surface Growth* (Cambridge University Press, 1995).
[2] J. Krug, *Adv. Phys.* **46**, 139 (1997).
[3] A.C. Dürr, F. Schreiber, M. Münch, N. Karl, B. Krause, V. Kruppa, and H. Dosch, *Appl. Phys. Lett.* **81**, *2276 (2002)*.

Principal Publication and Authors

A.C. Dürr (a,b), F. Schreiber (a,b), K.A. Ritley (a), V. Kruppa (a), J. Krug (c), H. Dosch (a,b), and B. Struth (d), *Phys. Rev. Lett.* **90**, 016104 (2003).
(a) Max-Planck-Institut für Metallforschung, Stuttgart (Germany)
(b) Universität Stuttgart (Germany)
(c) Universität Essen (Germany)
(d) ESRF

Two-stage Freezing of a Single Top Layer in a Smectic Membrane

Melting in two dimensions (2D) remains one of the unresolved and challenging problems in condensed matter physics. In the defect-mediated theory, the first melting step of a 2D crystal is the dissociation of dislocation pairs. This produces an anisotropic (hexatic) liquid characterised by quasi-long-range bond-orientational order while the positional order is limited to a finite correlation length. Only after a subsequent step of disclination unbinding, an isotropic phase is realised [1]. Among the systems with hexatic ordering, smectic liquid crystals are particular suitable for investigations as they can be suspended as membranes of controlled thickness over an opening in a solid frame [2].

Smectic-A (Sm-A) membranes consist of stacks of liquid layers. Upon cooling, a hexatic Sm-B phase may occur, and subsequently a 3D crystalline-B phase (Cr-B) with a hexagonal in-plane lattice and a weak coupling between the crystalline layers. We studied smectic membranes of the compound abbreviated as 4O.8, in which the Sm-A phase proceeds into Cr-B in a layer-by-layer fashion

involving an intermediate hexatic Sm-B phase. With decreasing temperature the surface layers undergo transitions: from Sm-A to Sm-B at 61.1°C; from Sm-B to Cr-B at 54.5°C, well before the second set of layers start their own freezing transitions at 51.1°C. Hence, the top layer at each side of the membrane may serve as a perfect model system to study crystallisation of a liquid in 2D.

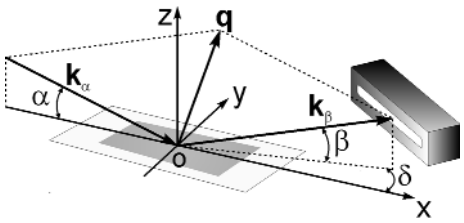

Fig. 86: Scattering geometry with smectic membrane and linear detector.

Grazing-incidence X-ray diffraction has been performed on 4O.8 membranes at beamline **ID10B**. The beam was focussed in the incident plane to about 24 µm and the incident and the exit angles were symmetrically set slightly above the critical angle. A linear detector was mounted parallel to the plane of the sample (**Figure 86**), catching in a single shot the lineshape associated with the in-plane positional ordering. **Figure 87a** shows for a seven-layer film the X-ray peak at q_0 = 14.3 nm^{-1}, corresponding to local in-plane hexagonal packing. It consists of a relatively narrow diffraction peak from the outermost hexatic Sm-B layers (fitted by a square-root Lorentzian) on top of a broad Lorentzian liquid peak from the five Sm-A interior layers. The integrated intensity of the former part is independent of the membrane thickness, which proves its origin in the two surface layers. The latter peak scales linearly with the number of liquid interior layers and its Lorentzian width $\xi \approx 1$ nm is independent of temperature (**Figure 87b**). With decreasing temperature the positional correlation length ξ of the hexatic top layers increases continuously from about 2.5 nm to more than 40 nm and then saturates. Clearly a pre-transitional growth of ξ is present above the hexatic-isotropic transition at 61.5°C. As we did not observe any thermal hysteresis in the hexatic linewidth, this surface transition is second order. Upon further cooling of the 4O.8 membrane, another transition occurs in the top layers at 55.5°C: the hexatic peak condenses into a sharp, resolution-limited peak from the Cr-B phase. This hexatic-crystal transition is weakly first-order with an abrupt change of the in-plane positional correlations.

In conclusion the two-step surface freezing of a single top layer in smectic membranes as seen by grazing-incidence X-ray diffraction agrees qualitatively with defect-mediated theory. However, other measurements do not give singularities as predicted. Hence the 2D melting scenario is probably not universal and the results may depend on the specific interactions in the system.

References

[1] P.M. Chaikin and T.C. Lubensky, *Principles of condensed matter physics* (Cambridge University Press, Cambridge, 1995).

[2] W.H. de Jeu, B.I. Ostrovskii and A.N. Shalaginov, *Rev. Mod. Phys.* **75**, 181 (2003).

Principal Publication and Authors

W.H. de Jeu (a), A. Fera (a), O. Konovalov (b) and B.I. Ostrovskii (a, c), *Phys. Rev. E* **67**, 020701 (2003).

(a) FOM-Institute for Atomic and Molecular Physics, Amsterdam (The Netherlands)

(b) ESRF

(c) Institute of Crystallography, Moscow (Russia)

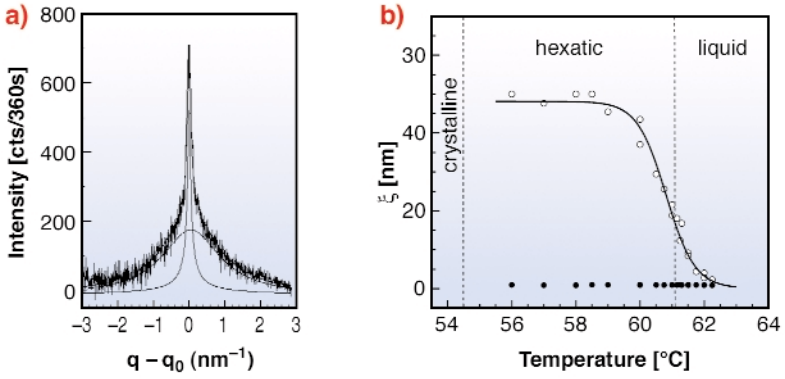

Fig. 87: (a) X-ray profile for a seven-layer membrane at 60°C with outer hexatic surface layers on a 'substrate' of five liquid inner layers. (b) Temperature dependence of the in-plane positional correlation length of the single hexatic surface layers (open circles) and the interior liquid layers (filled circles).

Thermal Fluctuations and Elasticity of Lipid Membranes

Lipid membranes are important model systems for biological membranes. They are intensively studied with regard to their structure, self assembly properties, phase behaviour, transport and elasticity properties, as well as their interaction with other macromolecules. From a statistical mechanics point of view they represent an interesting class of fluctuating quasi two-dimensional objects. Apart from k_BT, the thermal fluctuations are governed only by an intrinsic bending rigidity κ. The effect of the thermal fluctuations on the positional correlations and the scattering intensity distribution has been worked out in the framework of linear elasticity theory (Caillé model) for stacks with periodic boundary conditions, as a function of κ and the compressional modulus B (given by the second derivative of the interaction potential between two membranes at their equilibrium distance d). Recently, the model has been extended to include the boundary condition of a flat substrate on which a stack of lipids can be deposited [1].

The present experiment on thermal fluctuations has been carried out on samples with several hundreds of highly-oriented lipid membranes deposited on silicon surfaces and studied at full hydration under excess water, both in the gel and the fluid $L\alpha$-phase. The main aim was to map the diffuse scattering over a wide range of momentum transfer, see **Figure 88a**, both in radial q_r (parallel to the plane of the membrane) and q_z. Diffuse X-ray reflectivity measurements using 20 keV synchrotron beams have been carried out at the undulator beamline **ID01**, using both a fast scintillation counter and a multwire area detector. Data was collected mainly on the uncharged lipids dimyristoyl-sn-Glycero-Phosphocholine (DMPC) and oleoyl-Palmitoyl-sn-Glycero-Phos-phocholine (POPC), and also on charged phospholipids [2]. For data acquisition, angles of incidence were chosen that do not excite specular Bragg peaks. The typical intensity distribution on the CCD detector then consists of only a weak specular beam and two to four strong equidistant diffuse Bragg sheets. From the q_z value, the mean distance d can be obtained, *i.e.* for fully-hydrated DMPC membranes $d \approx 63$ Å, corresponding to a water layer of about 25 Å in between adjacent membranes. Importantly, the width (HWHM) of the diffuse Bragg sheets along q_z increases quadratically with q_r, before it saturates to at high q_r, see **Figure 88c** for a typical data set. The quadratic increase (solid line) is in line with the theoretical prediction and its steepness is given by the fundamental smectic length $\lambda = (\kappa/Bd)^{0.5}$. From the analysis of the q_z-integrated intensity with q_r the height-height correlation

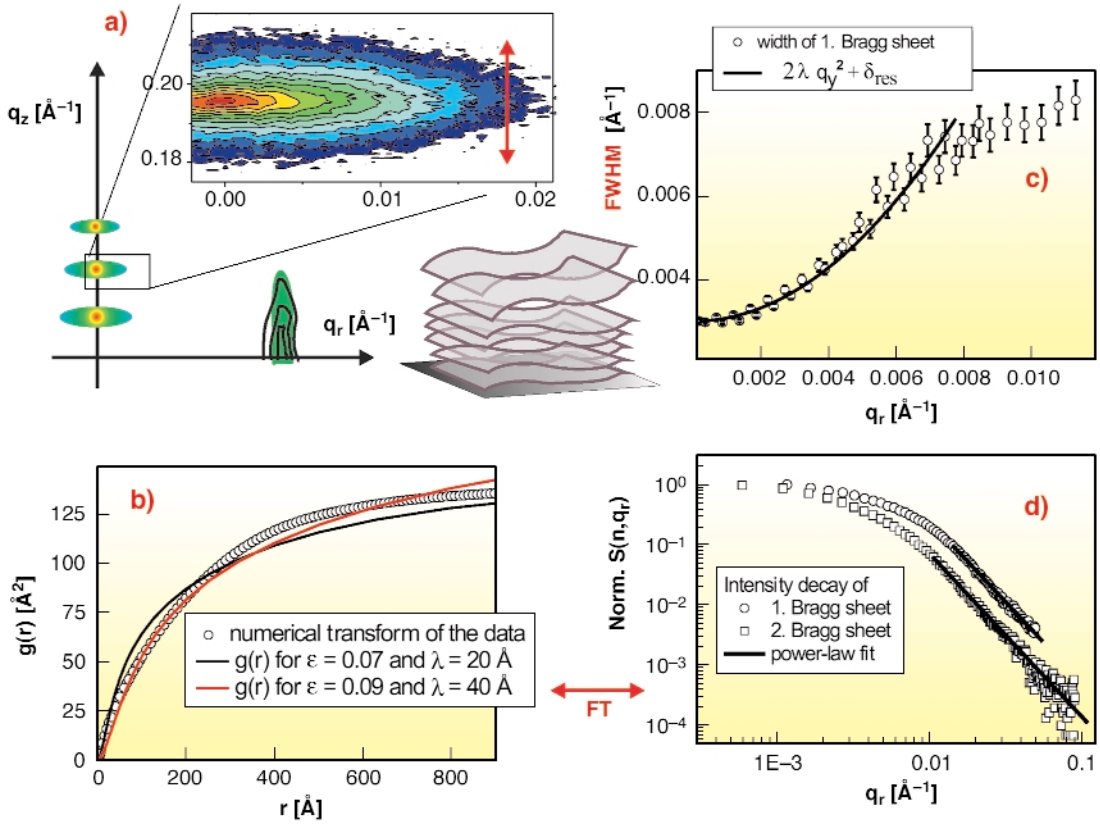

Fig. 88: (a) Typical diffuse scattering distribution of multilamellar lipid bilayers (DMPC, fluid phase). (b) Characteristic height-height self-correlation function of an averaged membrane in the stack as derived from the data, together with theoretic function acc. to [1]. (c) Increase in the width (vertical q_z-width) of the first Bragg sheet. (d) Decay of the (q_z-) integrated intensity of the the first two Bragg sheets n = 1 and n = 2.

function was calculated using a back transformation method. The resulting curve for DMPC in the fluid phase is shown in **Figure 88c** along with theoretic curves (solid lines) [1]. The parameters κ and B can be chosen to fit the curves at small, intermediate or large r, but should be regarded as effective parameters, which can vary significantly since the model cannot account for all data simultaneously. Note that this conclusion is currently a matter of debate [3].

Already on the level of the raw data, deviations from the predicted behavior is observed: (i) the power law exponent of the intensity decay shown in **Figure 88d**, and (ii) the saturation of the Bragg sheet width shown in **Figure 88b**. Both are observed at parallel wave vector components which where not accessible before (in unoriented bilayers or and at less brilliant sources). Therefore we must conclude that fluctuations on the corresponding length scales are not well described by the Caillé model. A number of reasons could limit the applicability of the model: (i) non-bending collective motions, (ii) non-linear elasticity terms, (iii) a length scale dependence of κ , (iv) breakdown of the mean field approach. Alternative more rigorous theories (renormalisation group theories, self-consistent theories) and computer simulations on reasonably large stacks of membranes and lateral system size may help to gain more understanding. On the experimental side, the studies of diffuse scattering are currently extended to cover also charged lipids and lipid/peptides mixtures.

References

[1] D. Constantin, U. Mennicke, C. Li, and T. Salditt, *EPJE* **12**, 283 (2003).
[2] G. Brotons, T. Salditt, M. Dubois, Th. Zemb, *Langmuir* **19**, 8235-8244 (2003).
[3] G. Pabst, comment on *PRL* **90**, 178101 (2003), *submitted*; T. Salditt, M. Vogel, W. Fenzl, Reply to comment by Pabst, *submitted*.

Principal Publication and Authors

T. Salditt (a), M. Vogel (b), W. Fenzl (b), *Physical Review Letters* 90, 178101 (2003).
(a) Universität Göttingen (Germany)
(b) Max-Planck-Institut für Kolloid- und Grenzflächenforschung Golm (Germany)

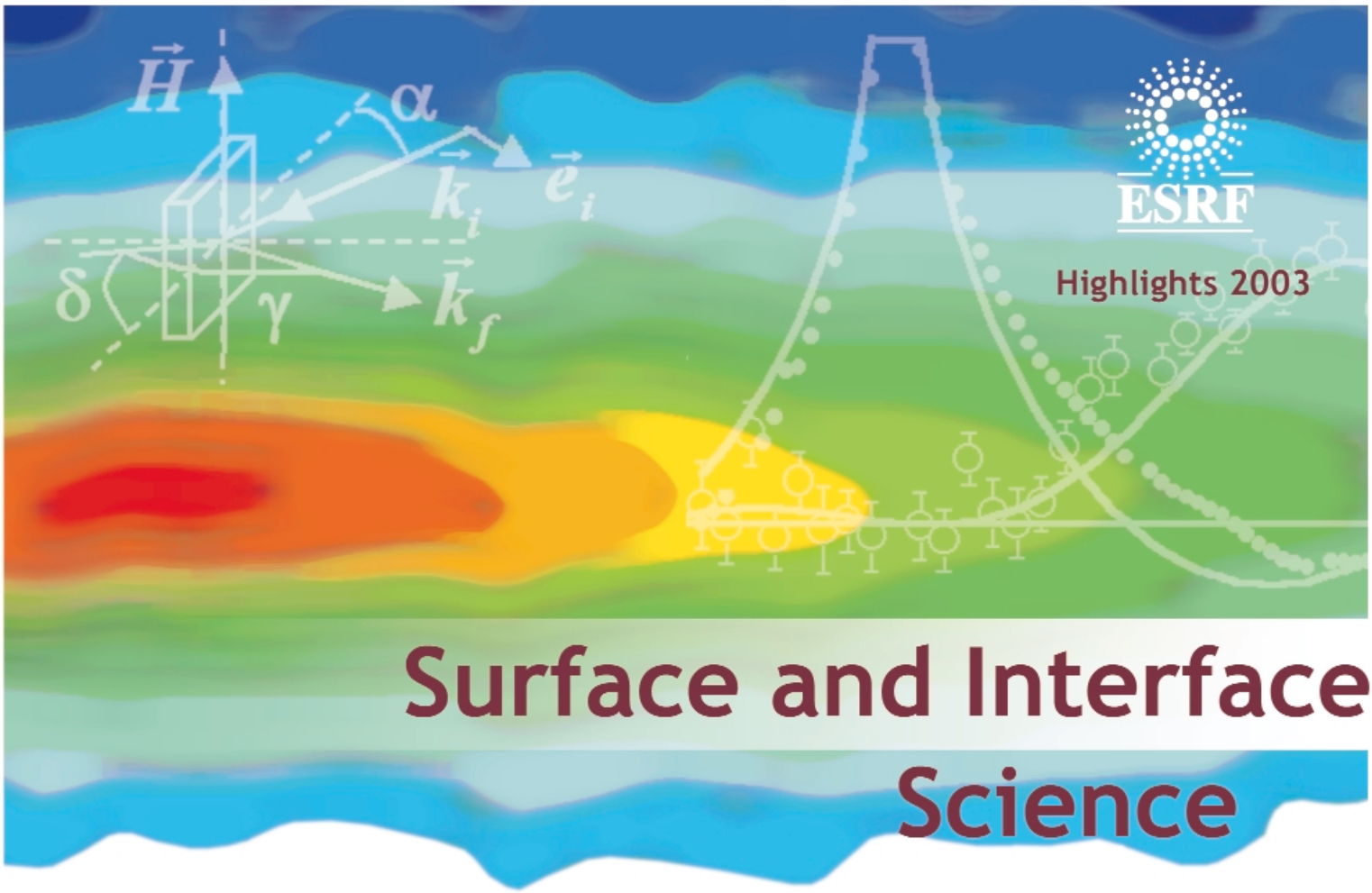

Introduction

Active research on the Surfaces and Interfaces Group beamlines has concentrated on many topics. In particular, strain, stress, growth and surface magnetism investigations high light the work performed in 2003

Intermixing and strain are two physical phenomena that play a major role in the electronic and optical properties of semiconductor nanostructures. A large research effort has been devoted to this topic over the last few years.

In what follows, the contribution of Schulli and collaborators show that by using grazing-incidence diffraction and anomalous scattering, the strain distribution and chemical composition of Ge dots deposited on Si substrates can be determined. The authors show that below the Ge islands there is a region of strained Si. Also, a detailed analysis reveals that the dots are mostly constituted of 80% of Ge and 20% of Si.

Similarly, Letoublon *et al.* investigated elongated islands of InAs (called “quantum sticks”) embedded in InP using the same methods. The authors determined the strain within the islands (6%) and demonstrated some intermixing.

In metallic systems strain and stress is important in the context of surface magneto-elasticity. The contribution by Meyerheim *et al.* on Ni/W110 shows that the W substrate experiences an important re-arrangement induced by the deposited Ni atoms. The reconstruction of the W substrate is correlated with a giant compressive stress measured by optical methods.

The study of the fundamental aspects of film growth is another topic of the forthcoming contributions. The report by Fruchart *et al.* illustrates the use of the small angle scattering technique during the growth of Co islands on a reconstructed Au(111) substrate: this method allows the study of the islands growth and percolation. This information is relevant for the magnetic properties of such nanoislands. In a similar frame of ideas, Robach *et al.* investigated the growth of Ni on Pt(111) and of Pt on Ni(111). It turns out that in a Ni/Pt/Ni/Pt multilayer, the consecutive Ni layers are arranged in a unusual hcp stacking sequence which is believed to be the origin of the peculiar magnetic properties of these multilayers.

Unusual growth is also observed in an electrochemical system by Renner *et al.* who investigate the electrochemical corrosion of Cu_3Au crystals. They observe the formation of a strained layer which grows with reverse packing sequence than that of the crystalline substrate. This acts as a protective layer against corrosion.

Finally, Torrelles *et al.* report on the determination of the structure of C60 adsorbed on the Ge(111) surface. It turns out that C60 accommodates onto the Ge substrate by making holes to sit on.

S. Ferrer

Direct Determination of Strain and Composition Profiles in SiGe Islands

Anomalous X-ray scattering at beamline **ID01** is employed for quantitative measurements of the Ge composition profile in islands on Si(001). Comparing the intensity ratios for X-ray energies below and close to the K edge of Ge at various Bragg reflections in the grazing-incidence diffraction setup, the sensitivity for the Ge profile is considerably enhanced at high momentum transfer. The method is demonstrated for SiGe dome-shaped islands grown on Si(001). It is found that the composition inside the island changes rather abruptly at the substrate interface whereas the lattice parameter relaxes continuously.

Ge islands on Si have been the subjects of numerous studies. Such islands show interesting morphological shape transitions as a function of growth parameters. From a series of studies, it is known that intermixing in such islands exists, but difficulties in the quantification of the composition profile along the growth direction remain. This profile, together with the strain distribution is of fundamental importance for the electronic band structure of embedded islands and thus for any application. Anomalous X-ray diffraction close to absorption edges can indeed be used to obtain the necessary chemical sensitivity for a direct determination of composition profiles in SiGe islands. In general, the energy and momentum dependency of the atomic scattering factor is expressed by $f(Q,E) = f_0(Q) + f'(E)+if''(E)$. With $f'(E)$ and $f''(E)$ being the energy-dependent correction that becomes important close to an absorption edge. f_0 equals the total number of electrons Z for forward scattering, but decreases for higher momentum transfer Q. Thus the anomalous scattering effects can be enhanced considerably by measuring Bragg reflections for high momentum transfers as shown in **Figure 89**, since $f'(E)$ and $f''(E)$ remain constant with Q. Evaluating the intensity ratio for the two energies E_1 and E_2 (inset in **Figure 89a**) at a given momentum transfer Q, one can link composition and lattice parameter without any model assumptions. To demonstrate the method, a SiGe island sample grown by molecular beam epitaxy on Si(001) has been investigated.

At a substrate temperature of 600°C, seven monolayers of Ge were deposited, leading to islands with a height of about 140 Å and a width at the base of about 700 Å. From the intensity ratios $I(E_1)/I(E_2)$ of the most sensitive reflections (620) and (800) the composition for a certain lattice parameter is directly extracted. A region with vanishing Ge-content exhibiting tensile strain with respect to the substrate is clearly visible. This can be attributed to the strained region in the Si-substrate

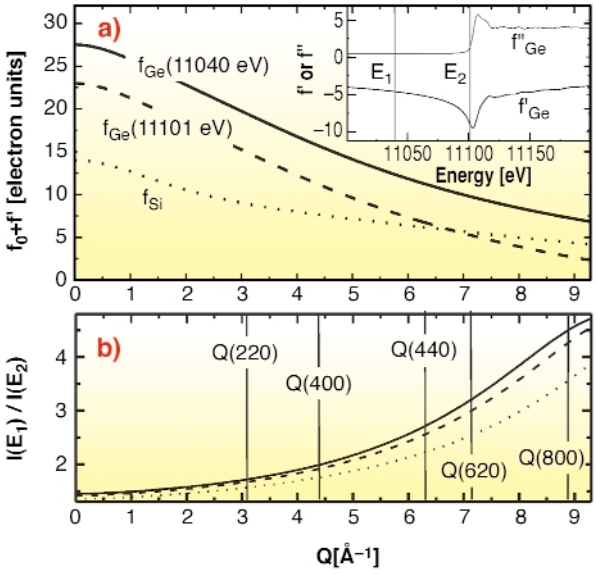

Fig. 89: (a) Momentum dependence of the scattering factors of Si (dotted line) and Ge for the two energies E1 and E2 (full and dashed line). Inset: anomalous corrections f' and f'' for Ge in the vicinity of the K-absorption edge. (b) Theoretical momentum dependence of the ratio of the diffracted intensities at E_1 = 11043 eV and E_2 = 11103 eV for pure Ge (solid line), $Si_{0.1}Ge_{0.9}$ (dashed line) and $Si_{0.3}Ge_{0.7}$ (dotted line).

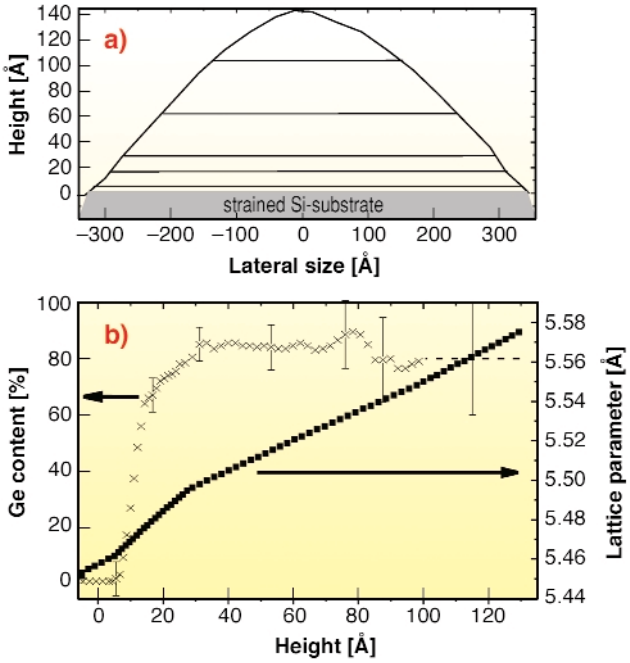

Fig. 90: (a) Cross-section profile of one dot extracted from the AFM data. The lateral size (solid straight lines) as determined from the angular scans can be attributed to a certain height. (b) The relaxation (black squares) Δa/a and the Ge-content (crosses) are plotted over the height z.

below the Ge-island. In a second step, we recorded line-scans perpendicular to the radial scan direction. These angular scans are sensitive to the lateral size of a region with fixed lattice parameter. Using the cross-section profile of the islands from atomic force microscopy, the

lateral size can be associated with a certain height within the islands (see horizontal lines in **Figure 90a**), linking the height with the in-plane momentum transfer Q. Combining all results we can finally reconstruct the Ge-concentration as a function of the height in the island. The result is shown in **Figure 90b**. The figure clearly shows a rather abrupt interface between Si and the SiGe-island, with an almost constant Ge content of roughly 80% above a height of 20 Å.

Principal Publication and Authors

T.U. Schülli (a,b), J. Stangl (a), Z. Zhong (a), R.T. Lechner (a), M. Sztucki (b), T.H. Metzger (b), G. Bauer (a), *Phys. Rev. Lett.* **90**, 066105 (2003).

(a) Johannes Kepler University Linz (Austria)

(b) ESRF

InAs Quantum Sticks: Determination of Strain, Size and Composition

The new generation of electronic and optoelectronic integrated circuits are nowadays based on semiconductor nanostructures. InAs quantum wires and quantum dots can be employed as active region materials of lasers and LEDs. To be suitable for devices, the nanostructures are encapsulated with InP or embedded in a superlattice. They must be homogeneous in size, shape and composition, to provide well-defined emission wavelengths. The knowledge of strain field, chemical gradients, chemical mixing at the interface, is therefore of a great importance.

We report on an X-ray study of InAs stick-like islands, quantum sticks, embedded in InP with a 10 nm thick cap layer. These samples are obtained by optimisation of the MBE growth parameters to minimise the As/P exchange and reduce the height dispersion of the InAs islands [1]. The strain of buried nanostructures is mainly related to their composition. It also depends on their size, morphology, and cap layer thickness. Tuning the X-ray energy near an absorption edge of atoms that belong to the nanostructures is a way to modify their scattering power and to enhance the chemical sensitivity of diffraction. We report on a general method that takes advantage of the full capability of anomalous diffraction and can be applied to the very interesting and challenging case of small size embedded nanostructures.

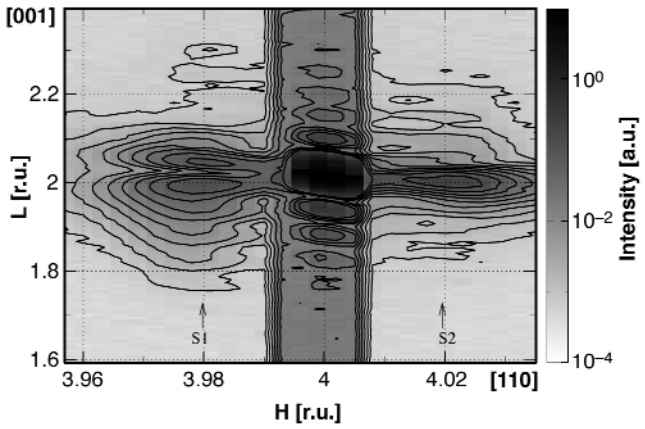

Fig. 91: Experimental diffraction map around the weak InP (442) reflection recorded at 11.840 keV in grazing-incidence geometry; S1 and S2 are correlation satellites due to the stick's short range periodicity along the [110] direction.

Grazing-incidence anomalous diffraction at the As K-edge (11.867 keV) was performed at the French Collaborative Research Group beamlines BM32 and BM2. **Figure 91** shows the diffraction intensity map in the vicinity of the (442) InP substrate reflection, recorded at 11.840 keV and at a grazing-incidence angle near to the critical angle. The spread of scattering in the [110] direction is due to both short range correlation and lattice strain in the real space. Whereas, in the [001] direction, this is due to the sharp strain evolution at the interface. We performed *l*-scans ($h = k = 3.98$) accross the satellite *S1*, at several energies close to the As *K*-edge. **Figure 92a** shows the experimental modulus of F_A, the As atoms partial structure factor, and F_T, the structure factor of all atoms (Thomson scattering). As deduced from the Full Width at Half Maximum (FWHM) of F_A, the quantum sticks height average value is about 2.54 nm. In order to determine the quantum sticks composition and the local strain accommodation, Grazing-incidence Diffraction Anomalous Fine Structure (DAFS) spectrum was measured at the maximum of F_A ($h = k = 3.98$ and $l = 1.9$) at the As *K*-edge. **Figure 92b** shows the experimental DAFS spectrum, that is perfectly reproduced with pure InAs quantum sticks.

Finite Difference Method (FDM) simulations were performed to map the strain produced by InAs quantum sticks embedded in InP and compare its Fourier transform to experimental diffraction intensity maps. **Figure 92a** shows the best calculated curves of F_A and F_T, obtained by optimising the height and width of the wires, as well as As/P intermixing at the InAs/InP interface. The FDM simulation reproduces well the relative positions of F_A and F_T, with a strain of about 6.1% with respect to InP substrate in the inner part of the wire. The experimental curves F_A and F_T are compatible with a weak As/P intermixing at the InP interface, that would spread over one monolayer.

In conclusion, we have shown that anomalous diffraction can be used to extract the structure factor of small size InAs nanostructures embedded in InP matrix. This study is a first step towards a 2D and 3D analysis of anomalous diffraction maps and grazing-incidence DAFS data to recover the strain, size, shape and composition of embedded nanostructures.

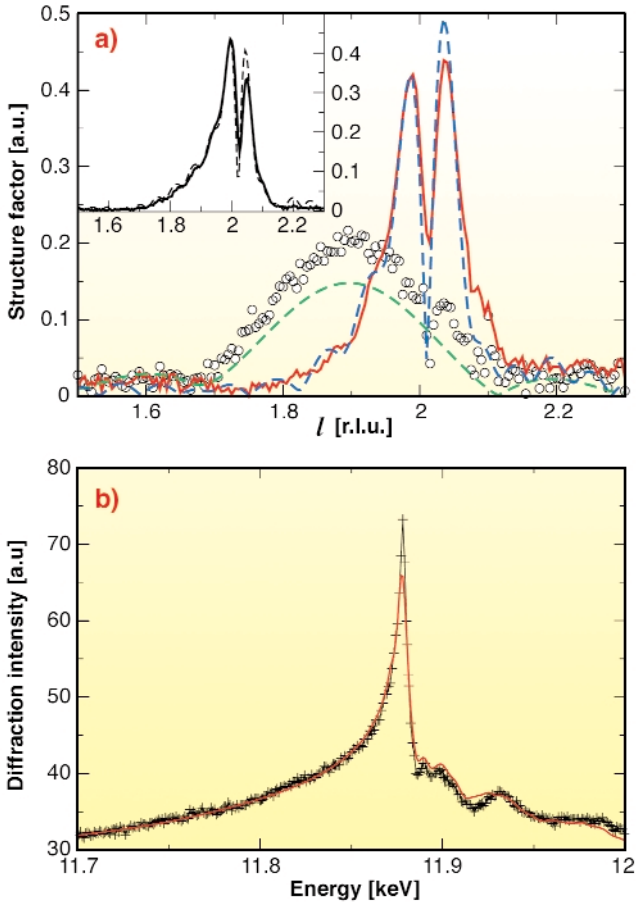

Fig. 92: (a) Experimental F_T (solid line) and F_A (ooo) modulus as a function of the reciprocal lattice unit *l* at h = k = 3.98 (across the satellite S1). F_A is the structure factor of all anomalous atoms, *i.e.* As atoms only. Also shown are best simulation curves (dashed line) obtained with a finite difference model made of pure InAs quantum sticks with a truncated triangle side profile. Inset shows the experimental (solid line) and simulated (dashed line) square root of the diffraction intensity at 11.867keV; at this energy, anomalous diffraction is maximised. (b) GIDAFS spectrum (+) recorded, at the As K-edge, at the maximum of the F_A profile (*l* = 1.9) and the best fit curve obtained with pure InAs structure (solid line).

References

[1] M. Gendry, C. Monat, J. Brault, P. Regreny, G. Hollinger, B. Salem, G. Guillot, T. Benyattou, T.C. Bru-Chevallier, G. Bremond, O. Marty. *J. Appl. Phys.* (2003).

Principal Publication and Authors

A. Letoublon (a), V. Favre-Nicolin (a), H. Renevier (a), M.G. Proietti (b), C. Monat (c), M. Gendry (c) O. Marty (d), C. Priester (e), *submitted to Phys. Rev. Lett.* (2003), cond-mat/0309522.

(a) CEA, Grenoble (France)
(b) CSIC-Universidad de Zaragoza (Spain)
(c) LEOM, UMR-CNRS 5512, Ecole Centrale de Lyon (France)
(d) LENAC, Université Lyon I (France)
(e) Institut d'Electronique, de Microélectronique et de Nanotechnologie, Villeneuve d'Ascq (France)

Correlating Structure and Magnetism in Thin-film Devices

Thin-film structures presenting perpendicular magnetic anisotropy (PMA) are widely studied for applications in high-density magnetic recording. PMA, with the film magnetisation pointing spontaneously along the perpendicular to the film, is an exceptional behaviour, as the shape of the thin film strongly favours magnetisation parallel to the film. Pt-Ni multilayers present PMA at room temperature [1-3], however PMA appears when the Pt layers are very thin (≈ 2 monoatomic layers (ML) thick). This is in contrast with Co-Pt multilayers where the Ni layers are very thin. PMA in Pt-Ni systems has been attributed to a bulk-like magnetoelastic effect in the Ni layers [3], but it is still unclear why very thin Pt layers are necessary.

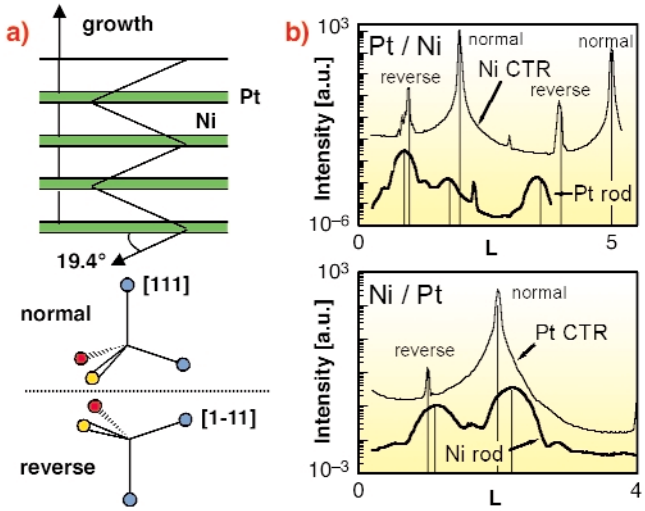

Fig. 93: (a) Schematics of the stacking sequence of the FCC (111) planes in a Pt-Ni multilayer. The [1-11] direction does a "zig-zag" when going from one layer to the next. This sequence gives a hexagonal symmetry to the multilayer, which, combined with the full magnetisation of very thin Pt layers, leads to perpendicular magnetic anisotropy. (b) Surface diffraction data showing the stacking conservation for Ni on Pt(111) and the stacking reversal for Pt on Ni (111). The comparison of the substrate and film diffraction rods enables are comparison of the stackings (ABC or ACB) of the substrate and the film, since the Bragg peaks for the two stacking appear at different L's on this rod.

Here we propose a new structural explanation for the PMA, that also explains the need for very thin Pt layers. This is the stacking reversal. The idea is that, upon growing Pt-Ni multilayers, Pt and Ni, which have a FCC structure, both grow with the [111] axis along the growth direction. They can *a priori* grow either with an ABCABC... stacking of the (111) planes, or a ACBACB... stacking. Usually, films tend to grow with the same

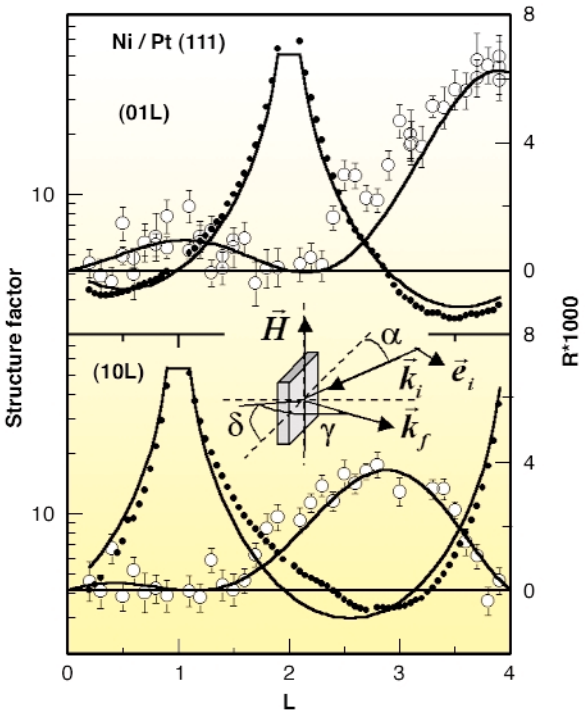

Fig. 94: Standard truncation rods of the Pt substrate (filled circles) and corresponding magnetic rods (open circles), for a 8 layer Ni film on Pt(111). The magnetic rods are obtained by measuring, at each L, the diffracted intensity for two directions of the applied magnetic field (pointing up, or pointing down), and forming the asymmetry ratio R(HKL)= (I↑-I↓)/(I↑+I↓). The atomic positions are first determined using the standard diffraction rods, then the atomic model is re-injected into the calculation of the magnetic rods, and from a fit we deduce the magnetic moments of the different Pt planes near the interface. The calculated magnetic rod (solid line) was obtained assuming that only the last Pt plane is magnetic, with a moment of 0.06 μB/atom at 300K.

stacking sequence as the substrate. We show that this is the case for Ni on Pt(111) (normal growth), but not for Pt on Ni(111), which grows with reversed stacking. As a consequence, Ni-Pt multilayers, will exhibit alternate packing sequences of the Ni layers as normal/reverse/normal/reverse… (**Figure 93a**).

Our study was performed on the **ID03** beamline, with only single interfaces, Pt films on a Ni(111) single crystal, and Ni films on a Pt(111) single crystal. We investigated the structure of the films with standard surface diffraction, and showed the stacking conservation for Ni on Pt, and the stacking reversal for Pt on Ni (**Figure 93b**). With resonant magnetic surface X-ray diffraction at the Pt L_{III} edge, we determined the profile of induced magnetic moment in the Pt near the interface (the "positions" of the magnetic moments). We showed that the Pt moment is concentrated in the Pt plane in contact with the Ni, for both a 8 ML Ni film on Pt (**Figure 94**) and a 4 ML Pt film on Ni.

We can explain how stacking reversal induces PMA with a symmetry argument: if one forgets about the Pt layers, and considers only the stacking of the Ni (111) planes, then the Ni-Pt multilayer is analogous to a thick Ni film with a hexagonal structure, with the c axis perpendicular to the layers. This is not HCP Ni but a hexagonal polytype with a period of two Ni layers. By analogy with the case of Co, whose HCP phase (easy axis along c) has a much larger magnetic anisotropy than the FCC phase (easy axes along <111>), this hexagonal Ni is expected to have a much larger magnetocrystalline anisotropy than FCC Ni, with an easy axis along c. This should favor PMA.

We think that very thin Pt layers are necessary for PMA because in order for the multilayer to act as a high magnetic anisotropy hexagonal material and not as quasi-isotropic "isolated" FCC Ni layers, the adjacent Ni layers need to exchange-coupled through the Pt layers. For this the Pt layers need to be fully magnetic. This is only true for Pt layers with a thickness of two atomic planes or less: we show that, at the Pt-Ni interface, the magnetisation of the Pt atoms is essentially concentrated in the Pt plane in contact with the Ni, the next Pt plane has a magnetisation at least three-times smaller.

References

[1] M. Angelakaris, P. Poulopoulos, N. Vouroutzis, M. Nyvlt, V. Prosser, S. Visnovsky, R. Krishnan, N.K. Flevaris, *J. Appl. Phys.* **82**, 5640 (1997).
[2] F. Wilhelm, *Ph.D. thesis*, dissertation.de, Berlin (2000).
[3] S.C. Shin, G. Srinivas, Y.S. Kim, M.G. Kim. *Appl. Phys. Lett.* **73**, 393 (1998).

Principal Publication and Authors

O. Robach (a), C. Quirós (a), H. Isérn (a), P. Steadman (a,b), K.F. Peters (a,c), S. Ferrer (a), *Phys. Rev.* **B 67** (2003) 220405(R).
(a) ESRF
(b) University of Leeds (UK)
(c) Hewlett Packard, Corvallis (USA)

Unusual Surface Reconstruction and Stress in Ni/W(110)

In studies of metal adsorption on the Mo-and W (110) surfaces it has been a common approach to neglect the question of whether there is a substrate relaxation or not. Furthermore, these surfaces are prototype examples for the study of the relation between geometric surface structure and surface mechanical stress. Using surface

X-ray diffraction (SXRD) we find a Ni-induced reconstruction of the W(110)-surface and directly correlate this to giant compressive stress measured simultaneously using optical laser beam deflection from the sample surface.

A 0.2 mm thick W(110) crystal was clamped at one end to allow free bending [1]. During Ni deposition, the crystal curvature and a SXRD intensity characteristic for the superstructure were measured simultaneously (**Figure 95a**). The emergence of the c-(1x7) superstructure [2] coincides with the formation of compressive stress at t > 220 equivalent to 0.8 ML Ni-coverage (**Figures 95b** and **95c**).

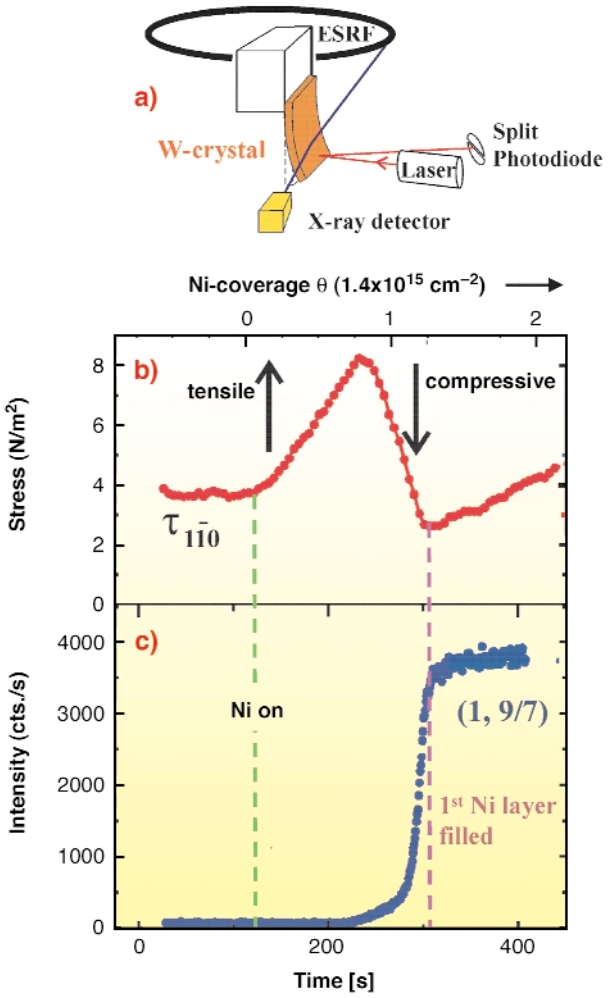

Fig. 95: Simultaneous measurement of stress and X-ray intensity. (a): experimental setup, (b): stress vs. Ni-coverage, (c): SXRD intensity vs. Ni-coverage.

After saturation of the c-(1x7)-reflection intensity (θ = 1.3 ML ≈ 310 s) the structure analysis using 144 reflections was carried out (structure model in **Figure 96a**). Both, Ni and W-atoms contribute to the reflections and give rise to an oscillatory intensity distribution along the rods (q_z). Only a slowly varying intensity would be derived considering one Ni layer only (**Figure 96b**). In **Figure 96a** several unit cells (one highlighted by the rectangle) are shown. Ni-and W-atoms are represented as green and blue balls, respectively. Ni-atoms form a distorted

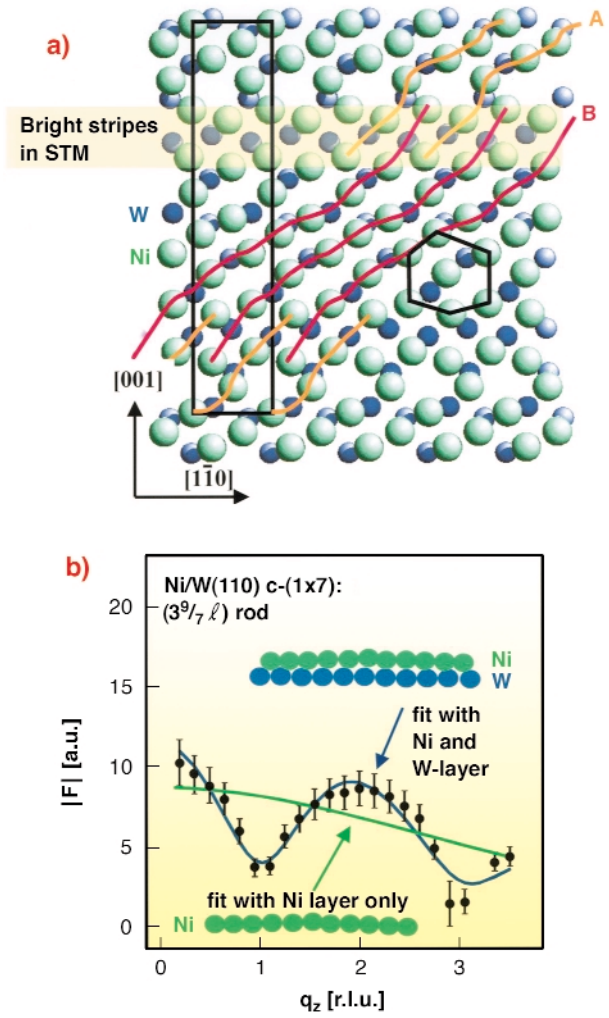

Fig. 96: Structure model for Ni/W(110) (a) and calculated super-lattice intensity along one rod for a one (Ni) and two (Ni/W) layer model (b). The data are shown as symbols.

hexagonal dense layer as indicated by the hexagon. The most important feature of the structure is the pronounced shift (up to 0.5 Å) of the first layer W-atoms out of their bulk positions along [1-10]. Ni-atoms are close to bridge sites forming 25 Å long alternating Ni-W-Ni chains (labeled as A and B). Where the chains overlap (see horizontal bright stripe) the Ni-atoms are located 0.3 Å above those in the rest of the unit cell explaining the contrast observed in STM [2].

In summary, our results elucidate the relation between compressive stress and the c-(1x7) structure in Ni/W(110) involving substantial substrate reconstructions. So far it has been assumed that the substrate surface is structurally "inert" in all studies of surface and in surface dynamics on the W-and Mo (110) surfaces. Thus, it appears tempting to state that, in general, unusual compressive stress of adsorbate-covered surface structures might indicate "unusual" surface structures not considered so far.

References

[1] D. Sander A. Enders and J. Kirschner, *Europhysics*

Lett. **45**, 208 (1999).
[2] D. Sander, C. Schmidthals, A. Enders, and J. Kirschner, *Phys. Rev. B* **57**, 1406 (1998).

Principal Publication and Authors
H.L. Meyerheim (a), D. Sander (a), R. Popescu (a), J. Kirschner (a), O. Robach (b), S. Ferrer (b) and P. Steadman (c), *Phys. Rev. B* **67**, 155422 (2003).
(a) MPI f. Mikrostrukturphysik, Halle (Germany)
(b) ESRF
(c) Diamond Light Source Ltd., Oxfordshire (UK)

Structure of the C_{60}/Ge(111)- (√13x√13)R14° Surface Reconstruction

The discovery of superconductivity as well as other fascinating properties of C_{60}-based materials has stimulated a large number of experimental investigations on the adsorption and growth of C_{60} molecules on metals and semiconductors [1]. The understanding of interfacial interactions constitutes one of the most important goals of the research in this area. However, charge transfer and local chemical-bond formation from metal and semiconductor surfaces to C_{60} adsorbates still need a more exhaustive understanding. Here we present a detailed analysis of the structure of the (√13x√13)R14° reconstruction of C_{60} on Ge(111).

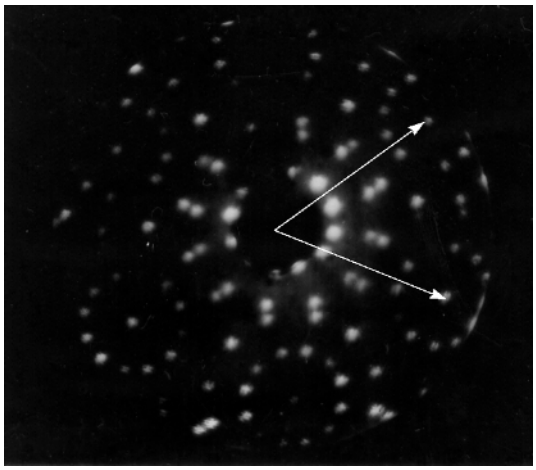

Fig. 97: LEED image of the C60/Ge(111)-($13^{1/2}$x$13^{1/2}$)R14 superstructure, which forms two domains, rotated against each other by 28° as marked by the arrows.

The bulk terminated Ge(111) surface consists of a buckled layer of hexagons, which provide threefold co-ordinated adsorption sites. Since each Ge surface atom exhibits one unsaturated "dangling" bond, the Ge(111) surface is unstable towards the formation of an ad-atom decorated, c(2x8) surface reconstruction. Ge(111)-c(2x8) surfaces have extensively been studied using a variety of methods such as low-energy electron diffraction (LEED), scanning tunnelling microscopy (STM), grazing surface x-ray diffraction (GIXRD) and *ab initio* methods. Upon adsorption of C_{60} onto the clean Ge(111)-c(2x8) surface and annealing to above 500°C, a (√13x√13)R14° reconstruction forms, which is amazingly stable. **Figure 97** shows a LEED pattern. **Figure 98** shows two STM images with the hexagonal arrangement of C_{60} molecules on Ge(111) recorded with a sample bias of (a) +2.0 V and (b) –2.0 V, *i.e.* imaging empty and occupied states of C_{60}, respectively. In contrast to the behaviour on other surfaces, C_{60} is immobile and desorbs as an intact molecule at above 600°C, which has to be compared with the bulk sublimation temperature of C_{60} of just about 200°C. We determined the atomic structure of the Ge(111):C_{60}-(√13x√13)R14° surface by using grazing-incidence X-ray diffraction (GIXRD) at the **ID32** beamline and direct methods for the data analysis.

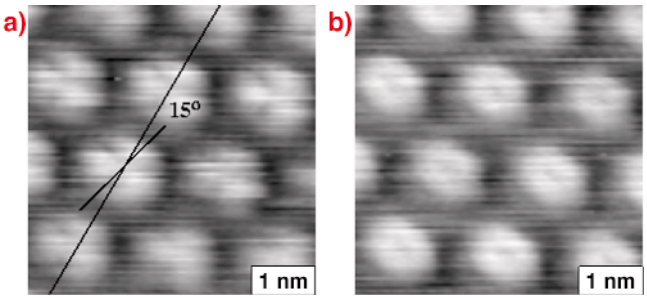

Fig. 98: STM images of the C_{60}/Ge(111)-(√13x√13)R14° structure: (a) empty and (b) occupied states. Within the resolution of the STM, the orientation of the fullerene molecules (long line) is tilted by about 15° with respect to the substrate (short line).

The sample was prepared in the ID32 surface characterisation laboratory, loaded into a portable UHV chamber, which was then mounted on the beamline's six-circle diffractometer. We measured around 1600 non-equivalent fractional order reflections. The analysis of the data set for this complex reconstruction was impossible by traditional means such as constructing and interpreting a two-dimensional Patterson map. For this reason we used three-dimensional direct methods [2]. The stronger peaks in the calculated "electronic density" map correspond to the contributions of the outermost surface Ge-bilayer. The analysis revealed the formation of a nano-pit in the unit cell (close to 1 nm in diameter), created by the removal of six Ge atoms, large enough to accommodate the fullerene molecule. Six Ge atoms from the topmost surface bilayer and three from the bilayer immediately underneath, *i.e.* the bottom of the pit, link each fullerene molecule to the surface with average C-Ge bond distances of 2.1 Å. The Ge atomic positions are otherwise almost bulk-like except for one adatom at a T4 position. The model is in perfect agreement with the STM images [1].

The fullerene molecules are located on the Ge surface with one of their hexagonal C-rings parallel to the surface. The refined structure with p*3* symmetry is shown in **Figure 99**. It reinforces the idea that the surface adsorption of C_{60} molecules is mostly accomplished via surface holes instead of strong rehybridisation.

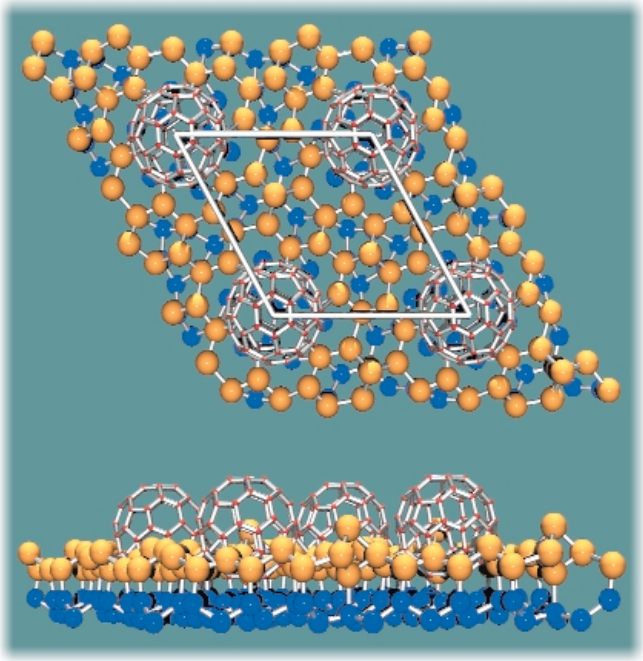

Fig. 99: Projected (top) and lateral (bottom) views of the C_{60}/Ge(111)-(√13x√13)R14° structure.

References

[1] K.R. Wirth and J. Zegenhagen, *Phys. Rev. B*, **56**, 9864-9870 (1997).

[2] X. Torrelles, J. Rius, C. Miravitlles and S. Ferrer, *Surf. Sci.* **423**, 338-345 (1999).

Principal Publication and Authors

X. Torrelles (a), T.L. Lee (b), O. Bikondoa (c), J. Rius (a), J. Zegenhagen (b), *to be published* (2004).

(a) Institut de Ciència de Materials de Barcelona, ICMAB-CSIC (Spain)

(b) ESRF

(c) University of Manchester (UK)

Super-cell Crystallography of Self-organised Deposits

Self-assembly consists of the spontaneous formation of nanostructures in the first stages of growth on a surface, by tailoring instabilities such as the Stranski-Krastanov growth mode. Self-assembly is currently of high interest because of its ability to produce nanostructures in a single-run process that are smaller (5-50 nm) and with a higher surface quality than present-day lithography can achieve. The most active field in self-assembly concerns semiconductor dots, with the prospect of designing new devices like single-electron transistors, single-photon emitters or tunable-wavelength quantum dot lasers.

Generally the structures fabricated by self-assembly display only a short-range positional order. Long-range order may be achieved by deposition on a template like surface reconstructions or arrays of parallel atomic steps arising from miscut crystalline surfaces. The order of these so-called self-organised deposits yields a much smaller size distribution than with self-assembly, which is of interest to control the dispersion of physical properties of the deposits. We have used grazing-incidence small angle X-ray scattering (GISAXS) to characterise self-organised Co/Au(111) dots. Grazing incidence yields surface sensitivity, while the small angle gives access to large distances in real space, thus probing the order between dots (instead of the order between atoms in conventional crystallography). The experiments were conducted in real-time under UHV in a dedicated chamber mounted on **ID32**. An excellent sub-atomic-layer sensitivity was achieved by minimizing the background signal, using a direct vacuum connection to the ring, double pairs of slights, a beam-stop and a cooled 16-bit camera [1].

Sub-atomic-layer Co deposition on reconstructed Au(111) yields a self-organised array of parallel rows of dots, with a period around 10 nm (**Figure 100**) [2]. The reciprocal space of this array consists of rods perpendicular to the surface, with scattering vectors connected with the super-cell of the array. Due to the high radius of the Ewald sphere scattering patterns consist of streaks elongated perpendicular to the sample's surface. The order of dots within rows (resp. between rows) is revealed with the beam shone perpendicular (resp. parallel) to the rows (**Figure 100**).

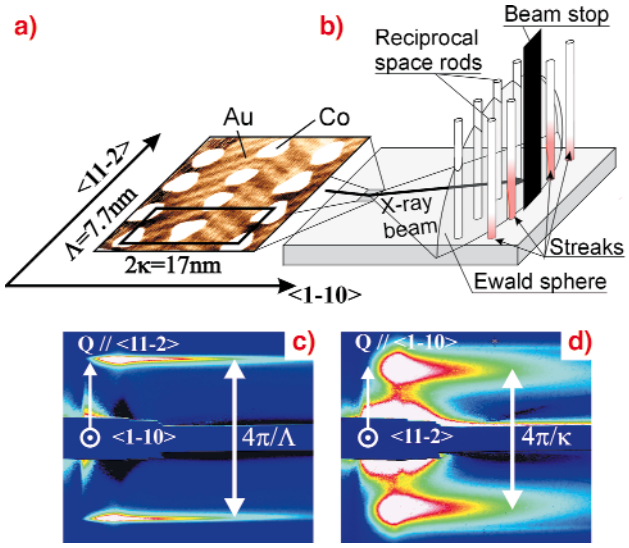

Fig. 100: (a) STM view of self-organised Co/Au(111) dots (b) Sketch of the experimental geometry (c-d) GISAXS patterns for two azimuths of the X-ray beam. The sample lies vertical at the left-hand side of the patterns.

The order is found to be of crystalline type within rows (narrow streaks) and of liquid type between the rows (broad peak).

For self-organised samples, the analogy between real-time GISAXS and reflection high-energy electron diffraction (RHEED) is striking, except that GISAXS investigates dots instead of atoms, and is more suitable to quantitative analysis because of the weak interaction between X-rays and matter. To illustrate this point, **Figure 101** displays the evolution during growth of the intensities I_1 and (normalised) I_2/I_1 of the first and second order peaks of **Figure 100c** (second order peaks not shown on in the figure). The intensity reflects both the order of the array and the shape function of the individual dots, explaining the very different behaviours of I_1 and I_2/I_1. In the sub-atomic-layer range the data is well reproduced by simulations based on Scanning Tunnelling Microscopy (STM) images and on a model of perfect percolation. For higher coverage percolation into a continuous film progressively occurs. The slow decay of I_1 with respect to the model indicates that the percolation is imperfect. Much smaller values are also expected from STM images, revealing that a significant periodic microstructure remains buried in the film even after apparent percolation is probed by STM at the free surface.

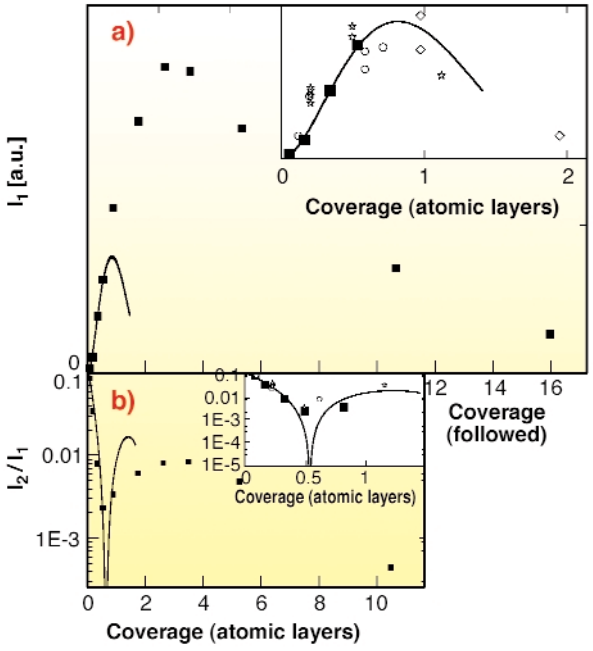

Fig. 101: GISAXS intensity versus Co/Au(111) coverage for first (top) and second (bottom) order streaks. Squares: experimental GISAXS (azimuth of Figure 100c) ; lines: model for perfect percolation ; symbols (insets only): intensity calculated from STM images topography.

In conclusion GISAXS is a promising technique to investigate self-organised deposits on surfaces in real time, revealing the reciprocal space of the array's super-cell. By a quantitative peak intensity analysis, like in conventional crystallography, valuable information is deduced on dots shape, size, order and percolation.

References

[1] G. Renaud, M. Noblet, A. Barbier, C. Revenant, O. Ulrich, Y. Borensztein, R. Lazzari, J. Jupille, C. Henry, *ESRF Highlights* ***1999***, 41 (1999).

[2] B. Voigtländer, G. Meyer, N.M. Amer, *Phys. Rev. B*, **44**, 10354 (1991).

Principal Publication and Authors

O. Fruchart (a), G. Renaud (b), A. Barbier (b,c), M. Noblet (b), O. Ulrich (b), J.-P. Deville (d), F. Scheurer (d), J. Mane-Mane (d), V. Repain (e), G. Baudot (e) and S. Rousset (e), *Europhys. Lett.*, **63**, 275-281 (2003).

(a) LLN, CNRS, Grenoble (France)

(b) CEA/DRFMC, Grenoble (France)

(c) CEA/DRECAM, Gif-sur-Yvette (France)

(d) IPCMS, Strasbourg (France)

(e) GPS-Jussieu, Paris (France)

Following the Corrosion of a Cu_3Au Alloy Crystal

In our humid atmosphere, most corrosion processes are electrochemical in nature, driven by contact potentials *e.g.* formed between dissimilar metals. For the basic understanding of corrosion and its prevention, high-resolution *in situ* structural methods capable of atomic resolution such as scanning probe or X-ray techniques are necessary. To this aim, we conducted Grazing-incidence X-ray Diffraction (GID) experiments at the beamline **ID32** on the potential controlled corrosion of Cu_3Au in sulphuric acid in a thin layer *in situ* X-ray cell shown in **Figure 102a** [1].

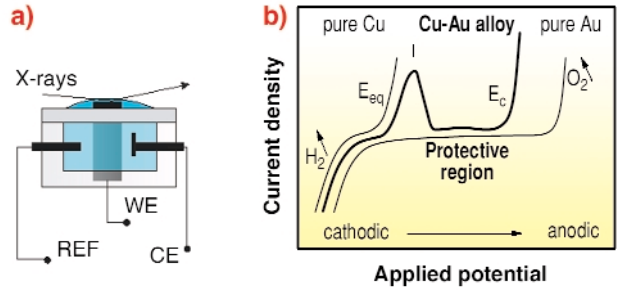

Fig. 102: a) Scheme of the electrochemical *In situ* X-ray cell with three electrodes; b) a voltamogram showing schematically the dealloying of Cu_3Au. Increasing the potential from cathodic (negative) to anodic (positive), a first peak in current (I) is assigned to Cu dissolution. With a further increase in potential, the current stops until a critical potential E_c, is reached.

The prototypical binary alloy Cu_3Au exhibits in its ordered phase a cubic, fcc-like lattice with Cu atoms occupying the face centred sites. The Cu-Au alloy in diluted sulphuric acid shows the following behaviour upon changing the electrode potential (**Figure 102b**): at potentials negative of

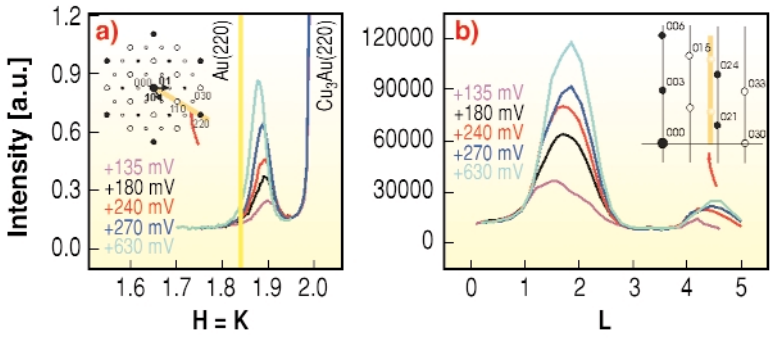

Fig. 103: a) In-plane scans along the h = k direction b) l is the l-scan on the peak in (a). The l-scans show that mainly the intensity of the peak grows, while the FWHM of these l-scans is nearly constant; l = 3 is the Bragg peak position for the layer-to-layer distance.

the equilibrium potential of Cu, there is no current flowing, and the alloy is stable. When the applied potential is increased, reaching the Cu equilibrium potential E_{eq}, current flows by dissolution of Cu ions, which is in this case the less noble metal. However the current flow slows down, unless a critical potential E_c is reached and the current, which is assigned to further Cu dissolution, rises quickly [2]. To date, detailed information available about the structural and compositional changes of the surface during this process is incomplete.

We use a hexagonal surface unit cell for the Cu_3Au, in which case the reciprocal l-direction is normal to the surface. The reciprocal lattice is shown in the inset of **Figures 102a** and **102b**. The X-ray cell with the mounted $Cu_3Au(111)$ crystal was filled with deaerated 0.1m H_2SO_4 solution under a controlled cathodic potential close to hydrogen evolution. At this stage we could only observe the Cu_3Au Bragg reflections, indicating an unaltered surface structure. After increasing the potential, however, a new peak was observed with a lattice constant in between the values expected for pure Au and Cu_3Au, which is understood by a layer of Au, which is epitaxially strained and/or alloyed Cu atoms. The new layer is aligned with the Cu_3Au substrate, but with a different stacking sequence compared to the fcc-like substrate, ACB instead of ABC.

By further increasing the potential in a stepwise manner we can follow the growth of this new layer, as shown in **Figure 103**. The intensity in the in-plane peak (**Figure 103a**) as well as in the l-scans (**Figure 103b**) increases, while the full-width height-maximum (FWHM) of the in-plane peaks decreases, indicating the lateral growth of islands. Meanwhile the FWHM of the l-scans stays nearly constant. From the FWHM ~ 1 for this forming layer, a constant thickness of about three monolayers can be estimated. This means, islands of constant thickness grow laterally and eventually cover the whole surface as a protective layer.

If we further increase the potential to values closer to the critical potential E_c we can observe the formation of thicker islands, as evidenced by a much smaller FWHM in the l-scan. The peak positions (in-plane and specular) now agree exactly with the lattice constant of bulk Au. The width along the surface normal is now much smaller than before, *i.e.*, we witness the formation of thicker gold islands. Thus, a passivating layer of a gold-rich alloy and a uniform thickness of only three monolayers initially protects the alloy until thicker gold islands are formed (**Figure 104**) and the intermediate, passivating layer disappears.

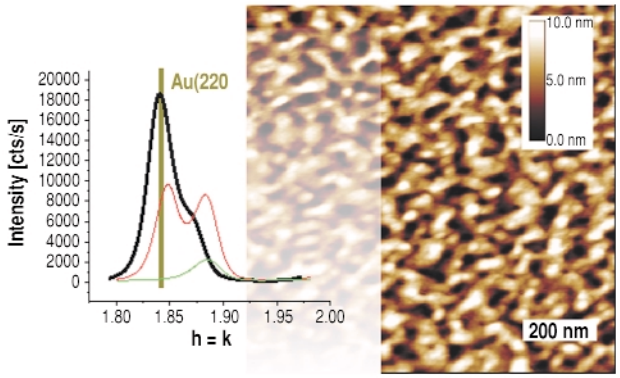

Fig. 104: Typical *ex situ* AFM image of a $Cu_3Au(111)$ surface treatment in the electrochemical cell close to the critical potential. GID shows, except for the Cu_3Au substrate peaks, only peaks characteristic of the lattice constant of gold (black line).

References

[1] see *e.g.* J. Zegenhagen, A. Kazimirov, G. Scherb, D.M. Kolb, D.-M. Smilgies, R. Feidenhans'l, *Surf.Sci.* **352-354,** 346 (1996).

[2] M. Stratmann, M. Rohwerder, *Nature* **410,** 420 (2001); H.W. Pickering, C. Wagner, *J.Electrochem.Soc*. **114**, 698 (1967); H. Gerischer, H. Rickert, *Zeitschrift für Metallkunde* **46,** 681 (1955).

Principal Publication and Authors

F. Renner (a), A. Stierle (b), T.L. Lee (a), S. Warren (a), B.C.C. Cowie (a), D.-M. Kolb (c), H. Dosch (b), J. Zegenhagen (a), to be published.

(a) ESRF

(b) MPI für Metallforschung, Stuttgart (Germany)

(c) Universität Ulm (Germany)

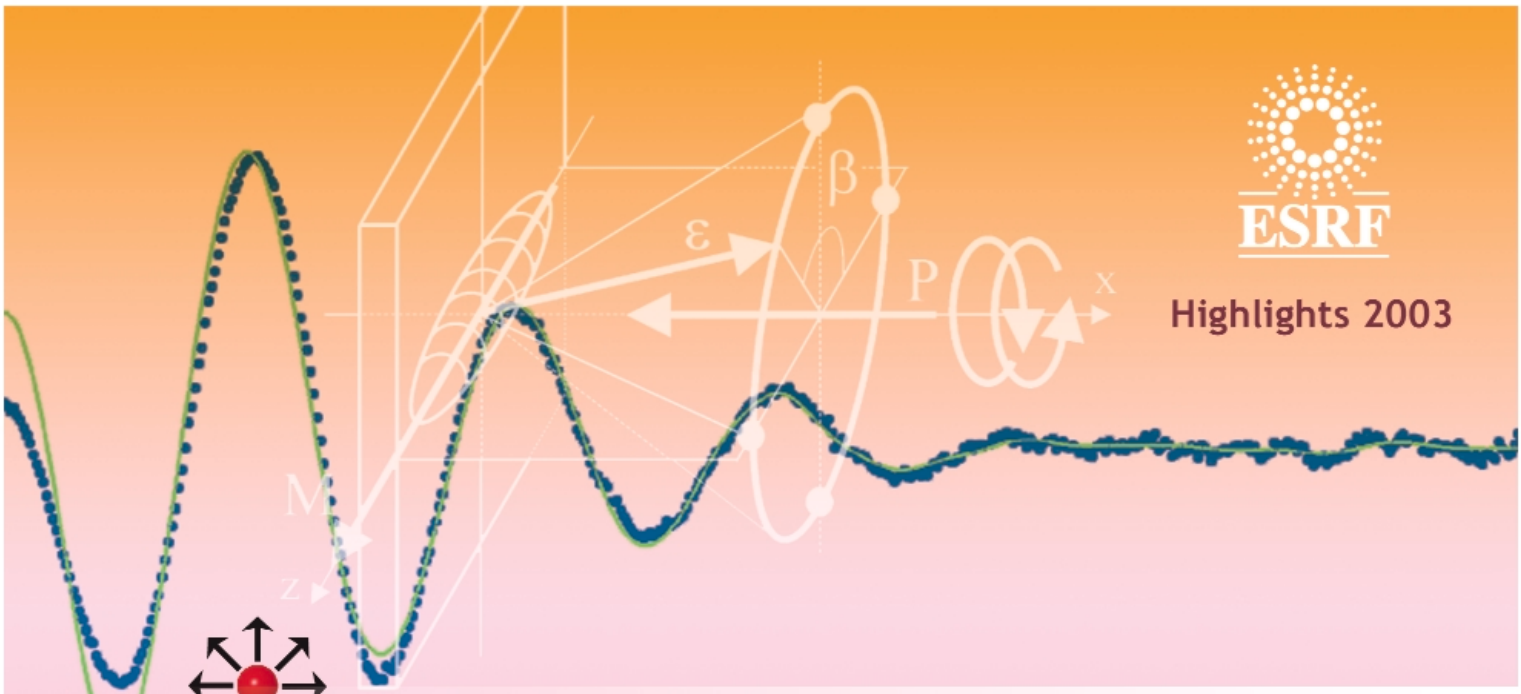

X-ray Absorption and Magnetic Scattering

Introduction

The activities in the X-ray Absorption and Magnetic Scattering group are broad and very diverse. This is reflected only partly in the following articles as a selection needed to be made from the many highlights of the last year. The Chapter is divided into three sections, each with a short introduction. The research topics of 'extreme conditions', 'dichroism studies' and 'X-ray scattering' cover many of the current and rapidly-developing areas of research in the group and give some indications of the medium and long-term evolution of the research. Nevertheless, several fields are not represented here. For instance, the wider importance of X-ray absorption (XAS) at the ESRF was recently highlighted in a workshop on "XAS at Third-generation Sources". Industrial activities, micro-XAS, extreme conditions, time-resolved studies – particularly from catalytic systems under real conditions (OPERANDO) – were all shown to be of great importance.

Another area that has been fruitful in the last few years, but falls outside the scope of the chosen articles, has been studies of oxides. Research in the last year has included cuprates studied by XAS and photoemission [1], manganates probed by EXAFS [2] and spin valves investigated by magnetic circular dichroism [3].

Finally, we look forward to many new scientific highlights in the coming years. The new 10T magnetic-scattering end station on ID20, as mentioned in the X-ray magnetic scattering section below, will bring new opportunities. Also we believe that new ideas will be stimulated by two workshops in 2004. The first is entitled "Polymorphism in Liquid and Amorphous Matter: experimental results and theoretical approaches" and the second is an "International Workshop on Resonant X-ray Scattering in Electrically Ordered Systems".

N. Brookes

References

[1] P.G. Steeneken *et al.*, *Phys. Rev. Lett.* **90**, 247005 (2003).
[2] M.C. Sánchez *et al.*, *Phys. Rev. Lett.* **90**, 045503 (2003).
[3] J. Camarero *et al.*, *Phys. Rev. Lett.* **91**, 027201 (2003).

Studies on Systems at Extreme Conditions

Introduction by S. Pascarelli, ESRF

Studies under extreme conditions of temperature and pressure represent one of the main research topics of the X-ray Absorption and Magnetic Scattering Group. Most of the activities in this area concern X-ray absorption fine structure studies (EXAFS and XANES) on beamlines BM29 and ID24 up to temperatures of 2500 K and pressures of 100 GPa. Very recently it also became possible to perform resonant magnetic X-ray scattering (RMXS) on beamline ID20, at pressures up to 3 GPa, variable *in situ*, and a range of temperatures reaching 1.5 K. The scientific issues addressed by these experiments cover many different fields and it is impossible to cite all of them. It is interesting however to highlight the trends that have emerged in the past year.

On the X-ray absorption beamlines BM29 and ID24, the simultaneous acquisition of X-ray diffraction and absorption spectra has been increasingly exploited to correlate changes in the local and electronic structure with long-range structural rearrangements occuring at phase transitions through the P-T phase diagram. In amorphous Ge, an abrupt change in both the local structure and electronic density of states near the Fermi level was observed to occur around 8 GPa, with no detectable long range order modification [1], indicating the occurrence of a polyamorphic phase transition. In the GeTe system, where a first phase transition transforms the crystal symmetry from rhombohedral to cubic, it was very surprising to see that upon decompression to ambient conditions the high pressure long range symmetry is preserved but the local structure recovers its initial rhombohedral arrangement [2].

The energy range of applications using the Diamond Anvil Cell (DAC) has increased considerably in the past year. Using drilled diamonds, it was possible to perform Ba L_3 XANES studies (5.2 KeV) on Ba-doped silicon clathrates, showing that the displacement of Ba atoms from the center of the cages is accompanied by changes in the Ba-Si hydridisation [3]. At the other extreme, successful EXAFS data was collected on Rb-doped systems (15.2 KeV), including silicon clathrates [4]. Here again the availability of simultaneous XRD detection was essential to correctly follow the onset of cage-collapse instability.

In the field of liquids, recent studies on RbBr acqueous solutions up to 2.8 GPa and 430 K have shown that, upon increasing pressure, water undergoes a structural transformation which involves considerable molecular reorientation [5]. Efforts are also being dedicated to implement additional techniques aimed at the study of the physical properties of liquids under extreme conditions, such as radiometric measurements of viscosity [6].

A clear interest towards μ-XAS applications is emerging. Using a 10 x 10 μm beam, mapping of the oxidation state of Fe in (Fe,Mg) silicates and in Mg-Fe-O-compounds subject to high pressure in a laser irradiated or externally heated DAC has allowed to shed light on the possible chemical reactions occuring in the Earth's lower mantle [7].

Finally, the recent feasibility of RMXS on beamline ID20 has opened the way to a wealth of information, both novel and complementary to neutron scattering, as the exploitation of resonance properties becomes possible and the phase diagram is enlarged for synchrotron X-rays (smaller samples become accessible). RMXS has been successfully applied on the classical mixed-valent system, SmS, to study the quantum critical point [8]. Equally, the application of pressure on doped $CeFe_2$, $Ce(Co_{0.07}Fe_{0.93})_2$, has led to a greater understanding of the magnetic ground state of $CeFe_2$ since it was possible to directly influence the hybridisation of the itinerant electrons.

References

[1] E. Principi, A. Di Cicco, F. Decremps, A. Polian, S. De Panfilis, and A. Filipponi, submitted (2003)
[2] M.V. Coulet, G. Aquilanti, J.Y. Raty, W. Crichton, C. Bichara, S. Pascarelli, and J.P. Gaspard (in preparation).
[3] A. San Miguel, A. Merlen, P. Toulemonde, A. Aouizerat, B. Massenelli, F. Tournus, S. Pascarelli, G. Aquilanti, T. Le Bihan, J. P. Itié and S. Yamanaka (in preparation)
[4] N. Bendiab, A. Merlen, P. Toulemonde, A. San Miguel, P. MacMillan, G. Aquilanti, S. Pascarelli (in preparation)
[5] A. Filipponi, S. De Panfilis, C. Oliva, M.A. Ricci, P. D'Angelo, and D. Bowron, *Phys. Rev. Lett.* **91**, 165505-1 (2003)
[6] W. Crichton, S. De Panfilis, S. Pasternak, M. Mezouar and G. Monaco (in preparation).
[7] L. Dubrovinsky, I.Yu. Kantor, A. Kantor, C.A. McCammon, S. Pascarelli, G. Aquilanti, W. Crichton (in preparation).
[8] P. Deen, N. Kernavanois, D. Braithwaite and L. Paolasini (in preparation).

A Workshop on "Polymorphism in Liquid and Amorphous Matter: experimental results and theoretical approaches" will take place at the ESRF on 7-9 July 2004. The organisation of this event is a joint collaboration between several groups at the ESRF and the CECAM.
The aims of this Workshop are to create the opportunity to join experimental, computational and theoretical scientists on a common subject in order to trigger synergetic collaborations and to attempt to define directions for future investigations.

High-pressure Evolution of the Electronic and Local Structure of Bromine

The diatomic molecule can be considered as the most simple condensed-matter object. In spite of this simplicity, it still reserves many hidden surprises [1]. When diatomic molecules are brought together they can form perfectly arranged structures called molecular crystals. The main characteristic of this class of crystals is that the molecule is preserved and the intra-molecular distance is much smaller than any other interatomic distance within the crystal. Among the molecular crystals, bromine is one of the simplest and is constituted of weakly interacting layers of zig-zag Br_2 molecules. The other halogens (I_2 and Cl_2) share the same crystal structure. What happens when we try to compress this crystal? The best known part of the play is the last act: at a given point the inter-molecular distance becomes comparable to the dimer inter-atomic distance and the molecule is said to dissociate. In general this takes place abruptly through a first-order phase transition and for bromine this happens at the rather high pressure of 80 GPa. All studies on bromine have agreed that the molecule does not show any change up to the dissociation pressure. However, we have recently shown through experiments at the ESRF [2] that the initially semiconducting bromine crystal, metallises at a much lower pressure of about 25 GPa. Is the bromine molecule ignoring these abrupt changes that deeply modify the electronic structure of the crystal? To answer this question we have studied the high-pressure evolution of the bromine molecule with the most sensitive technique for the measurement of short interatomic distances, *i.e.* X-ray absorption fine structure (EXAFS). The experiments were carried out at **ID24**, the energy-dispersive EXAFS beamline, where pressure was applied using a diamond-anvil cell. **Figure 105** shows the pressure evolution of the EXAFS oscillations that contain the information of the local structure around a bromine atom. The fit of the oscillations was done using a constrained structural model including the crystallographic parameters obtained by high pressure X-ray diffraction experiments and, as shown in **Figure 105**, the fit is entirely satisfactory. Note that this study constitutes the highest pressure EXAFS experiment ever done. The evolution of the bromine interatomic distance in the molecule is shown in **Figure 106**. The first surprise is that the evolution of the bromine intra-molecular distance is not monotonic, but it first increases, and then decreases at a higher pressure. We shall recall here that no structural transformation has been observed below 80 GPa. The second surprise is that this change of behaviour takes place precisely at the metallisation pressure. Our results demonstrate that from the electronic point of view we have two totally different types of molecular crystals, above and below 25 GPa, sharing the same crystal structure. We can even be more affirmative and say that after 25 GPa the bromine molecule in a crystal goes a step further in the loss of its molecular character by delocalising part of its electrons in the crystal.

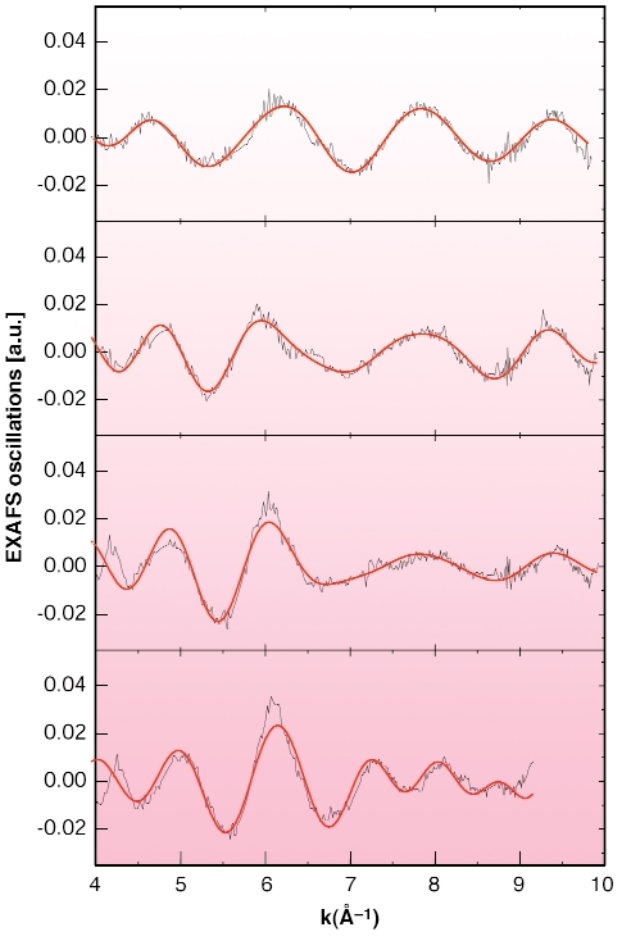

Fig. 105: EXAFS oscillations of bromine as a function of pressure.

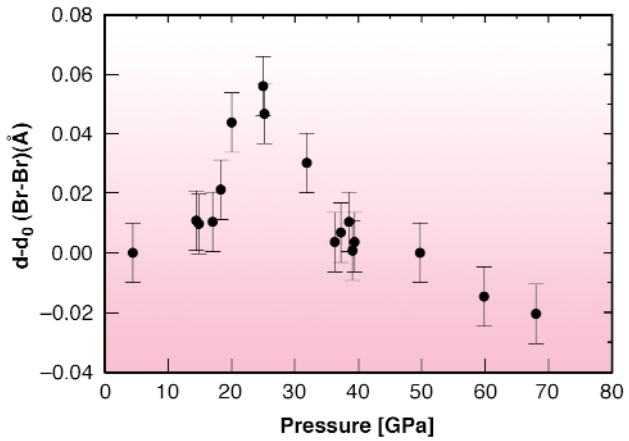

Fig. 106: Relative evolution of the molecular Br_2 distance with pressure. The change of behaviour takes place at the metallisation pressure.

References

[1] T. Kenichi, S. Kyoko, F. Hiroshi and O. Mitsuko, *Nature* **423**, 971 (2003).

[2] A. San Miguel, H. Libotte, J.-P Gaspard, M. Gauthier, J.-P. Itié and A. Polian, *Eur. Phys. J.* B **17**, 227-233 (2000).

Authors
A. San-Miguel (a), H. Libotte (b), J.P. Gaspard (b), M. Gauthier (c) and S. Pascarelli (d)
(a) Université Lyon 1 and CNRS (France)
(b) Université de Liège, Sart-Tilman (Belgium)
(c) Université Paris VI and CNRS (France)
(d) ESRF

Icosahedral Ordering in Liquid and Undercooled Metals

Local ordering in liquid condensed phases can show signatures of five-fold symmetry that are forbidden in crystals. Current experimental knowledge of liquids is limited to the pair distribution, leaving considerable uncertainty in the determination of the local geometrical structure. The presence of this particular type of local symmetry can be studied by taking advantage of experimental techniques such as X-ray absorption spectroscopy (XAS) which is sensitive to local higher-order correlations through multiple-scattering of the photoexcited electron from a core level.

Accurate experiments on liquid and undercooled liquid Cu have been performed at the ESRF, exploiting the potential of **BM29** [1] for combined XAS and X-ray diffraction measurements under extreme conditions. We have applied a new Reverse Monte Carlo (RMC) multiple-scattering data-analysis method incorporating all of the advances included in our original XAS MS data-analysis program (GNXAS [2]). The samples were pellets constituted by dispersions of submicrometric Cu grains into a graphite matrix suitable for high-temperature measurements (see **Figure 107**). The sample can be easily undercooled down to 100 K below the melting point as already observed for other metals and semiconductors.

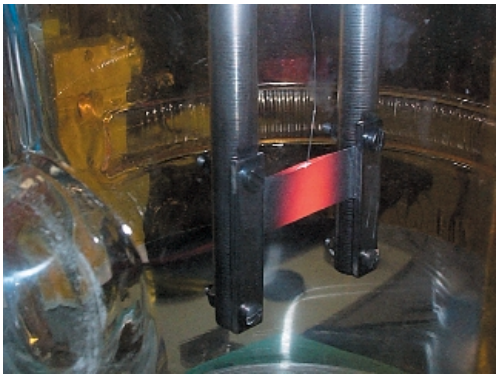

Fig. 107: Cu pellet at high temperature inside the graphite crucible of the L'Aquila-Camerino XAS-XRD oven available at BM29.

The XAS structural signal of liquid Cu measured at 1398 K (l-Cu) is compared with the two-body component of the RMC multiple-scattering simulation in **Figure 108**. The RMC simulation has been performed in a 864-atom cubic box of fixed density, while considering both the XAS experimental data and the published g(r) curve obtained by neutron diffraction (ND). The RMC curve reproduces almost exactly the shape of the ND and XRD g(r) at long distances while the first-neighbour peak, determined with very high accuracy, is narrower and shifted to shorter distances. The high-frequency oscillation of the residual curve (red) shows that the simple two-body $\gamma^{(2)}$ contribution is not able to reproduce the experimental curve and that higher-order terms have to be included in the simulation.

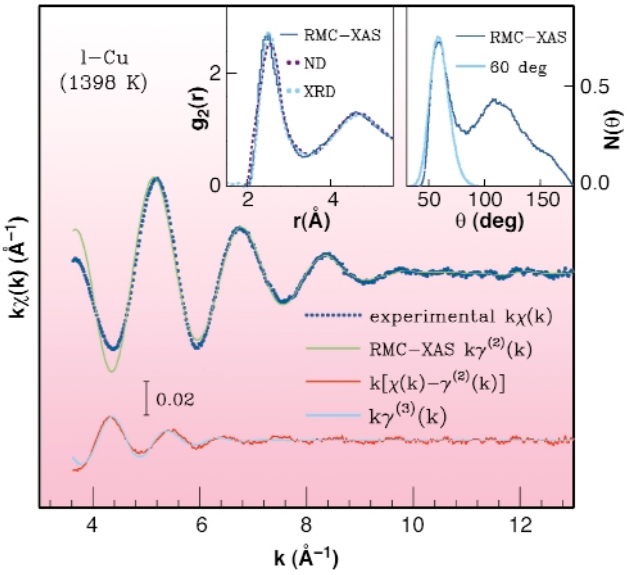

Fig. 108: XAS experimental data of liquid Cu compared with the results of a RMC multiple-scattering simulation.

In a monoatomic close-packed liquid, the most commonly occurring local three-body configuration is expected to be an equilateral triangle formed by first neighbours. The difference spectrum (lower curve in **Figure 108**) is compared with a XAS three-body signal calculated using a Gaussian three-body distribution for equilateral triangles. In fact, the main component of the XAS three-body signal is associated with the peak of the bond-angle N(θ) distribution associated with nearly-equilateral triangular configurations, as shown in the upper-right inset of **Figure 108**.

A geometrical analysis of our final RMC atomic configurations has been carried out in terms of the W_6 spherical harmonics invariant (**Figure 109**). The W_6 distribution of the liquid is found to be very broad and strongly asymmetric towards negative values extending down to the ideal value for a perfect icosahedral cluster. The N(θ) (see left inset in **Figure 109**) corresponding to W_6 values very near to the icosahedral limit shows a distinct peak at 60° and a second peak around 110° with a clear minimum at 90°, similar to the ideal case shown by red ticks in the inset. A suitable upper limit (W_6 = -0.09) corresponds to a broadening of about 10 degrees around the ideal icosahedron values and can be taken as a reasonable borderline for evaluating the fraction of nearly-icosahedral configurations (around 10%).

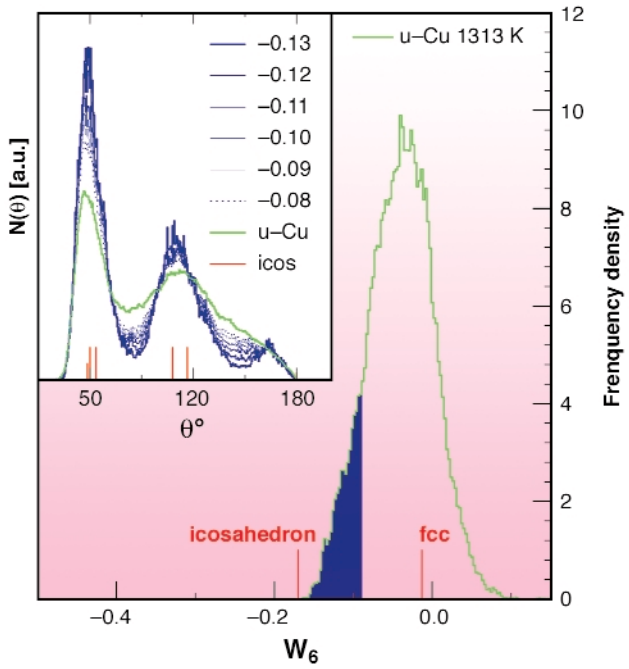

Fig. 109: Histogram of the frequency density of the W_6 invariant monitoring the local geometry around each atom in liquid Cu. The bond-angle distribution related to selected regions of the W_6 distribution is shown in the inset.

In conclusion, novel X-ray absorption experimental results on liquid and undercooled liquid copper, interpreted using an advanced data-analysis method based on multiple-scattering simulations are shown to contain direct information on triplet correlations making feasible a reliable determination of the bond-angle distribution and fraction of icosahedral configurations in liquids. A detailed statistical analysis of local geometry in liquid Cu shows that a significative although limited fraction (10%) of local atomic configurations has a clear five-fold symmetry.

References

[1] A. Filipponi, V.M. Giordano, S. De Panfilis, A. Di Cicco, E. Principi, A. Trapananti, M. Borowski, and J. P. Itie', *Rev. Sci. Instr.* **74,** 2654-2663 (2003).
[2] A. Filipponi, A. Di Cicco and C.R. Natoli, *Phys. Rev. B* **52**, 15122 (1995).

Principal Publication and Authors

A. Di Cicco (a), A. Trapananti (a), S. Faggioni (a), and A. Filipponi (b), *Phys. Rev. Lett.* **91**, 135505 (2003).
(a) INFM, Universita' Di Camerino (Italy)
(b) INFM, Universita' dell'Aquila (Italy)

X-ray Dichroism Studies

Introduction by A. Rogalev, ESRF

Over the past decade, X-ray spectroscopies have undergone a continuous expansion. This area has been boosted by the developments in the synchrotron radiation instrumentation, which have made it possible to produce high fluxes of circularly-polarised X-ray photons. The development of X-ray Magnetic Circular Dichroism (XMCD) into a well-established technique with an extensive list of applications and the experimental evidence of X-ray Optical Activity (XOA) in non-centrosymmetric systems are particularly interesting. These spectroscopies, being element specific and orbital selective, proved to be remarkable tools for the investigation of the electronic structure of various materials.

XMCD, with the help of the magneto-optical sum rules, has as its major strength the capability of disentangling the spin and orbital contributions to the total magnetic moment carried by an absorbing atom. Despite several approximations used to derive XMCD sum rules, thorough experimental and theoretical studies have proved their validity for the L-edges of the *3d*-, *4d*- and *5d*- transition metals as well as for M-edges of the *4f*- and *5f*-elements. However, in the case of the L-edges of rare-earth elements those approximations appear to be too crude and, therefore, straightforward application of the sum rules results in erroneous conclusions. The way to overcome this difficulty is to combine the theory with the experiment. This is nicely illustrated in the contribution by H. Wende *et al., where* the magnetic moment carried by the 5d electrons of a rare-earth atom has been determined for the first time. This approach extends the range of applications of XMCD to the rare-earth elements and other compounds that are of great technological importance.

Magnetic materials exhibit intrinsic "easy" and "hard" magnetisation directions. The preferred orientation of magnetisation is one of the most important properties of magnetic materials and is determined by the Magnetocrystalline Anisotropy Energy (MAE) which is usually strongly-increased in thin films due to the symmetry breaking. Notwithstanding this, our knowledge about the microscopic origin of MAE is rather scarce since its detailed study has become possible only with the advent of XMCD. Using this technique, P. Gambardella *et al.* have shown that the MAE of Co clusters, deposited on a Pt(111) surface, vary drastically with the cluster size (1 to 40 atoms), even if the latter is changed by only one single atom.

Dichroic effects can be observed not only in X-ray absorption but also in X-ray Resonant Raman Scattering

(RRS); the latter has the potential of giving information that is hardly accessible to other spectroscopies. Using circularly-polarised X-rays incident perpendicularly to the sample magnetisation direction and monitoring the integrated intensity of emitted photons over the energy range of the selected de-excitation channel, L. Braicovich *et al.* have demonstrated that it is possible to measure both charge and magnetic multipole moments of the absorbing/emitting atom. Moreover, this experimental arrangement is shown to be optimal to test the validity of the RRS sum rules and it allows one to make a direct comparison of the experimental results with *ab-initio* calculations.

Unlike X-ray magneto optical effects such as magnetic RRS or XMCD which are governed by pure electric dipole (E1E1) or electric quadrupolar (E2E2) transitions, X-ray optical activity is associated with transition probabilities that mix multipole moments of different parities, namely E1E2. Recent work by the ESRF ID12 team and in the Theory Group has revealed that various X-ray optical activity spectra are related to orbital anapole moments and to a whole set of parity-mixing operators [1]. Recently derived X-ray optical activity sum rules may offer unique experimental access to the ground state expectation values of those operators. Furthermore, *ab-initio* calculations of the anapole moment are also under way. As the first attempt, the Stark-induced anapole moment of alkali atoms have been calculated by the ESRF Theory Group using a relativistic formulation of the current density functional theory with spin-orbit correction.

Reference

[1] J. Goulon *et al.*, *JETP*, **97**, 402-431 (2003).

Quadrupolar and Dipolar Contributions to XMCD at the Tb $L_{2,3}$ Edges: Experiment versus Theory

Since the first measurement of X-ray magnetic circular dichroism (XMCD) at the $L_{2,3}$ edges of rare-earth compounds, extensive series of experiments have been performed. This is due to the great technological importance of these materials, *e.g.* in high-performance permanent magnets and information storage devices. The dipolar transition (E1: 2p→5d) made these spectra appear promising for studies of the role of 5d electrons in the complex magnetic phenomena of the rare-earth materials. Unfortunately, the contribution of the quadrupolar transitions (E2: 2p→4f) makes the interpretation of the spectra difficult. Experiments in the past at second-generation synchrotron radiation facilities did not permit measurements of XMCD spectra with detailed fine structure that was free of noise. Only the present performance of the **ID12** beamline with the gap-scan

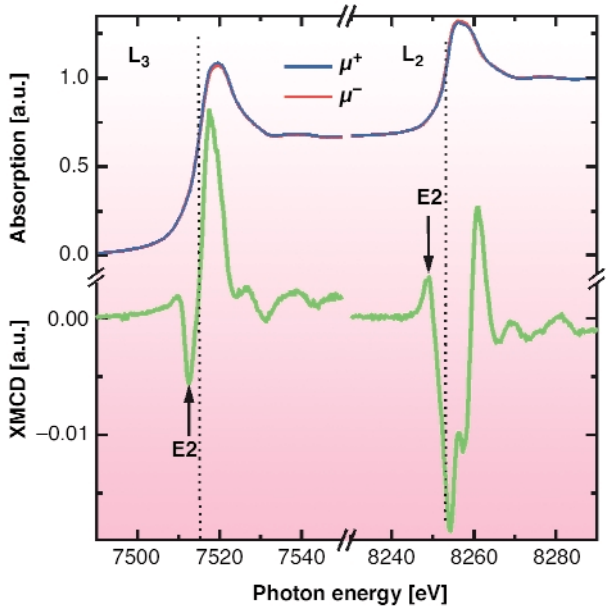

Fig. 110: Normalised Tb X-ray absorption coefficients for right (μ^+) and left (μ^-) circularly polarised X-rays (top) and corresponding XMCD spectra (bottom). Quadrupolar transitions (2p→4f) are marked with arrows.

technique enables us to detect these fine structures with excellent quality, as shown in **Figure 110** [1]. These experimental spectra present a challenge for *ab initio* theory. Finally, the theory has the advantage of disentangling the E1 and E2 transitions. Heretofore, no simple method has been reported to separate the quadrupolar contributions from the dichroic spectra, since even in angular-dependent XMCD measurements, an overlap of the two contributions is observed. The identification of the quadrupolar contributions in the dichroic spectra is essential for the proper application of the sum rules to determine the magnetic moments. Most of the XMCD data reported in the literature were obtained from rare-earth compounds, which are complicated systems including various many-body interactions. Here we used a single-element Tb crystal with small static disorder, which is very helpful to achieve a fundamental understanding of the rare-earth XMCD signal. The helicity-dependent absorption spectra at 10 K are presented at the top of **Figure 110** at both the L_3 and the L_2 edges and the corresponding XMCD spectra are shown at the bottom. A shoulder peak in the L_2 XMCD centred at 5 eV above the absorption edge is observed. This indicates a clear improvement of the quality of XMCD compared to spectra published previously, where this feature could not be detected. In order to disentangle the various fine structures we calculated the XMCD within the local spin density functional approximation by using the most recent version of the real-space multiple scattering code FEFF8 [1]. The calculations presented in **Figure 111** demonstrate that the main contributions at the L_2 and L_3 edges originate from E1 transitions, but the narrow fine structures in the pre-edge regime are due to the E2 transitions. Also the onset of the magnetic EXAFS

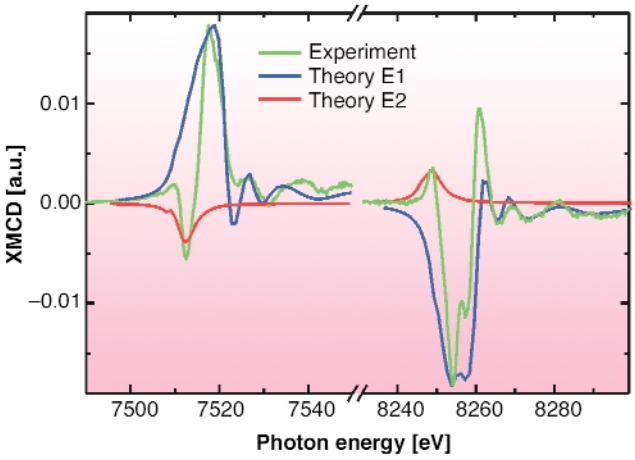

Fig. 111: Comparison of experimental (green) and theoretical XMCD spectra at Tb $L_{2,3}$ edges: dipolar (blue) and quadrupolar (red) contributions.

oscillations is reproduced by the theory [2]. The dipole transition matrix elements are strongly spin-dependent for the rare-earth elements. Therefore, even after separating the E2 and E1 contributions, the results of the sum rule application must be corrected for this effect with the help of the theory. If these corrections are not carried out, an apparent 5d spin moment per atom of $\mu_S^{5d} = -0.27\ \mu_B$ is obtained, and hence erroneously, an antiparallel orientation of the 5d to the 4f moments would be concluded. However, by including the spin dependence of the matrix elements in the sum rule analysis, we obtained $\mu_S^{5d} = +0.37\ \mu_B$, accentuating the need for this correction. This now opens the new and fascinating possibility to use the XMCD technique also for rare-earth elements and compounds with its full strength (element- and shell-specificity, determination of spin and orbital magnetic moments).

References

[1] H. Wende *et al.*, *J. Appl. Phys.*, **91**, 7361-7363 (2002).
[2] H. Wende *et al.*, *J. Synchrotron Rad.*, **8**, 419-421 (2001).

Authors

H. Wende (a), A. Scherz (a), G. Ceballos (a), C. Sorg (a), K. Baberschke (a), A. Ankudinov (b), J.J. Rehr (b), F. Wilhelm (c), A. Rogalev (c), D.L. Schlagel (d), T.A. Lograsso (d).
(a) FUB, Berlin (Germany)
(b) University of Washington, Seattle (USA)
(c) ESRF
(d) Ames Laboratory, Ames (USA)

Giant Atomic Magnetic Anisotropy

Magnetic materials play a key role in present-day technology and industry. In many instances their usefulness is determined by the magnetic anisotropy, *i.e.* by the extent to which the magnetisation retains or switches its orientation in response to thermal or magnetic stimuli. Owing to its importance, different sources of magnetic anisotropy have been investigated over the past 100 years. Studies on ferromagnetic bulk materials and thin films have highlighted the dependence of the magnetocrystalline anisotropy energy (MAE) on crystal symmetry and atomic composition [1]. While the exchange interaction among electron spins is purely isotropic, the orbital magnetisation, via the spin-orbit interaction, connects the spin magnetisation to the atomic structure of a magnetic material, hence giving rise to magnetic anisotropy [2]. Surface-supported nanoparticles offer additional degrees of freedom to tune the MAE by modifications of the particle size, shape, and coupling with the substrate. This makes nanosized systems attractive for basic investigations as well as for miniaturised data storage applications. To date, it is still unclear how anisotropic behaviour sets in and evolves in nanoscale particles. The key issues are the dependence of magnetic anisotropy on the details of the atomic coordination, its relation to the atomic magnetic moments, and the intrinsic upper limits to the MAE in a magnetic compound.

Gas phase atoms with unfilled electronic shells possess large spin (**S**) and orbital (**L**) magnetic moments according to Hund's rules and no magnetic anisotropy, owing to spherical symmetry (**Figure 112**). Experiments on beamline **ID08** revealed the sudden appearance of magnetic anisotropy as a magnetic atom is deposited onto a nonmagnetic surface caused by symmetry reduction and interaction with the substrate electron states. X-ray magnetic circular dichroism (XMCD) measurements probed the magnetism of Co atoms deposited on a Pt(111) surface (**Figure 113a**). Application of the XMCD sum rules yields $\mathbf{L} = 1.1 \pm 0.1\ \mu_B$ and $\mathbf{S} + 7\mathbf{D} = 1.8 \pm 0.1\ \mu_B$ for single Co atoms, where **D** is the spin dipole moment. **S** is calculated in the LSDA scheme to be 2.1 μ_B. The unusually large orbital magnetisation compared to bulk Co ($\mathbf{L} = 0.15\ \mu_B$) can be explained as a result of the reduced Co coordination [3], which allows the survival of Hund's-type correlations in the 3*d* orbitals.

The MAE of single Co atoms on Pt, obtained from quasi-static magnetisation cycles measured by XMCD at the L_3 Co edge in the out-of-plane (easy) and in-plane (hard) directions, exceeds 9 meV/atom (**Figure 112**). This value is larger than that of any known magnetic compound, including bulk hcp Co (0.045 meV/atom) and $SmCo_5$ (1.8 meV/Co atom). While the reduced symmetry of the Co adatoms as compared to the gas-phase constitutes the necessary condition to exhibit anisotropic behaviour, the magnitude of the MAE is attributed to the localisation of the 3*d*-electrons, which augments the spin-orbit energy due to increases in **S** and in the local density of states near the Fermi level, and to the strong 5*d* spin-orbit coupling of the neighbour Pt atoms.

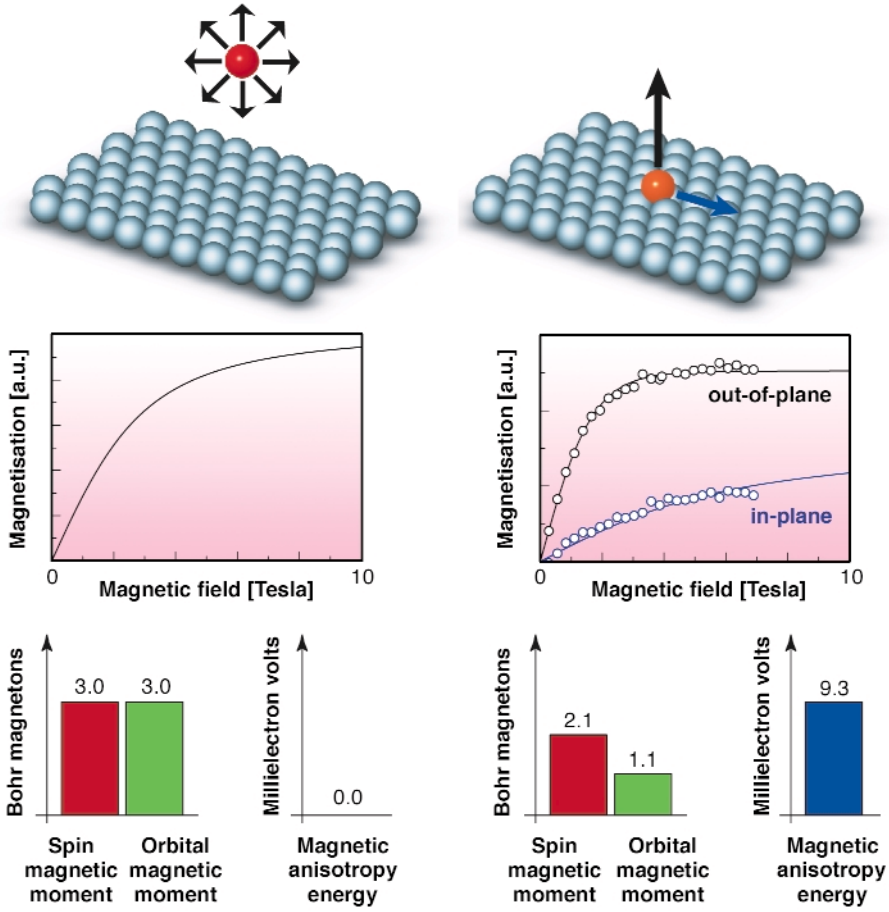

Fig. 112: Magnetisation of a gas phase Co atom (left) compared to that of a Co atom on a Pt surface (right). Co/Pt was chosen as a model system due to the large MAE of bulk CoPt alloys. Co atoms were deposited *in situ* in ultra-high-vacuum conditions on a Pt(111) surface at temperature T = 5.5 K in order to inhibit surface diffusion.

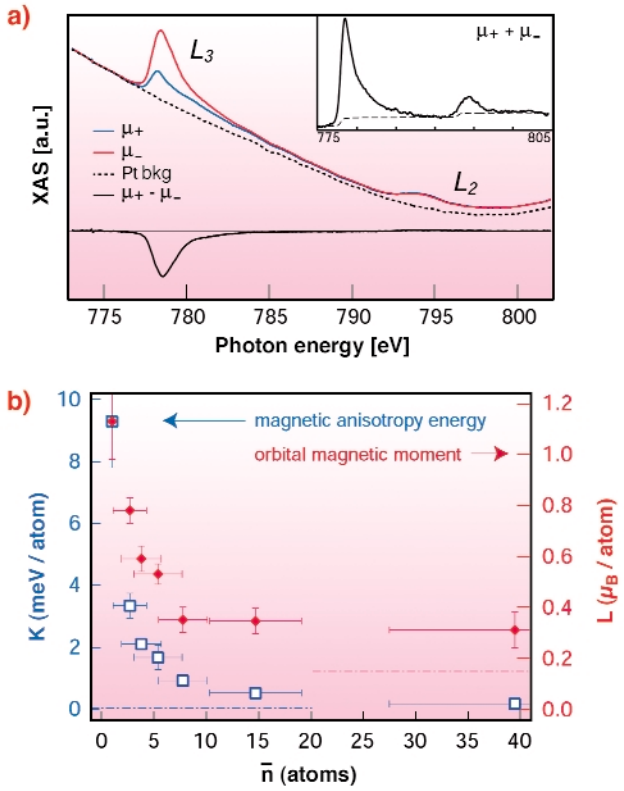

By assembling Co nanoparticles containing up to 40 atoms, the MAE was further shown to depend critically on the atomic coordination. The results plotted in **Figure 113b** demonstrate a clear correlation between the MAE and **L**, both decrease abruptly for single atom increments of the average cluster size. These results were matched by *ab initio* calculations and constitute a first step towards understanding how the magnetic anisotropy develops in finite-sized magnetic particles.

References

[1] J. Kanamori, in *Magnetism* Vol. 1, edited by G.T. Rado and H. Suhl (Academic Press, New York 1963); U. Gradmann, in *Handbook of Magnetic Materials* Vol. 7, edited by K.H.J. Buschow (Elsevier, Amsterdam 1993).

[2] G. van der Laan, *J. Phys.: Condens. Matter* **30**, 3239 (1997).

[3] P. Gambardella *et al.*, *Nature* **416**, 301 (2002).

Fig. 113: (a) XAS spectra recorded over the $L_{2,3}$ edges of isolated Co atoms on Pt(111) with X-ray polarisation parallel (blue line) and antiparallel (red line) to a 7 T applied magnetic field at 5.5 K, and corresponding XMCD (black line). The inset shows the sum of the two XAS spectra after subtraction of the Pt background signal (solid line) with a two-step function for edge jump removal (broken line). (b) MAE, *K*, (squares) and orbital magnetic moment, L, (diamonds) as a function of the average size of two-dimensional Co clusters on Pt(111). The dashed lines represent the values of MAE and orbital moment for bulk hcp-Co (blue and red, respectively).

Principal Publication and Authors
P. Gambardella (a,b), S. Rusponi (a,b), M. Veronese (c), S.S. Dhesi (d), C. Grazioli (c), A. Dallmeyer (e), I. Cabria (e), R. Zeller (e), P.H. Dederichs (e), K. Kern (a,b), C. Carbone (c,e) and H. Brune (a), *Science* **300**, 1130 (2003).
(a) EPF Lausanne (Switzerland)
(b) MPI Stuttgart (Germany)
(c) CNR-ISM, Trieste (Italy)
(d) ESRF
(e) FZ Jülich (Germany)

Experimental Exploitation of Sum Rules in X-ray Resonant Raman Scattering

In X-ray resonant Raman scattering (RRS) the sample is excited with monochromatic incident X-rays ($h\nu_{in}$) and outgoing photons are measured vs. energy ($h\nu_{out}$). At an absorption edge, the process is resonant and gives site and element-specific information. In spite of the success of RRS, the crucial area of sum rules remained so-far unexplored although theoretical work on magnetic systems was already done in the mid 90's [1,2]. The lack of experimental work came from requirements for a completely new experimental approach.

Let us describe the ground-state in terms of charge and angular-momentum expectation values in a multipolar expansion and consider the electric-dipole transitions. X-ray absorption is a first-order process giving access to ground-state properties of first order in magnetic-circular dichroism and of second order in linear dichroism. On the other hand, RRS is a second-order process where sum rules give information up to the fourth order.

The sum rules require the intensity of a given edge with well-defined quantum number *j*. Since RRS depends on $h\nu_{in}$ and $h\nu_{out}$, the integrated RRS (IRRS) signal is obtained by integrating along both energy axis. In the theory the IRRS signal is a sum of terms containing ground-state moments of given order times an angular distribution with a symmetry characteristic of that order. As a consequence, once a convenient geometry is chosen, the angular dependence of the IRRS signal gives direct information on the moments of given order. This concept is understood by a qualitative argument on the charge quadrupole in the IRRS experiment in perpendicular geometry (**Figure 114a**). Let us consider the IRRS-sum signal for opposite circular polarisations without measuring the scattered X-ray polarisation. The situation has left-right mirror symmetry and the IRRS-sum signal in the green points does not distinguish between opposite magnetisation directions. Along the cone (magenta trajectory) the IRRS-sum signal changes due to the charge quadrupole of the sample and the difference between the points in vertical (magenta) and horizontal (green) plane is characteristic for the charge quadrupole. This "conical scan" has the advantage that the emission always has constant angle with the surface so that the self-absorption does not change along the trajectory.

In 3*d* magnetic systems, the scattering channel with the best contrast contains a final state with a 3*s* hole, *i.e.* $2p^63d^n \rightarrow 2p^53d^{n+1} \rightarrow 2p^63s^12p^{n+1}$. The experimental problem is how to measure the IRRS signal along trajectories such as the conical scan or other trajectories required since this is basically impossible with traditional RRS instruments based on gratings or crystals. The new idea is to measure directly the intensity integrated along $h\nu_{out}$ with a suitable device and to measure it vs. $h\nu_{in}$ and angles. The concept is understood from **Figure 114b** showing the traditional RRS spectrum of Co metal (L_3 excitation) containing the 3*s* region (red) and 3*d* valence region (blue). The interesting signal is the integral of the 3*s* channel, which is either measured using: (i) a filter of atomic number *Z*-1 (Fe in our example) in front of a diode; (ii) a bandpass defined with a multilayer, as we did recently, which improves selectivity and versatility. The signal is measured vs. $h\nu_{in}$ (IRRS spectra) and integrated along $h\nu_{in}$ after background subtraction.

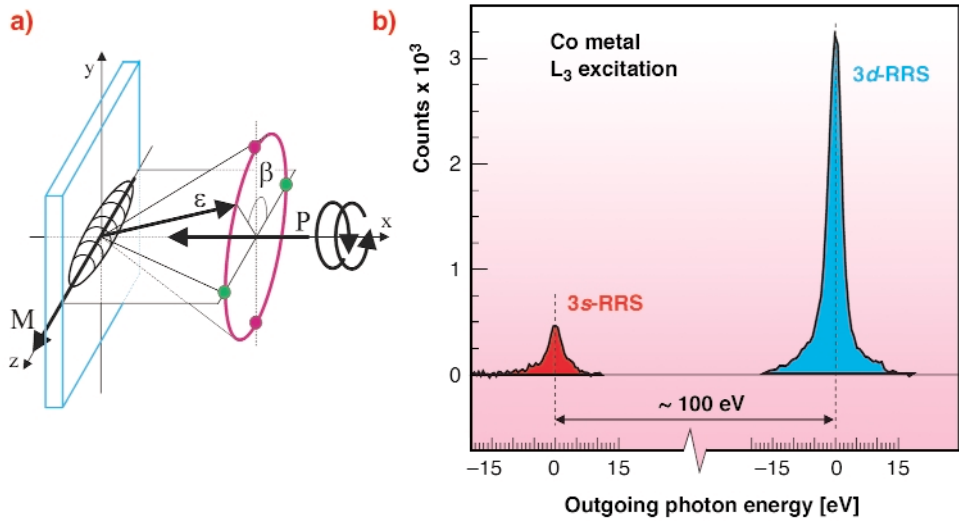

Fig. 114: a) schematics of the experiment. b) traditional RRS spectrum of Co metal.

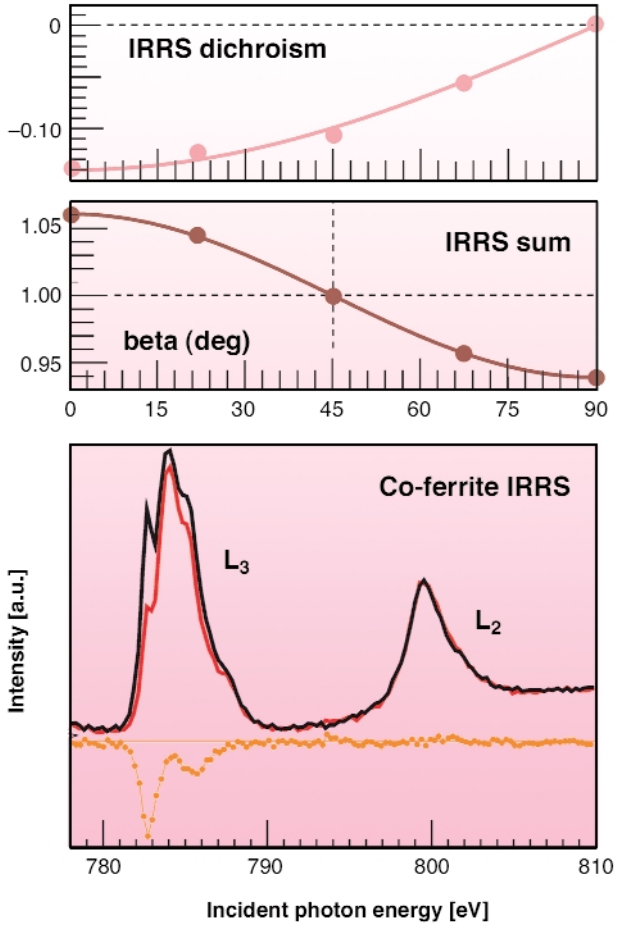

Fig. 115: Lower panel: Integrated RRS (IRRS) spectra of Co in a ferrite in the geometry of Figure 114 (dichroism in orange). Mid panel: IRRS sum signal along the conical scan (brown). Top panel: IRRS dichroism (pink).

Figure 115 gives the IRRS spectra of Co in a ferrite measured in the green points of **Figure 114** with opposite helicities together with the dichroism (orange). The angular dependence of the integrated dichroism (pink curve) and of the IRRS-sum signal (brown curve) can be used together with other scans based on small sample rotations around the *y*-axis (**Figure 114**). In this way, and by taking advantage of absorption measurements, one obtains information on moments up to order four as in the original reference.

References

[1] G. van der Laan, B.T. Thole, *J. Phys. Condens. Matter* **7**, 9947 (1995).
[2] M. van Veenendaal, P. Carra, B.T. Thole, *Phys. Rev. B* **54**, 16010 (1996).

Principal Publication and Authors

L. Braicovich (a), A. Tagliaferri (a), G. van der Laan (b), G. Ghiringhelli (a), N.B. Brookes (c), *Phys. Rev. Lett.* **90**, 117401 (2003).
(a) INFM, Dipartimento di Fisica del Politecnico, Milano (Italy)
(b) Daresbury Laboratory, Warrington (UK)
(c) ESRF

Ab initio Methods to Compute Anapolar Moments in Molecular Systems

The anapole moment is defined as the second moment of the current density: $\Omega = (-\pi/c)\int d^3\mathbf{r}^2\mathbf{j}$
It was first introduced by Zel'dovich in 1958 to describe parity violating interactions in nuclei. Recent experimental [1] and theoretical [2] studies have shown the importance of such an operator also in the description of non-centrosymmetric crystals.

Non-centrosymmetric systems which have both electric dipole moment (parity mixing) and magnetic dipole moments (unpaired spins) generate an anapole moment. In a relativistic scheme the electronic current is defined as: $\mathbf{j} = c\psi^\dagger \boldsymbol{\alpha}\psi$
where $\boldsymbol{\alpha}$ is the Dirac spin matrix.

In electronic distributions, the importance of anapolar moments is related to the optical activity of non-centrosymmetric systems. For instance, the X-ray dichroic signals measured on such crystals are characterised by the interference of electric-dipole (E1) and electric-quadrupole (E2) transitions [1]. Recent work by the ESRF Theory Group has led to the development of sum rules [2] that relate the E1-E2 interference signals to the expectation value of the anapole operator that Marri and Carra have defined, in a non-relativistic scheme, in terms of three contributions:
-pure orbital anapole moment $\Omega_L = [\mathbf{n}\times\mathbf{L} - \mathbf{L}\times\mathbf{n}]/2$
-pure spin anapole moment $\Omega_S = [\mathbf{n}\times\mathbf{S}]$
-mixed spin-orbital anapole moment $\Omega_{SL} = [[\Omega_L,\mathbf{L}]^{(2)},S]^{(1)}$

The sum rules provide valuable information about edge-selective optical activity; nevertheless they cannot measure the expectation value of the anapole operator.

Owing to the complexity of the mathematical derivations of the second moment of the relativistic current density, analytical estimations of anapolar moments have been performed only on small size systems, ranging from single atoms to model molecules of 4 atoms. Numerical (*ab initio*) calculations are required in this case.

Within this context, we present the first *ab initio* calculation of the anapole moment that uses a relativistic formulation of the current density with spin-orbit correction.

The computation uses the Amsterdam Density Functional (ADF) code (www.scm.com). An implemented version, with Dr. E. van Lenthe, University of Amsterdam, allows the computation of the anapole moment in molecular systems. Nevertheless, in order to compare with previous analytical results, we restricted the first applications to a Stark-induced anapole moment on alkali atoms, for which analytical estimations [3] were performed.

	Analytical		*Ab initio*	
Element	α_E (units of a_0^3)	Ω (units of a_0^4)	α_C (units of a_0^4)	Ω (units of a_0^3)
H	4.5	0.103	4.3	0.10
Li	163.7	3.75	130.0	2.92
K	295.6	6.78	237.6	5.52
Rb	330.0	7.57	269.7	6.28
Cs	413.7	9.59	307.6	7.19
Fr	326.0	7.48	183.8	4.20

Table 1: Estimates for the alkali-metal ground states, polarisability and anapole moment. The first two columns are estimations based on analytical derivations, the last two were computed with the ADF *ab initio* program.

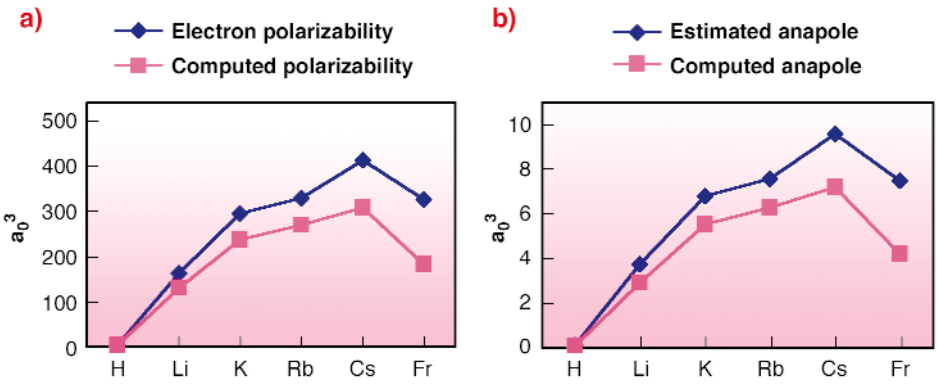

Fig. 116: (a) Electron polarisability for the alkali atoms. Comparison of computed *ab initio* values and "mixed" estimated and experimental values from ref. [3]; (b) Anapolar moment for the alkali atoms. Comparison of the computed *ab initio* and estimated values from ref. [3].

Computed electric polarisabilities α_E and anapole moments by the two-component formalism (ADF code) are shown in **Table 1** together with the analytical estimations. It should be stressed that estimated results consider neither spin-orbit nor scalar relativistic corrections.

Estimated and computed values have similar trends (**Figure 116**). Nevertheless the difference in the absolute value can be attributed to two different factors:

• The computed *ab initio* anapole includes relativistic corrections that are usually neglected by analytical work. This is coherent with the largest deviation obtained for francium. In this case the relativistic effects are most important and so the approximations used in the analytical development are no longer valid.

• The *ab initio* electron polarisabilities and anapole moments are very sensitive to the choice of the basis set used for the wavefunction description. Several test are undertaken to optimise the results.

References

[1] J. Goulon, A. Rogalev, F. Wilhelm, C. Goulon-Ginet, P. Carra, D. Cabaret and Ch. Brouder, *Phys. Rev. Lett.*, **88**, 237401, (2002) and references therein.
[2] I. Marri and P. Carra, *Phys. Rev. B*, **69**, accepted.
[3] R. Lewis, S.M. Blinder, *Phys. Rev.* A, **52**, 4439 (1995).

Author

V. Vetere
ESRF

X-ray Magnetic Scattering

Introduction by L. Paolasini and C. Detlefs

The resonant X-ray scattering technique continues to merge with other, associated techniques used to resolve complex problems associated with the electronic and magnetic properties of solids. Most notable is the extension towards soft X-ray energies, where the giant resonant effects at $L_{2,3}$ edges of *3d* transition metals and $M_{4,5}$ edges of rare-earth metals can be accessed. However, the long-wavelength reduces the accessible reciprocal space and strongly restricts this application to the systems with a long magnetic and structural periodicity.

The intensive activity to investigate the forbidden lattice reflections, enhanced at the absorption edges, by the photon polarisation analysis (both circular and linear) and its angular dependence (azimuthal scans) have yielded a rich variety of experimental results, stimulating an intense theoretical activity to understand the change in the local symmetries at the origin of the multipole transitions involved in the resonant processes. The continuous effort to develop the experimental set-up and to push toward more extreme sample environment conditions is a consequence of the complex relationship between the long-range magnetic and electronic ordering phenomena, and the necessity to separate unambiguously the tensorial matrix elements involved in the physics of multiple ordered states. This effort concerns the main thermo-dynamical parameters involved in the Condensed Matter Physics: the development of high pressure at low temperature, the

introduction of the magnetic field and the extension of the temperature range for the azimuthal setup.

The ongoing ID20 upgrade and refurbishment program, which will be completed after the summer of 2004, can be seen as having the main objective of overcoming the present difficulties.

The main goal of this program is the installation of a superconducting cryomagnet for resonant X-ray scattering experiments under a magnetic field up to 10 Tesla. It will be housed in a separate hutch, with a non-magnetic diffractometer able to support the heavy load with very precise position reproducibility.

Resonant X-ray scattering is an increasingly important probe for studies of the electronic and magnetic properties of strongly correlated electron systems. The ongoing technical developments, along with improved theories, will allow a host of novel and unique experiments in the near future. We are looking forward to this exciting period.

Dynamics of Long-wavelength Phason Fluctuations in the Icosahedral Quasicrystal i-AlPdMn

The diffraction patterns of quasicrystals display both resolution-limited Bragg reflections and rotational symmetries incompatible with periodicity (as for instance the 5-fold symmetry). This particular type of long-range aperiodic order is referred to as quasiperiodicity. In a high-dimensional description of quasicrystals, the overall atomic arrangement in physical space ($E_{//}$) can be viewed as a 3D section of a 6D periodic lattice decorated with 3D atomic domains defined in a complementary (or internal or perpendicular) space $E_{\perp}$. When considering the symmetries that leave the i-phase free-energy invariant, we expect 6 hydrodynamic long-wavelength modes: 3 associated with rigid translations of the solid along $E_{//}$, the usual acoustic phonons, and 3 associated to phase displacements along $E_{\perp}$, the so called phason degrees of freedom [1]. In quasicrystals, phasons correspond to internal atomic rearrangements, where atoms jump between sites with similar local environment. These jumps are correlated and the corresponding dynamical process is a diffusive one. A clear signature of the existence of long-wavelength phason fluctuations occurring in quasicrystals is the predicted and indeed observed specific anisotropy of the diffuse scattering near Bragg peaks [2]. However, the dynamics of phason fluctuations implies very slow relaxation times.

X-ray Intensity Fluctuation Spectroscopy (XIFS) is a unique technique taking advantage of the coherence properties of the incident X-ray beam to study atomic length scale fluctuations of domains occurring on 10^{-3}-10^{3} s time scales [3]. With a coherent beam, the resulting intensity distribution exhibits a spiky structure originating from constructive and destructive interferences between scattering domains. Any time evolution of these scattering domains' distribution due to fluctuations in the sample results in a time evolution of the speckle intensity distribution.

Using XIFS on beamline **ID20**, we were able to make the first characterisation of the dynamics of long-wavelength phason fluctuations in the i-AlPdMn quasicrystalline phase. With a 10 µm pinhole just before the sample, the partial coherence β of the set up was evaluated to 5% for the low angle 7/11 Bragg reflection. The scattering geometry of the entire set up allowed us to measure the diffuse intensity distribution for a range of phason wavevectors **q** centred around the (τ,-1,0) direction where $\tau = (1+\sqrt{5})/2$ is the golden mean. The diffuse scattering patterns were collected on a 2D CCD camera located at 1.85 m from the sample. A fast shutter on the incoming beam permitted a time acquisition of 1 to 5s and a time-dependence analysis of the intensity correlation from 2 to 1000 s. From room temperature up

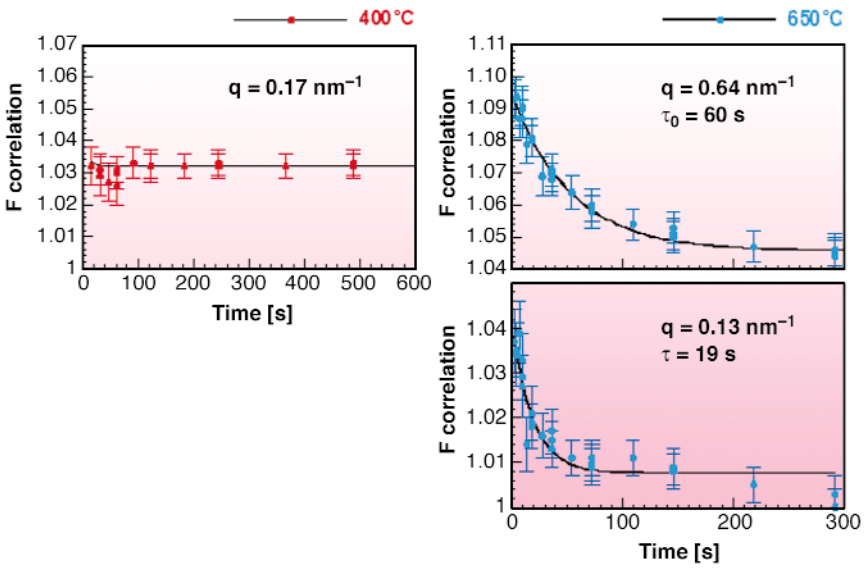

Fig. 117: Correlation functions $F_{corr.}(q,t)$ for different temperatures and q phason wavevectors along the (τ,-1,0) direction.

to 500°C, the intensity correlation function, defined as $F_{corr.}(\mathbf{q},t) = \langle I(\mathbf{q},t)(I(\mathbf{q},t+t')\rangle_{t'}/\langle I(\mathbf{q},t')\rangle_{t'}^2$ where $\langle\ \rangle_{t'}$ is the average over a time t', was found to remain constant over the time of measurement. This behaviour is consistent with frozen-in phason fluctuations at low temperatures. Around 550°C, an activation of the diffusive process is perceptible with a very slow time evolution of $F_{corr.}(\mathbf{q},t)$. At 650°C, the intensity correlation function exhibits an exponential time dependence of the form $F_{corr.}(\mathbf{q},t)=1+\beta.\exp(-t/\tau_0(\mathbf{q}))$ with a characteristic decay time $\tau_0(\mathbf{q})$ decreasing as the phason wavevector **q** increases (see **Figure 117**). As expected for a diffusive process, $\tau_0(\mathbf{q})$ obeys a q^{-2} law with a phason diffusion constant D_{phason} (650°C) = 1.5 10^{-16} $m^2.s^{-1}$ (see **Figure 118**). In principle, three phason modes contribute to the diffusive intensity. However, the mode with the slowest time constant dominates the measured signal and is the only one observed. **Figure 118** can thus be regarded as a "dispersion" relation of a phason mode propagating along the (τ,-1, 0) direction with a polarisation along $E_\perp$.

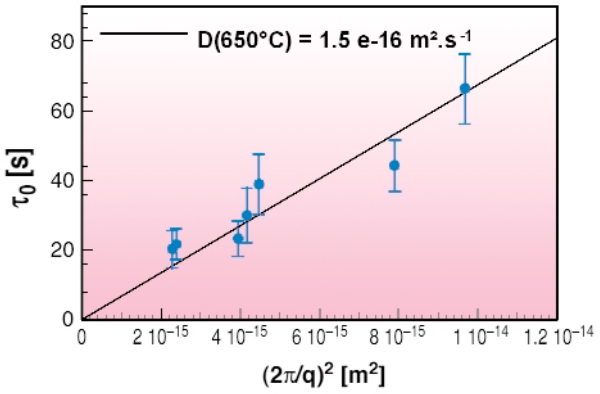

Fig. 118: Evolution at 650°C of the characteristic decay τ_0 as a function of the square of the phason wavelength $\lambda^2 = (2\pi/q)^2$. A linear fit to the data allows extraction of the phason diffusion constant D_{phason} for this temperature.

References

[1] T.C. Lubensky *et al.*, *Phys. Rev. B* **32**(11), 7444 (1985).
[2] M. de Boissieu *et al.*, *Phys. Rev. Lett.*, **75**, 89 (1995).
[3] M. Sutton, K. Laaziri, F. Livet, and F. Bley, *Opt. Express* **11**, 2268-2277 (2003).

Authors

S. Francoual (a, b), F. Livet (a), M. de Boissieu (a), F. Yakhou (c), F. Bley (a), A. Létoublon (d), R. Caudron (e,f), J. Gastaldi (g), *Phys. Rev. Lett.* **91**(22), 225501/1-225501/4 (2003).
(a) LTPCM, St Martin d'Heres (France)
(b) ILL
(c) ESRF
(d) DRFMC, SP2M, CEA-Grenoble (France)
(e) LEM, ONERA-CNRS, Chatillon (France)
(f) LLB, CEA-CNRS, Saclay (France)
(g) CRMC2, Marseille (France)

Isolating Interface Magnetocrystalline Anisotropy Contributions in Magnetic Multilayers

Magnetic valves are used billions of times each day to read information from computer hard disks. These valves rely on a phenomenon known as giant magnetoresistance which in turn is highly sensitive to interface magnetism in magnetic multilayers. However, interface magnetism is still relatively poorly understood due largely to the lack of a suitable probe. Fortunately, recent work on beamline **ID08** has shown that Soft X-ray Resonant Magnetic Scattering (SXRMS) combined with Soft X-ray Standing Waves (SXSW) offers unique new insights into interface magnetism. Fe/CeH_2 multilayers provide an ideal system to demonstrate the magnetic interface sensitivity of this new probe since the magnetisation orientates perpendicular to the layers and splits up into a regular spin-up and spin-down stripe domain configuration at low temperatures. The stripe domains act, so to speak, as a magnetic diffraction grating for SXRMS [1] while the high quality of the multilayer interfaces produces standing waves allowing interface sensitivity. For transition metal/rare-earth interfaces, very little is understood about the mechanism behind this spin reorientation. On one hand, the strong interface crystalline field acts on the 4*f* orbital moment resulting in a single-ion anisotropy model of the spin reorientation. On the other hand, the magnetocrystalline anisotropy energy (MAE) of the transition metal 3*d* states could directly induce the spin reorientation, without a contribution from the 4*f* orbital moment, through interface 3*d* - 5*d* hybridisation. Despite the significance of these phenomena, making a distinction between the two mechanisms has proven difficult.

Soft X-ray resonant magnetic scattering is sensitive to the element-specific stripe domain structure of Fe and Ce through resonant transitions to the 3*d* and 4*f* unoccupied states, respectively. **Figure 119** shows SXRMS spectra measured, at the Fe L_3 edge, using left (open circles) and right (solid circles) circularly polarised light. The integrated intensity variation of the first- (open squares) and second-order (open circles) magnetic satellites with temperature is shown in the inset **Figure 119**. The different behaviour of the two features is clearly evident below 120K and it can be shown that the second-order peak is related to the spin-orbit anisotropy and therefore a probe of the magnetocrystalline anisotropy [2]. The deviation between the first and second-order magnetic Fe SXRMS contributions at 120K arises from an additional magnetic anisotropy contribution due to a Ce 4*f* single-ion anisotropy. Evidence for such a mechanism comes from magnetic scattering at the Ce M_5 edge. **Figure 120** shows SXRMS spectra recorded at the Ce M_5 edge as a function of temperature (solid circles with lines); the spectra recorded after the stripes have been destroyed in a magnetic field are also shown (dashed lines). The inset

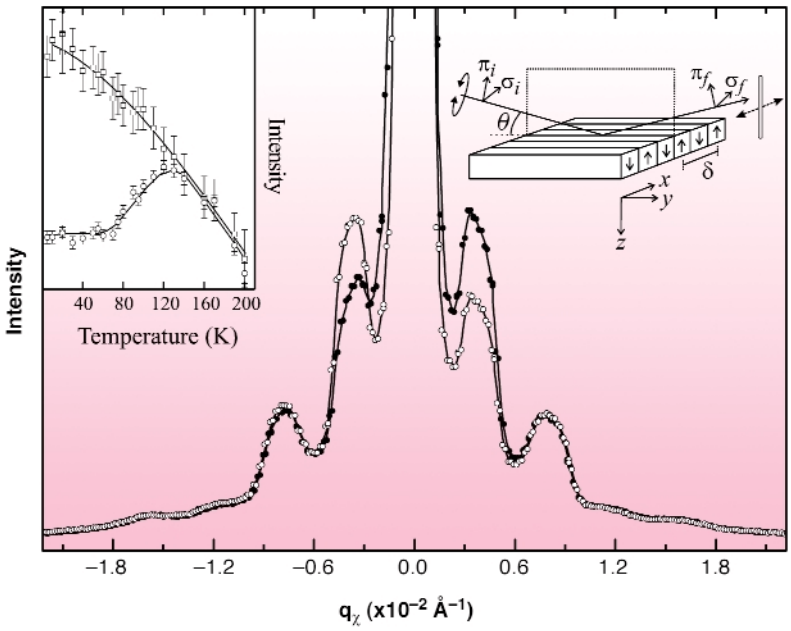

Fig. 119: SXRMS spectra measured at the Fe L_3 edge using left (open circles) and right (solid circles) circularly-polarised light. The inset shows the intensity changes of the first- (open squares) and second-order (open circles) peaks as a function of temperature; the lines are guides to the eye. The experimental geometry is shown with the up and down arrows representing the stripe domains.

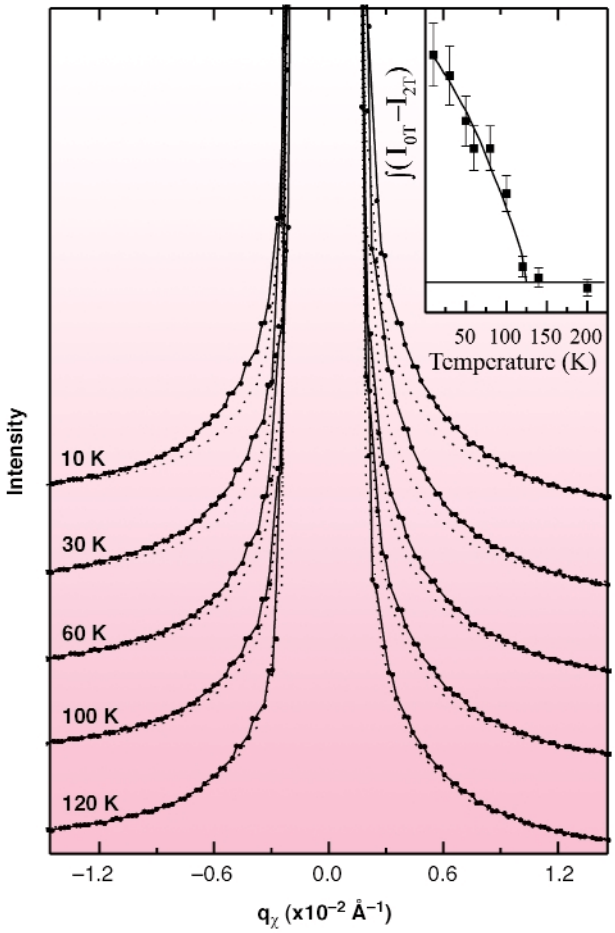

Fig. 120: Temperature dependence of the Ce SXRMS spectra (solid circles with lines). The SXRMS scattering recorded after the stripes have been destroyed in an applied magnetic field of 2T is also shown for each temperature (dashed lines). The inset shows the temperature dependence of the integrated difference between the spectra recorded with and without a 2T field and represents the temperature dependence of the Ce 4*f* perpendicular magnetic moment and magnetic anisotropy.

of **Figure 120** shows the integrated difference between the pairs of spectra for each temperature, which represents the Ce 4*f* perpendicular moment and MAE. The temperature dependence of the Ce 4*f* single-ion anisotropy contribution is noticeably different since the weak first-order magnetic Bragg peaks are only visible below 100 K (much lower than the spin reorientation temperature), as shoulders.

The first- and second-order resonant magnetic scattering contributions have been related to the interface and bulk regions of the Fe layers using SXSW. They are generated within the multilayer due to the long wavelength matching the multilayer periodicity. Interface sensitivity was achieved by tuning the standing-wave maxima to coincide with the interfaces. In this way, a difference in the angular dependence of the magnetic satellites demonstrated that the first- and second-order contributions probe different magnetic properties localised at the bulk Fe and interface Fe sites. At the spin reorientation, the magnetic anisotropy driving the perpendicular magnetic anisotropy is then dominated by the Fe interface MAE, which most likely arises from Ce 5*d* - Fe 3*d* hybridisation, and not the Ce 4*f* single-ion anisotropy.

References

[1] H. A. Dürr *et. al.*, *Science*, **284**, 2166 (1999).
[2] S. S. Dhesi, G. van der Laan, E. Dudzik, A. B. Shick, *Phys. Rev. Lett.*, **87**, 067201 (2001).

Principal Publication and Authors

S.S. Dhesi (a,b), H.A. Dürr (c), M. Münzenberg (d), W. Felsch (d) *Phys. Rev. Lett.*, **90**, 117204 (2003).
(a) ESRF
(b) Diamond Light Source (UK)
(c) BESSY (Germany)
(d) Universität Göttingen (Germany)

Magnetic Profilometry in Multilayers

Although X-ray reflectivity specular or off-specular diffuse scattering have been widely applied during the last decade to characterise the morphology of nano-structured materials, it is only recently that progress in synchrotron radiation instrumentation allows an increasing use of X-ray resonant magnetic reflectivity experiments. The strength of this approach is to combine the shell magnetic sensibility of the X-ray magnetic circular dichroism and the spatial sensitivity of the Diffracted Anomalous Near Edge Spectroscopy (DANES). A promising application is the study of interfacial effects in nano-structured materials, which are known to influence magnetic effects such as perpendicular magnetic anisotropy or giant magnetoresistance.

In this experiment, we focus on a system made of an alternating stacking of rare-earth and *3d* transition metal layers. In this category of materials, the Ce/Fe multilayers are certainly one of the most unusual rare-earth/*3d* magnetic multilayers, because, depending on the strain effect into the Ce layers, the cerium *4f* electrons tend to be delocalised and strongly interact with the *3d* electrons. In the case of α-Ce, which is usually non-magnetic in its bulk state, a net magnetic moment has been observed in Ce/Fe systems [1]. Even more surprising is the observation that this "induced" polarisation persists when a 15 Å thick La layer is introduced in between Fe and Ce layers. Since La induced polarisation is known to be strictly limited to the two first atomic planes, a hybridisation by Fe, via the La-*5d* states, is likely to be excluded. To look at the mechanism behind these fascinating magnetic properties, we used X-ray resonant magnetic reflectivity to derive the magnetic structure of the Ce layer along the growth axis.

The experiment has been carried out at beamline **ID12** using an in-vacuum reflectometer to measure the scattered intensity from a $[Fe(30Å)/La(15Å)/Ce(10Å)/La(15Å)]_{57}$ multilayer. The Ce magnetic contribution have been successfully collected for five superlattice reflections by measuring the scattering intensity $I^{+/-}$, for opposite directions of an applied magnetic field, versus the incident photon energy. To avoid any experimental artefact, the asymmetry

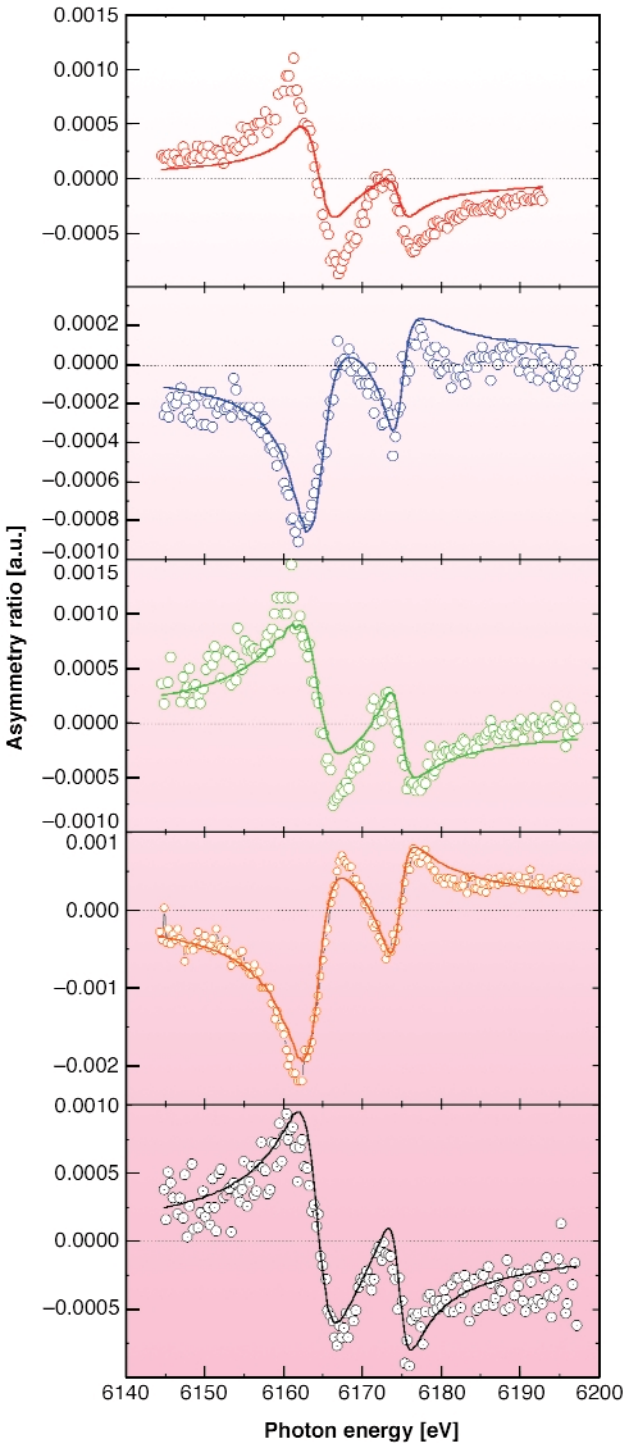

Fig. 121: Energy dependence at the Ce L_2 of the magnetic R for the five superlattice reflections. The lines represent the simulation using the magnetic profile displays in Figure 122.

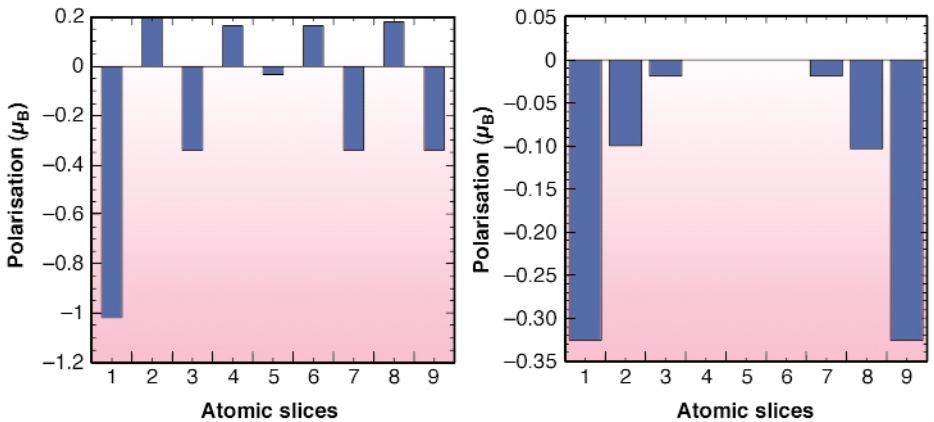

Fig. 122: Profile of the Ce 5d polarisation across Ce sublayer in $Fe_{30Å}/La_{15Å}/Ce_{10Å}/La_{15Å}$ multilayer (left) and $CeH_{2\ (19Å)}/Fe_{(25Å)}$ (right).

ratios R = $(I^+-I^-)/(I^++I^-)$ have also been measured by reversing the polarisation of the incoming beam. As displayed in **Figure 121**, we succeeded in measuring high-quality energy-dependent asymmetry ratio spectra at the Ce L_2 edge at different wavevectors perpendicular to the layers. The changes in shape and amplitude of these spectra depend on the superlattice reflections, which indicates a non-uniform distribution of the Ce *5d* polarisation.

For a quantitative description of the Ce *5d* magnetic polarisation, the kinematical approach has been used here to refine the five spectra simultaneously. The structural parameters were independently determined by X-ray diffraction and resonant reflectivity. The amplitudes of the Ce *5d* polarisation in each atomic plane have been adjusted to fit the experimental data. The Ce 5d magnetic profile obtained from this analysis is displayed in **Figure 122**. This unexpected antiferromagnetic-like behaviour has been ascribed to an intrinsic property of α-Ce and strongly related to the delocalisation of the *4f* states in such strained multilayers. This result was supported by changing the strain which acts as a pressure effect implying a relocalisation of the *4f* states of Ce [2]. When Ce switches to its γ-like phase, through introduction of H_2 into the layer, we show that Ce adopts a *5d* magnetic profile decreasing from the interface, as already reported in a few other systems.

Finally, and beyond the Ce case, this experiment shows that magnetic reflectivity associated with a detailed structural investigation offers a unique possibility to selectively probe the spatial magnetic distribution of nano-structured materials. Moreover, the small part of the reciprocal space probed in reflectivity allows an extension of this approach to the L edge of *3d* metals and M edges of rare-earth [2].

References

[1] M. Arend *et al.*, *Phys. Rev.* B **59**, 3707 (1999).
[2] N. Jaouen *et al.*, *Appl. Phys.* A, **73**, 711-715 (2001).

Principal Publication and Authors

N. Jaouen (a,c), J.M. Tonnerre (a), D. Raoux (a), W. Felsch (b) and A. Rogalev (c), *Phys. Rev* B **66**, 134420 (2003).
(a) Laboratoire de Cristallographie, CNRS, Grenoble (France)
(b) I. Physikalisches Institut Universität Göttingen, (Germany)
(c) ESRF

Resonant Magnetic X-ray Scattering in Co-doped $CeFe_2$

The magnetic ground state of $CeFe_2$ has historically been controversial. Although the ground states of the heavy rare-earth (RE) laves phases with Fe (formula $REFe_2$) are well understood, that of $CeFe_2$ is considerably more complex as a consequence of the hybridisation of the anomalous *f* electrons in Ce, with the 3*d* states of iron [1].

Resonant Magnetic X-ray scattering (RMXS) experiments performed on a Co-doped single crystal of $CeFe_2$ (grown at Ames Laboratory, Iowa State University, Ames, Iowa USA) allowed us to re-examine this challenging problem.

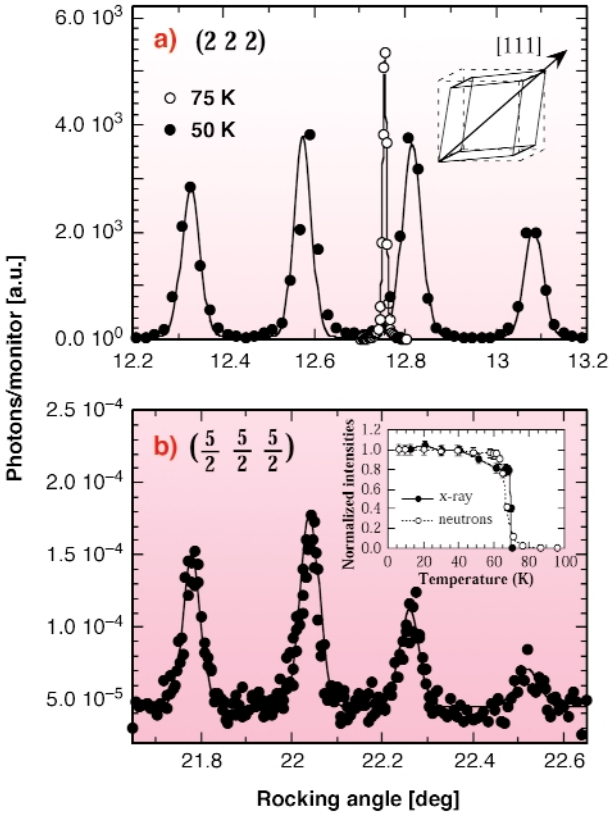

Fig. 123: a) Splitting of the crystallographic Bragg (222) reflection due to the rhombohedral distortion; b) Magnetic reflection ($^5/_2$ $^5/_2$ $^5/_2$) split in the corresponding rhombohedral domains.

The experiments were carried out at beamline **ID20** on a sample of $CeFe_2$ doped with 7% Co, at which concentration the antiferromagnetic ground state is stabilised below 69 K. Between this temperature and the Curie temperature of 210 K the material is a "nominal" ferromagnet, as is the pure compound. Below the discontinuous antiferromagnetic transition, a rhombohedral distortion splits the Bragg peaks along the <111> directions into four crystallographic domains. Exploiting the high Q-resolution available on ID20, it was possible to isolate the contribution of a single magnetic domain, as shown in **Figure 123**. By tuning the incident photon energy to the Ce L_3 and at the Fe K edges on performing linear polarisation analysis of the scattered photons, it was possible through the resonant X-ray scattering process to probe the magnetically-polarised 4f and the 3d electronic states respectively. Since these processes are also sensitive to the magnetic moment

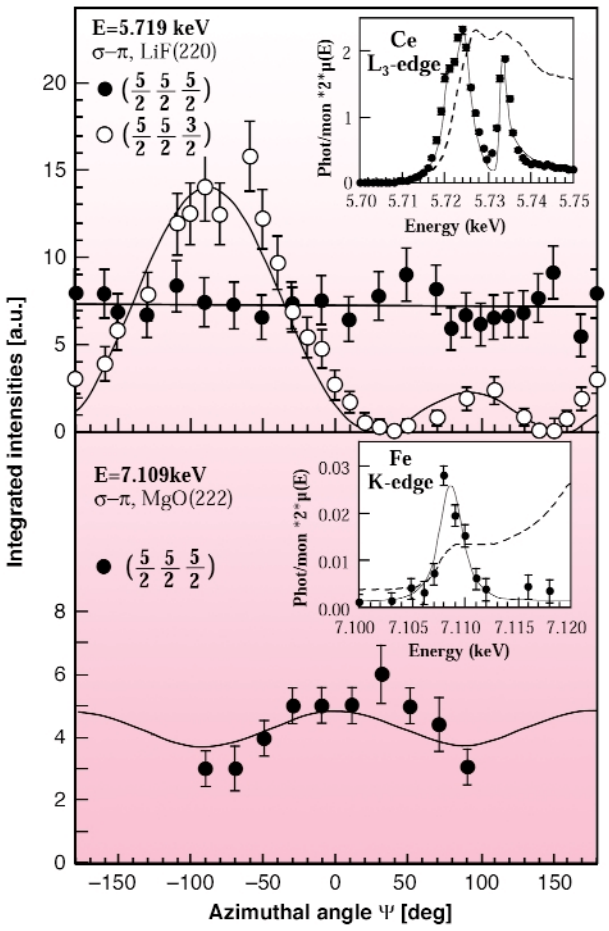

Fig. 124: Azimuthal dependence of RMXS intensities of the magnetic reflections ($^5/_2\ ^5/_2\ ^5/_2$) and ($^5/_2\ ^5/_2\ ^3/_2$) at the Ce L_3 edge (upper panel) and at the Fe K-edge (lower panel). The insets show the resonant enhancement around the Ce and Fe absorption edges.

directions, by rotating the sample around the scattering vector (indicate azimuthal scans), we can determine the moment direction of both Ce and Fe magnetic sublattices. The results indicate that the Ce moments to be parallel to the propagation vector [$^1/_2$,$^1/_2$,$^1/_2$] within each magnetic domain. The excellent fit of such a simple model to the experimental points in **Figure 124** (top panel) leaves little doubt as to this assignment. The difficulty is that all previous neutron-diffraction results appear inconsistent with this interpretation [2]. In addition, Mössbauer spectroscopy (sensitive to the Fe atoms) was inconsistent with a simple collinear arrangement of the Fe moments [3]. Indeed, the azimuthal scans at the Fe K-edge (**Figure 124**, bottom panel) shows a modulation in the azimuthal dependence, indicating that not all the Fe moments can lie along the [111] direction. Unfortunately, however, the enhancement at the Fe K edge is so weak that a definite assignment of the Fe moment orientation in the AF state cannot be obtained with RMXS.

A neutron experiment was then designed at the D10 instrument, Institute Laue Langevin, using a single crystal and gathering a larger data set than previously collected with polycrystalline samples. The analysis of this data set (330 reflections measured, reducing to 72 inequivalent data points) showed unambiguously that the Fe moments are noncollinear. The resulting configuration is shown in **Figure 125**. Indeed the molecular field provided by the Fe moments has its major component along the [111] direction in **Figure 125**; thus forcing the much smaller Ce moments to be along this direction (in agreement with the synchrotron experiments as shown in **Figure 124**). However, in addition, there is a noncollinear component with the smaller Fe moment of 1.1 μ_B.

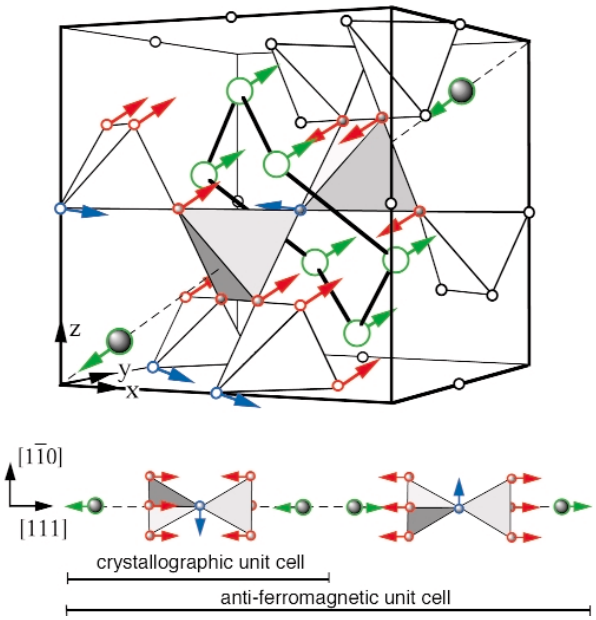

Fig. 125: Magnetic structure of the antiferromagnetic state obtained combining neutron and RMXS scattering results. The smaller "blue" Fe moments are indeed dynamic in nature, both in the antiferromagnetic ground state and in the ferromagnetic state.

The resulting model can be used to rationalise many of the unusual and conflicting experimental results reported for this material in literature, and can explain the dynamical properties of the magnetic ground state found in pure $CeFe_2$ [4].

References

[1] O. Eriksson *et al.*, *Phys. Rev. Lett.* **60,** 2523 (1988).
[2] S. J. Kennedy and B. Coles, *J. Phys. Cond. Mat.* **2**, 1213 (1990).
[3] J-P. Sanchez *et al.*, *Hyperfine Interact.* **133**, 5 (2001).
[4] L. Paolasini *et al*, *Phys. Rev. Lett.* **90,** 057201 (2003); *Phys. Rev. B* **58,** 12117 (1998).

Authors

L. Paolasini (a), B. Ouladdiaf (b), N. Bernhoeft (c), J–P. Sanchez (c), P. Vulliet (c), G. H. Lander (d), and P. Canfield (e)
(a) ESRF
(b) ILL
(c) CEA-Grenoble (France)
(d) European Commission, JRC, Karlsruhe (Germany)
(e) Iowa State University (USA)

E1-E2 X-ray Resonant Scattering

Near-edge X-ray absorption (and particularly its dichroism) and X-ray scattering are powerful techniques in the study of the microscopic properties of matter.

Until a few years ago, experimental investigations and theoretical treatments have mainly focussed on resonant processes involving pure E1 (electric dipole) and E2 (electric quadrupole) transitions between core levels and empty valence states. Only recently Goulon and his collaborators [1] have pointed out the importance of the study of resonant absorption processes induced by the E1-E2 interference. They have observed three new effects, termed respectively X-ray natural, nonreciprocal and magnetochiral dichroism. In each case the inner-shell excitation is controlled by the E1-E2 interference. Observing a non-vanishing signal thus requires an ordered structure and the breaking of space inversion symmetry.

A theoretical interpretation of these effects has been given by Carra *et al.* [2]; it relates the observed spectra to microscopic polar and magnetoelectric properties of the sample.

The importance of E1-E2 processes in resonant X-ray scattering has emerged from experiments of Templeton and Templeton [3] and numerical calculations by Elfimov *et al.* [4]. A description of these effects, which requires an analytical study of the properties of the $f_{E1\text{-}E2}$ scattering amplitude, has been given by the ESRF theory group; working within an atomic model and using a spherical tensor representation, it has been shown that $f_{E1\text{-}E2}$ can be written as a linear combination of pairs of irreducible tensors of increasing rank K = 1,2,3. Each pair is given by the scalar product between a geometrical factor (dependent on light polarisation and wave vector) and the ground-state expectation value of an effective one-electron operator (order parameter) obtainable from the orbital and spin angular momentum **L** and **S**, the electric dipole **n** = **r**/r and from the magnetoelectric tensors $\Omega_{\mathbf{L}} = (\mathbf{L}\times\mathbf{n}\text{-}\mathbf{n}\times\mathbf{L})/2$ and $\Omega_{\mathbf{S}} = (\mathbf{n}\times\mathbf{S})$.

In particular, it has been shown that the spin-independent scattering amplitude describing excitations at the K-edge can be written as a linear combination of three orbital polar (O^{K+}) and three orbital magnetoelectric (O^{K-}) order parameters (the operators O^{K+} and O^{K-}, for K = 1,2,3 are listed in **Table 2**. Notice that the operators depicted in red cannot be detected by X-ray absorption experiments, as their angular dependence vanishes in the forward direction). The order parameters ($O^{K\pm}$) can be independently measured by selecting appropriate experimental conditions.

The presence of $O^{1+} = \mathbf{n}$ in the resonance-scattering amplitude indicates the possibility of observing ferroelectric and antiferroelectric Bragg peaks using X-ray resonant scattering.

K	O^{K+}	O^{K-}
1	**n**	$\Omega_{\mathbf{L}} = (\mathbf{L}\times\mathbf{n}\text{-}\mathbf{n}\times\mathbf{L})/2$
2	$(\Omega_{\mathbf{L}},\mathbf{L})^2$	$(\mathbf{n},\mathbf{L})^2$
3	$(\mathbf{n},(\mathbf{L},\mathbf{L})^2)^3$	$(\Omega_{\mathbf{L}},(\mathbf{L},\mathbf{L})^2)^3$

Table 2: Spinless order parameters.

Ferroelectric reflections could be observed, for instance, near the Ti K-edge (≈ 4966 eV) in barium titanate by selecting the σ→σ channel (*e.g.* $\varepsilon_f = \varepsilon_0 = \varepsilon_\perp$ where ε_f and ε_0 are the polarisations of the outgoing and incoming photon; for the definition and notation adopted see **Figure 126**) when the quantisation axis z is such that $\boldsymbol{U}_2.\hat{z} = \pm 1/\sqrt{5}$.

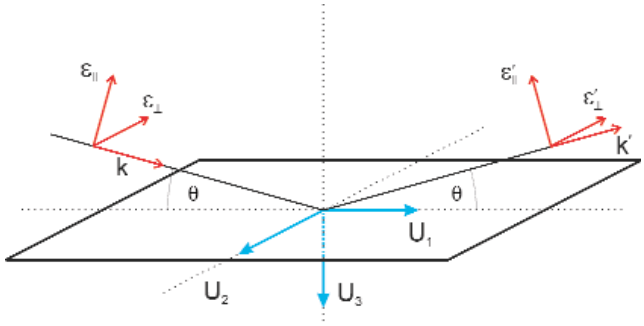

Fig. 126: Scattering geometry. The basis U_1, U_2 and U_3 are respectively given by: $U_1 = (\hat{k} + \hat{k}')/2\cos\theta$, $U_2 = (\hat{k} \times \hat{k}')/\sin 2\theta$ and $U_3 = (\hat{k} - \hat{k}')/2\sin\theta$.

In summary, our theoretical studies of the excitation mechanism involving non-pure transitions as E1-E2, open up new possibilities for the investigation of the electronic properties in noncentrosymmetric crystals using X-ray absorption and resonant scattering. The results obtained indicate the possibility of detecting Bragg peaks from ferroelectric, antiferroelectric and magnetoelectric crystals using X-rays at resonance.

References

[1] J. Goulon, A. Rogalev, F. Wilhelm, C. Goulon–Ginet, P. Carra, D. Cabaret, and C. Brouder, *Phys. Rev. Lett*. **88**, 237401 (2002), and references therein.

[2] P. Carra, A. Jerez and I. Marri *Phys. Rev. B* **67**, 045111 (2003).

[3] D. H. Templeton and L.H. Templeton, *Phys. Rev B* **49**, 14850 (1994).

[4] I.S. Elfimov, N.A. Skorikov, V.I. Anisimov and G.A. Sawatzky, *Phys. Rev. Lett*. **88**, 015504 (2002); **88,** 239904 (E) (2002).

Principal Publication and Authors

I. Marri (a) and P. Carra (b), *in print Phys. Rev. B* **69** (2004).

(a) S³ and INFM, Università degli Studi di Modena e Reggio Emilia (Italy)

(b) ESRF

Fig. 127: Tomographic images showing the internal structures of the head of an earwig (*Forficula auricularia*), allowing the visualisation of the skeleton and muscles (Courtesy W.K. Lee, *APS*, O. Betz, *Zoologisches Institut, Kiel* and P. Cloetens, *ESRF*).

X-ray Imaging

Introduction

The X-ray imaging and microanalysis research effort, while of very wide application, exhibits a few easily-identifiable trends. These result from both the scientific demands and new technical capabilities such as improvements in the optics, detectors and computers and also in the stability of the X-ray source. These trends are the combination of medical imaging and therapy, the technical effort to produce higher spatial and temporal resolutions, and the implementation of adequate sample environments for *in situ*, real-time, experiments.

Biomedical research is an important activity, where there is an intimate link between X-ray imaging and radiotherapy. Our activity in this area is highlighted this year by the article on the treatment of brain tumours, an illness where the present number of treatments, and their efficiency, is unfortunately quite poor. The area of Microbeam Radiation Therapy (MRT) was described in last years *Highlights*. MRT is a very promising technique that is being actively developed at a preclinical stage. This development is carried out by identifying the best conditions to increase the survival, or even cure, the treated animals, and through more fundamental studies, at the cellular level, so that we can better understand the mechanisms of the action of the microbeams. Another radio-therapeutic approach is presented here: tomography-like radiotherapy combined with a contrast agent, which we call “Photoactivation Therapy”, PAT. This type of radiation therapy uses a monochromatic beam with an energy optimised for an enhancement of the dose deposited at the level of the tumour; the choice of the energy depends on the heavy element (platinum or iodine) used as the dose-enhancing agent. The survival curves obtained are more than encouraging. A major effort is being made to gain simultaneously a deeper understanding of the biological mechanisms involved in PAT and to investigate its clinical impact and implementation. The second article in this chapter describes the application of the K-edge subtraction method, originally developed for coronary angiography, to functional lung imaging of an animal model, using Xe gas as contrast agent. This medical-imaging investigation allows a deeper understanding of the factors affecting ventilation, which are very important for a better treatment of diseases like asthma.

A second area of intense research is Imaging with very high spatial resolution. **Figure 127** shows a recent example, where the inner part of an insect head has been visualised using tomography. The report on X-ray imaging of vascular networks, also emphasises the necessity of high spatial resolution: to understand the physiological role of the micro-vascularisation of the brain, visualisation of the vascular structure at the micrometre or even sub-micrometre scale is required. This was achieved for the first time using microtomography with an appropriate contrast agent.

As indicated above, an important feature of the X-ray imaging field is the very wide range of applications making use of the techniques. In addition to the biomedical applications, there are numerous applications from the fields of

materials science and physics, which also benefit from the unique possibilities on the beamlines.

Porosities in quasicrystals are well visualised with phase-contrast imaging. The pore sizes were found to be much higher than those observed on crystals of the same composition. The evolution of the pores during a high vacuum annealing appears compatible with a vacancy diffusion mechanism; however, their origin remains a puzzle. This article also emphasises the importance of the sample environment, which allow *in situ* and real-time measurements.

Other highlight articles concern the analysis of grain compaction by X-ray microtomography this helps our understanding of the slow dynamics of non-equilibrium systems. Another example concerns the investigation of GaN, a very important material for new electronic devices. In this last case, the homogeneity is a key parameter, which was investigated in highly-doped Mn-GaN by using microanalytical techniques.

Synchrotron radiation microanalysis is an essential tool for many environmental studies, which, in addition to using the established techniques, involve development of new ones. Combined X-ray transmission, fluorescence and Compton scattering helical microtomography is a developing technique, which allows a precise quantitative reconstruction of the internal elemental composition and structure of the measured slice. This new method was applied to the investigation of a fly-ash particle.
A new super-hard shock-induced polymorph of carbon was identified (probably resulting from a meteorite impact), that had not been predicted by any theoretical calculation.
The degassing of sulphur during volcanic eruptions is a very important subject that remains unsatisfactorily explained. The evolution from Fe^{3+} to Fe^{2+} under conditions close to those in magmas during their ascent from the Earth's mantle to the surface was investigated by μXANES. Understanding the redox conditions furthers our knowledge of the whole process.

The intense activity in all of the areas mentioned will clearly lead to new developments in the near future. This is particularly true for radiation therapy and "nano-tomography". In this last case, an effort is foreseen to improve the spatial resolution to the 100 nm range, and in the longer term, to a few tens of nm.

J. Baruchel

Radiation Therapy using Monochromatic X-rays

Review of new developments in fundamental and applied research at ID17 by F. Esteve on behalf of the INSERM U647 RSRM Team Members (INSERM-RSRM CHU/ESRF Grenoble, France)

Despite considerable efforts in cancer therapy, brain tumours like gliomas, are still considered to be some of the most radioresistant tumours. Incidence rate of gliomas is about 5/100 000 and virtually no patient with high-grade glioma survives for more than five years after the disease diagnosis.

The research programs developed by the RSRM team, with the active support of beamline **ID17**'s staff, have explored and confirmed the potential of high-flux monochromatic beams for radiation therapy purposes. At ID17 appropriate infrastructure has allowed the development and the optimisation of innovative chemo-radiotherapy treatments against brain tumours using the particular properties of synchrotron radiation.

Theoretically, to irradiate high-Z elements at their respective K-edge absorption energy leads to Auger electrons and photoelectrons releasing a large amount of energy in their immediate vicinity. For this phenomenon to occur, called *photoactivation*, requires a powerful monochromatic radiation beam of appropriate energy is required. To date, only synchrotrons allow the production of high-fluence monochromatisable X-rays necessary to reach the above requirements.

We first assessed the enhancement of dose delivered to tumours cells [1], when using the appropriate wavelengths. For instance, when using iodine as a high-Z compound, the optimal energy deposit is obtained close to 50 keV. Extensive cell survival curves studies after irradiation were performed by using various combinations of high-Z compounds, either a simple iodinated contrast agent or chemotherapy drugs containing a heavy element [2] (platinum or iodine). The first preclinical trials were carried out on rats bearing F98 brain glioma using the method previously developed for brain perfusion imaging. These very first preclinical trials [3] have shown that it is possible to master the irradiation procedure with regards to the wavelength choice and to the ballistic (**Figure 128**), thus leading to an optimal energy deposit in the tumour while sparing surrounding tissues. The same procedure was then used to test the combination of chemotherapy and radiotherapy.

At the same time, analysis of the onset of DNA damages dependency on the wavelength and the added high-Z compound was also carried out. *In vitro* experiments

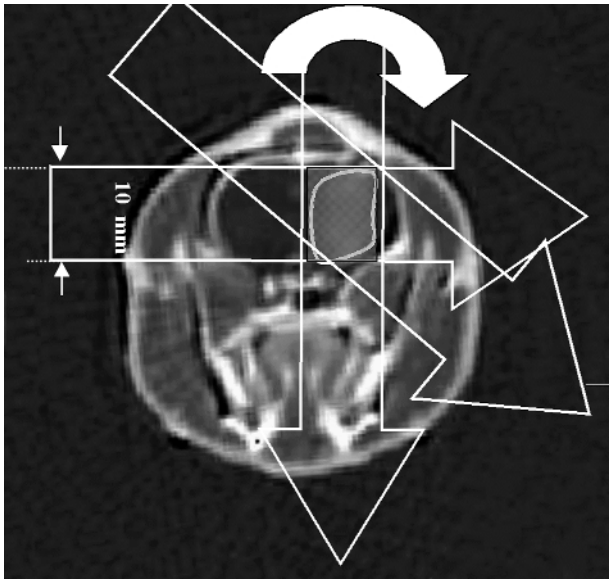

Fig. 128: Irradiation protocol: the tumour is centred on the rotation axis. The beam dimensions are reduced (10 mm wide by 0.8 mm thick). A cylinder of 10.4 mm height and 10 mm diameter is then homogeneously irradiated in tomographic mode. The iodine delineates the tumour volume. When targeted with the appropriate photon wavelength, a dose enhancement effect is caused by the photo electrons emitted by the iodine, leading thus to a better tumour control.

were performed with drugs or contrast agents widely used in clinics to check the different achievable radiosensitisations at the DNA scale.

Hence, to irreversibly damage the DNA of tumour cells, an ideal anti-cancer treatment would consist of combining DNA-binding photoactivable high-Z compounds with monochromatic synchrotron irradiation at their K-edge energy. Among the candidate drugs, molecules containing platinum atoms (Z = 78; K-edge energy: 78.4 keV), such as cis-diamminedichloroplatinum (II) (CDDP), are widely used in anti-cancer treatments. The RSRM team has attempted to observe the synchrotron CDDP photoactivation effect *in vitro* and *in vivo*, which they have called PAT-Plat. For the first time, a molecular model explaining the biological mechanisms involved in PAT-Plat was proposed and its clinical impact is being investigated [4].

There is now evidence that unrepaired DNA double-strand breaks (DSBs) are the key lesions responsible for cell lethality. In response to radiation, mammalian cells activate two independent DSB repair pathways: 1) the non-homologous end-joining (NHEJ), consisting roughly of the ligation of broken DNA strands. This repair pathway depends upon the protein kinase DNA-PK activity; 2) the homologous recombination, consisting of inserting homologous copies of lacking fragments inside the break. This pathway is mediated by the RAD51 protein, which, when activated, appears in cell nuclei as discrete dots called *foci* (**Figure 129**). Unlike radiation, CDDP does not induce DSBs but DNA adducts, generally repaired by a RAD51-dependent recombination. Furthermore, it is known that high concentrations of CDDP inhibit the DNA-PK activity and block the NHEJ repair pathway. Hence, CDDP treatments combined with radiation raise the question of the interplay between two major DNA repair pathways.

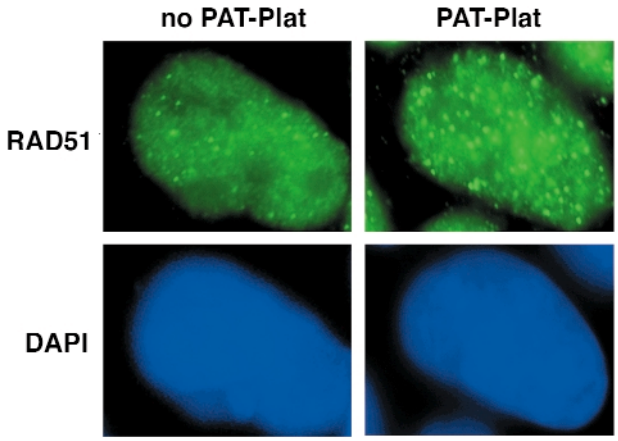

Fig. 129: Wavelength dependency of the DNA damages repair mechanisms. RAD51 nuclear relocalisation in human head and neck carcinoma SQ20B cells treated with CDDP and exposed to synchrotron radiation. Representative examples of RAD51 foci (green dots) in cells irradiated at 78.0 keV (below the platinum K-edge) (left panels) or at 78.8 keV (above the platinum K-edge; PAT-Plat conditions). Cell nuclei are counterstained with DAPI dye (blue). The number of foci is much higher above the platinum K-edge.

After irradiation at synchrotron X-ray energy above the platinum K-edge (PAT-Plat conditions), CDDP-treated cells showed three times more DSBs than at energies below the platinum K-edge. Furthermore, these DSBs induced in excess at energy above the platinum K-edge were preferentially produced at the close vicinity of the CDDP-induced DNA adducts and were more slowly repaired than in any other conditions [4]. These findings suggest that PAT-Plat produces specifically more complex and more severe DNA damage in CDDP-treated cells than at any other energy. DNA-PK activity was found to be completely deactivated while RAD51 foci appeared more numerous in each cells, as if PAT-Plat effect would result in the inhibition of NHEJ and forces cells to repair by a recombination pathway [4] (see **Figure 129**). PAT-Plat effect was therefore suggested to be particularly efficient in recombination-deficient cells like tumours. Hence, PAT-plat conditions were naturally applied *in vivo* to rats bearing glioma. Preliminary studies showed encouraging results with a striking protraction of life span (about 200 days after tumour inoculation) associated with a progressive disappearance of tumour tissue [5]. Our very last experiments led to the most protracted survival (34% at one year) ever reported with this radioresistant glioma model and demonstrate the interest of powerful monochromatic X-ray sources as new tools for cancer treatments [6].

References

[1] F. Estève, S Corde, H. Elleaume, J.F. Adam, A. Joubert, A.M. Charvet, M.C. Biston, J. Balosso, J.F. Le Bas, *Academic Radiology,* Aug 9 Suppl 2: S540-3 (2002).

[2] S. Corde, PhD thesis, October 2002; and paper submitted to *British Journal of Cancer.*

[3] J.F. Adam, H. Elleaume, A. Joubert, M.C. Biston, A.M. Charvet, J. Balosso, J.F. Le Bas, F. Estève, *Int. J. Radiat. Oncol. Biol. Phys.,* **57**(5), 1413-1426 (2003).

[4] S. Corde, J. Balosso, H. Elleaume, M. Renier, A. Joubert, M.C. Biston, J.F. Adam, A.M. Charvet, T. Brochard, J.F. Le Bas, F. Estève, and N. Foray, *Cancer Research* **63,** 3221-3227 (2003).

[5] M.C. Biston, A. Joubert, H. Elleaume, J.F. Adam, A.M. Charvet, S. Corde, J.F. Le Bas, F. Estève and J. Balosso, *12th International Congress of Radiation Research,* Brisbane, (August 2003).

[6] M.C. Biston, A. Joubert, J.F. Adam, H. Elleaume, S. Bohic, A.M. Charvet, F. Estève, N. Foray, J. Balosso, accepted, *Cancer Research* (2004).

Synchrotron Radiation CT of Regional Pulmonary Ventilation

The K-edge Subtraction (KES) method was originally developed for human coronary angiography. Subsequently the method has been used in many other fields of medical imaging. For KES imaging, a contrast agent is introduced into the organ to be imaged, and two simultaneous images are recorded using two X-ray energies that bracket the K-absorption edge of the contrast agent. The difference image in a logarithmic scale yields the distribution of the contrast agent while the signal from the other parts of the object is eliminated.

The KES method has been applied to functional lung imaging of an animal model (rabbit) using the stable Xe gas as the contrast agent [1]. The rabbit is anaesthetised and mechanically ventilated, and methods for fast tomographic imaging were developed. The absolute concentration of the Xe gas could be determined as a function of time within cross-sectional slices of the lung. The time evolution of the concentration follows a simple exponential function, and the time constant τ and the specific ventilation ($s\dot{V}=1/\tau$) can be determined at each individual volume element of the slice. The spatial resolution is 0.1 mm^3, which is two orders of magnitude better than the resolution achieved by any other method for lung imaging. Additionally, the noise level of the images is an order of magnitude lower than the noise level achieved by traditional Xe-enhanced CT imaging.

An adequate recruitment of the different lung compartments is an important factor in anaesthesia and intensive care, where mechanical ventilation is used. In the present work the effects of the tidal volume (VT) of inspiration on the ventilation distributions were studied in much greater detail than in previous studies. Overall differences between lung compartments were observed, but the uniformity of ventilation improved in each compartment when VT was increased. A series of ventilation maps is shown in **Figure 130**. For each slice, the time constants have a log-normal distribution, which is interpreted to arise from the fractal structure of the bronchial tree. The excellent spatial resolution of the KES method with Xe gas as the contrast agent allows studies of the fractal structure over many more generations than has been possible before. This will allow the first measurement of the size of the functional unit of lung ventilation. Future studies are expected to lead to a deeper understanding of the factors affecting ventilation.

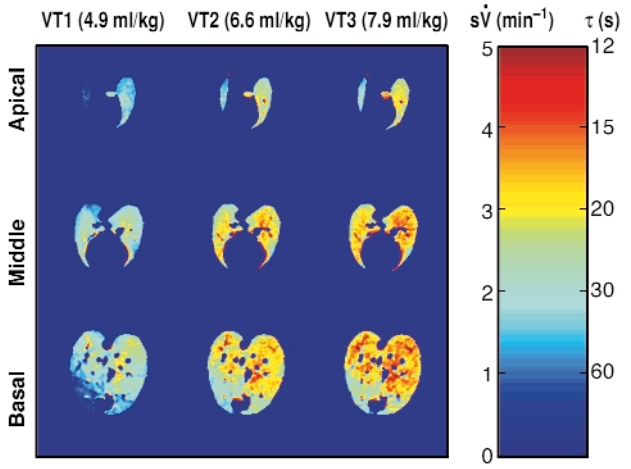

Fig. 130: Maps of specific ventilation ($s\dot{V}$) and time constant (τ) in one rabbit, obtained at apical, middle and basal lung levels, for 3 different tidal volumes (VT: volume of air inspired in each respiratory cycle). The color scale is given in (min^{-1}) and in (s), respectively. $s\dot{V}$ increased in all lung regions when VT increased. There was a significant difference in $s\dot{V}$ between dorsal and ventral areas at the basal lung level.

Reference

[1] S. Bayat *et al.*, *Phys. Med. Biol*. **46,** 3287 (2001).

Principal Publication and Authors

L. Porra (a), S. Monfraix (b,c), G. Berruyer (b), C. Nemoz (b), W. Thomlinson (b,d), P. Suortti (a), A.R.A. Sovijärvi (e), and S. Bayat (b), *J Appl. Physiol, in press.*

(a) University of Helsinki (Finland)

(b) ESRF

(c) UMR CNRS 5525, Université Joseph Fourier, Grenoble (France)

(d) Canadian Light Source (Canada)

(e) Helsinki University Central Hospital (Finland)

High-resolution X-ray Imaging of Vascular Networks

There is growing interest in high-resolution imaging of vascular structures for different physiological or pathological problems [1]. In the context of brain vascular imaging, *in-vivo* synchrotron tomography has permitted the measurement of contrast agent concentration and local blood flow for the whole brain of a rat with the unprecedented spatial resolution of 350 micrometres [2]. This resolution still remains inadequate compared with the few micrometre scale of small vessels. Since 50% of the vessel diameters in the cerebral cortex are distributed between 3 to 10 micrometres, micrometre resolution is necessary to get important information about the vascular network at the scale of small capillaries. Even if synchrotron X-rays offer such an opportunity, a specific biological sample preparation is needed. A contrast agent concentration much larger than those of CT-scan angiography has to be injected into the vascular network. Moreover, the total vascular relative volume is only 3 to 5% in either human or rat brain. Hence, the effective vascular contribution to X-ray absorption or phase contrast represents a cumulated thickness of a few tens of micrometres only, along the few millimetres of the total X-ray path inside the tissue. This is why we have developed a sample preparation specific to synchrotron high-resolution X-ray tomography that has permitted the visualisation of the micro-vascular structure of the brain's cortical grey matter. The X-ray absorption inside the sample is due to the cumulated contribution of the epoxy-resin around and inside the biological sample and the injected solution inside the vascular network. The histograms shown in **Figure 131** have been obtained from the three-dimensional attenuation maps of barium injected samples for an X-ray energy of 20 keV and a sample-detector distance D = 13 mm at the **ID19** beamline. This histogram shows two well-separated peaks. The first one is associated with the epoxy-resin, while the second one corresponds to contrast-agent absorption in the vessels. Volume renderings of the resulting 3D images are shown in **Figure 132a** and **132b**, which are maximum-intensity projections of barium injected samples. The vessel density observed on these images illustrates the quality of the preparation, while the apparent high vessel density of the rather loose vascular network results from the projection over a one-millimetre thickness. These

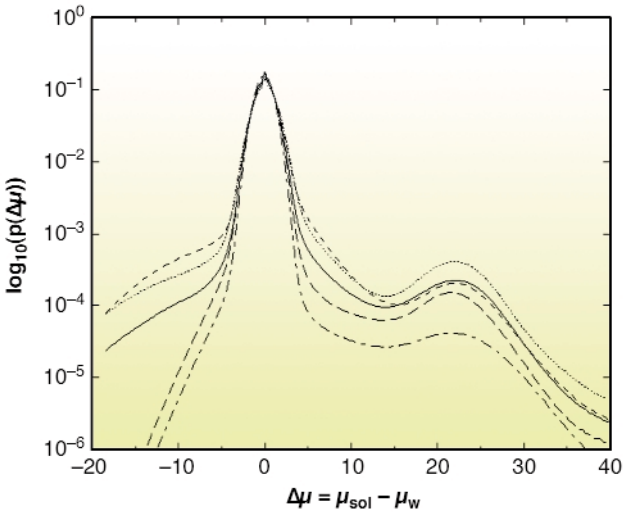

Fig. 131: Normalised histograms p(Δμ) of the relative linear attenuation coefficient $\Delta\mu = \mu_{sol}$-μ_w measured from the same rat, for an injected barium concentration equal to 600 mg/ml.

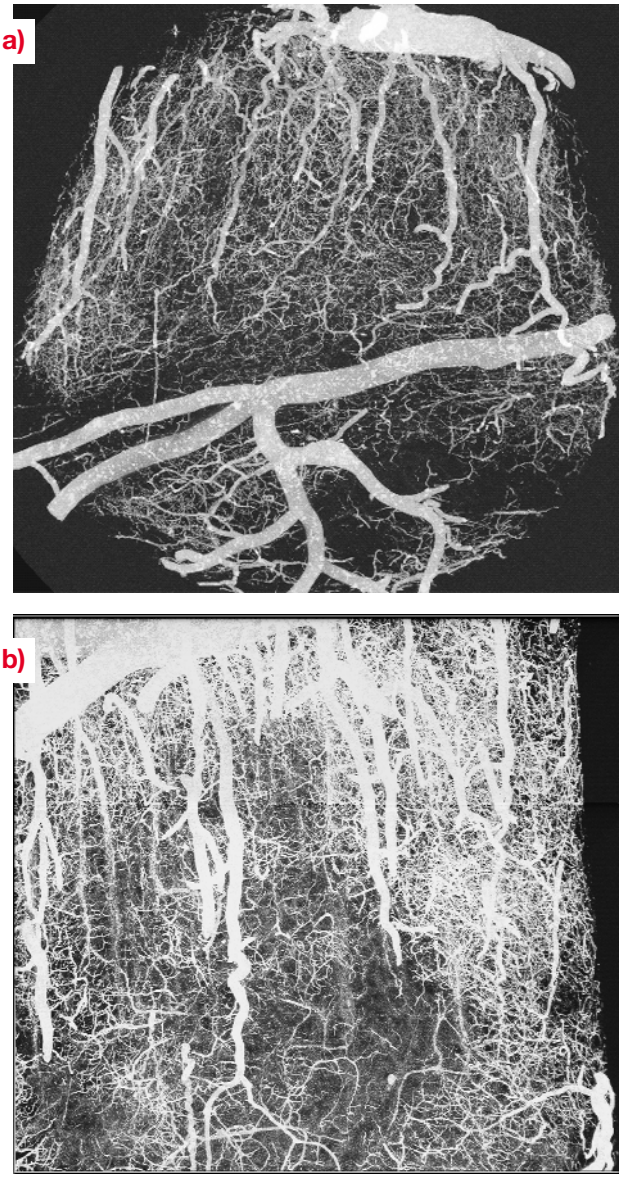

Fig. 132: Volume renderings of a rat brain cortical sample injected with barium (600mg/ml), obtained at 20 keV in absorption mode with a voxel size equal to 1.4 micrometre. Maximum intensity projections have been performed for volumes with a size equal to Δx = 1.5 mm, Δy = 1.5 mm, Δz = 1 mm. (a) projection in the x-y plane of a sample extracted from the fronto-central cortex, (b) x-z projection for a sample from the frontal region.

renderings also demonstrate the quality of the local vessel contrast obtained with the highest barium concentration (600 mg/ml). The views show columnar structures that spread through the grey matter depth from the pial surface. Those renderings are, to our knowledge, the first visualisation of the vascular structure of the cortex's grey matter over its entire thickness, on the micrometre scale. The quantitative analysis of the 3D images will provide important morphometric information, of interest to different areas where the micro-vascularisation plays a key role such as physiological and pathological angiogenesis and brain functional imaging whose basic principles rely on cortical micro-vascularisation.

References

[1] A.S. Popel, A.R. Pries, and D.W. Laaf, *J. Neuro. Meth,* **111,** 911-913, (1998); R. Weissleder and U. Mahmood, *Radiology,* **219**, 316-333, (2001).
[2] H. Elleaume, A.M.. Charvet, S. Corde, F. Estève and J.F. Le Bas, *Physics in Medecine & Biology*, **47**, 3369-3385, (2002).

Principal publication and Authors

F. Plouraboué (a), P. Cloetens (b), C. Fonta (c), A. Steyer (d), F. Lauwers (e) and J-P Marc-Vergnes (e), submitted to *J. Microsc.* (2003).
(a) IMFT, UMR 5502, Toulouse (France)
(b) ESRF, Grenoble, (France)
(c) CERCO, UMR 5549, Toulouse, (France)
(d) Université de Paris I, (France)
(e) INSERM U455, Toulouse, (France)

Investigation of the Porosity in Icosahedral Al-Pd-Mn Quasicrystals

Defects are known to modify the physical properties of crystalline solids. This general feature also applies to quasicrystals, and it is therefore necessary to obtain as perfect as possible quasicrystalline single grains to identify intrinsic or defect-related properties. High quality quasicrystals have been grown that display rocking curve widths comparable to those of the best metallic crystals. Nevertheless, porosity is systematically observed in the volume of Al-Pd-Mn quasicrystals. These pores occupy a volume fraction much higher than the one observed in usual crystals (like Al), and their size can also be approximately 1000 times bigger in the quasicrystal than in the simple metal. The formation mechanisms of pores known from crystals do not seem to explain satisfactorily the porosity in quasicrystals and hence the origin of these pores remains unclear. Two hypotheses have been proposed to explain the occurrence of porosity. The first one assumes that pores are generated from the condensation and migration of thermal vacancies [1], whereas the second suggests that they could be an intrinsic characteristic of the quasicrystalline structure [2]. When starting the present work, there was no experimental evidence proving the overall validity of one of these hypotheses.

We have performed an *in situ* study, using synchrotron X-ray phase contrast radiography, of the porosity evolution in an icosahedral Al-Pd-Mn quasicrystalline single grain during two annealing cycles up to 800°C. The high-temperature experiments were carried out at the **ID19** beamline in an unstrained sample heated in an ultra high vacuum chamber designed at the CRMC2 (Marseille, France). The phase contrast radiographs were recorded on a CCD-based camera, using an optics providing a spatial resolution of the order of 1-2 µm.

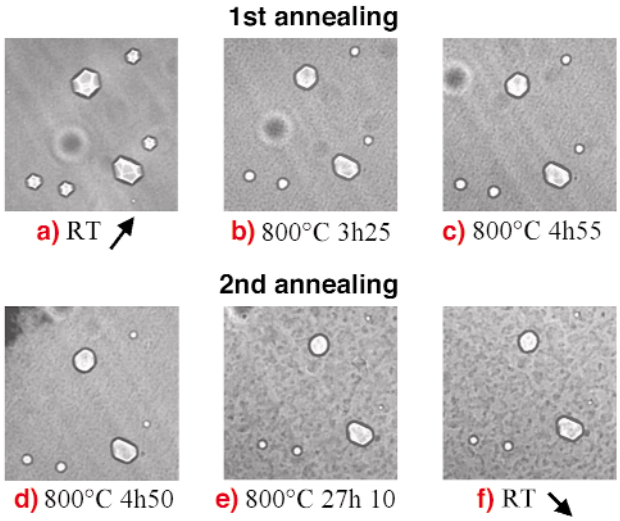

Fig.133: Evolution produced by annealing at 800°C, of the porosity in an Al-Pd-Mn quasicrystalline single grain.

Figure 133 shows the porosity evolution in a small region of the sample during both annealing cycles. The size of pores decreases very rapidly during the first annealing cycle (**Figures 133a** to **133c**). Moreover the shape of the pore images changes from faceted to round and the white line contrasts observed inside the pores images, which are associated with the edges of the dodecahedral shape of the pores, disappear. During the second annealing cycle (**Figures 133c** to **133e**), the sizes of the pores further decrease, though less rapidly than in the first cycle. The shape of the pores images becomes more and more round with the annealing time. Two different parts can be observed in the shrinkage curves shown in **Figure 134** (independently of the pore size and of the number of cycles): a steep first part, composed of few data points, with a high shrinkage rate (part I) and a second one with a smaller shrinkage rate (part II). These two shrinkage regimes were analysed using the diffusion-annealing model developed by Volin and Balluffi [3] for

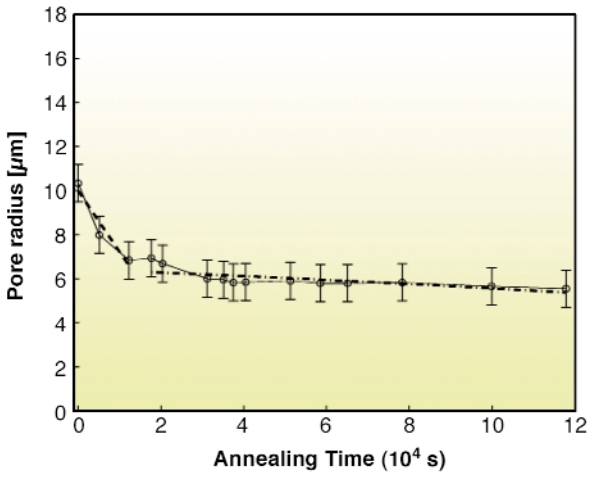

Fig. 134: Shrinkage of the pore dimension with annealing time.

the shrinkage of nanometric pores in thin quenched and annealed foils of pure crystalline aluminium. This model assumes that atoms are transported to pores from the external surfaces by migration of vacancies and that a local vacancy equilibrium is maintained at all interfaces, implying that the kinetics is diffusion-controlled. The "part II" regime was found consistent with the self-diffusion of aluminium whereas the "part I" one was explained by an accelerated diffusion in the deformed structure or an equilibration of the vacancy concentration in the bulk.

These results indicate an influence of the vacancy diffusion on the high temperature evolution of porosity that could support the hypothesis of vacancy condensation. However, such a simple approach should lead to a uniform distribution of pores in the volume of quasicrystals. This is not consistent with the observed variation of the size distribution of pores, which could indicate more complex influences, during the solidification process, on the porosity formation. In order to check this hypothesis as well as to get an insight of the porosity nucleation mechanisms, *in situ* solidification experiments are currently in progress.

References

[1] C. Beeli, T Gödecke and R. Lück, *Phil. Mag. Let.* **78**(5), (1998), 339.
[2] C. Janot, L. Loreto, R. Farinato, L. Mancini, J. Gastaldi and J. Baruchel, *Mat. Res. Soc. Proc.* **553**, (1999), 55.
[3] T. E. Volin and R.W. Balluffi *Phys. Stat. Solidi*, **25**, (1968), 163.

Principal Publication and Authors

S. Agliozzo (a), J. Gastaldi (b), H. Klein (c), J. Härtwig (d), J. Baruchel (d), E. Brunello (d), *Phys. Rev. B*, accepted.
(a) Institute for Scientific Interchange, Torino (Italy)
(b) CRMC2, CNRS, Marseille (France)
(c) CNRS, Grenoble (France)
(d) ESRF, Grenoble (France)

Analysis of Granular Compaction by X-ray Microtomography

The slow dynamics of out-of-equilibrium systems remains a source of debate. Even though granular media are not thermal systems, their relaxation under weak mechanical perturbations have a formal analogy with the slow dynamics of out-of-equilibrium thermal systems. This analogy is based on the idea that the geometry of the system is more important than any other parameter as the type of driving energy or the mechanical interaction between particles. Slow compaction of shaken granular packing - the progressive increase of the packing fraction - appears to provide fundamental information for the investigation of the above analogy. The study presented here used X-ray microtomography to characterise the microstructure of granular packing undergoing compaction.

We used an experimental setup simular to previous ones [1,2]: 200-400 μm diameter glass beads were poured to a height about 80 mm in an 8 mm inner-diameter glass cylinder. This was vertically shaken for a given number *N* of sinusoidal excitations at a frequency of 70 Hz. Microtomographical analysis at beamline **ID19** was then used to reconstruct granular packings (**Figure 135**). The intensity of the vibration is characterised by Γ, the maximal applied acceleration normalised by gravity. The pixel size is 4.91 μm and the spatial resolution is 10 μm.

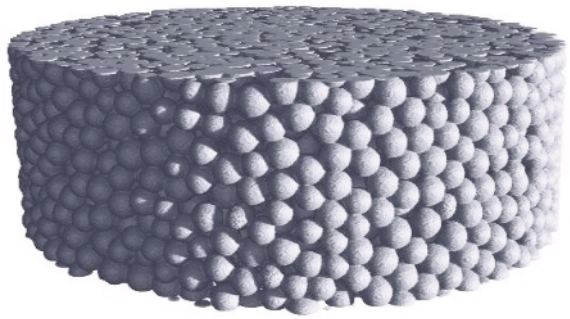

Fig. 135: Part of a reconstructed packing.

By comparison with the small decrease in the average distance between grains accompanying compaction, evidence of a transformation in the packing microstructure appears to be better described by the size of the interstitial voids. Following previous work [3] we defined a pore size via the Voronoi tessellation and normalised it by the mean volume of a grain <*w*>. **Figure 136** presents the evolution of the pore volume distribution for Γ = 3.0 at different stages of the compaction. An exponential decay law is found for the distribution of the voids, at least for the pores larger than octahedral pores. The exponential shape persists during the compaction of the packing yet with a

reduction of the tail. These results were found to be very close to results of numerical simulations [3] where there were only geometric constraints in a packing of identical hard spheres. This agreement emphasises the fundamental importance of the steric constraint between the grains that rules the local rearrangements of grains allowed by the shaking energy.

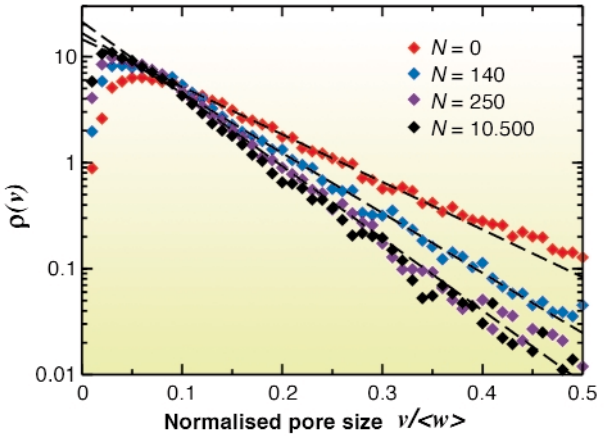

Fig. 136: Evolution of the volume distribution of the pores for Γ = 3.0 at different stages of the compaction.

This study should be completed by considering individual grain motion at each degree of excitation in order to tackle the problem of diffusivity in granular media.

References

[1] B. Knight, C.G. Fandrich, C.N. Lau, H.M. Jaeger, and S.R. Nagel, *Phys. Rev. E* **51**, 3957 (1995).
[2] P. Philippe and D. Bideau, *Europhys. Lett.* **60**, 677 (2002).
[3] P. Philippe and D. Bideau, *Phys. Rev. E* **63**, 051304 (2001).

Principal Publication and Authors

P. Richard (a), P. Philippe (b), F. Barbe (c), S. Bourlès (a), X. Thibault (d) and D. Bideau (a), *Phys. Rev E* **68**, 020301(R) (2003).
(a) Université Rennes I – CNRS, Rennes (France)
(b) ESPCI – CNRS, Paris (France)
(c) INSA Rouen – CNRS, Rouen (France)
(d) ESRF

Quantitative 3D Elemental Microanalysis by Combined X-ray Transmission, Fluorescence and Compton Helical Microtomography

The understanding, control and modification of environmental, chemical and biological processes necessitate their thorough investigation. Certain trace elements (*e.g.* Cr, Se) play an important and not fully understood role in these processes. Therefore, non-destructive, quantitative, 3D, *in situ* investigation of the trace element distribution at (sub)micrometre resolution and their relationship with morphological features is of great interest. While several existing methods (absorption, phase contrast, Compton-tomography) can provide information about the internal structure at the (sub)micrometre scale, only a few techniques (*e.g.* X-ray fluorescence, energy filtered transmission electron microscopy, particle induced X-ray emission tomography) are capable of revealing information about the internal elemental composition. Among these methods only X-ray fluorescence tomography is non-destructive. X-ray fluorescence tomography is based on the detection of characteristic X-ray fluorescence photons. It provides the internal distribution of each chemical element that yields a significant fluorescence signal. However, no information can be obtained about the composition and morphology of the light elements (Z < 13 at ID22) due to their 'non-detectable' fluorescence signals. Since the measured elemental distributions can be significantly modified by the self-absorption within this partly unknown matrix, complementary information is necessary for the quantification of the elemental distributions.

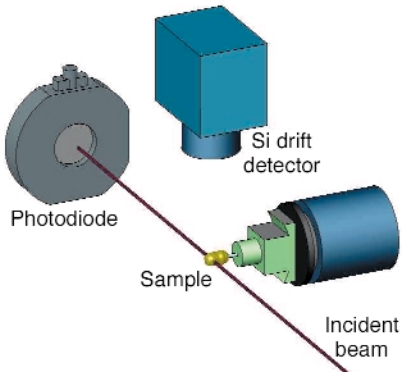

Fig. 137: Experimental setup for a combined transmission, fluorescence and Compton tomography experiment. The sample is scanned in the monochromatic beam of 1-3 μm² (vertical-horizontal) spot-size. Two photodiodes measure the intensity of the incident and of the transmitted beam (indicated in the figure). A Si drift detector measures the fluorescence and Compton signals.

In order to obtain precise quantitative internal elemental distributions, a new non-destructive X-ray technique has been developed at **ID22** by combining simultaneous transmission, fluorescence and Compton microtomography [1] (see **Figure 137** for the experimental setup). Conventional transmission tomography provides the distribution of the total absorption coefficient inside the sample. Compton tomography is based on the signal originating from inelastic single-scattering. With appropriate corrections it can be used for reconstructing the internal electronic density distribution. With the combination of the information of the three tomographic techniques (Integrated Tomographic Technique, ITT [1]) a precise quantitative reconstruction of the internal elemental composition and structure of the measured slice can be obtained.

In order to obtain a truly-volumetric reconstruction, 3D combined XRF/Compton/transmission tomography was performed by a helical scan of the sample in the microbeam. It has been proven that, for a given measurement time, helical tomography provides better longitudinal resolution than conventional tomography. This method was applied for the first time to the combined tomography technique at ID22. A set of planar projections was obtained from the raw helical scan data via the fullscan interpolation method. The quantitative reconstruction of each planar slice was obtained by the Integrated Tomographic Technique (ITT).

Figure 138 shows an application of this method for the investigation of a single waste fly ash particle. Waste fly ash is created during the combustion process in power plants and it consists of fine particles containing potentially toxic trace metals (*i.e.* Pb, Ni, Cu, Cd) in concentrated amounts. Failure to properly tackle the problems associated with the utilisation and disposal of fly ash has serious environmental consequences (air and water pollution). The development of routines for intelligent ash management necessitates knowledge of the chemical properties (quantitative elemental distribution, speciation, morphology) of the ash material at bulk- and micro-level. Individual particle analysis is also a unique method for verifying the theoretical models of fly ash forming mechanisms. In **Figure 138** the distributions of Rb, Mn and Fe are shown as an example. The combined helical tomography reveals that the external layer of the particle has different elemental composition than its inner part. The presence of a fragmented part with higher iron concentration can also be distinguished. These observations give unique information about the possible fly ash formation mechanisms (*e.g.* volatilisation, condensation, diffusion, solid solution formation) during combustion.

In conclusion, a new method to reconstruct the 3D internal elemental composition and its relation with the sample structure has been developed and tested at ID22.

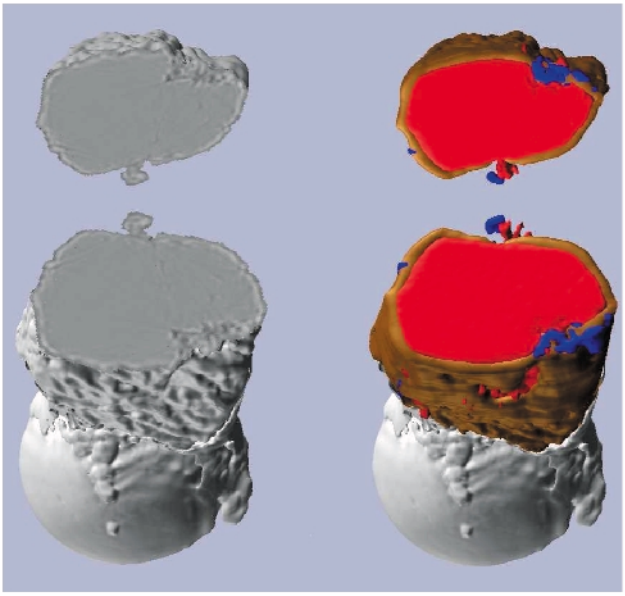

Fig. 138: Three-dimensional rendering of conventional transmission tomography (left) and of the distribution of Rubidium (red), Manganese (brown) and Iron (blue). The sample is glued on the top of a silica capillary, which is partly visible in the lower part of the images. The fly ash particle has been scanned with 7 helical turns, 12 µm/turn helical pitch, 120 angular steps per turn of 3 degrees each, times 80 vertical translation steps of 3 µm each. The measurement time was 1 s/step. Voxel size 3x3x3 µm^3.

References

[1] B. Golosio, A. Simionovici, A. Somogyi, L. Lemelle, M. Chukalina, A. Brunetti, *J. Appl. Phys.* **94**, 145-156 (2003).
[2] B. Golosio, A. Somogyi, A. Simionovici, P. Bleuet, L. Lemelle, J. Susini, accepted for *Appl. Phys. Lett.*.
[3] M. C. Camerani Pinzani, B. Golosio, A. Somogyi, A. Simionovici, B. M. Steenari, I. Panas, accepted for publication in *Anal. Chemistry.*

Authors

B. Golosio (a), A. Somogyi (a), A. Simionovici (a, b), P. Bleuet (a), J. Susini (a)
(a) ESRF
(b) Laboratoire de Sciences de la Terre de l'ENS Lyon (France)

Reversible Reduction-oxidation Processes in Natural Silicate Melts and Magmas

Iron and sulfur may be considered as the couple of elements buffering the redox state of magmas during their ascent from Earth's mantle to the surface. However, the determination of both the redox state of magmas and

the relative variation of the [$Fe^{3+}/(Fe^{3+}+Fe^{2+})$] atomic ratio is challenging because these magmas evolve, crystallise and lose most of their volatile constituents (H_2O, CO_2, H_2S, SO_2, HCl) before being emitted during volcanic eruptions. In addition, the effects of the cooling rate may induce bias in the determination of the redox state of Fe, because of rapid electron exchange. This problem may be addressed by direct *in situ* measurements of the chemical environment of Fe in silicate melts, as a function of temperature.

Previous micro-X-ray absorption spectroscopy (μXANES) experiments indicated that the energy resolution allows an accurate discrimination between the pre-edge features of Fe^{2+} (7111.5 eV) and Fe^{3+} (7113.2 eV) [1]. We provide, here, the first *in situ* μXANES spectra at the iron K-edge (7130 eV) of H_2O-rich silicate glass/melt trapped in natural quartz. The experiments were carried out between 20 and 800°C, using the X-ray Microscopy beamline **ID21**.

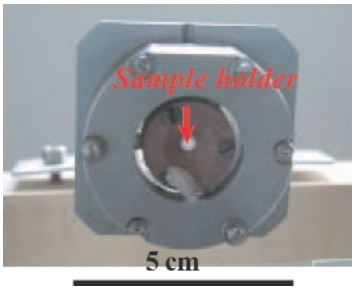

Fig. 139: Water-cooled furnace installed on beamline ID21.

The crystals were prepared as double face polished, 150 μm thick lamella in order to preserve the inclusion in the centre of the crystals and thus isolated from the surroundings. They were placed in a water-cooled furnace (**Figure 139**). The different series of μXANES spectra were collected, in transmission mode, on melt/glass inclusions by decreasing the temperature from 800 to 20°C, in steps of 100°C. The energy was scanned between 7050 and 7350 eV, using a fixed-exit Silicon (220) monochromator. The synchrotron X-ray source was demagnified down to a 2x2 μm^2 probe by using Fresnel zone-plate lenses [2]. In addition, μXANES spectra were acquired at room temperature on a series of reference Si-rich glasses (~70 wt% SiO_2) comparable in composition to the quartz hosted glass inclusions, but with a [$Fe^{3+}/\Sigma Fe$)] ratio varying from 0.05 (reduced) to 0.85 (oxidised). New spectra were also done on basaltic reference glasses (~50 wt% SiO_2). The centroid energy of the pre-edge position (intensity-weighted average of the each component energy) correlates with the Fe^{3+} /ΣFe ratios in both the Si-rich (rhyolitic) and basaltic glasses. Accordingly, this correlation may apply to a large variety of glass samples from basalt to rhyolite. It is confirmed here that an accurate determination of the redox state of Fe in silicate glasses cannot be retrieved with reference to mineral standards.

Figure 140a shows that the pre-edge features significantly and progressively evolved towards a reduced state (Fe^{2+}) at high temperature, up to 797°C, and towards the oxidised (Fe^{3+}) pole when cooling down to 20°C. The μXANES spectrum acquired at 20°C, after experiments involving progressive temperature decrease, is illustrated in **Figure 140b**. It demonstrates the dominance of Fe^{3+} in the pre-edge structure, a shift of the centroid position by nearly 0.5 eV and an increase in the energy of the main edge compared to high temperature. Similar behaviour was reproduced during different series of experiments. These features clearly reflect iron oxidation in melt. However, cycling experiments with variable cooling rates show that the reduction-oxidation process is reversible. Although hydrogen diffusion through the host quartz crystals

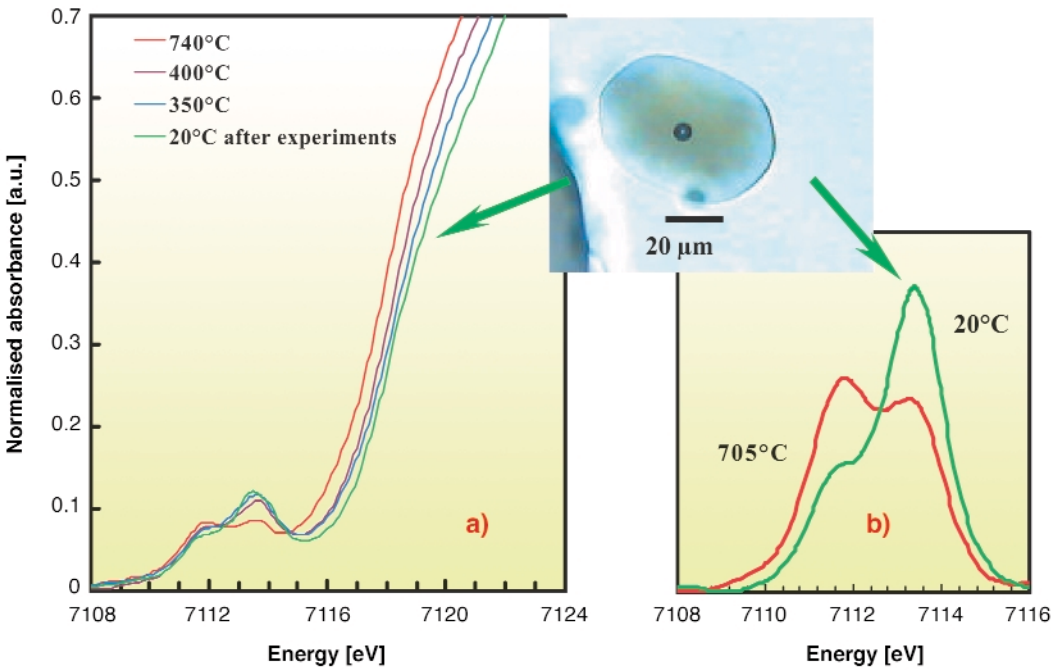

Fig. 140: (a) *In situ* micro-XANES spectra at the iron K edge in melt/glass at different temperatures; (b) Pre-edges in melt/glass inclusion at 705°C and 20°C after the series of experiments. The microphotograph illustrates the glass inclusion, at 20°C, after a series of experiments. The contraction bubble appeared during cooling.

along the course of experiments cannot be totally ruled out, the main process would involve the oxygen ions of the silicate melt as donor or receptor of electrons. Such a process would be confirmed by future dispersive energy experiments at the iron K-edge.

References

[1] Métrich *et al*. *Geophys. Res. Lett*. **29/11**, doi 10.1029/2001GL014607 (2002) *and refs. therein.*
[2] Di Fabrizio *et al*., *Nature* **401**, 895 (1999).

Principal publication and Authors

N. Métrich (a), J. Susini (b), E. Foy (a), D. Massare (a), F. Farges (c), S. Lequien (a), L. Sylla (a), and M. Bonnin-Mosbah (a), *submitted to Geochimica et Cosmochimica Acta.*
(a) CNRS-CEA, CE-Saclay, Gif sur Yvette (France)
(b) ESRF
(c) Université de Marne La Vallée (France)

A New Natural, Super-hard, Transparent Polymorph of Carbon

Cubic diamond (space group *Fd3m)* and hexagonal lonsdaleite (space group $P6_3/mmc$) are the hardest natural materials known. *Ab initio* molecular dynamics calculations give more insight in details of the possible graphite-diamond inversion mechanism [1]. This process includes a pressure-induced sliding of the graphite atom planes towards orthorhombic stacking, from which a fast structure collapse to both hexagonal and/or cubic diamond takes place [1].

Shock-induced diamonds were reported from several impact craters [2]. Polished sections of shocked gneisses from the Popigai Crater, Russia contain transparent multiphase carbon platelets each displaying considerably variable relief (**Figure 141**). A large (70 µm) transparent platelet with very high relief on one side (height up to 10 µm above the section surface) was studied first by Raman and subsequently by X-ray powder-diffraction and fluorescence synchrotron at **ID22**. The part with highest relief displays uneven surface with rough gouges (**Figure 141a**). The 0.25 micrometre diamond powder used for polishing did not succeed in cleanly producing a flat polished surface and hence to erase the scratches and gouges formed during cutting of the section slab.

Synchrotron fluorescence point mapping revealed no other element heavier than carbon (except lead metal scraped from the polishing disc). X-ray diffraction mapping of the platelet indicated the presence of three

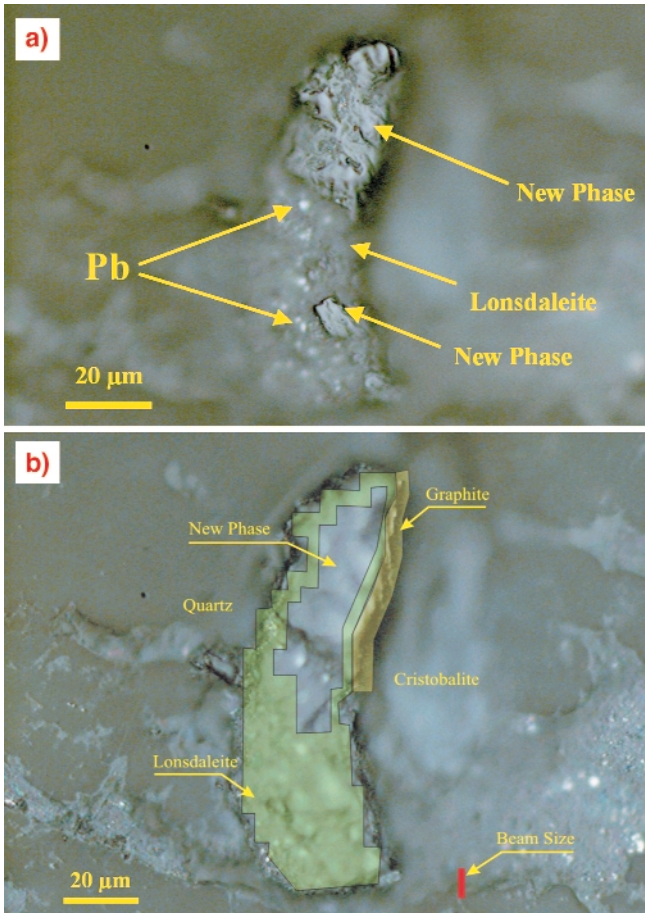

Fig. 141: (a) A Reflected light photograph focused 10 µm above the surface thus depicting the surface features of the new carbon phase with gouges and metallic lead oxide (Pb; arrow) scraped from the polishing disc; (b) Results of the synchrotron X-ray diffraction, imaging and X-ray fluorescence fine-scale mapping laid out on the microscopic photograph shown in (a) depicting the spatial settings of the various carbon phases. The figure shows also the size of the synchrotron beam (lower right, red) for comparison.

distinct crystalline carbon phases in a remarkable concentric shell-like setting (**Figure 141b**), in addition to an amorphous carbon phase. The portion with the highest relief of 10 µm above the section surface is a new super hard polymorph of carbon. This new phase is enveloped by lonsdaleite (hexagonal diamond). The outer most 7-µm thick shell is secondary 2H graphite. Lonsdaleite occupies the portion with a lower relief than that of the new phase, thus manifesting its lower polishing hardness. The X-ray pattern of the highest relief portion is different from that of any known carbon polymorph. The pattern also contains the (111) and (200) reflections of metallic Pb. Twenty-three diffraction lines (**Figure 142**) were obtained from the super-hard carbon [2]. They could be unambiguously indexed in terms of a cubic cell (space group *Pm3m*) with a = 14.697(1) Å; cell volume a^3 = 3174.58 Å^3.

The Diffraction patterns of lonsdaleite and the new phase indicate the extremely small grain size of the

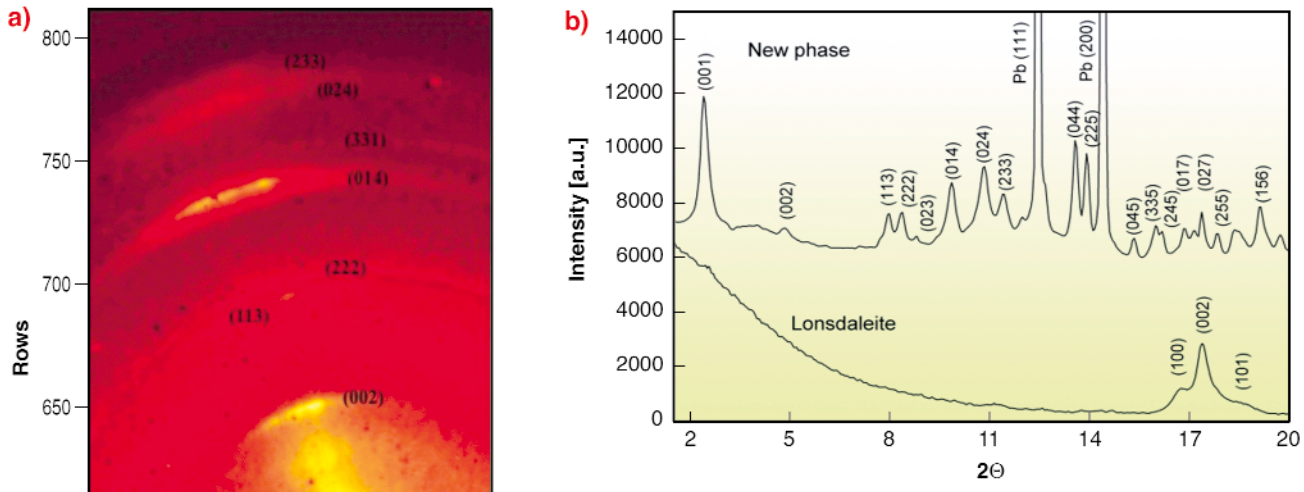

Fig. 142: X-ray diffraction pattern of the new carbon phase. (a) Diffraction picture of the new carbon polymorph demonstrating the preferred orientation due to shock-induced dynamic deformation (streaking of the diffraction spots). (b) The full X-ray patterns of the new phase along with the strongest lines of metallic lead (Pb (111) and Pb (200)) reflections (upper panel) and lonsdaleite (lower panel). The high background of continuum in the lonsdaleite pattern at 2 θ < 11° is due to the presence of an amorphous carbon phase.

crystallites (< 40 nm) of both phases and demonstrate a remarkable high degree of preferred orientation and texturing (**Figure 142a**). Nevertheless, obtained reflection intensities were used with fixed space group *Pm3m* and a variable number of atoms per unit cell for trail structures. However, the diffraction data and the calculated unit cell do not allow an unambiguous calculation of the density.

Here we show that a natural shockwave induced by a large meteorite impact event led to the transformation of graphite to a new crystalline super-hard and transparent polymorph of carbon in gneisses from the Popigai crater, Russia. The synchrotron studies indicate that the new super-hard carbon species occupies the interior of a multiphase assemblage and is entirely enveloped by lonsdaleite and graphite. Polishing hardness of this new phase is greater than that of lonsdaleite. This species was neither encountered in a static or dynamic high-pressure experiment nor predicted by theoretical calculations.

References

[1] S. Scandolo, G.L. Chiarotti, E. Tosatti, *Phys. Rev*. **B 53**, 5051 (1996).

[2] A. El Goresy, L.S. Dubrovinsky, Ph. Gillet, S. Mostefaoui, G. Graup, M. Drakopoulos, A.S. Simiionovici, V. Swamy and V.L. Masaitis, *Comptes Rendus* **335**, 889 (2003).

Principal Publication and Authors

A. El Goresy (a), L.S. Dubrovinsky (b), Ph. Gillet (c), S. Mostefaoui (a), G. Graup (a), M. Drakopoulos (d), A.S. Simionovici (d), V. Swamy (e) and V.L. Masaitis (f), *Comptes Rendus* **335**, 889 (2003).

(a) Max-Planck-Institut für Chemie, Mainz (Germany)
(b) Bayrisches Geoinstitut, Bayreuth (Germany)
(c) Ecole Normale Supérieure de Lyon (France)
(d) ESRF
(e) ERCT, Montréal (Canada)
(f) Karpinsky Geological Institute, St. Petersburg (Russia)

Manganese K-edge X-ray Absorption in Highly Mn-doped GaN with Micrometre Resolution

Conventional electronic devices rely on the transport of electrons in a semiconductor such as silicon. Nowadays, however, the spin of the electron rather than its charge is being exploited to create a new generation of spintronic devices which will be smaller, more versatile and more robust than those currently making up silicon chips and circuit elements. Since Dietl *et al.* predicted that GaN doped with ~ 5 at.% of Mn should exhibit a Curie temperature exceeding room temperature [1], there has been tremendous advances on both the realisation of high-quality (Ga,Mn)N and on the theory of ferromagnetism in these spin-based semiconductors. However, one of the

key unanswered question is whether the resulting material is indeed an alloy of (Ga, Mn)N or whether it remains as GaN with clusters, precipitates or second phases that are responsible for the magnetic properties.

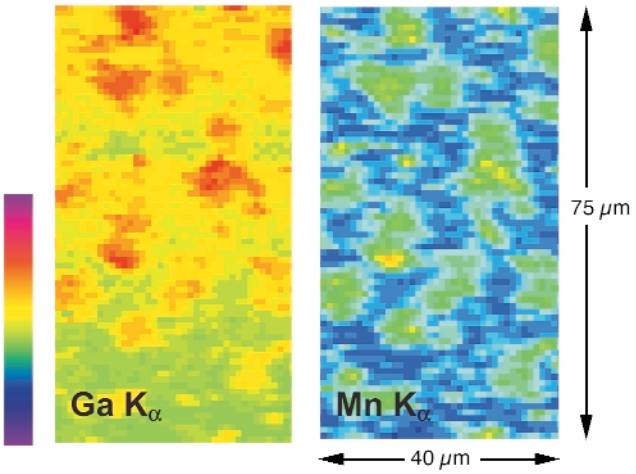

Fig. 143: Ga and Mn maps of the highest Mn doped GaN sample obtained by measuring their Kα line intensities. The pixel size is 1x1 mm². Red colour indicates high fluorescence intensity, blue colour low intensity.

Therefore, in the present report elemental maps of Mn and Ga were taken at **ID22** (beam size 1x1 μm², photon flux ~ 5 x 10^{10} ph/s at Mn K-edge) on molecular-beam-epitaxy grown GaN:Mn layers deposited with Mn concentrations ranging from 10^{18} up to 10^{21} cm^{-3}. Uniform patterns with no intensity changes are observed for most of them, showing a homogeneous distribution of both elements at the length scale of the beam size. However, for the highest Mn concentration (5.4 x 10^{21} cm^{-3}), in addition to a visible roughness, **Figure 143** reveals a close correlation between the Mn and Ga location confirming that there is a partial substitution of Ga by Mn [2]. It is also clear that the Mn atoms are somewhat interrelated among themselves, and they are not randomly distributed in the GaN lattice. Possibly at higher Mn level, local strain fields energetically favour the formation of Mn clusters by a mechanism similar to that of self-assembled growth of strained quantum dots. Because the surface atom diffusion length and the local strain field are both finite, Mn clustering would become more probable for strongly doped layers.

Figure 144 displays the Mn K-edge XANES data recorded at an incident angle θ = 45 ± 5°. We attribute the main feature (A) to dipole-allowed transitions of photoelectrons from Mn 1*s* states to unoccupied 4*p*-like states. Usually, the large density of unfilled *d* states from the transition metal do not contribute to a K edge, but in the absence of inversion symmetry mixing of the Mn 3*d* with N 2*p* character states from the surrounding atoms takes place [3], giving rise to the pre-edge peaks (B). The substitutional incorporation of a transition metal generally increases linearly the intensity of this pre-edge structure, showing a progressive participation of 3*d* orbital in the bonding. However, this strong hybridisation is not observed. The clear smoothing and broadening in the relative amplitude of all the distinguishable oscillation features reflects a change in the local chemical and crystallographic environment around manganese, supporting strongly the presence of doping-induced short-range disorder at very high manganese levels. This tendency is consistent with photoluminescence and Raman results. The higher Mn concentrated samples present a bound exciton transition less pronounced and more broadened, with a displacement towards lower energies. In good agreement, Raman frequency shifts of the corresponding E_2 phonon mode confirm the doping-induced tensile strain in the GaN layers. No evidence of additional secondary phases and/or disorder activated phonon modes were observed, supporting that the long-range order was retained.

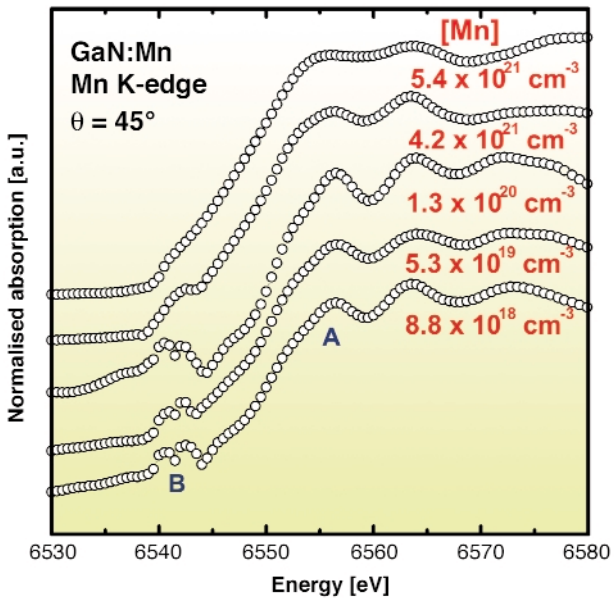

Fig. 144: XANES spectra as a function of the Mn content.

In summary, scanning μ-XRF shows the cluster formation on the micrometre scale for highly-doped GaN ([Mn] ~ 5.4 x 10^{21} cm^{-3}), while the incorporation of doping-induced defects, which clearly lower the short-range symmetry of GaN, was detected by XANES.

References

[1] T. Dietl, H. Ohno, F. Matsukara, J. Cibert, D. Ferrand, *Science,* **287**, 1019-1022 (2000).
[2] M. Sato, H. Tanida, K. kato, T. Sasaki, Y. Yamamoto, S. Sonoda, S. Shimizu and H. Hori, *Jpn. J. Appl. Phys.* **41**, 4513 (2002).
[3] F.W. Kutzler, C.R. Natoli, D.K. Misemer, S. Doniach, K.O. Hodgson, *J. Chem. Phys.*, **73**, 3274-3287 (1980).

Authors

G. Martínez-Criado (a), A. Somogyi (a), M. Hermann (b), M. Eickhoff (b), and M. Stutzmann (b)
(a) ESRF
(b) Walter Schottky Institute, Technical University Munich (Germany)

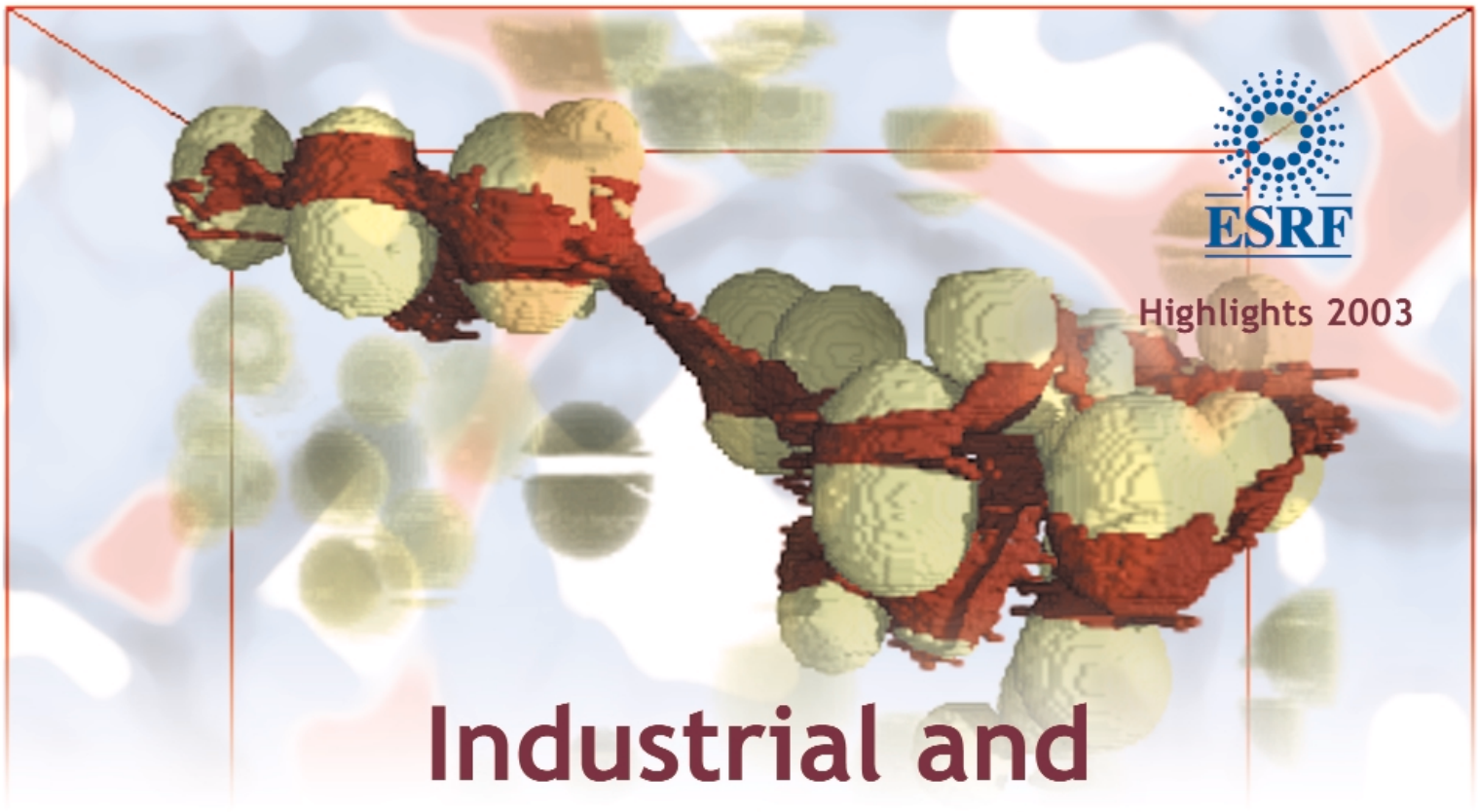

ESRF

Highlights 2003

Industrial and Applied Research

Introduction

With a growth of more than 50% in terms of beamtime sales with respect to 2002, industrial activity at the ESRF continues to expand acquiring an increasingly significant role in the overall research activities.

While macromolecular crystallography is leading this progress with more than 70% of the total beamtime dedicated to industrial activities in 2003, new techniques are attracting both European and non-European companies in the field of chemistry. The industrial demand for the X-ray Absorption Fine Structure (EXAFS) and Small Angle Scattering (SAXS) techniques has considerably increased.
The success of MXpress, the data collection service implemented for macromolecular crystallography, and the forthcoming installation of automated sample changers represents a great improvement of the service for proprietary research.

Industrial activity at the ESRF goes beyond the sale of beamtime.

Technology transfer at different levels of complexity is becoming a central activity of our Industrial and Commercial Unit (ICU).

The present involvement in more than twenty European projects and the large number of proposals on behalf of research and industrial organisations to participate in new projects, gives a fair idea of the role of the ESRF in all the fields of European applied research.

In the following chapter, after a short presentation of the MXpress service, a few examples of applied research by small-angle scattering, powder diffraction and imaging techniques are given.

F. Comin

MXpress: a Macromolecular Crystallography Data Collection Service for Industrial Companies

Structural biology has developed rapidly over the last decade, driven by the various genome projects around the world and by advances in the field of biomolecular crystallisation. X-ray diffraction from macromolecular crystals is used to reveal the atomic arrangement of proteins, nucleic acids and viruses. In this respect, macromolecular crystallography is a powerful tool in the drug-design process. The outstanding properties of the X-ray beams provided by synchrotron radiation sources are now essential for collecting high-quality diffraction data. Pharmaceutical companies appreciate the rapid data collection on very small crystals and at higher resolution than with conventional X-ray sources.

Fig. 145: Dr E. Gordon (left) and Dr S. Monaco (right), the two scientists taking care of the MXPress service.

The ESRF's crystallography beamlines have seen a large increase in demand for beamtime from industry in recent years. Companies are also requesting faster access to the synchrotron facilities. Therefore, a data collection service was set up, whereby the user sends their frozen samples to ESRF. The experiments are carried out by two scientists (S. Monaco and E. Gordon, Figure 145) and the collected data are sent back to the users, usually within a few weeks. This procedure is advantageous for both parties since industrial personnel no longer have to travel to ESRF on a regular basis and they benefit from fast sample processing by on-site staff experienced in both crystallography and synchrotron radiation, while the ESRF improves the overall efficiency of its beamlines. This service is called MXpress. The pilot study began in February 2002 with a limited number of samples per month being sent by Aventis Pharma, Paris.

Several tools for automation of the crystallography beamlines have been implemented over the last two years (see 'Further steps towards beamline automation' for more details). MXpress has been used as the test bench for some of these tools and has encouraged development of the others. PXweb (Figure 146), our beamlines Laboratory Information Management (LIM) system, is intimately linked to the MXpress service since it allows on-line reporting of the current experiment. As it is a Web service, users can provide ESRF staff with an exhaustive description of the dewar contents and follow the experiment being carried out in real time. During data collection they can retrieve their data through the internet and interact with the staff present on-site and so modify the experiment's progress. Other very recent tools are the automatic sample centring software from EMBL Grenoble currently available on ID14-3, and the DNA software for automated data collection and processing currently available on all ESRF MX beamlines. This

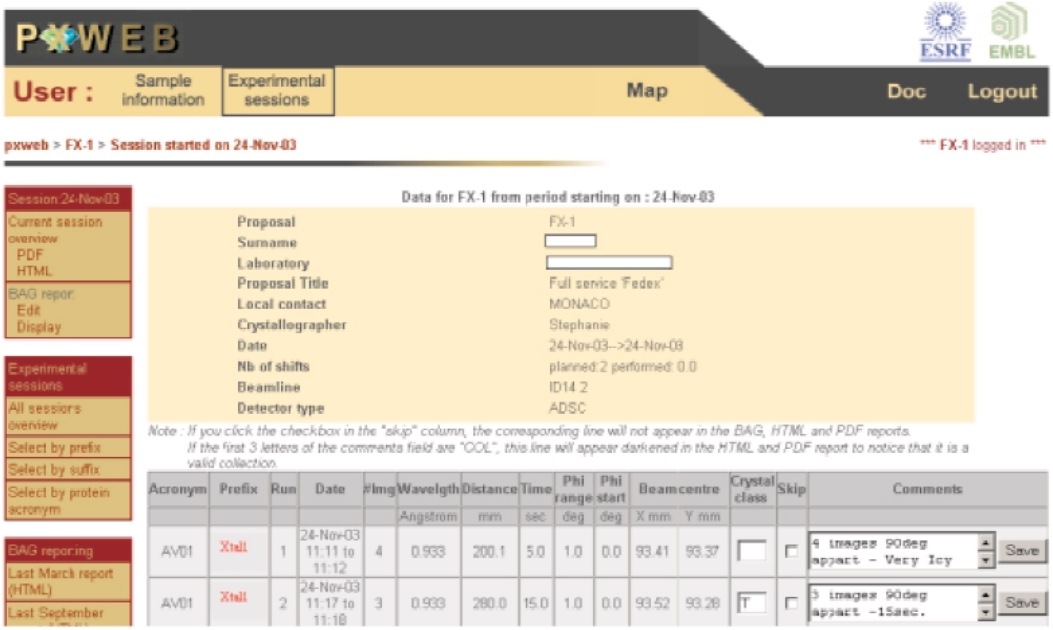

Fig. 146: Pxweb, the ESRF's Macromolecular crystallography LIM system.

software uses two reference diffraction patterns to deduce the crystal orientation in the beam and propose a data collection strategy. Finally the EMBL-ESRF sample changer has been available on ID14-3 since December 2003 and will be installed on the other beamlines starting mid 2004.

The MXpress service was made available to other industrial companies in January 2003. There are now 10 different sites around the world sending samples to ESRF on a regular basis and over 600 samples were screened in 2003. Further developments and improvements may eventually lead to the possibility of offering a complete structure-determination service to industrial companies.

Authors
S. Monaco and E. Gordon.
ESRF

Quantification of the Microstructure Variation in Human Hair with Relative Humidity by Small-angle X-ray Scattering

Hair care is an important part of Unilever's Home and Personal Care business. The physical appearance of hair is closely correlated to its microstructure, and although the microstructure of hair is well known [1], the fine detail of its control has eluded us because of the considerable natural variation within the hair itself. We have developed a method using the **ID02** high-brilliance beamline to combat this natural variation and furthermore permit quantification of the change in microstructure as a consequence of some physical or chemical perturbation, essentially using the hair as its own control. **Figure 147a** shows the small-angle scattering from a single hair fibre. Each image represents the scattering from the hair at nine points along the fibre separated by 0.5 mm. The radial average of this data is shown in **Figure 147b** and this demonstrates the reproducibility obtainable within a single fibre itself.

Although the "intra-fibre" reproducibility within this 4 mm length is excellent we find that if we venture outside these boundaries data consistency is lost. Furthermore comparison of the scattering from adjacent hairs with the average from the first hair, (**Figure 148**), shows that the "inter-fibre" reproducibility is less good.

Ergo quantification can only be performed on a single fibre and considered as the displacement from a fixed

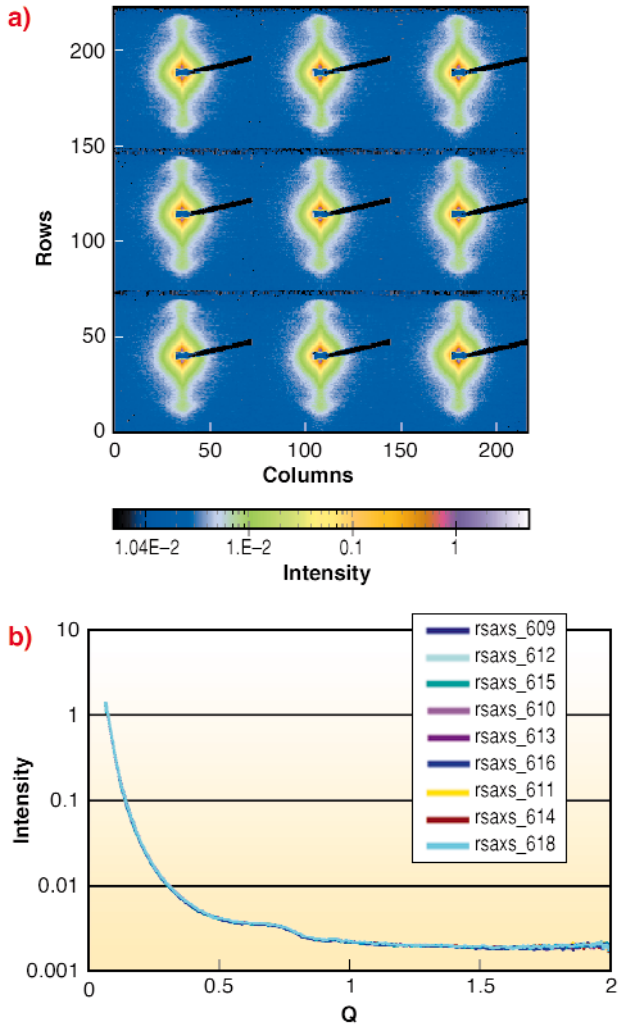

Fig. 147: (a) SAXS images from nine points along a single fibre separated by 0.5 mm, (b) the radial averaged data plotted as an overlay.

starting position. This approach has been used to determine the effect of varying humidity for both virgin and bleached human hair in response to changes in humidity, and the humidity-dependent variation in micro-fibril separation is shown in **Figure 149**.

Each data point is the average of five measurements along an individual fibre and the error bar represents the standard deviation on the value reported. The red curve highlights the problem faced in terms of acute substrate variation, and more data is currently undergoing analysis. Despite each hair starting from a different absolute value, a consistent change in peak position is observed with increasing relative humidity, and an interesting trend is observed where the response to change in humidity appears to change between 50 and 60% relative humidity. Work in progress [2] will provide evidence to show that this behaviour is consistent with the two-phase mechanical model of Feughelman [3]. The marriage of controlled humidity equipment with the beamline was not straightforward and the contributions of the ID02 team are gratefully acknowledged.

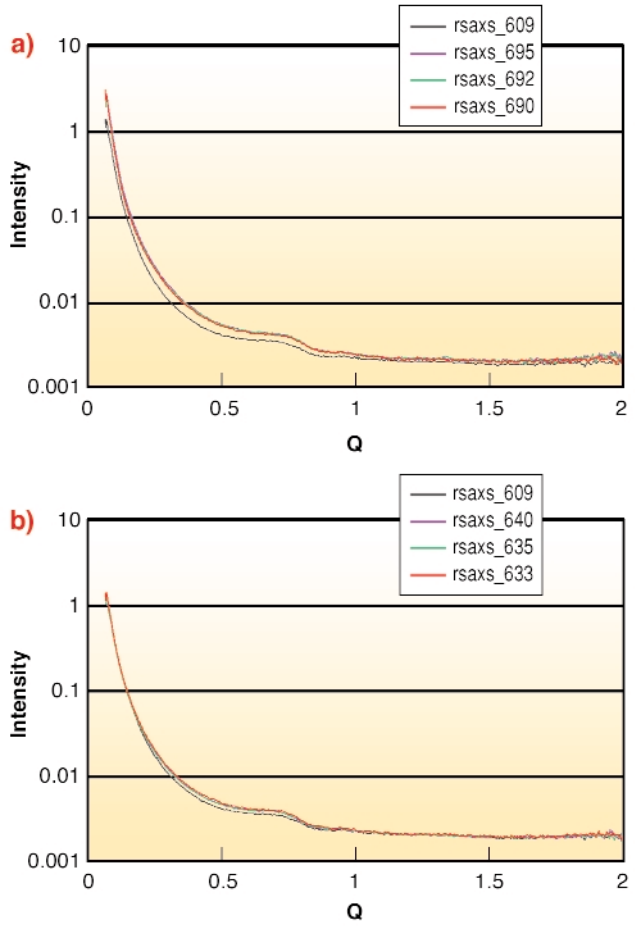

Fig. 148: Comparison of inter fibre scattering between different hairs. The black is the average scattering from Figure147, these are compared to the beginning (pink), middle (green) and ends (red) for two other fibres taken from the same woman's head.

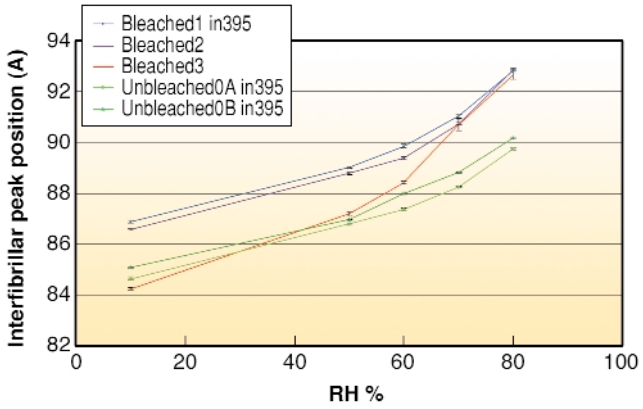

Fig. 149: Change in microfibril separation with humidity (RH).

References

[1] *Chemical & Physical Behaviour of Human Hair*, C. Robbins, 2nd Ed., New York, Van Nostrand, Reinhold Co. (1988).

[2] I.M. Tucker, F.I. Bell, Y. Leray, P. Carpenter, T.E. Lyons, J. Hubbard, S. Ward, P.A. Cornwell, N. Theyencheri, P. Panine, T. Weiss, T. Oikawa, R. Skinner, submitted to *Biochimica et Biophysica Acta-General Subjects,* (Dec 2003).

[3] M. Feughelman, *Textile Res. J.*, **29**, 223-228 (1959).

Authors

I.M. Tucker, R. Skinner, T.E. Lyons, J. Cotterall.

Unilever Research & Development Port Sunlight, Wirral (UK)

Template Burning inside Zeolite Framework Monitored by *in situ* X-ray Powder Diffraction

Zeolites are microporous crystalline materials constituted by corner-sharing [TO_4] tetrahedra where T = Si or Al (other metals such as Ti, Fe, Ga etc… can be introduced into the framework together with or instead of Al). Zeolites are widely employed in the modern industrial chemistry as highly-selective catalysts, because of their molecular-shape selectivity in chemical reactions, which is driven by the size and shape of the internal channels and cavities (**Figure 150**). The internal structure of zeolites gets organised during their synthesis by organic molecules acting as templates. The framework structure develops progressively around the template by T-O-T connection of simple [TO_4] units. However, before being used as catalysts, the internal channels and the cavities of the zeolites have to be made free of the template and this is commonly achieved by heating the zeolite in O_2 flux. Insertion of Ti or Fe in the MFI zeolitic lattice results in TS-1 and Fe-MFI materials, which are important catalysts for a number of low-temperature oxidation reactions with aqueous H_2O_2 as oxidant [1] and in the one-step oxidation of benzene to phenol using N_2O as oxidant [2].

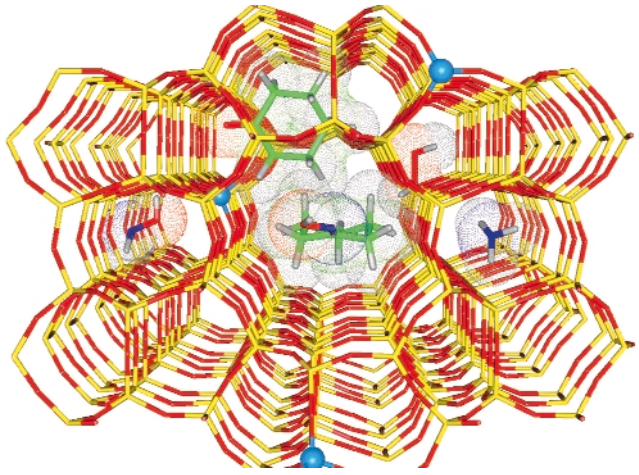

Fig. 150: Molecular graphics representation of the TS-1 framework after template removal: red sticks O atoms, yellow sticks Si atoms; blue balls Ti atoms (substituting Si). The key reactants and products of the cyclohexanone ammoximation reaction (catalysed inside TS-1), see Figure 151.

As an example of catalytic reaction inside TS-1, **Figure 150** reports a pictorial representation the cyclohexanone ammoximation reaction (a key step in the Nylon 6 production, where cyclohexanone is converted into cyclohexanonoxime). The scheme for this reaction is presented in **Figure 151**.

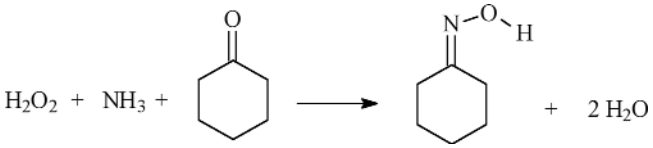

Fig. 151: The cyclohexanone ammoximation reaction.

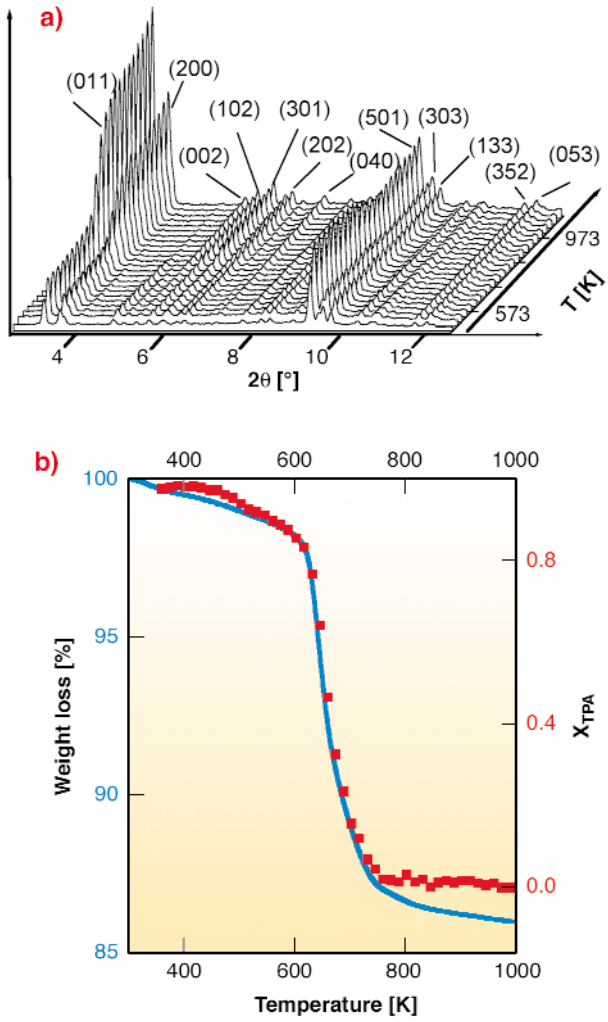

Fig. 152: (a) Evolution of the XRPD patterns in the 2.5-12.5° 2θ-interval (corresponding to 14.2-2.8 Å d-spacing) as a function of the temperature during the *in situ* template burning of TS-1, λ = 0.82667(6) Å. Main reflections have been indicated. (b) Direct comparison between the refined TPA+ occupancy factor (scattered red squares, right axis) and the per cent loss of weight (continuous blue line, left axis) during the template burning process inside TS-1.

The high X-ray flux available at the ESRF, combined with the use of a suitably-designed area detector setup available on the BM8 beamline (GILDA), allowed to follow the structural changes occurring during the template burning processes inside TS-1 and Fe-MFI zeolites in real time by XRPD (see **Figure 152a**). The Rietveld full profile analysis yields the template occupancy factor vs. T (**Figure 152b**, solid squares, right axis) in good agreement with the thermo-gravimetric data. The model for the refinement of the template molecule derives from the single crystal XRD study performed on the **ID11** beamline [3].

By monitoring the evolution of the *a*, *b* and *c* lattice parameters vs. temperature it has been observed that the volume changes anisotropically during the whole process, for both TS-1 and Fe-MFI, following the inequalities $b(T)/b_0 < c(T)/c_0 << a(T)/a_0$, being a_0, b_0 and c_0 the starting lattice parameters. These results imply that the zeolite crystals are subject to remarkable stress forces during the burning process, and that the strong anisotropic contraction contributes to crack formation in the zeolite crystals. These data allow us to have, for the first time, a complete view of the structural rearrangements induced by the template burning process on the zeolitic framework.

Isothermal runs have also been performed, and the results of the kinetic analysis indicate that the template burning is a diffusion-limited process with monodimensional advancement. The rate limiting step of the reaction is the diffusion of the volatile products of the burning process out of the crystal. Chemical and steric considerations indicate that the straight channels along the *b* axis are the more favorable direction for the molecule diffusion and removal. Corresponding Arrhenius plots result in an apparent activation energy values of 151 ± 11 kJmol^{-1} and of 159 ± 7 kJmol^{-1} for TS-1 and Fe-MFI, respectively.

References

[1] S. Bordiga, A. Damin, F. Bonino, G. Ricchiardi, C. Lamberti and A. Zecchina,. *Angew. Chem. Int. Edit.* **41**, 4734-4737 (2002).

[2] G. Berlier, G. Spoto, S. Bordiga, G. Ricchiardi, P. Fisicaro, A. Zecchina, I. Rossetti, E. Selli, L. Forni, E. Giamello and C. Lamberti, *J. Catal.*, **208,** 64-82 (2002).

[3] L. Palin, C. Lamberti, Å. Kvick, F. Testa, R. Aiello, M. Milanesio and D. Viterbo, *J. Phys. Chem. B,* **107**, 4034-4042 (2003).

Principal publication and Authors

M. Milanesio (a), G. Artioli (b), A.F. Gualtieri (c), L. Palin (d,e), C. Lamberti (d), *J. Am. Chem. Soc.*, **125**, 14549-14558 (2003).

(a) University of Piemonte Orientale (Italy)
(b) University of Milano (Italy)
(c) University of Modena (Italy)
(d) University of Torino (Italy)
(e) now at the ESRF (France)

In situ Characterisation of Aluminium Foams using X-ray Microtomography

Metal foams can now be produced with Ni or Al alloy in open or closed-cell morphology. Open cell morphologies are achieved by coating a polymer foam and also by replicating salt preforms. These two techniques allow a very good control of the structure of the foam. Closed-cell morphology is mainly obtained with aluminium alloys and whatever the process (liquid route or powder route) the control of the foaming process and thus of the final structure is not easy. This may lead to foams which present an inhomogeneous structure. Classical mechanical models do not take into account such a structural heterogeneity, thus the question of the influence of inhomogeneity on the mechanical properties is still an open question. Owing to the good contrast between air and the constitutive materials, X-ray absorption techniques can be used to image the structure. For example, X-ray radiography has been used to study the foaming of metal foams, X-ray tomography was successfully used to characterise bone, polymer foams and also metal foams at various resolutions.

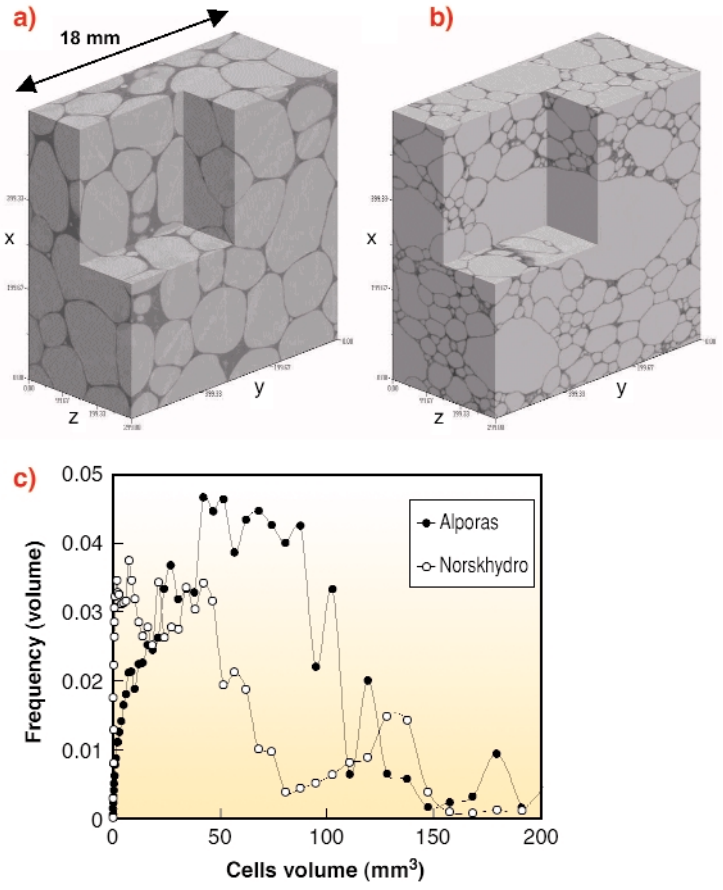

Fig. 153: a) 3D rendering of Alporas foam; b) 3D rendering of NosrkHydro foam; c) Cell size distribution obtained from 3D granulometry.

The aim of the experiments was to characterise the 3D structure of the various aluminium foams that are available and to study their *in situ* behaviour during compression and tensile tests using a specific device [1]. They were performed at beamine **ID19** at energy ranging from 18 to 25 KeV and with 10-30 micrometre optics. 900 projections were recorded on the 1024x1024 FRELON camera. From the data obtained, 3D quantitative analysis of the various aluminium foams allowed a comparison of four kinds of closed cell aluminium foams, produced by various processing routes (IFAM, Alporas, NosrkHydro, Formgrip), in terms of cell size distribution (even when they are not well closed), aluminium phase distribution and connectivity of the cells. **Figure 153** presents two closed cell aluminium foams and their cell size distribution. This clearly shows the quite good homogeneity of the Alporas foam, whereas the NosrkHydro foam presents some large cells (volume ~ 150 mm^3) that are visible on the 3D rendering.

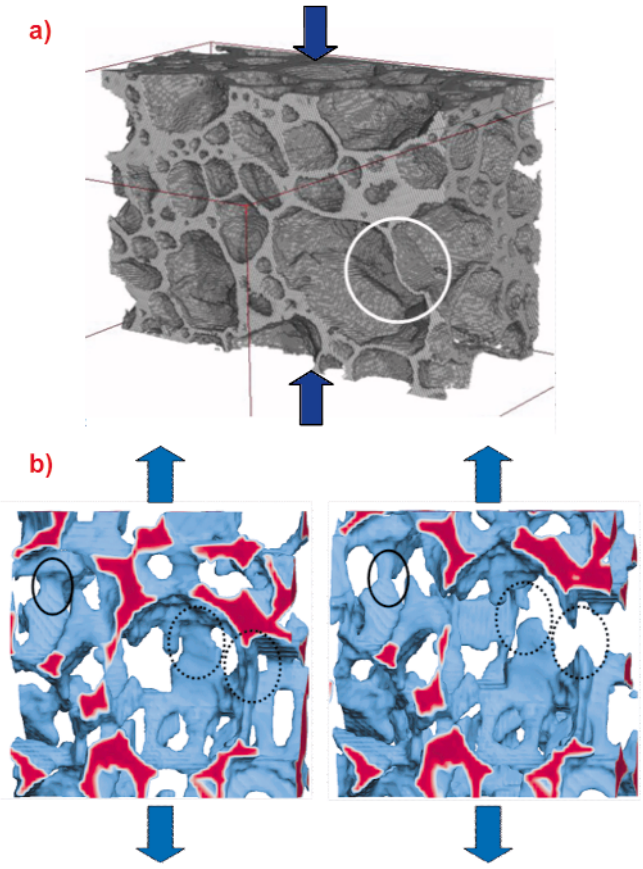

Fig. 154: a) Damage mechanism in a closed cell Al foam (NorskHydro) during *in situ* compression test. Plastic buckling of a cell wall is indicated with the circle (width of the specimen ~ 15 mm); b) *In situ* damage mechanism in a pure Al foam (salt replication technique made at EPFL) during *in situ* tensile testing. Two successive stages are represented. Continuous black circle shows plastic straining of a strut and discontinuous black circle rupture of struts (width of the specimen ~ 1 mm).

In situ experiments were also performed in order to clearly identify the mechanical mechanisms that occur during the

compression (closed cell foam) and tensile testing (open cell foam). The main mechanisms are: plastic buckling of cell walls (see **Figure 154a**) when the constitutive material is quite ductile (IFAM, Alporas) which may be followed by rupture at higher strain for less ductile foams (FormGrip). NorskHydro foam presents rupture of the cell walls due to the brittle nature of the constitutive material. Concerning the open-cell foams, the tensile behaviour of Ni [2] and pure aluminium foam investigated allows us to draw conclusions concerning the damage mechanisms: **Figure 154b** shows clearly that a pure aluminium foam undergoes plastic straining of struts and also rupture of the struts. Furthermore the strain does not seem to be homogeneous along the sample.

This work is still in progress and some questions remain without definitive answers. Indeed, if the main mechanism observed at the cellular scale are now well understood, the correlation of what is locally observed and the macroscopic behaviour of the foam is not well established. 3D density mapping combined with 3D strain mapping and FEM analysis from the tomography data will certainly be useful to answer this question.

References

[1] J-Y. Buffière, E. Maire, P. Cloetens, G. Lormand, R. Fougères., *Acta Met* , **47**, 1613 (1999).
[2] T. Dillard, F. Nguyen, S. Forest, Y. Bienvenu, J.D. Bartout, L. Salvo, R. Dendievel, E. Maire, P. Cloetens, C. Lantuéjoul, in "Cellular Metals: manufacture, properties, applications", J. Banhart, N. Fleck, A. Mortensen Eds, Verlag MIT Publishing, 301 (2003).

Principal Publications and Authors

A. Elmoutaouakkil (a), L. Salvo (a), E. Maire (b), G. Peix (b), *Adv. Eng. Mat.*, **4**(10), 803 (2002); E. Maire (b), A. Elmoutaouakkil (a), A. Fazekas (a), L. Salvo (a), *MRS bull.*, **28**(4), 284 (2003).
(a) GPM2, INP Grenoble (France)
(b) GEMPPM, INSA Lyon (France)

Damage in Metals Studied by High-resolution *in situ* Tomography

Metallic materials are widely used because of their structural properties. When examined carefully and at the micrometre scale, they are found to be heterogeneous. Even if their volume fraction is low, the heterogeneous regions, hereafter called “inclusions”, play a key role in the rupture of metallic materials.

This rupture is due to a damage process which is composed of different phases:

- Damage initiation by cleavage of the inclusions, by inclusion/matrix interface decohesion or by matrix cracking around the inclusions
- Damage extension
- Damage linkage by coalescence and the percolation of a macroscopic crack between the initiation sites

The different phases of this process have been studied more theoretically than experimentally. Moreover, existing experimental studies were performed by non-destructive surface or by post-mortem destructive observations. None of these two methods allows a perfect quantification of damage.

The aim of the present work was to bring a unique experimental contribution to the characterisation of damage in model materials by using high-resolution X-ray attenuation tomography on the **ID19** beamline.

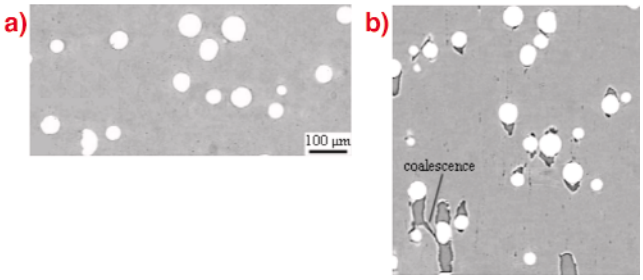

Fig. 155: Two slices extracted from a tomographic reconstruction of a) initial, and b) deformed states of the soft matrix model Aluminium/ceramic composite showing damage initiation, extension and coalescence.

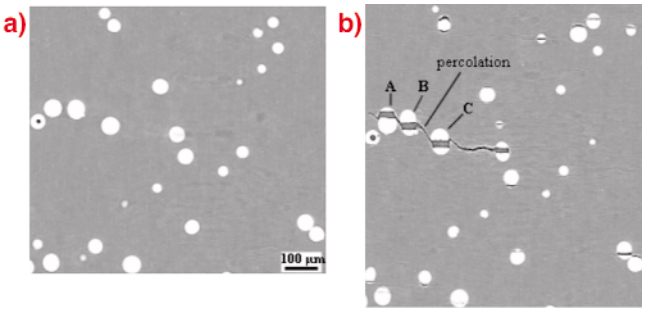

Fig. 156: Same as Figure 155 for the hard matrix composite.

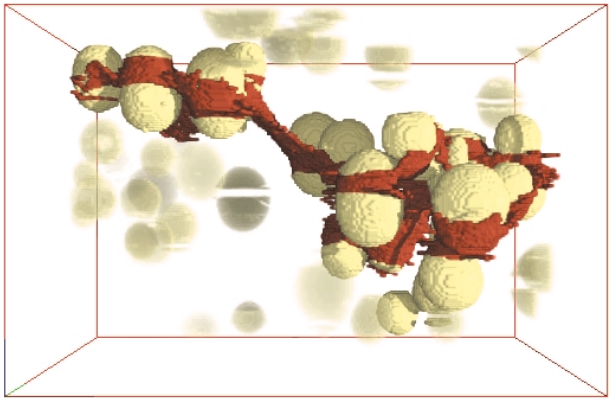

Fig. 157: Three-dimensional view of the same region as that shown in Figure 156 with the particles concerned by the percolation of the crack.

X-ray tomography has been coupled with *in situ* tensile tests to study the damage mechanisms in different model materials at a voxel resolution of 2 µm. The samples were produced specifically for the study. They consisted of two different aluminium matrices (a soft pure aluminium and a hard 2124 aluminium alloy) each containing 4% of spherical hard ceramic particles. The samples were loaded and scanned at increasing values of the plastic strain. The damage mechanisms could be clearly imaged and analysed from these experiments. **Figures 155** and **156** show the initial (a) and the final (b) stages of the two materials reinforced with 4% of inclusions *i.e.* the soft (**Figure 155**) and the hard (**Figure 156**). These images show the damage initiation, growth and then coalescence stages in the hard and soft materials. The difference between the two is the nature of the initiation mechanism: inclusion/matrix decohesion for the soft and inclusion cleavage for the hard material. **Figure 157** shows a 3D visualisation of a large crack percolating between microcracks. The breakthrough compared to classical studies is that these two damage initiation mechanisms could be quantified very precisely and without any possible ambiguity from these 3D images [1]. This quantification is, to our knowledge, the first unambiguous one attempted on materials with such a controlled microstructure. This allowed us to analyse the classical models widely used in this field, in the light of new experimental results.

It is usual in this field of materials science to try to define damage initiation criteria which will help to predict the rupture of materials. The main damage initiation criteria developed so far in the literature were compared to our experimental results. It was shown that the normal stress and the stored elastic energy in the inclusions were the best two criteria. The intrinsic properties of our inclusions were inversely calculated from the comparison between our experimental results and finite-element calculations. The distribution of the rupture stresses in the different particles was well described by a Weibull type expression.

We have also studied damage growth [2]. Compared to the classical Rice and Tracey [3] type predictions for this mechanism we found that:

- There is a threshold for the growth of previously initiated voids
- Growth is delayed by the initiation stage
- The growth rate is scattered from one void to the other, the Rice and Tracey prediction providing an upper bound estimation for this rate

For these various reasons, the overall damage growth rate is much slower in our materials than in the predictions. This new information is an important result in the field and suggests to further study the phenomenon with this kind of technique.

References

[1] L. Babout, W. Ludwig, E. Maire and J.Y. Buffière, *Nuclear Instruments and Methods in Physics Research B,* **200**, 303 (2003).
[2] L. Babout, E. Maire, J.Y. Buffière and R. Fougères, *Acta Mater.*, **49**, 2055 (2001).
[3] J.R. Rice and D.M. Tracey *J. Mech. Phys. Solids*, **17**, 201 (1969).

Authors

E. Maire (a), L. Babout (a), P Cloetens (b).
(a) INSA Lyon (France)
(b) ESRF

Evaluation of 2D Radiographic Texture Analysis for Assessing 3D Bone Micro-architecture

The prevalence of osteoporosis increases significantly with life expectancy in industrial countries. Osteoporosis is a bone disease characterised by low bone mass and structural deterioration of bone tissue, leading to bone fragility and an increased susceptibility to fractures of the hip, spine, and wrist. The clinical evaluation of osteoporosis relies on Dual X-ray Absorptiometry (DXA) which provides an estimation of the Bone Mineral Density (BMD) typically on the spine and on the hip. Unfortunately, an important overlap of BDM values is observed in patients with and without fractures, and BMD alone is not sufficient to predict individual fracture risk. Another factor to take into account in the biomechanical resistance of bone, is its micro-architecture. The latter has conventionally been investigated using histomorphometry, but during the last decade tomographic techniques have been more and more employed [1]. Though, due to the requirements in terms of spatial resolution this investigation is limited to in vitro examinations on bone biopsies.

Standard X-ray radiography associated with texture analysis has been proposed by different teams to get *in vivo* architectural information. Although the information delivered by a single radiograph is somehow limited, the discrimination of osteoporotic patients and healthy subjects has been demonstrated in clinical studies [2]. However, the most appropriate texture parameter(s) and the optimal imaging conditions for the description of bone micro-architecture are still unknown.

The purpose of this collaborative project (CEA-LETI, CREATIS, ESRF, CHU Nîmes and Lille) was to develop a method for evaluating the relationships between 3D micro-architecture parameters and 2D texture parameters, and for optimising the conditions of

radiographic image acquisition. It is expected that such conditions could be implemented on new generations of bone densitometers such as the LEXXOS, developed by CEA-LETI and DMS, based on a 2D digital radiography flat panel technology.

A procedure based on the use of reference images of representative human bone samples acquired using 3D-synchrotron X-ray microtomography was developed at the ESRF. Thirty-three cylindrical samples (diameter 14 mm) were taken in calcaneus and femoral neck, from cortical to cortical to be close to *in vivo* conditions. Imaging was performed on the microtomography setup developed on beamline **ID19**. To have a sufficient field of view, a spatial resolution of 15 µm was used, and scans at different heights were acquired to encompass the entire sample (total height: 30 to 40 mm). **Figure 158** shows a 3D display of a reconstituted entire sample as well as one 2D slice.

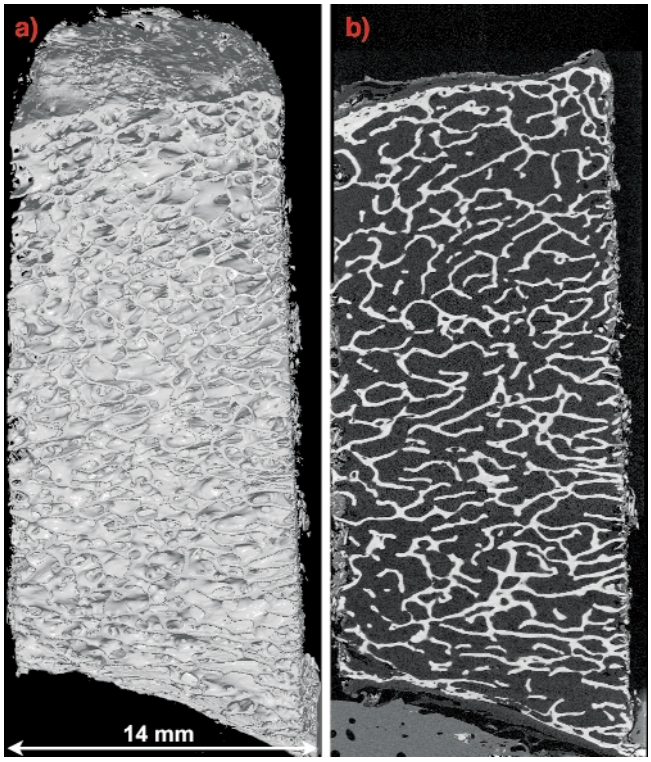

Fig. 158: Calcaneus bone sample (mo10) imaged using synchrotron radiation microtomography on beamline ID19 at the ESRF (voxel size: 15 µm): (a) 3D display of the reconstituted entire sample (b) 2D vertical slice.

These digital three-dimensional images were further used both for calculating three-dimensional quantitative architecture parameters of trabecular micro-architecture, and simulating realistic X-ray radiographs under different acquisition conditions using the Sindbad software (CEA-LETI) [3]. **Figure 159** illustrates simulated radiographs of two samples at a spatial resolution of 50 µm.

Texture analysis was then applied to these simulated 2D radiographs using software developed at CREATIS including a large variety of methods (co-occurrence,

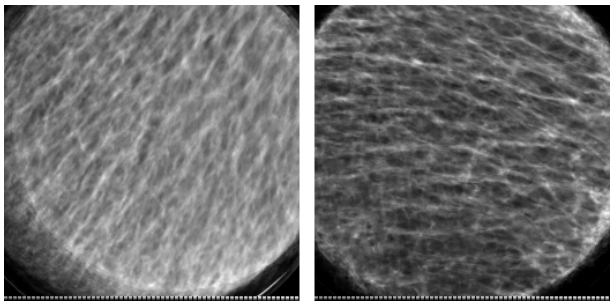

Fig. 159: Radiographs simulated from the 3D discrete images of two entire calcaneus samples (pixel size: 50 µm). left: same sample as Figure 158, right: sample moca4.

spectrum, fractal…) and delivering more than one hundred parameters per image. The set of texture parameters was sequentially reduced according to different criteria to find the most relevant ones to three dimensional architecture. Finally, six texture parameters significantly correlated to bone micro-architecture parameters were selected. The relevance of these parameters will be confirmed by further tests on physical radiographs of the samples acquired in different experimental conditions (energy range and spatial resolution). The implementation of such a technique on a bone densitometer would allow to supplement the standard BMD with an architectural index for expected better discrimination with respect to the fracture risk.

References

[1] F. Peyrin, M. Salome, S. Nuzzo, P. Cloetens, A.M. Laval-Jeantet, J. Baruchel, *Cellular and Molecular Biology*, **46**(6): 1089-1102, (2000).

[2] L. Pothuaud, E. Lespessailles, R. Harba, R. Jennane, V. Royat, E. Eynard, C.L. Benhamou , *Osteoporosis Int.*, **8**, 618-625, (1998).

[3] R. Guillemaud, J. Tabary, P. Hugonnard, F. Mathy, A. Koenig, A. Glière, *PSIP*, (2003).

Principal Publication and Authors

F. Peyrin (a,e), L. Apostol (a, e), E. Boller (e), O. Basset (a), C. Odet(a), S. Yot (a), J. Tabary (b), J.M. Dinten (b), V. Boudousq (c), P.O. Kotzki (c), X. Marchandise (d), SPIE Med. Imaging, 2004.

(a) CREATIS (France)
(b) CEA-LETI (France)
(c) CHU Nimes (France)
(d) CHU Lille (France)
(e) ESRF

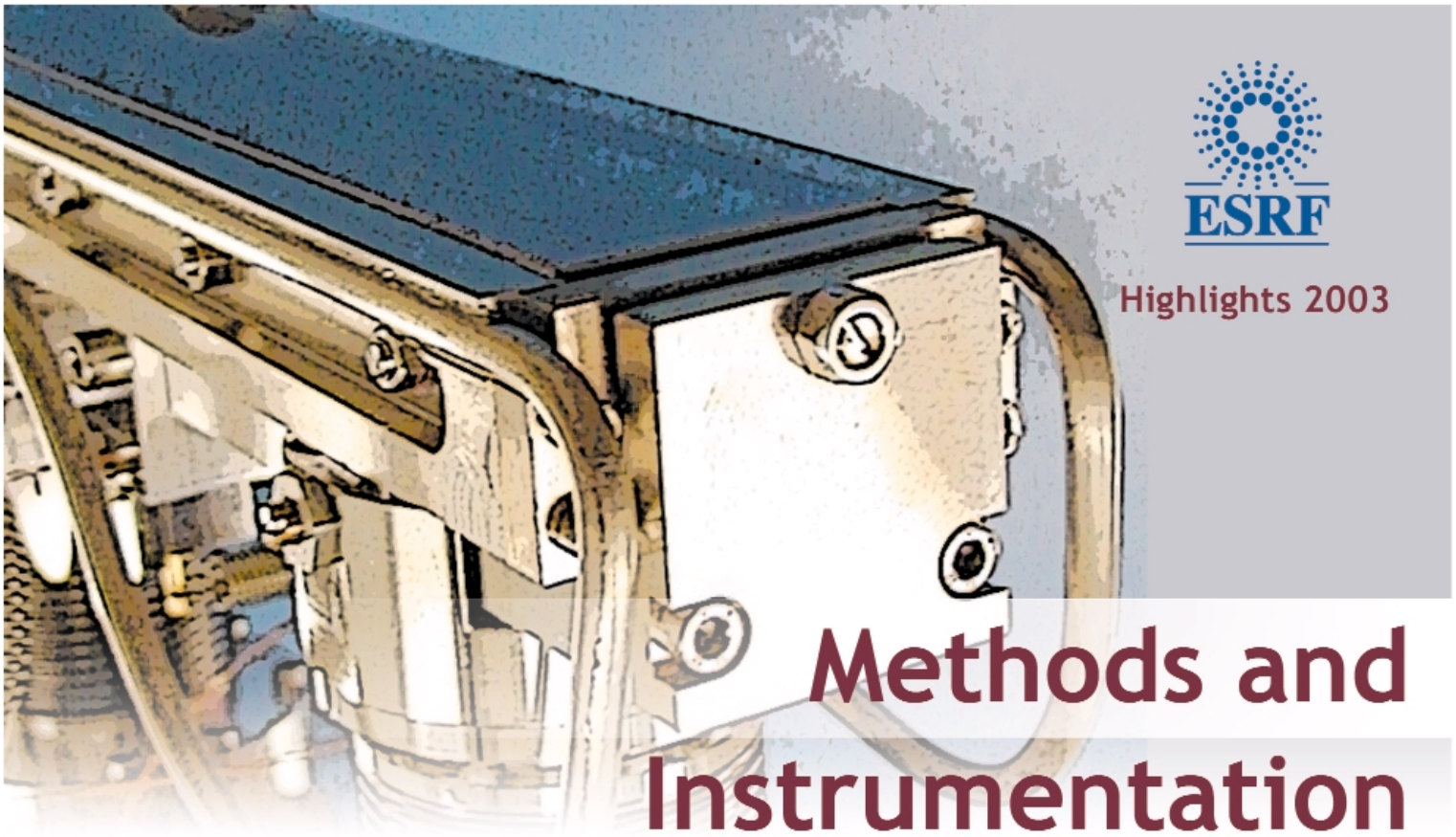

ESRF

Highlights 2003

Methods and Instrumentation

Introduction

One of the pillars of the success of the ESRF is the continual development of new methods and instrumentation. These developments are often driven by the interaction between new technological possibilities and the evolving scientific needs. Consequently, the ESRF user community is involved in developing new methods and instrumentation. Three areas deserve a special mention: optics, sample environment and detectors.

The developments in optics, of which various examples are given in this year's highlights, are particularly exciting and are a good example of the interaction between the desire to have ever smaller focal spot sizes, and the development of better optical elements. The impact of new multilayers, has been so important that the ESRF management has approved the construction of a new multilayer fabrication facility.

Another area of increasing importance is the sample environment, or non-ambient conditions. More and more experiments require heating, cooling, high pressures, magnetic fields, laser illumination or a combination of these parameters. In order to answer to these increasing demands, a new Sample Environment Support Service (SESS) has been created. The SESS will provide a pool of equipment, including cryostats, furnaces and high-pressure cells, provide expert support for the experiments, and work on various projects in collaboration with the scientists.

The third area of increasing activity is X-ray detectors. The increasing automation of experiments calls for improved diagnostics tools that record the intensity, position and shape of the X-ray beam. At the same time, the so-called pixel detectors, which are based on micro-electronic chips coupled to semiconductor diode chips, are starting to be used in the experiments. Whereas most other developments can be performed in-house, the field of X-ray detectors requires international collaborations. The ESRF is increasingly active in European collaborations, and applying for funding within the Sixth Framework Program of the European Commission.

One of the most exciting developments of the past year is the extension of photoelectron spectroscopy to higher energies. The availability of high-energy photons in the 14 keV range with 10-50 meV energy resolution opens up a completely new and as yet unexplored territory. The first results are given here.

Improvements of the X-ray source, with correspondingly increased heat load, also require redesign of the optics in order to preserve the beam quality. Two examples are given in this year's highlights. The first one is a study of a cryogenically-cooled Si monochromator under extreme heat load. The second example is the development of an asymmetrically-cut backscattering monochromator for inelastic scattering. As stated before, multilayers have rapidly evolved over the last years, and are extending experimental capabilities on many beamlines. An example of a double multilayer monochromator and a multilayer for broad-band focusing is given. Another interesting contribution describes X-ray magnetic scattering at 1 Kelvin, for which a special cryostat has been developed.

X-ray microscopy is a rapidly-developing field, thanks, in part, to the developments in X-ray optics. Here the development of diffractive optical elements for so called differential interference contrast X-ray microscopy is presented.

H. Graafsma

Extending Photoelectron Spectroscopy up to 14.5 keV: First Results

X-ray photoelectron spectroscopy (XPS) performed with soft X-ray laboratory sources is well known under the name ESCA (electron spectroscopy for chemical analysis). At synchrotron radiation sources, XPS is also well established, using harder X-rays and detecting electrons with kinetic energies up to several keV. Now, at beamline **ID32**, we have extended photoelectron spectroscopy into the 10 keV range.

The advantages to using high-energy XPS are many: an almost complete elimination of surface effects when studying material properties; the availability of monochromatic X-rays with 10 - 50 meV resolution; the possibility of combining photoemission with X-ray diffraction and standing waves; the accessibility of buried interfaces to photoemission studies. Of special interest is the study of valence band states and core states with low binding energy, since they carry information on the chemical and electronic properties of the material. Photoelectrons interact strongly with the atoms of the material from which they are produced, rapidly losing their characteristic kinetic energy. Thus, if a material is investigated by "normal" XPS, mostly its surface, rather than its bulk properties, is revealed. High kinetic energy electrons interact less strongly, hence travel further before being scattered, and as a consequence they carry with them information about chemical and electronic properties of the bulk.

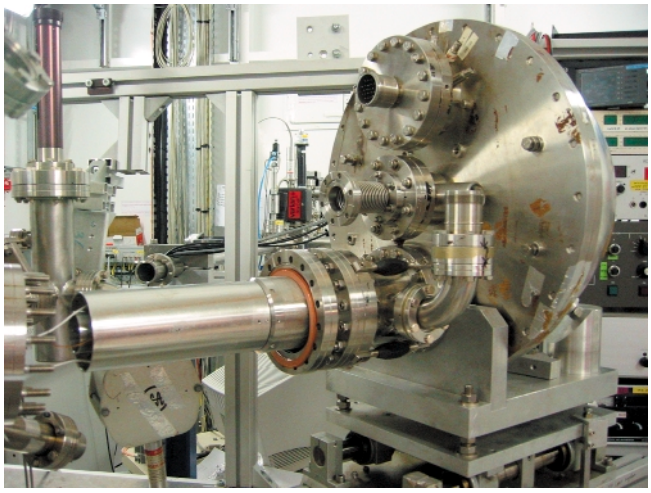

Fig. 160: Mounting of the pre-lens on the commercial PHI analyser.

The fundamental challenge at these high photon energies is that the absorption of the X-rays by these valence band and shallow core states decreases at a far faster rate than signal is gained by detecting more material from deeper in the sample. Our knowledge about cross sections and the escape depths of high-energy photoelectrons is exclusively based on theoretical calculations [1], which need to be tested experimentally.

Our approach was pragmatic since we wanted first to establish sublevel cross sections and gain experimental experience before embarking on the purchase or development of new instrumentation. So we extended the kinetic energy range of our existing electron analyser and built a refocusing lens, which allows the retardation of electrons emerging from a sample biased at up to +10 kV relative to ground (**Figure 160**). The electrons are handed over at ground potential to the “Omega” retarding lens (0 to -4.5 keV) of a Perkin Elmer PHI Model 10-360 hemispherical analyser equipped with a 16-channel detection system. The pre-retarding lens was modelled with the SIMION code.

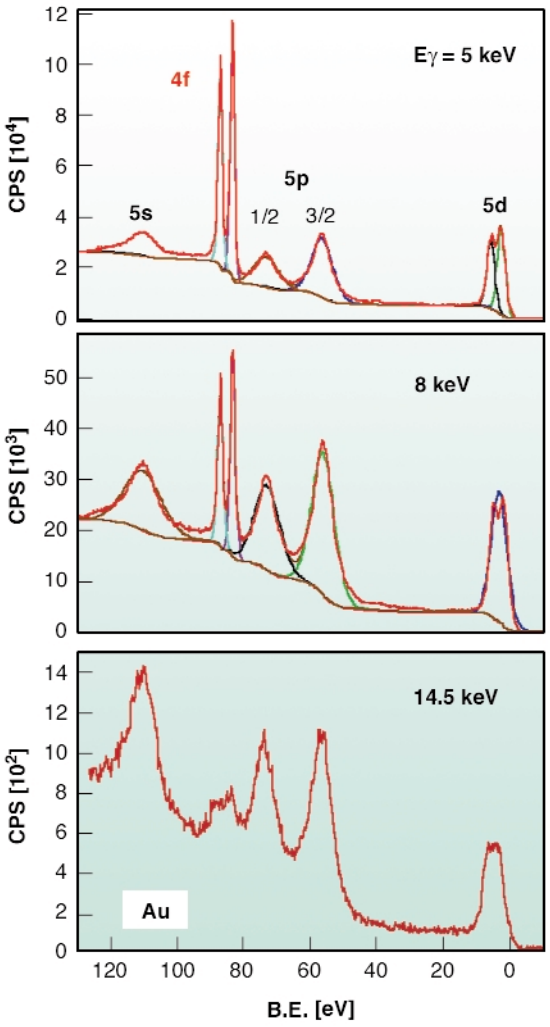

Fig. 161: The faster decrease of the cross section for the 4f than for the other levels with increasing photon energy is also predicted by theory.

Experiments were carried out at beamline **ID32**, using X-rays from a Si(111) monochromator (10^{-4} resolution) and a Si(444) post-monochromator (40 meV resolution at 8 keV) for some measurements. We performed a variety of measurements on Au, graphite and $YBa_2Cu_3O_7$, a 90 K superconductor, up to 14.5 keV (**Figure 161**). We succeeded in measuring the Au 5d, 5p, 4f and 5s cross-sections between 5 and 13.5 keV on an absolute scale comparing them to the established cross section of C1s (**Figure 162**). A preliminary evaluation gives cross sections

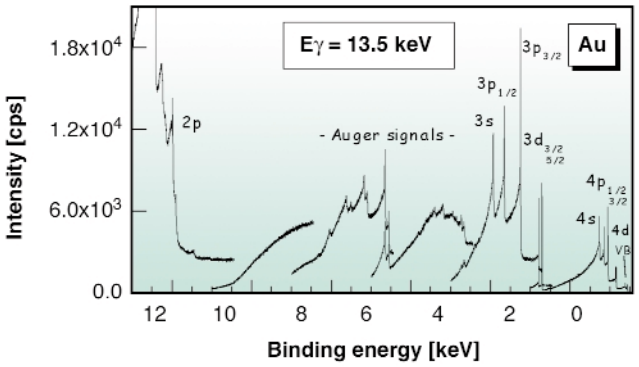

Fig. 162: Overview of the full energy range of the Au levels from 2p to the valence band in one spectrum.

two to ten times higher than predicted by theory [1]. The count rates will allow valence band investigations in further detail in this energy range.

The best resolution obtained was limited to 250 meV at the Au Fermi edge at room temperature, determined by the noise and stability of our power supplies. However, given the inherent simplicity of the setup, we consider the resolving power of 32000 remarkable. We know that our initial experimental situation is not ideal and we can envisage a few simple technical improvements; such as focussing of the X-ray beam onto the sample and power supply improvements which would increase our electron energy resolution. This would open up the possibilities for new experiments in bulk systems, interfaces and material science.

References

[1] J.H. Scofield, *Lawrence Livermore Report UCRL-51326* (1973).

Authors

S. Thiess (a), B. Cowie (a), C. Kunz (b), T.-L. Lee (a), M. Renier (a) and J. Zegenhagen (a).
(a) ESRF
(b) Universität Hamburg (Germany)

Performance of a Cryogenically cooled Silicon Monochromator Under Extreme Heat Load

High brilliance and stability are key parameters at third generation synchrotron radiation sources. Having already increased the storage ring current from 100 to 200 mA, the ESRF is now considering 250 mA and above. This increases the flux but poses technical problems for handling the heat load. Heating of the monochromator crystal by a small X-ray beam leads to a temperature gradient and forms a bump on the surface of a monochromator crystal due to a non-homogeneous lattice expansion. The common way to tackle the problem is to cool the silicon crystal to 125 K, where silicon has zero thermal expansion [1].

In order to cope with the foreseen increase of the heat load, we examined the performance of an indirectly-cooled cryogenic silicon monochromator at the Nuclear Resonance beamline **ID18** [2]. At a nominal electron current of 200 mA, the maximum power of X-rays from three U32 undulators is 450 W in the central cone (1.2×0.6 mm², horizontal × vertical) and 1000 W within a maximum 2×4 mm² aperture. **Figure 163** shows the results of the rocking curve measurements. The heat load was varied by closing the gaps of the undulators (red) and, alternatively, by opening the vertical slit at various sizes of the horizontal slit (blue, green, and cyan circles). The heat-load effects are small: they cannot be revealed with 14.4 keV radiation utilizing the Si (111) reflection up to the highest heat load of 870 W (**Figure 163a**). The Si (333) reflection at 43.2 keV is more sensitive, it shows that the monochromator reaches the best performance in a heat-load range of 250-350 W (**Figure 163b**). Here the rocking curve width almost coincides with the theoretical value. The thermal-induced broadening in this range is about 0.8 μrad.

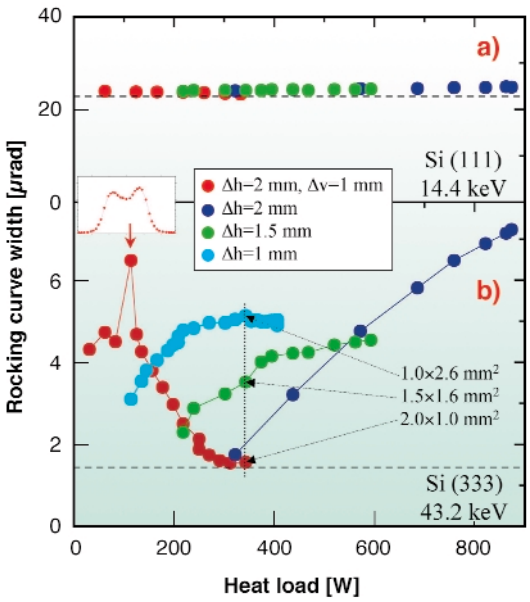

Fig. 163: Rocking curve width (FWHM) of the Si (111) reflection for 14.4 keV (a) and of the Si (333) reflection for 43.2 keV (b) X-rays as a function of heat load. The dashed horizontal lines show the rocking curve widths calculated for ideal crystals.

The observed thermal broadening is not uniquely determined by the heat load but also depends on the slit size. At a fixed heat load of 340 W (**Figure 163b**, vertical dotted line), the broadening differs significantly for various slits sizes. Note that at this heat load the monochromator performance becomes better when the same heating power is concentrated in a smaller area. We attribute this

effect to a displacement of the spot of the monitored radiation relative to the thermal bump on the crystal surface. The same effect can cause broadening and even splitting of the rocking curve when the undulator gap is tuned out of the optimal value (see inset).

In order to reveal the dependence of the performance on only the heat load, we carried out measurements with fixed undulator gaps and fixed slit size of 2×1 mm^2. The heat load was varied by ramping the current in the storage ring. **Figure 164** shows the total flux, spectral density, and the width of the vertical angular profile of the 14.4 keV radiation measured for the Si (111) reflection. The angular profile was measured directly after the monochromator and, alternatively, with the addition of a collimating compound refractive lens. The total flux dependence is exactly linear and does not reveal any heat load effects. The increase of the spectral density becomes steeper at 250 W, revealing better performance at elevated heat load. The width of the angular profile becomes close to the expected value at the same heat load. When collimation is applied, the width of the angular profiles reaches the angular resolution in the heat load range of 250-400 W. Here the thermal distortions are estimated to be less than 0.7 µrad.

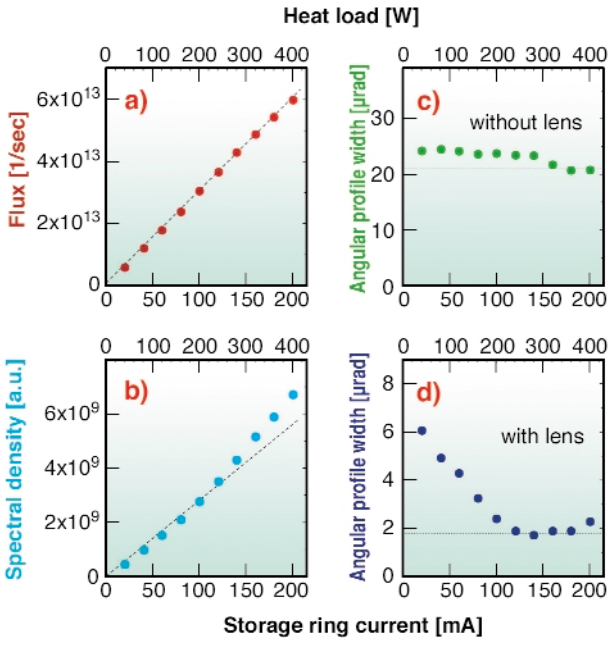

Fig. 164: Flux (a), spectral density (b), and width (FWHM) of the angular profile of radiation after the monochromator without (c) and with (d) collimation of the beam by a compound refractive lens. Dashed lines are to guide the eyes. Horizontal dotted lines show the theoretically expected width of the angular profile (c) and the resolution of angular profile measurements (d).

Thus, the cryogenically-cooled silicon monochromator performs almost ideally up to the highest available heat load of ~400 W. The data analysis suggests that this performance should not significantly degrade up to ~600 W.

References

[1] D.H.Bilderback, A.K.Freund, G.S.Knapp, D.M.Mills, *J. Synchrotron Rad.*, **7** 53-60, (2000).

[2] R.Rüffer, A.I.Chumakov, *Hyperfine Interactions*, **97-98**, 589-604 (1996).

Principal Publication and Authors

A. Chumakov (a), R. Rüffer (a), O. Leupold (a), J.-P. Celse (a), K. Martel (a), M. Rossat (a) and W.K. Lee (b,a), *J. Synchrotron Rad.* (2004).

(a) ESRF

(b) APS, Argonne (USA)

Development of an Asymmetrically-cut Backscattering Monochromator for Very High Energy Resolution Inelastic X-ray Scattering

Inelastic X-ray scattering (IXS) with meV energy resolution has become a routine tool for the study of phonon dispersions, and is applied to a large class of different materials. At the ESRF beamlines **ID16** and **ID28** are fully dedicated to this technique. One of the key components is the very high-energy resolution monochromator, which is located downstream of the cryogenically-cooled silicon (1 1 1) premonochromator. It utilises a high-order Bragg reflection from a perfect silicon crystal close to backscattering geometry in order to achieve an energy resolution in the meV range and to match the vertical X-ray beam divergence. In contrast to conventional monochromators, where the energy is scanned by changing the incidence angle, in the present case the monochromator temperature is varied [1,2]. As a matter of fact: $\Delta E/E = \Delta d/d = \alpha(T)\cdot\Delta T$, where $\Delta E/E$ and $\Delta d/d$ are the relative changes in lattice spacing and energy, respectively, and $\alpha(T)$ is the silicon thermal expansion coefficient. Considering that $\alpha(T)$ is $2.58\cdot10^{-6}$ K^{-1} around room temperature, meV energy resolution requires an accurate temperature control **in the mK regime.** This is achieved by a careful design of the monochromator mount and a sophisticated active-feedback temperature control system.

Following the upgrade of the X-ray source (full equipment of the straight section with short period undulators operating at gaps down to 11 mm), and the consequent increase in photon flux, a degradation of the energy resolution for reflection orders n = 9,11 and 13 was observed. This phenomenon is due to a temperature gradient within the diffracting volume of the silicon crystal, caused by the power density of the incident

X-ray beam from the premonochromator. For example, at the silicon (11 11 11) reflection order (21747 eV) the incident photon flux amounts to $4.2 \cdot 10^{13}$ photons/sec (200 mA ring current, three undulators at 12 mm gap), corresponding to a power density of 35 mW/mm^2. This seemingly moderate power density is sufficient to degrade the energy resolution, broadening it from 1.4 meV (full-width-half maximum, FWHM) to 1.8 meV (see **Figure 165a**), and to induce a strong asymmetry of the line shape when all three undulators are utilised.

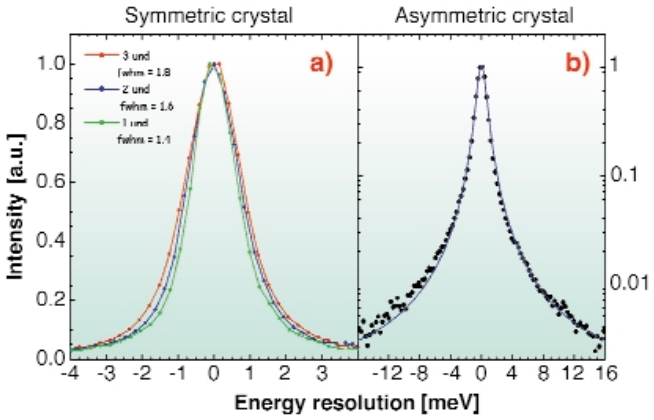

Fig. 165: Instrumental energy resolution function measured on ID16 at the silicon (11,11,11) reflection in 2/3 filling mode. (a) symmetrically cut monochromator crystal using one (green line), two (blue line) and three (red line) U35 undulators, respectively. (b) asymmetrically cut monochromator crystal (α = 80°) and three U35 undulators closed. The full line is a fit of a Lorentzian curve with FWHM= 1.4 meV.

This problem was solved by an improved design of the monochromator mount and the utilisation of an asymmetrically cut silicon crystal (**Figure 166**). The chosen asymmetry angles of α = 80° (ID16) and α = 85° (ID28) lead to a power density reduction by about a factor 6 and 12, respectively. As is shown in **Figure 165b**, this intervention brought back the instrumental energy resolution to the previous values in terms of FWHM and line shape: we record an energy resolution of 1.4 ± 0.1 meV at the silicon (11,11,11) reflection order, independently of the number of undulators used, and up to 200 mA ring current. Equally, we record an instrumental resolution function of 3 meV and 0.9 meV at the silicon (9 9 9) and (13 13 13) reflection orders respectively. In view of these results we are confident that the monochromator will be able to cope with the increase in the ring current planned for the near future.

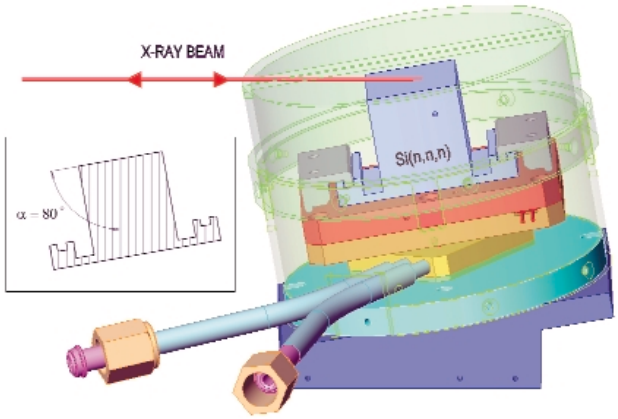

Fig. 166: The very high resolution asymmetrically cut backscattering monochromator with its temperature control mount. The inset shows the crystal with the silicon (n n n) planes, indicating the asymmetric angle.

References

[1] F. Sette, G. Ruocco, M. Krisch, C. Masciovecchio, R. Verbeni, *Phys. Scripta,* **T66**, 48-56 (1996).

[2] R. Verbeni, F. Sette, M. Krisch, U. Bergmann, B. Gorges, C. Halcoussis, K. Martel, C. Masciovecchio, J.F. Ribois, G. Ruocco, H. Sinn, *J. Synchrotron Rad..* **3**, 62-64 (1996).

Authors

R. Verbeni, C. Henriquet, D. Gambetti, K. Martel, M. Krisch, G. Monaco, F. Sette.

ESRF

Multilayers as Monochromators and Focusing Devices

Amongst potential applications of multilayers in third generation synchrotron optics, high-flux monochromators and dedicated focusing devices are the most relevant. In the first case the multilayer acts as a Bragg reflector and one benefits from the about 100 times wider intrinsic bandwidth of a multilayer compared to a perfect crystal. Focusing multilayers require curved substrates and an additional lateral thickness gradient to account for the variation of the Bragg angle. To date, about half of all ESRF beamlines have been equipped with multilayer-based optics, either permanently or for dedicated experiments. Recently, two new devices have been developed and tested.

Double-multilayer Monochromator

A double-reflection multilayer monochromator has been developed at BM5 in order to fulfil two different functions. As a primary monochromator, it provides a higher bandwidth and a higher photon flux than the Si(111) Bragg crystal monochromator. In combination with the crystal monochromator, it rejects harmonics and the beam exit can be kept fixed. An additional aim is to preserve the beam coherence. Optical and geometrical requirements led to the design of two $[Ru/B_4C]_{70}$ multilayers with a

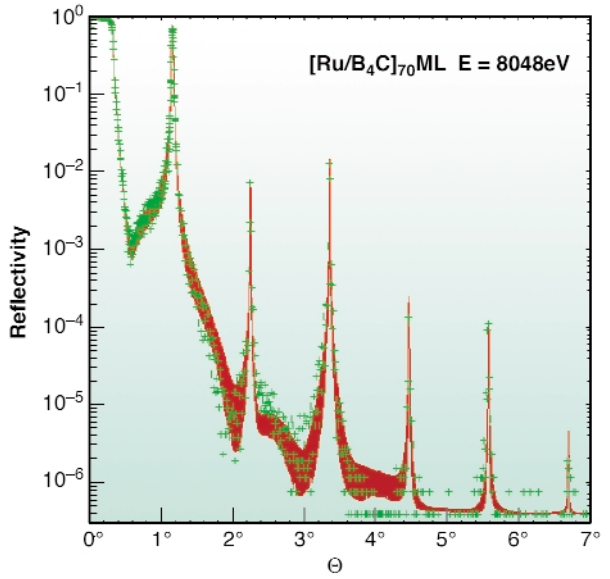

Fig. 167: Measured specular reflectivity versus incidence angle (crosses) and numerical simulation (red curve) of a Ru/B_4C multilayer.

d-spacing of 4.0 nm coated on 300 mm long super-polished Si substrates. The fabrication was done at the ESRF Multilayer Laboratory using a sputtering technique. Although the reflecting surfaces are flat, the finite source distance imposed a lateral thickness gradient of about 1% on the d-spacing to obtain a maximum reflectivity over the whole length of the mirror.

Figure 167 shows the measured specular reflectivity of one multilayer at a photon energy of 8048eV (crosses) superimposed by a simulation (red curve). The latter was then used to calculate the expected performance over a part of the energy range accessible at BM5. **Figure 168** illustrates the estimated intensity after two multilayer reflections at a grazing angle of 1.15° (red curve) starting from the bending magnet source spectrum (blue curve), and including the transmission through all Be windows (green curve). The graph shows that, used as a primary monochromator, lower energies and harmonics of the multilayer itself are reduced by a factor of 10^{-3} to 10^{-4}. In combination with the Si(111) crystal monochromator, the third crystal diffraction harmonic is strongly attenuated, thanks to the pronounced refraction effect that shifts the multilayer Bragg angles (see arrows in **Figure 168**).

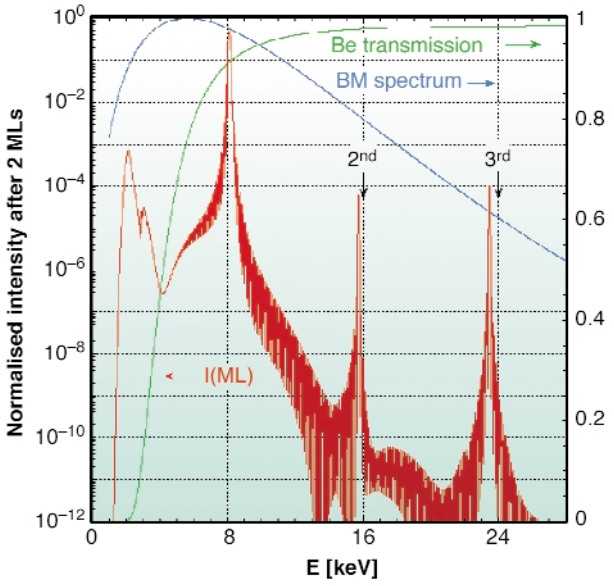

Fig. 168: Estimated intensity versus energy after two multilayer reflections (red curve) on a logarithmic scale, taking into account the bending magnet source spectrum (blue curve) and the transmission through all Be windows (green curve), shown on a linear scale.

Measurements on BM5 confirm that the flux density is 86 times higher than after the Si(111) monochromator at 17.5 keV, thanks to the high reflectivity (70% for 2 reflections) and to the wider bandpass (2%). At 8 keV, where the beam spectral purity is critical, the multilayers allow the rejection of the Si(111) third harmonic by a factor $2 \cdot 10^{-7}$. Small substrate or multilayer imperfections would immediately affect the coherence of the X-ray beam after reflection. The Talbot technique allows measurement of the resulting virtual source size increase, by recording diffraction images of a periodic object at different distances [1]. The so-obtained vertical source size of 84 μm corresponds to the values measured without multilayers, showing that the latter do not visibly degrade the beam coherence. The multilayer monochromator has been commissioned as a permanent part of the beamline optics at BM5.

Double-graded Multilayers for Broadband Focusing

To further increase the effective bandwidth of MLs, non-periodic or depth-graded layered structures can be designed [2]. It would be desirable to merge this approach with the above-mentioned lateral gradient required for curved optics. This would allow the fabrication of a focusing mirror with fixed focal distance and large beam acceptance over a wide energy range. The underlying concept is illustrated in **Figure 169** and is similar to that of DuMond diagrams [3]. In the energy dispersion relation E = E(θ) (Bragg equation) the angular dependence has to be interpreted in terms of the distance f from the position on the mirror to the focal spot, that is θ = θ(f), thus leading to E = E(f).

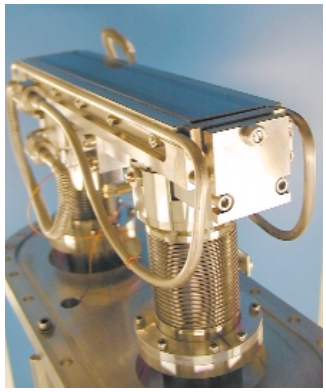

BM5 monochromator: multilayer mounted on its water-cooled holder.

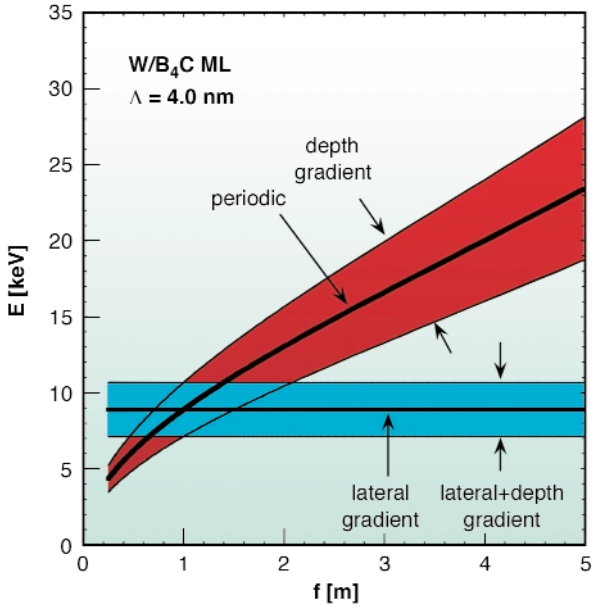

Fig. 169: Energy dispersion of different multilayers. Thick solid lines represent periodic multilayers either with or without lateral gradient. A purely depth-graded multilayer covers the red zone. A combination of lateral and depth gradient is indicated by the blue area.

Following this idea, a double-graded focusing multilayer mirror with a length of 270 mm and a focal distance of 285 mm was designed and fabricated at the ESRF Multilayer Laboratory. Based on a W/B_4C coating, it should provide a constant reflectivity of 50% in a bandwidth of 9% about a mean energy of 9 keV. Focusing experiments were carried out at APS on the undulator beamline 7ID. The focal line was recorded with a CCD camera while varying the photon energy of the incoming beam. The measured line width remained stable at about 8 µm, mostly limited by the figure error of the bent substrate. The total intensity is plotted in **Figure 170** as a function of the photon energy. The experimental data (circles) differ considerably from the ideal prediction (dashed line). However, after inclusion of attenuation and alignment corrections, a good simulation of the data is possible (solid line). We are currently developing a device to be installed at ESRF beamlines.

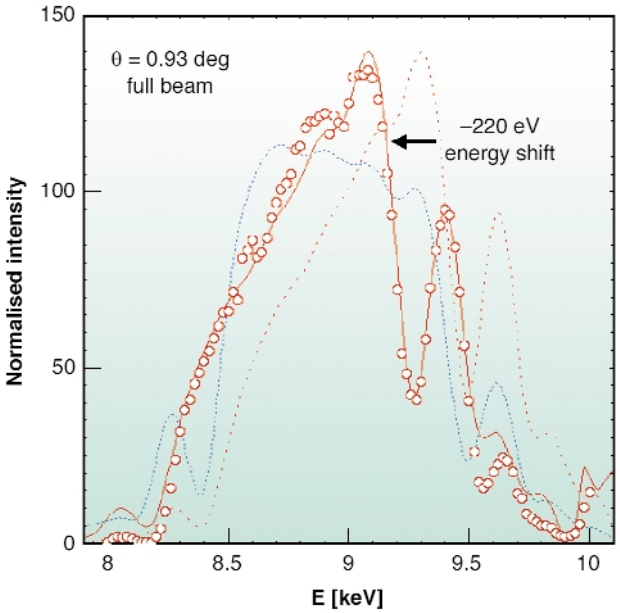

Fig. 170: Normalised total intensity of the focal line measured on the CCD detector (circles) versus photon energy. The dashed blue line indicates the ideal spectrum, the solid red curve is the result after corrections due to absorption and energy shift.

References

[1] P. Cloetens, J.-P. Guigay, C. De Martino, J. Baruchel, M. Schlenker, Opt. Lett. 22, 1059 (1997).
[2] Ch. Morawe, E. Ziegler, J.-Ch. Peffen, I.V. Kozhevnikov, Nucl. Instr. and Meth. A 493, 189 (2002).
[3] J.W.M. DuMond, Phys. Rev. 52, 872 (1937).

Principal publications and authors

Th. Bigault (a), E. Ziegler (a), Ch. Morawe (a), R. Hustache (a), J.-Y. Massonat (a), G. Rostaing (a), SPIE Proceedings 5195 (2003); Ch. Morawe (a), J.-Ch. Peffen (a), E.M. Dufresne (b), Y.S. Chu (c), A.T. Macrander (c), SPIE Proceedings 5195 (2003).

(a) ESRF
(b) University of Michigan (USA)
(c) APS (USA)

Resonant X-ray Magnetic Scattering Studies at 1.0 Kelvin on XMaS

XMaS has in routine use a prototype adaptation of a closed-cycle refrigerator system developed by the cryogenics group at the ILL. A continuous flow of ^{4}He gas, forced through a Joule-Thomson jet, provides the additional cooling at the displex tail that reduces the sample environment base temperature from the 10 K of the standard displex down to 1.7 K. The system can be used in both vertical and horizontal scattering geometries and can be combined with a number of other experimental techniques, for example, with azimuthal scans and also with the XMaS 1.0 Tesla electromagnet.

Recently, an experiment was performed with ^{3}He replacing the ^{4}He flowing through the Joule-Thomson jet. A base temperature of 1.0 K was achieved in a resonant X-ray magnetic scattering (RXMS) experiment to investigate the spin density wave (SDW) antiferromagnetism formed in $TmNi_2B_2C$. $TmNi_2B_2C$ is a celebrated compound because of the co-existence of superconductivity (T_c = 11 K) and magnetism (T_N = 1.5 K) at low temperatures. The (1±τ 1±τ 10) spin density wave satellites, at T = 1 K, together with the (1 1 10) Bragg intensity are shown in **Figure 171**. Polarisation analysis was used to measure the σπ component of the scattered intensity (*i.e.* the component of the incident σ photons scattered with a π-phase shift).

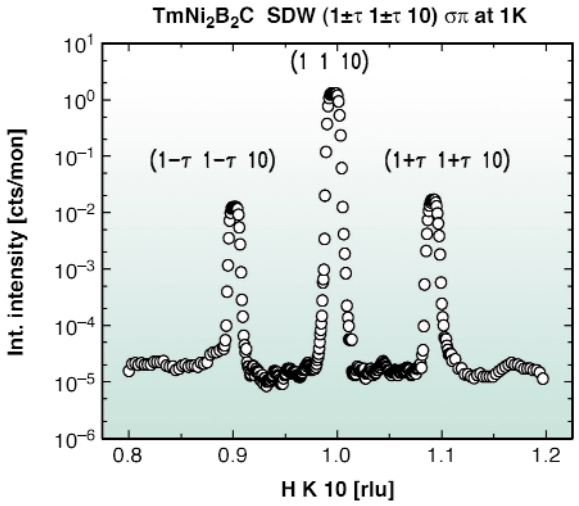

Fig. 171: The (1±τ 1±τ 10) SDW satellites and central (1 1 10) Bragg peak of $TmNi_2B_2C$ at 1.0 K.

Dipole RXMS scatters photons uniquely with this polarisation, whereas the presence of the central (110) Bragg peak in the π channel arises only through 'cross-talk' (σπ leakage through the analyser). **Figure 172** shows the temperature dependence of the (1+τ 1+τ 10) SDW together with data from neutron scattering. Very good agreement is found between the thermal evolution of the magnetic sublattice and T_N for both scattering techniques.

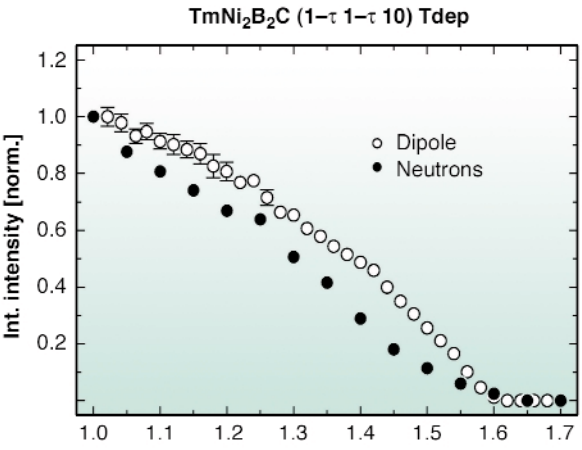

Fig. 172: The temperature dependence of the (1+τ 1+τ 10) SDW RXMS satellite intensities (open circles) compared with published neutron data (filled circles).

It was found necessary, during the acquisition of the RXMS data, to attenuate the beam by two orders of magnitude to avoid excessive local heating of the sample by the intense X-ray beam. Future measurements are planned using an exchange gas to try to reduce this effect.

Authors
D. Mannix (a), P. Thompson (a), S. Pujol (b) and X. Tonon (b).
(a) XMaS UK CRG Beamline, ESRF
(b) ILL

Diffractive Optical Elements for Differential-interference Contrast X-ray Microscopy

X-ray microscopy at multi keV energies often suffers from low contrast imaging of specimens with low absorption. These specimens, called phase objects, retard or advance light that passes through them due to spatial variation in their refractive index and/or thickness. Phase contrast is often employed to image such objects, but the technique induces halo artifacts, is restricted to very thin specimen preparations, and cannot take advantage of the full condenser and objective apertures. Unlike phase contrast, differential-interference contrast (DIC) converts gradients in the object optical path length into amplitude differences that can be visualised as improved contrast in the resulting image. The phase object is sampled by two mutually coherent waves that have a lateral displacement called the shear and a phase displacement called the bias. If the shear is in the order of the object details, this is imaged into an intensity distribution that is a function of the spatial gradient of the object phase distribution. DIC does not yield accurate measurements of object's refractive index or thickness because both beams traverse the same region of the object. However, it is useful to determine the orientation of phase gradients and, capitalising on the full objective aperture, to produce thin optical sections free of obscuring disturbances from object features positioned beyond the focal plane. In the visible light-beam sharing is achieved by illuminating the phase object with a plane-polarised beam which is split by a Wollaston prism. Due to the extreme difficulties in fabricating polarising and

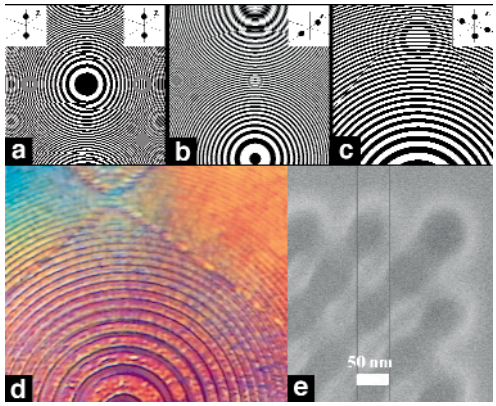

Fig. 173: Optical functions and details of designed DOEs generating: two coplanar spots (a), two coaxial spots (b), four coplanar spots (c). Notice that the left and right parts in (a) are different because they have different biases (0 and π/4 respectively). Optical microscope (d) and SEM (e) images of the fabricated four spot DOE. Optical microscope image represents the central part of the DOE and the SEM image represents the outermost region of the DOE showing the high resolution obtained in fabrication.

refractive components for the X-ray region, a zone plate doublet was proposed for X-ray beam shearing [1]. Nevertheless, this zone-plate doublet does not allow control of bias retardation [2].

We generalised the zone plate concept to Diffractive Optical Elements (DOEs) that can incorporate both the beam shearing and bias retardation functions [3]. The DOE can be seen as an element that generates two spots with a specified phase difference between them. Moreover, its optical function is not limited to this case and can be generalised to more complex shearing configurations, as shown in **Figure 173**. DOEs of this type were fabricated at the Lilit beamline (Elletra) using high resolution electron-beam lithography and electroplating, by modulating the thickness of the gold absorber grown on a silicon-nitride membrane.

The functionality of the DOEs was tested in full-field X-ray microscopy at beamline **ID21**. **Figure 174a** displays the topography of an array of yeast cells which has an absorption lower than 2% at 4 keV. One can see that sub-micrometre details are clearly outlined. The image was obtained with the two coaxial spot DOEs which had a long depth of focus and hence the specimen could be immediately focused, avoiding cell damage. These DOEs can be introduced also in scanning microscopy and can be combined with X-ray fluorescence to obtain simultaneously topographical and morphological information from the specimen.

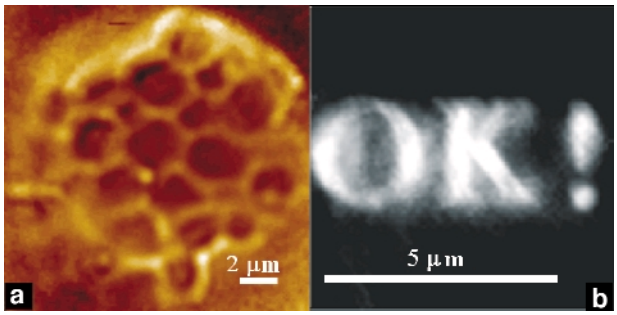

Fig. 174: a) Image of an aggregate of yeast cells obtained with the two coaxial spot DOE (axial shear = 1 mm, bias = 0); b) X-ray beam shaping: continuous intensity pattern generated in a plane situated 5 cm after a DOE calculated to generate the logo 'OK !'.

Following a similar approach, we also calculated and fabricated DOEs to perform X-ray beam shaping. They can replace the zone plate condenser to optimise the specimen illumination (*e.g.* uniform or a general pattern). **Figure 174b** displays general X-ray beam shaping obtained from such a DOE.

In conclusion we have demonstrated phase DOEs that, for the available X-ray sources, accomplish a variety of new functions useful for X-ray microscopy. Moreover, the freedom in redistributing the wavefront suggests a maskless way to transfer the information onto a substrate. The sensitive material on the surface can be either a resist or a precursor gas, in the case of chemical vapour deposition, whose interaction with the surface can be induced by photons.

References

[1] T. Wilhein, B. Kaulich, E. Di Fabrizio, F. Romanato, S. Cabrini, and J. Susini, *Appl. Phys. Lett.* **78**, 2082 (2001).

[2] B. Kaulich, T. Wilhein, E. Di Fabrizio, F. Romanato, M. Altissimo, S. Cabrini, B. Fayard, and J. Susini, J. Opt. Soc. Am A **19**, 797-806 (2002).

[3] E. Di Fabrizio, D. Cojoc, S. Cabrini, B. Kaulich, T. Wilhein, and J. Susini, J. Phys. IV France **104**, 177-183 (2003)

Principal Publication and Authors

E. Di Fabrizio (a), D. Cojoc (a,f), S. Cabrini (a), B. Kaulich (b), J. Susini (c), P. Facci (d), T. Wilhein (e), *Optics Express*, **11**, 2278 (2003).

(a) Lilit Beamline, TASC-INFM, Elettra Sincrotrone, Trieste (Italy)

(b) Elettra Sincrotrone, Trieste (Italy)

(c) ESRF

(d) INFM - University of Modena (Italy)

(e) University for Applied Sciences, Remagen (Germany)

(f) 'Politehnica' University of Bucharest (Romania)

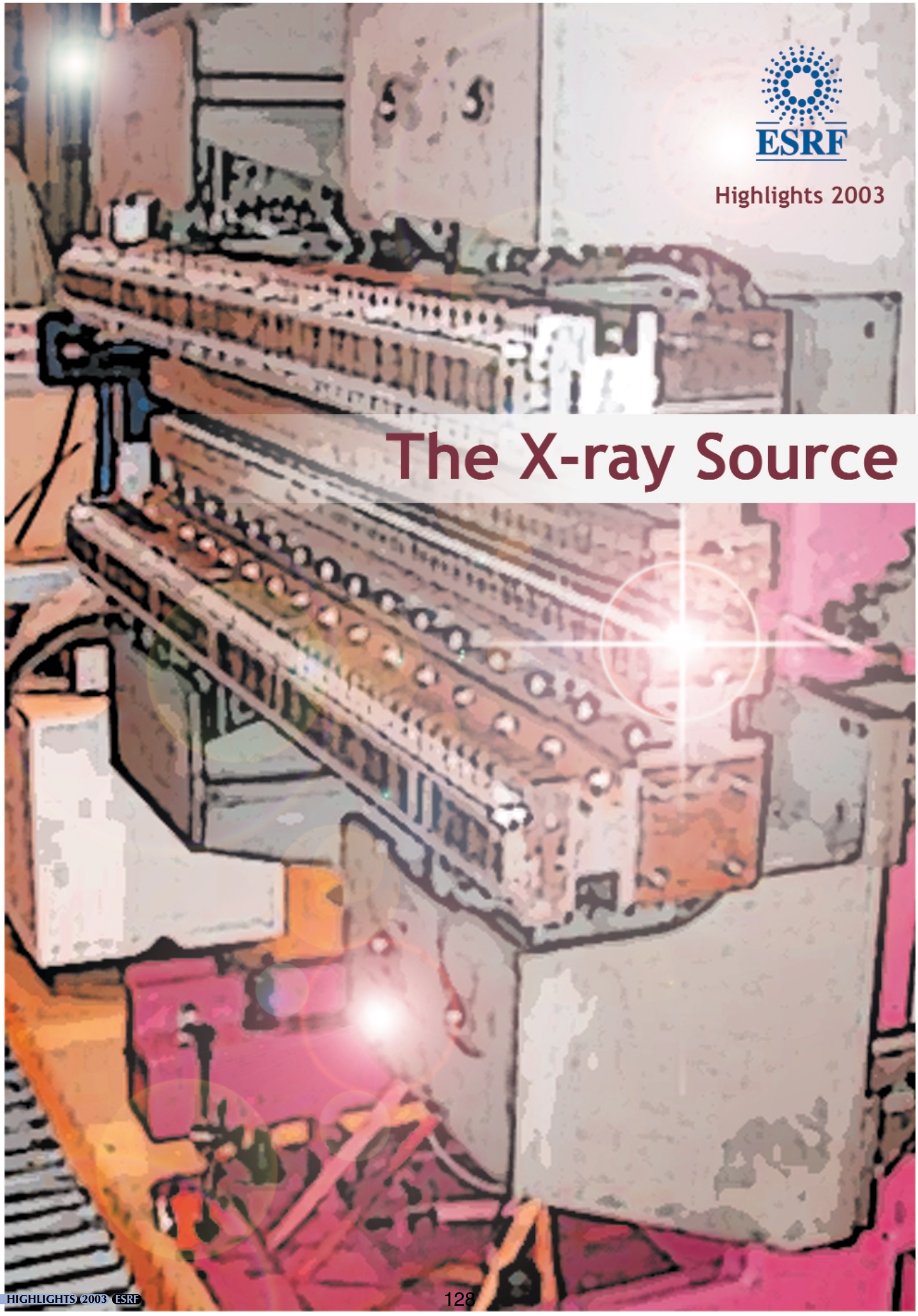

ESRF

Highlights 2003

The X-ray Source

Introduction

Throughout 2003, the Machine Division continued its efforts to improve performance and carried out a number of developments, which are described below.

Machine Parameters

The **Table 3** below presents a summary of the characteristics of the electron beam of the storage ring:

Energy	[GeV]	6.03
Maximum Current	[mA]	200
Horizontal emittance	[nm]	4
Vertical emittance (*minimum achieved)	[nm]	0.03 (0.01*)
Coupling (*minimum achieved)	[%]	0.6 (0.25*)
Revolution frequency	[kHz]	355
Number of bunches		1 to 992
Time between bunches	[ns]	2816 to 2.82

Table 3: Main global parameters of the electron beam.

The following **Table 4** gives the main optics functions, electron beam sizes and divergences at the various source points. For insertion device source points, the beta functions, dispersion, sizes and divergences are computed in the middle of the straight section. Two representative source points of bending magnet radiation have been selected, corresponding to an angle of observation of 3 mrad (9 mrad) from the exit, which corresponds to different magnetic fields. Electron beam profiles are Gaussian and the size and divergence are presented in terms of rms quantities. The associated full width half maximum sizes and divergences are 2.35 times larger. Horizontal electron beam sizes and divergences are given for the uniform filling modes and apply to almost all filling patterns except for the single bunch, for which a slightly larger size and divergence is attained due to the increased energy spread of the electron beam. Vertical electron beam sizes and divergences apply to the Uniform, 2x1/3 and Hybrid filling modes only. In order to increase the lifetime of the stored beam, the vertical beam sizes and divergences are increased by a typical 50% in 16 and single bunch filling patterns.

The lifetime, bunch length and energy spread depend to a large extent on the filling pattern. These are given in the following **Table 5** for a few representative filling patterns. It should be noted that in both the 16 bunch and single bunch filling patterns the energy spread and bunch length decay with the current (the value indicated in the table corresponding to the maximum current). The bunch lengths are given for the usual RF accelerating voltage of 8 MV.

Filling pattern		Uniform	16-bunch	Single bunch
Maximum current	[mA]	200	90	15
Lifetime	[h]	75	9	6
Rms energy spread	[%]	0.11	0.12	0.22
Rms bunch length	[ps]	20	48	72

Table 5: Current, lifetime, bunch length and energy spread in various representative filling modes.

Summary of Machine Operation

In 2003, a total of 680 shifts, representing 5441 hours, were dedicated to the Users. This year once again, high figures have been maintained. From this year onwards, special care must be taken in interpreting the 'refill time', availability and Mean Time Between Failures (MTBF) figures. This is due to the fact that since 5th February 2003 the Front End shutters remain open during refills. This year, contrary to previous years, we therefore consider the X-ray source availability based on the assumption that the beam can be used during the refill. With this definition in mind, the beam availability reached

		Even ID Section (ID2,ID6…)	Odd ID Section (ID1,ID3 …)	Bending Magnet 3 mrad	Bending Magnet 9 mrad
Field	[T]	Depends on ID	Depends on ID	0.4	0.85
Horiz. Beta Functions	[m]	35.2	0.5	1.41	0.99
Horiz. Dispersion	[m]	0.137	0.037	0.061	0.045
Horiz. rms e- beam size	[µm]	402	59	100	77
Horiz rms e- divergence	[µrad]	10.7	90	116	111
Vert. Beta Functions	[m]	2.52	2.73	34.9	34.9
Vert. rms e- beam size	[µm]	7.9	8.3	29.5	29.5
Vert. rms e- divergence	[µrad]	3.2	3	0.85	0.85

Table 4: Beta functions, dispersion, rms beam sizes and divergences for the various source points of the ESRF.

RUN NUMBER	TOTAL 2002	2003-01	2003-02	2003-03	2003-04	2003-05	TOTAL 2003
Start		24/01/03	28/03/03	06/06/03	29/08/03	24/10/03	
End		19/03/03	28/05/03	07/08/03	15/10/03	18/12/03	
Total number of shifts	855	162	183	186	141	165	837
Number of USM shifts	687	131	149	152	114	134.1	680.1
Beam available for users (h)	5319	1018.8	1147.3	1175.5	888.5	1044.9	5275
Availability	98%	98.7%	97.5%	97.3%	98.1%	98.3%	97.95%
Dead time for failures	2%	1.3%	2.5%	2.7%	1.9%	1.7%	2.05%
Dead time for refills	1.2%	1.5%	1.3%	0.6%	0.6%	0.9%	1%
Average intensity (mA)	146	125	134	148	124	142	135.3
Number of failures	95	21	40	32	23	22	138
Mean time between failures (h)	57.8	49.9	29.8	38	39.7	48.8	39.4
Mean duration of a failure (h)	1.2	0.7	0.7	1	0.8	0.8	0.81

Table 6: Statistics of shifts, dead time, mean time between failures and beam availability in 2003.

97.95% in 2003. If the refill time were to be considered as non-available time, the beam availability would have been 96.95%. However in order to be consistent, we have to take into account all the failures which occur during refills. These failures, which were transparent to the Users with the injection 'Front-End closed', are now visible and contribute to a reduction in the MTBF. With this revised way of counting, the MTBF reached 39.4 hours. This figure remains good and reflects the fact that on average, the beam is interrupted only 48 minutes every 39.4 hours. Note that 28 failures out of 138 occurred during injection and would not have been accounted for in the MTBF computation of previous years. Removing the failures during injection would give an MTBF of 49.5 hours in 2003, compared to 58 hours in 2002.

This lower MTBF in 2003 is essentially due to the partial unavailability of HQPS. The HQPS system consists of 10 x 0.8 MW Diesel Engines coupled to a rotating accumulator and an alternator. It is capable of eliminating the electron beam losses originating from the voltage and phase drops which occur during stormy weather (somewhat frequent in the Grenoble area during spring and summer due to the surrounding mountains). The HQPS system has been successfully operating for 7 years and has recently suffered some damage. Repairs were carried out and the system was operated in its normal fashion from June to November, once again protecting the machine infrastructure. Unfortunately it had to be stopped again following the appearance of abnormal wear on the bearings. Detailed investigations into the problem are being made with the help of the companies who manufactured the various components, and under the leadership of an Expert appointed by the "Tribunal de Grenoble".

Finally, let us mention some excellent periods of delivery with 14 periods of uninterrupted beam greater than 79 hours (including one period of 156 hours and two periods of 144 hours!)

Filling Patterns

Figure 175 presents the distribution of the various filling modes used in 2003. The larger share of the 16 bunch filling mode as compared to 2002 is not significant since, for reasons of convenience, some of the 16 bunch shifts slipped from 2002 to 2003. The multi-bunch modes of operation (uniform and 1x1/3 filling patterns) provide the highest current and the longest lifetime of the stored beam and correspond to 59% of the total beamtime. The other modes of operation aim at providing a particular filling pattern to users making use of the time structure of the electron beam.

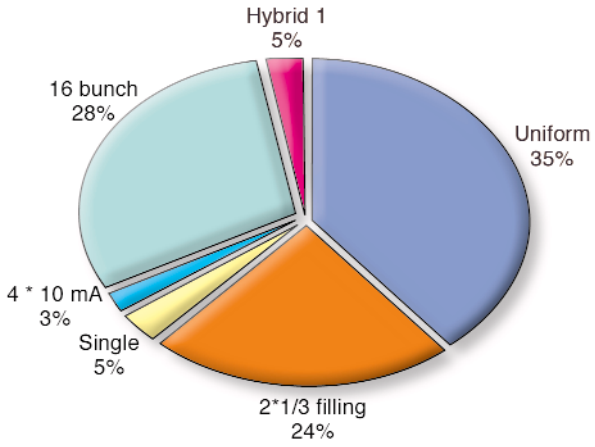

Fig. 175: Distribution of the 2003 user time in the various filling modes.

A new hybrid mode has been developed consisting in 24 groups of 8 bunches + 1 bunch of 4 mA. This mode is delivered with a 200 mA current and a reasonable lifetime (~ 30 hours). It is targeted to simultaneously satisfy the maximum number of users including the majority who are looking for maximum current as well as those who need such a time structure with many empty buckets in between the filled bunches. The usual RF knockout technique of cleaning the residual parasitic bunches resulted in a contrast ratio as large as 10^9

between the filled and the unfilled buckets. Such a filling pattern was developed for the first time in 2002. Two weeks of this beam were successfully delivered in 2003 with two refills per day. It is intended to make this the standard hybrid mode in 2004.

Some difficulties were experienced in 2002-3003 with single bunch delivery. Whereas in previous years it was possible to reach an intensity of 20 mA, this is no longer true and in spite of a great deal of effort to find the optimum parameters, the maximum single bunch current offering sufficient stability and low emittance dropped to 14 mA in 2003. Although the reason for this limitation has not been precisely determined, it is strongly suspected that it comes from an increase in both the horizontal and vertical coupling impedance induced by the discontinuities and resistivity of the recently installed small aperture vacuum vessels. In order to continue satisfying the User community using single bunch and those interested in both the time structure and a sufficient beam current, a new mode has been developed and was successfully delivered for 23 shifts during the last run of the year. It consists in 4 bunches of 10 mA equally distributed around the circumference. With a lifetime of 5 hours and a total maximum intensity of 40 mA, this mode will most likely replace the single bunch one in the future.

Injection with Front-End Open

Until February 2003, the shutters located in the front end of all beamlines were closed for a few minutes before and during injection, resulting in some temperature variations on the monochromators and/or the first mirrors of the beamlines. This thermal transient resulted in an interruption in data acquisition at each injection, ranging from several minutes up to one hour. The shutters are now left open during injection, allowing the operation to be truly continuous. Thanks to the naturally long lifetime of the electron beam, top-up can be carried out at a very low repetition rate (typically once every 12 hours in the most demanded multi-bunch modes). This is beneficial for the most sensitive and/or advanced beamlines, since it reduces the necessity of gating the data acquisition at frequent injection times. A software counter, which can be used to synchronise the data acquisition, informs the beamlines of the injection schedule.

Before implementing the injection with front end (FE) open, a feasibility study was carried out to verify that it would comply with the radiation protection policy. The Euratom/96-29 recommends a maximum dose of 1 mSv/year for the category of personnel who are not exposed. The ESRF applies this recommendation to all ESRF staff. Taking into account a rate of 2000 hours of work/year yields a maximum dose rate of 2 microSv every 4 hours. The accidental steering of an electron beam pulse freshly injected from the booster into a beamline with its front end open would result in an integrated dose which would greatly exceed this limit. But a detailed study has demonstrated that it is impossible to steer a beam from the booster into a beamline, if a beam is already stored in the storage ring. Consequently, injection with FE open is only allowed if the measured stored beam before injection is greater than 5 mA.

Measurements were carried out to assess dose values outside the hutches of the beamlines during injection with front end open for different machine tunings and filling modes. They have shown that, under normal operation conditions, the injection losses, as well as the losses due to bunch cleaning, in all filling modes produce very low dose rates. Significant dose values were only measured with seriously degraded storage ring optics, resulting in a poor injection efficiency. Nevertheless, radiation monitors have been installed outside the optics hutches on all beamlines, fast enough to interlock the corresponding front end if dose limits exceeded the authorised level during injection (**Figure 176**).

Fig. 176: Ionisation Chamber monitoring the dose rate close to the hutch of a beamline.

Indeed, the measured dose around the beamline hutches is dominated by the background level in the experimental hall or in a few beamlines by the Bremsstrahlung generated by the residual pressure in the ID vessel. No significant dose values are integrated during the injections.

The demagnetisation of permanent magnetic material exposed to high-energy electrons was observed at the ESRF in 1993 on two undulator segments made with NdFeB material. Nowadays, the much tighter diagnostic and control of the losses during injection, by means of the network of neutron and Bremsstrahlung detectors, has made such accidents very unlikely for undulators with in-air magnets (magnetic gap > 11 mm). Consequently, the magnetic gap of undulators and wigglers is maintained unchanged during injection, thereby maintaining the heatload unchanged in the beamlines. In-vacuum undulators are built with more resistant material (Sm_2Co_{17}). When they are closed to a gap of 5 or 6 mm, even though the injection efficiency when optimal settings are achieved is normally close to 90-100%, it is expected that important accidental electron beam losses will take place from time to time in some of the in-vacuum undulators. For this reason it has been decided to limit the minimum gap to 8 mm (instead of 6 mm) for all in-vacuum undulators during injection. For the corresponding beamlines, this generates a maximum 30% heat load variation over a few minutes. At present we have insufficient information on the long-term effects on magnets subjected to such losses. In the future it is planned to reduce the 8 mm gap limit as low as possible following a detailed quantitative study performed on the ID6 machine beamline.

Progress with NEG Coated Insertion Device Vacuum Chambers

Long, small-aperture Insertion Device (ID) vacuum chambers are difficult to pump due to the low conductance. As a result the collision of the electrons with the residual gas may produce a large amount of Bremsstrahlung gamma rays. When hitting a material, this Bremsstrahlung produces a cascade of lower energy particles, some of them energetic enough to go through a few centimetres of lead. As a consequence a significant dose rate can be recorded outside the hutch. To reduce this dose rate to an acceptable level, one must control the residual gas pressure in the insertion device vacuum chamber. To do so, the ESRF has developed, in collaboration with CERN, a process of coating the inner surface of the ID vessels with a thin, Non Evaporable Getter (NEG) material. Such material provides distributed surface pumping along the whole length of the chamber and reduces the photon-induced desorption. By the end of 2003 14 NEG coated ID chambers of different lengths, apertures and material will have been installed on the ring totalling a cumulated length of 60 m. The first chamber was coated at CERN, but in 2002 the ESRF developed its own NEG coating facility and 4 of the most delicate ID chambers were coated in-house in 2003. These chambers, made of aluminium, are 5 m long and have an 8 x 57 mm internal aperture. They were installed on the ID6 straight section and the Bremsstrahlung produced on-axis was monitored using a detector located in the ID6 optics hutch. Out of the 4 chambers, two have been considered successful and put into operation on the ID26 and ID20 straight sections. **Figure 177** shows the Bremsstrahlung dose rate recorded vs. integrated ring current for the last three chambers installed. One observes a large dispersion of the results. The two lower curves correspond to chambers for which the coating is considered as successful. These chambers are now in operation on ID26 and ID20. A large number of bursts are visible on the upper curve. These bursts were correlated with small electron beam losses and are likely to come from the collision of the beam with a small piece of NEG material falling from the aluminium surface.

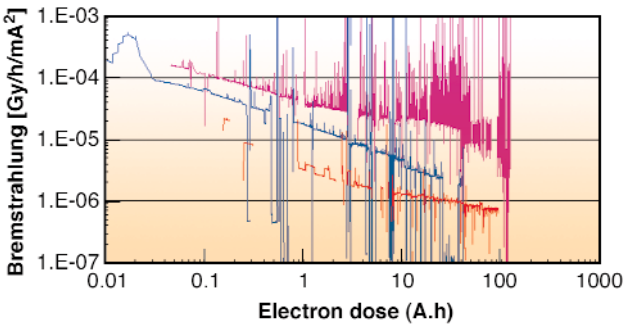

Fig. 177: The Bremsstrahlung measured on axis of three different NEG coated, 8 mm aperture ID chambers as a function of the integrated electron current. Each curve corresponds to a different chamber.

A careful inspection of the defective chambers with an endoscope has confirmed the expectation of a lack of adhesion of the coating material in a few places. Experience in the past has shown that aluminium is more prone to such adhesion problems than stainless steel and that such problems are probably linked to insufficient cleaning/conditioning of the surface prior to the coating by magnetron sputtering. As a result of this, the whole coating process has since then been reviewed in depth in order to eliminate such problems in the future. Further development is going on. A so-called quadrupole vacuum chamber has been NEG coated. Such chambers have a large transverse dimension due to the pumping port and cannot be inserted into a solenoid of reasonable size. Consequently, an array of permanent magnets rather than a solenoid was used to create the field necessary for the magnetron sputtering.

Insertion Devices

The complete list of Insertion Device segments installed on all ESRF beamlines can be consulted at: http://www.esrf.fr/Accelerators/Accelerators/StorageRing/IDs/

The gradual replacement of 16 mm external aperture ID chambers with 10 mm aperture chambers is followed by an appropriate refurbishment of the undulator segments. As a result the long-standing 42 mm typical undulator period of a fully tuneable undulator has evolved into a 32-35 mm period.

In 2003, three in-vacuum undulators were manufactured. All three devices will be installed during the winter shutdown. They are dedicated to operation at high photon energy (40 keV-100keV) inaccessible with conventional undulators (see **Figure 178**). The status of ESRF in-vacuum undulators is summarised in **Table 7**.

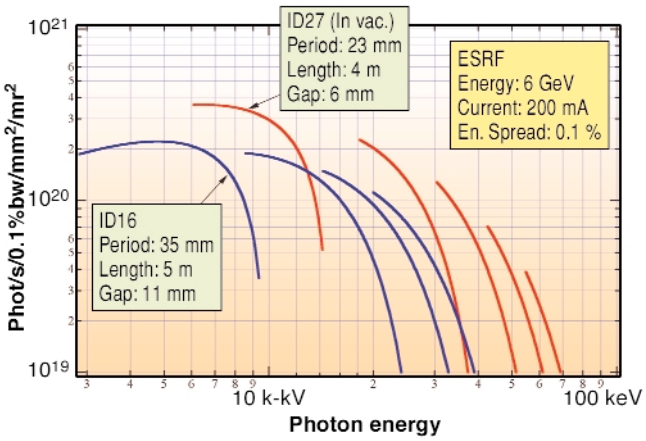

Fig. 178: Brilliance achieved on ID16 and expected brilliance for ID27 with two in-vacuum undulators operated at a minimum gap of 6 mm.

The last device in Table 5 (ID11 U22) is a hybrid undulator based on permanent magnets and soft iron poles. For the same period and gap, hybrid undulators provide higher peak fields than PPM devices. This is particularly relevant to in-vacuum undulators where the gap/period ratio reaches 0.3. Indeed, the measured peak field of the newly built ID11 U22 hybrid undulator is 0.875 T for a gap of 6 mm while it reaches only 0.72 T for a pure permanent magnet undulator of the same period and magnetic gap. Due to specific difficulties in the shimming, the hybrid technology has so far been avoided for in-vacuum undulators. Following a thorough study carried out in 2003 with the ID11 U22 hybrid undulator, it is now believed that most difficulties have been solved. For obvious reasons pertaining to performance, all future in-vacuum undulators will use the hybrid technology. In 2003 a prototype revolver support was built. Three additional support structures are expected for delivery at the end of 2003. The revolver support can accommodate two different magnetic assemblies mounted on a rotating girder (see **Figure 179**).

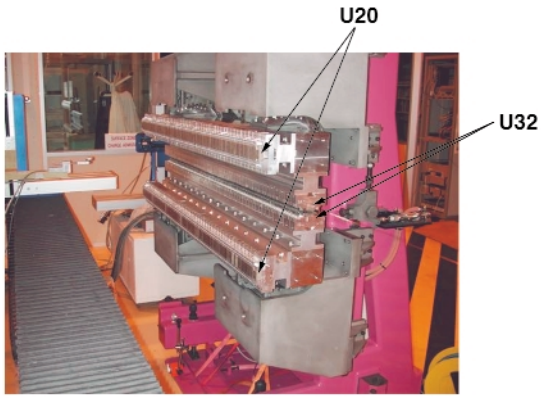

Fig. 179: Revolver support equipped with a U32 and a U20. This device is now installed on the ID18 straight section.

	Period [mm]	Length [m]	Magnetic Structure	Min. Gap Gap	Rms Phase error [deg] @ 6 mm	Field int. [G.cm]	Operation
ID11	23	1.6	Hybrid	5	?	< 70	Jan 99
ID22	23	2	PPM	6	1.9	< 26	Jul 01
ID9	17	2	PPM	6	< 5	< 15	Jul 01
ID29	21	2	PPM	6	2.3	< 15	Dec 02
ID13	18	2	PPM	6	< 5	< 15	Jul 02
ID27	23	2	PPM	6	2.3	< 15	Jan 04
ID27	23	2	PPM	6	2.3	< 15	Jan 04
ID11	22	2	Hybrid	6	2.4	< 25	Jan 04

Table 7: Status of in-vacuum undulators, all of them based on Sm_2Co_{17} permanent magnet material. The stated maximum field integrals apply to both the vertical and horizontal field integrals to all gap values between 30 and 6 mm. PPM stands for the pure permanent magnet technology while hybrid structures are made of permanent magnets and iron poles. The phase errors are given at the minimum gap where the requirements are most severe.

Such a structure is designed to be interchangeable with any existing 1.6 m undulator segment in operation. A typical use of the revolver support involves a non-tuneable short period undulator (17 to 27 mm) providing 2-3 times enhanced brilliance in a limited photon energy range and a standard fully tuneable undulator (32 to 35 mm).

The status of revolver development is presented in Table 8.

Straight Section	Period 1 [mm]	Period 2 [mm]	Operation
ID18	32	20	Jan 2004
ID10	35	27	Aug 2004
ID28	32	17.6	Oct 2004
ID16	32	26	Dec 2004

Table 8: Status of revolver undulators, all devices are 1.6 m long and will be operated with an 11 mm minimum magnetic gap.

In parallel to the intensive production of new insertion devices, mechanical wear on one of the oldest magnetic measuring benches was discovered, preventing the completion of phase shimming. A new Hall probe-scanning bench has been designed, built and put into operation in 2003. It makes use of the recently available linear motor which allows a scan to be made at a speed 4 times higher with higher mechanical stability and less vibration resulting in higher accuracy and improved repeatability (x5) of the measured field. A copy of such a bench has since been produced for the Swiss Light Source.

Current ramping

A beam current of 250 mA was stored in the machine for the first time in 2001. However, the radiation induced outside the shielding exceeded the authorised level and tests were temporarily interrupted. After a campaign of systematic shielding reinforcement, experiments resumed in April 2003. Stable beam at 250 mA was stored in one-third filling mode. With this partial filling (330 bunches) of the circumference, the periodic beam loading of the cavities induces a spread in synchrotron frequencies along the bunch train that prevents the constructive built-up of Higher Order Mode (HOM) driven coupled bunch instabilities. The machine is now operated at this current during the restart period following each shutdown, in order to speed up the vacuum conditioning time required by the installation of new vacuum vessels. In the uniform filling mode, the stabilisation of the longitudinal coupled bunch instabilities is more difficult and has to be performed by a precise temperature optimisation of the RF cavity temperatures. A beam current of 250 mA was also achieved in that filling pattern but the HOM driven instabilities still need to be mastered in the whole [0 – 250 mA] current range. The final assessment of operating conditions will be performed in the forthcoming months.

As far as vacuum and heat load are concerned, the one-third filling mode is the most demanding. No abnormal pressure or temperature rise on critical components like ceramic chambers, crotches, bellow flat absorbers or RF windows was observed when ramping the current from 200 to 250 mA. The lifetime is in excess of 55 h in uniform filling mode (to be compared to 80 hours at 200 mA). This lifetime reduction is due to the higher residual pressure in the ring, the higher density of electrons in the bunch (Touschek lifetime) and to the increase in the chromaticity in order to stabilise the resistive wall instability.

Measurement of the vacuum chamber coupling impedance

The beam intensity in the storage ring is limited by several effects, depending on the filling pattern: thermal limitations, beam instabilities… The beam instabilities are driven by the interaction of the electromagnetic field induced by the beam and its environment, typically the surrounding conductive vacuum chamber or RF cavities. This interaction is characterised by the so-called “coupling impedance”, relating the perturbations seen by the beam, due to the presence of the vacuum chamber, to the beam intensity. For better performance, this impedance should be kept as low as possible. However, the finite conductivity of the chamber and any variation of the chamber cross-section will contribute to the impedance. The coupling impedance can be defined for any portion of the chamber, and all impedances add up to give the total ring impedance. Among the main contributions to this impedance, we can find:

- All narrow gap chambers, like low gap ID chambers, in-vacuum undulators, NEG coated chambers.
- RF accelerating cavities, bellows, flanges, tapers and transitions contributing to resonator-like objects in the impedance.

As discussed earlier, the stability of the single bunch mode of operation has been significantly reduced in the last two years since the installation of the 8mm aperture vacuum chambers got under way. In the long term about 20 of these chambers will be installed and the stability of the beam in the multibunch filling pattern could also be

affected through the so-called resistive wall effect. It is therefore essential to follow the evolution of the storage ring impedance and to validate the technological choices of the ID chambers. Theoretical values of impedance can be computed at the design phase, but they require extensive numerical simulations and do not take into account the unavoidable imperfections. Recently, we started using a new method to measure the impedance of selected portions of the vacuum chamber [1].

The coupling impedance can be expressed by 3 complex functions of the frequency: the longitudinal impedance, related with bunch lengthening and longitudinal instabilities, and the horizontal and vertical impedances, related to tune shifts and transverse instabilities. The method we use applies to the vertical impedance (though it can also be used for horizontal impedance).

This method consists in displacing the beam vertically, using a static orbit deviation, to the place where we want to measure the impedance. The effect of the impedance is to induce an angular kick proportional to the displacement, the bunch intensity and the imaginary part of the effective impedance (impedance integrated over the bunch spectrum). This small kick is measured by subtracting the orbit deviations measured by displacing a low intensity beam (where the effect of impedance is negligible) and a high intensity beam. We use two different set-ups:

- Local measurements where we apply a local orbit bump and measure the impedance of a single straight section, including the adjacent dipoles.
- Global measurements where we apply a series of orbit oscillations probing the impedance all around the machine, and a processing extracting an impedance value for each straight section.

The final result is the imaginary part of the effective impedance. Though this number does not provide any information as to the behaviour of the impedance versus frequency, it is a relevant figure of merit for estimating the consequences on the beam.

Figure 180 summarises the values measured since May 2003 using the global measurement set-up. It shows the reproducibility of the method and the properties of various types of straight sections.

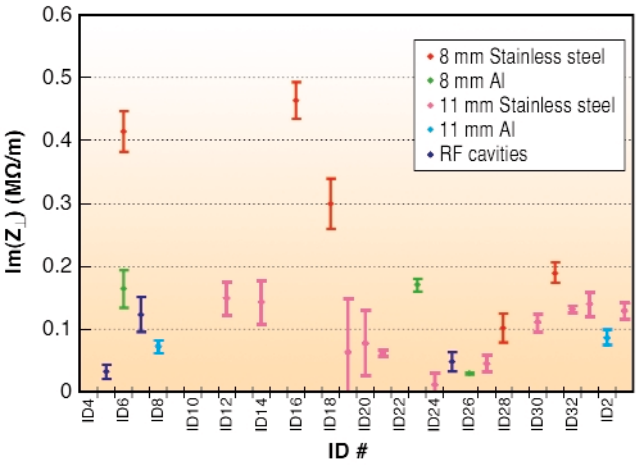

Fig. 180: Vertical effective impedance measured on several straight sections of the storage ring.

The largest values are reached by some 8 mm internal aperture stainless steel chambers, with a large dispersion between the five similar chambers. Local measurements performed on a few straight sections are in good agreement with these values. Local measurements performed in the short straight section of the achromats confirm that the impedance is much lower in these areas.

In conclusion one could say that, unlike theoretical estimates, the direct measurement of impedances takes into account all fabrication errors and imperfections, resulting in a significant dispersion of measured values for identical vacuum chambers. The measured values are also larger than the theoretical estimates. This is especially true for stainless steel 8 mm aperture chambers. The aluminium 8 mm aperture chambers have a better behaviour and show consistently low values. Finally the measurements confirm the expected fact that the impedance is mainly localised in the small aperture insertion device straight sections, the short straight section of the achromats making a lower contribution.

Reference

[1] L. Emery, G. Decker, J. Galayda, PAC 2001, Chicago.

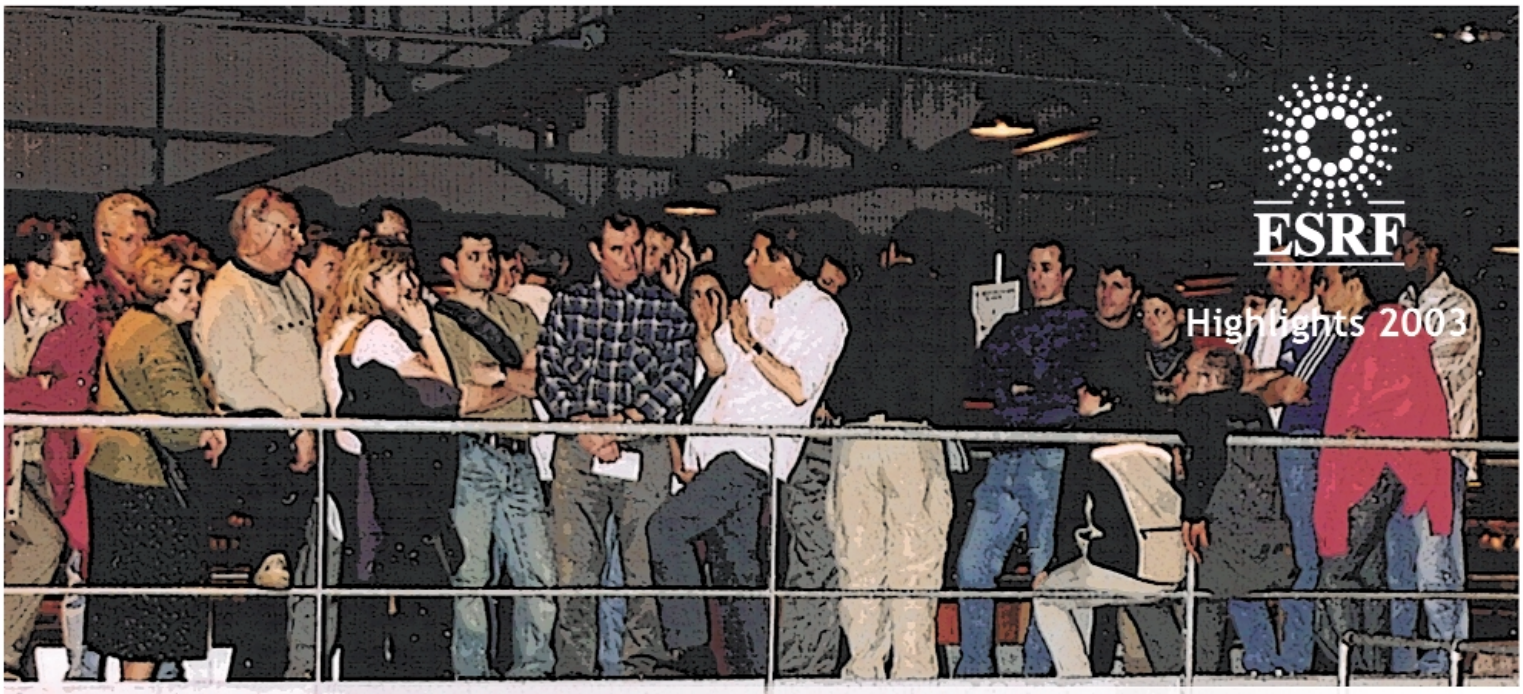

ESRF

Highlights 2003

Facts and Figures

Member and Associate Countries

Members' share in contribution to the annual budget:

27.5% France
25.5% Germany
15% Italy
14% United Kingdom
4% Spain
4% Switzerland
6% Benesync (Belgium, The Netherlands)
4% Nordsync (Denmark, Finland, Norway, Sweden)

Additional contributions
(percentages refer to Members' total contribution):

1% Portugal
1% Israel
1% Austria
0.38% Czech Republic
0.2% Hungary

The Beamlines

All thirty of the ESRF public beamlines have been operational since 1999. Two of these possess two end-stations, so there are thirty two end-stations in total, which can be run independently. An additional sixteen beamline branches, situated on bending magnets, are devoted to Collaborating Research Groups (CRG). Eleven of the CRG beamlines are now in operation (including GRAAL), the others are being commissioned or under construction. **Figure 181** shows the location of the beamlines in the experimental hall; a list of the public beamlines is presented in **Table 9**; and a list of the CRG beamlines in **Table 10**.

A new beamline complex dedicated to protein crystallography is under construction on ID23 as part of the Partnership for Structural Biology (PSB). The first beamline branch has recently been commissioned and is starting users' operation. A second branch will be constructed in 2004.

The High Pressure beamline will be moved to a new location, ID27, that was previously used for an industrial beamline. The beamline will be rebuilt in a refurbished form.

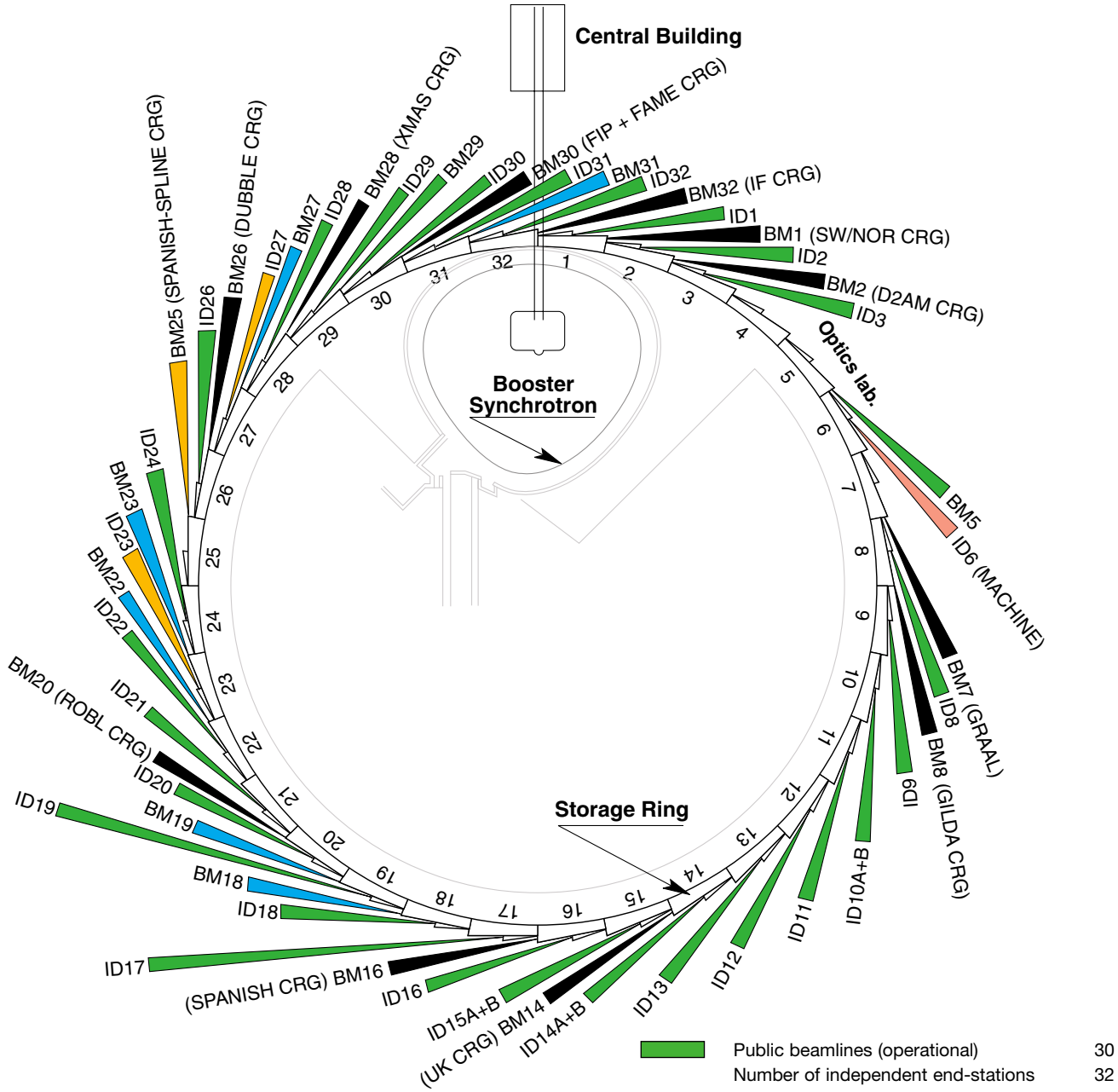

Fig. 181: Experimental hall with the operational and scheduled beamlines (public and CRG beamlines).

SOURCE POSITION	NUMBER OF INDEPENDENT END-STATIONS	BEAMLINE NAME	STATUS
ID1	1	Anomalous scattering	Operational since 07/97
ID2	1	High brilliance	Operational since 09/94
ID3	1	Surface diffraction	Operational since 09/94
ID8	1	Dragon	Operational since 02/00
ID9	1	White beam	Operational since 09/94
ID10A	1	Troika I + III	Operational since 09/94
ID10B	1	Troika II	Operational since 04/98
ID11	1	Materials science	Operational since 09/94
ID12	1	Circular polarisation	Operational since 01/95
ID13	1	Microfocus	Operational since 09/94
ID14A	2	Protein crystallography EH 1	Operational since 07/99
		Protein crystallography EH 2	Operational since 12/97
ID14B	2	Protein crystallography EH 3	Operational since 12/98
		Protein crystallography EH 4	Operational since 07/99
ID15A	1	High energy diffraction	Operational since 09/94
ID15B	1	High energy inelastic scattering	Operational since 09/94
ID16	1	Inelastic scattering I	Operational since 09/95
ID17	1	Medical	Operational since 05/97
ID18	1	Nuclear scattering	Operational since 01/96
ID19	1	Topography	Operational since 06/96
ID20	1	Magnetic scattering	Operational since 05/96
ID21	1	X-ray microscopy	Operational since 12/97
ID22	1	Microfluorescence	Operational since 12/97
ID23	2	Macromolecular crystallography	Under construction/commissioning
ID24	1	Dispersive EXAFS	Operational since 02/96
ID26	1	X-ray absorption on ultra-dilute samples	Operational since 11/97
ID27	1	High pressure	Under construction (to replace ID30)
ID28	1	Inelastic scattering II	Operational since 12/98
ID29	1	Multiwavelength anomalous diffraction	Operational since 01/00
ID30	1	High pressure	Operational since 06/96
ID31	1	Powder diffraction	Operational since 05/96
ID32	1	SEXAFS	Operational since 11/95
BM5	1	Optics - Open Bending Magnet	Operational since 09/95
BM29	1	X-ray absorption spectroscopy	Operational since 12/95

Table 9: List of the ESRF public beamlines in operation and under construction.

SOURCE POSITION	NUMBER OF INDEPENDENT END-STATIONS	BEAMLINE NAME	FIELD OF RESEARCH	STATUS
BM1	2	Swiss-Norwegian BL	X-ray absorption & diffraction	Operational since 01/95
BM2	1	D2AM (French)	Materials science	Operational since 09/94
BM7	1	GRAAL (Italian / French)	Gamma ray spectroscopy	Operational since 06/95
BM8	1	Gilda (Italian)	X-ray absorption & diffraction	Operational since 09/94
BM14	1	UK CRG	Macromolecular crystallography (MAD)	Operational since 01/01
BM16	1	SPANISH CRG	Structural biology (MAD, SAX)	Operational in 2003
BM20	1	ROBL (German)	Radiochemistry & ion beam physics	Operational since 09/98
BM25	2	SPLINE (Spanish)	X-ray absorption & diffraction	Construction phase
BM26	2	DUBBLE (Dutch/Belgian)	Small-angle scattering & interface diffraction Protein crystallography + EXAFS	Operational since 12/98 Operational since 06/01
BM28	1	XMAS (British)	Magnetic scattering	Operational since 04/98
BM30	2	FIP (French) FAME (French)	Protein crystallography EXAFS	Operational since 02/99 Operational since 08/02
BM32	1	IF (French)	Interfaces	Operational since 09/94

Table 10: List of the Collaborating Research Group beamlines in operation and under construction.

User Operation

During the year 2003 the full complement of 30 public beamlines, together with 9 additional beamlines operated by Collaborating Research Groups (CRGs) were open for user experiments. **Figure 182** shows the increase in the number of applications for beamtime since 1998, and confirms that although the main beamline construction effort was complete by 1999, the number of proposals for beamtime continues to rise.

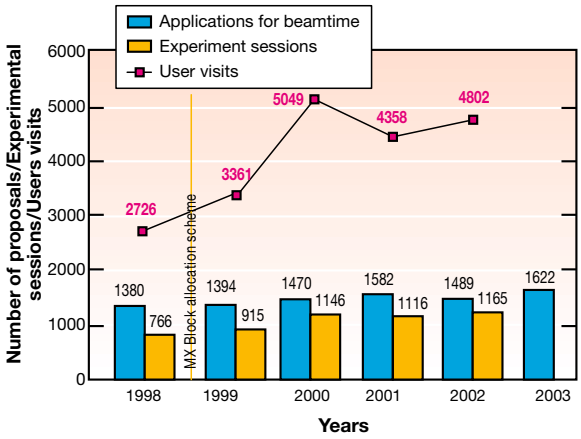

Fig. 182: Numbers of applications for beamtime, experiments carried out, and user visits, 1998 to 2002. N.B. Final numbers of experiments and user visits for 2003 were not available at the time of going to press.

Proposals for experiments are selected and beamtime allocations are made through peer review. Review Committees of specialists for the most part from European countries and Israel, have been set up in the following scientific areas:

- chemistry
- hard condensed matter: electronic and magnetic properties
- hard condensed matter: structures
- materials engineering and environmental matters
- macromolecular crystallography
- medicine
- methods and instrumentation
- soft condensed matter
- surfaces and interfaces

The Review Committees met twice during the year, some six weeks after the deadlines for submission of proposals (1 March and 1 September). They reviewed a total of 1622 applications for beamtime, and selected 769 (47%), which were then scheduled for experiments.

Features of this period have been:

- the convening of a Medical review committee, to assess research projects in medicine.
- increasing numbers of projects concerned more with applied than basic research in materials science, engineering and environmental matters. As shown in **Figure 183**, experiments in these areas accounted for 12% of the total number of shifts scheduled in the first half of 2003, an increase from 10% in 2002.
- the continued successful operation of the Block Allocation Group (BAG) scheme for macromolecular crystallography users. This scheme, designed to encourage groups of users to block together their multiple requests for beamtime, and the scheduling of their experiments, encompassed 39 groups from Europe and Israel in 2003.

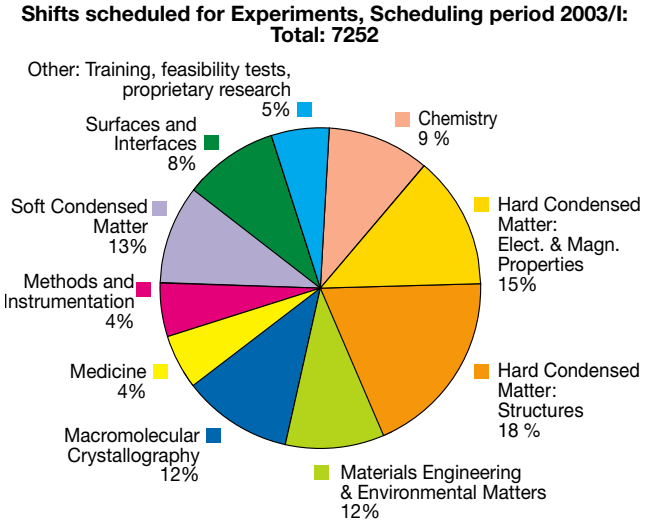

Fig. 183: Shifts scheduled for experiments, from March to August 2003, by scientific area.

Requests for beamtime, which is scheduled in shifts of 8 hours, totalled 25 740 shifts or 205 920 hours in 2003, of which 12 486 shifts or 99 888 hours (48.5%) were allocated. The distribution of shifts requested and allocated, by scientific area, is shown in **Table 11**.

Scientific field	Total shifts requested	Total shifts allocated
Chemistry	2 746	1 253
Hard condensed matter:		
• Electronic and magnetic prop.	3 849	1 950
• Structures	5 495	2 314
Materials engineering & environmental matters	3 238	1 475
Macromolecular crystallography	2 652	1 669
Medicine	895	459
Methods & instrumentation	1 061	497
Soft condensed matter	3 490	1 633
Surfaces & interfaces	2 314	1 236
Totals	**25 740**	**12 486**

Table 11: Number of shifts of beamtime requested and allocated for user experiments, year 2003.

The first half of 2003 saw 2639 visits by scientists to the ESRF under the user programme, to carry out 641 experiments. **Figure 182** shows the rapid rise in the number of user visits since 1998, the higher numbers in

recent years reflecting in part the multiple visits made by macromolecular crystallography BAG teams. The peak in 2000 is due to a somewhat longer scheduling period, and correspondingly higher overall number of experimental sessions, and visits by users.

Overall, the number of users in each experimental team averaged 4 persons, and they stayed for some 4 days. Users responding to questionnaires indicate that they particularly appreciate the assistance they receive from scientists and support staff on beamlines, and smooth administrative arrangements, in addition to the quality both of the beam and of the experimental stations. Facilities on site, such as preparation laboratories, a canteen and the Guesthouse, also make an important contribution to the quality of user support.

On the beamlines, beamtime losses tended to occur because of occasional difficulties with samples, computing, or with the beamline components. Such beamtime losses, however, remained below 5% of the total shifts scheduled for experiments during the period.

Administration and Finance

Expenditure and income 2002

Expenditure	kEuro	kEuro	Income	kEuro
Machine			2002 Members' contributions	63 945.5
Personnel		4 375.2	Funds carried forward from 2001	0.0
Recurrent		2 069.4		
Operating costs	*1 639.8*		Other income	
Other recurrent costs	*429.6*		Scientific Associates	3 521.6
Capital		4 113.2	Sale of beamtime	1 315.2
Machine developments	*4 113.2*		Other sales	385.7
Beamlines, experiments and in-house research			Compensatory funds	802.0
			Funds from Slab settlement	29.0
Personnel		19 511.4	Scientific collaboration and Special projects	559.7
Recurrent		6 383.2	Bank loans	242.0
Operating costs	*3 538.3*		Other	866.1
Other Recurrent costs	*2 844.9*			
Capital		7 869.0		
Beamline developments	*5 295.4*			
Beamline refurbishment	*2 573.6*			
Technical and administrative supports				
Personnel		14 796.3		
Recurrent		8 865.8		
Capital		3 665.3		
Unexpended committed funds				
Funds carried forward to 2003		18.0		
Total		**71 666.8**	**Total**	**71 668.8**

Revised expenditure and income budget for 2003

Expenditure	kEuro	kEuro	Income	kEuro
Machine			2003 Members' contributions	64 872
Personnel		4 750	Funds carried forward from 2002	18
Recurrent		2 098		
Operating costs	*1 685*		Other income	
Other recurrent costs	*413*		Scientific Associates	3 123
Capital		4 082	Sale of beamtime	1 525
Machine developments	*4 082*		Other sales	235
Beamlines, instruments, experiments and in-house research			Compensatory income	1 281
			Scientific collaboration and Special projects	955
Personnel		20 255	Other	1 525
Recurrent		6 589		
Operating costs	*3 588*			
Other Recurrent costs	*3 001*			
Capital		8 560		
Beamline developments	*4 149*			
Beamline refurbishment	*4 411*			
Technical and administrative supports				
Personnel		14 770		
Recurrent		8 879		
Capital		2 976		
Industrial and commercial activity				
Personnel		385		
Recurrent		190		
Total		**73 534**	**Total**	**73 534**

Expenditure 2002 by nature of expenditure

	kEuro
PERSONNEL	
ESRF staff	37 127.8
External temporary staff	29.3
Other personnel costs	1 525.9
RECURRENT	
Consumables	6 227.4
Services	9 001.0
Other recurrent costs	2 089.9
CAPITAL	
Buildings, infrastructure	1 949.7
Lab. and Workshops	344.5
Machine incl. ID's and Fes	4 113.3
Beamlines, Experiments	7 869.0
Computing Infrastructure	1 274.2
Other Capital costs	96.8
Unexpended committed funds	
Funds carried forward to 2003	18
Total	**71 666.8**

Revised budget for 2003 by nature of expenditure

	kEuro
PERSONNEL	
ESRF staff	38 439
External temporary staff	80
Other personnel costs	1 641
RECURRENT	
Consumables	6 039
Services	9 416
Other recurrent costs	2 301
CAPITAL	
Buildings, infrastructure	1 277
Lab. and Workshops	388
Machine incl. ID's and Fes	4 082
Beamlines, Experiments	8 560
Computing Infrastructure	1 068
Other Capital costs	243
Total	**73 534**

2003 manpower
(posts filled on 31/12/2003)

	Cadres	Non cadres	PhD students	Total
Staff on regular positions				
Machine	24	41	1	66
Beamlines, instruments and experiments*	208	66.3	25.5	299.8
General technical services	52.6	65.6		118.1
Directorate, administration and central services	25.3	54.6		80
Sub-total	*309.9*	*227.5*	*26.5*	*563.9*
Other positions				
Short term contracts	7	13.9		20.9
Scientific collaborators	5			5
Staff under "contrats de qualification" (apprentices)		14		14
European Union grants	4			4
Temporary workers		1		1
Total	**325.9**	**256.4**	**26.6**	**608.8**
Absences of staff (equivalent full time posts)				24.2
Total with absences				*584.6*
External funded research fellows	*16*			

** Including scientific staff on time limited contract.*

Financial resources in 2001, 2002, 2003 and 2004, by programme
(current prices in MEuro for the respective years)

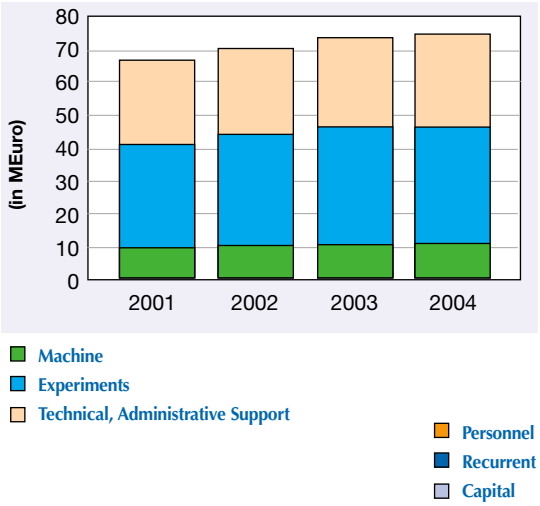

Financial resources in 2001, 2002, 2003 and 2004, by nature of expenditure
(current prices in MEuro for the respective years)

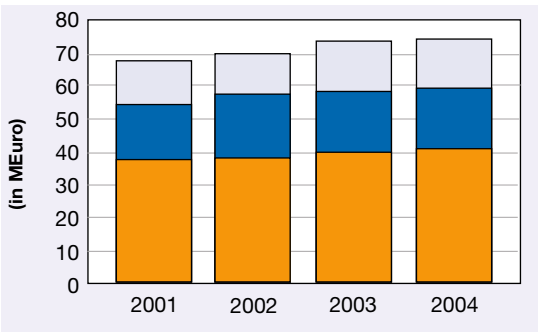

Organisation chart of the ESRF (as of January 2004)

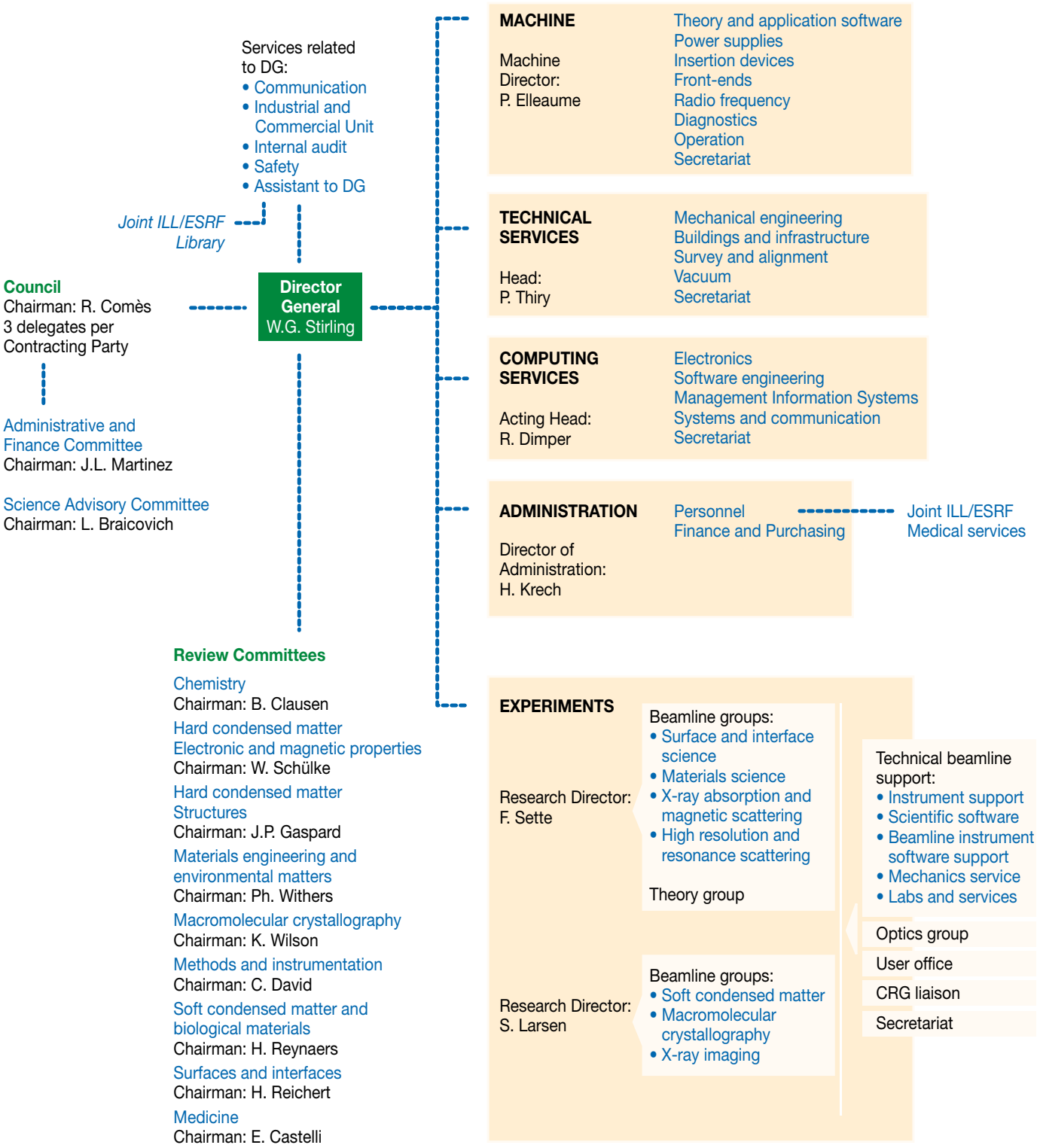

We gratefully acknowledge the help of:
J. Baruchel, N. Brookes, F. Comin, P. Elleaume,
S. Ferrer, A. Freund, H. Graafsma, Å. Kvick,
S. Larsen, G. Leonard, R. Mason, C. Morawe,
S. Pascarelli, C. Riekel, R. Rüffer, F. Sette,
W.G. Stirling, McSweeney, K. Witte.

Editor
G. Admans
Layout
Pixel Project
Printing
Imprimerie du Pont de Claix

Communication Unit
ESRF
BP220 • 38043 Grenoble • France
Tel. (33) 4 76 88 20 25 • Fax. (33) 4 76 88 24 18
http://www.esrf.fr